DOE-ER-0313/41
Distribution
Categories
UC-423, -424

FUSION MATERIALS
SEMIANNUAL PROGRESS REPORT
FOR THE PERIOD ENDING
December 31, 2006

Prepared for
DOE Office of Fusion Energy Sciences
(AT 60 20 10 0)

DATE PUBLISHED: March 2007

Prepared for
OAK RIDGE NATIONAL LABORATORY
Oak Ridge, Tennessee 37831
Managed by
UT-Battelle, LLC
For the
U.S. DEPARTMENT OF ENERGY

FOREWORD

This is the forty-first in a series of semiannual technical progress reports on fusion materials science activities supported by the Fusion Energy Sciences Program of the U.S. Department of Energy. This report focuses on research addressing the effects on materials properties and performance from exposure to the neutronic, thermal, and chemical environments anticipated in the chambers of fusion experiments and energy systems. This research is a major element of the national effort to establish the materials knowledge base of an economically and environmentally attractive fusion energy source. Research activities on issues related to the interaction of materials with plasmas are reported separately.

The results reported are the product of a national effort involving a number of national laboratories and universities. A large fraction of this work, particularly in relation to fission reactor irradiations, is carried out collaboratively with partners in Japan, Russia, and the European Union. The purpose of this series of reports is to provide a working technical record for the use of program participants, and to provide a means of communicating the efforts of fusion materials scientists to the broader fusion community, both nationally and worldwide.

This report has been compiled and edited under the guidance of R. L. Klueh, Glenda Hamlin and Teresa Roe, Oak Ridge National Laboratory. Their efforts, and the efforts of the many persons who made technical contributions, are gratefully acknowledged.

G. R. Nardella
Research Division
Office of Fusion Energy Sciences

TABLE OF CONTENTS

1.0 VANADIUM ALLOYS

PROGRESS IN CONSTRUCTION OF A V-4CR-4TI THERMAL CONVECTION LOOP AND TEST FACILITY – ORNL Loop Team: B. A. Pint, S. J. Pawel, M. Howell, J. L. Moser, G. Garner, M. Santella, P. F. Tortorelli, and J. R. Distefano (Oak Ridge National Laboratory)

OBJECTIVE

The objective of this project is to operate a flowing Li experiment to test the Li compatibility in a thermal gradient of V-4Cr-4Ti and a multi-layer electrically-insulating coating needed to reduce the magneto hydrodynamic (MHD) force in the first wall of a lithium cooled blanket. The experiment is planned to start in February of 2007 and run for 1,000h at 700°C.

SUMMARY

A test loop made of stainless steel (SS) was fabricated and tested in the vacuum chamber to establish the test procedures, condition the refractory metal furnaces and identify potential problems. The vacuum system, furnaces and cold-leg preheating system performed well. At ~550°C peak temperature, a thermal gradient of ~175°C was achieved with a Li velocity of ~4 cm/s. The major problem identified was temperature measurement. This issue is being addressed by increasing the number of thermal wells from one to four in the V-4Cr-4Ti loop. Fabrication of the V-4Cr-4Ti loop has begun. Two-layer (Y_2O_3/V) coatings on V-4Cr-4Ti substrates have been fabricated and will be placed in the hot and cold legs of the loop along with uncoated specimens.

PROGRESS AND STATUS

Introduction

A self-cooled lithium blanket concept is attractive for a fusion reactor because of lithium's tritium breeding capability and excellent heat transfer characteristics. Due to compatibility issues at >500°C, vanadium alloys [1] are the most likely structural materials for this concept. One of the critical issues for this, and any liquid-metal concept, is the need to reduce the pressure drop associated with the magneto hydrodynamic (MHD) force due to the high magnetic field in the reactor.[2,3] One solution to the MHD problem is to apply an electrically insulating coating to decouple the structural wall from the liquid metal.[4] The coating must be thin, durable and have a high electrical resistivity. It also must be almost crack-free to prevent shorting.[5,6] The current focus of the U.S. program on reducing the MHD pressure drop is on durable multi-layer coatings or a flow-channel insert.[7,8] Both of these solutions have been previously proposed;[4,9,10] however, little experimental verification has been conducted. Both concepts rely on excellent compatibility of a relatively thin V or V alloy layer to prevent Li from contacting and degrading the insulating ceramic layer. Initial capsule and in-situ testing of multi-layer coatings have shown promising results.[11] However, a flowing Li test with a temperature gradient is needed to validate the compatibility of such thin layers. A brief summary of the vanadium-lithium compatibility literature[12] indicated a wide range of results with no systematic study of the effects or relative importance of alloying elements and Li impurities. Ideally, a monometallic loop with relatively high purity Li and V specimens is needed to clarify the range of results found for V alloys in Li and preparations for a flowing Li thermal convection loop experiment are currently underway. The current plan is to run the loop for 1000h with a maximum temperature of 700°C beginning in February 2007. The loop will be destructively evaluated after the test with characterization completed later in 2007.

Results and Discussion

Stainless steel test loop. A vacuum of ~10^{-5} Pa is needed to run a high temperature V-4Cr-4Ti loop to avoid excessive oxygen uptake, and concomitant embrittlement, by the vanadium alloy tubing during the

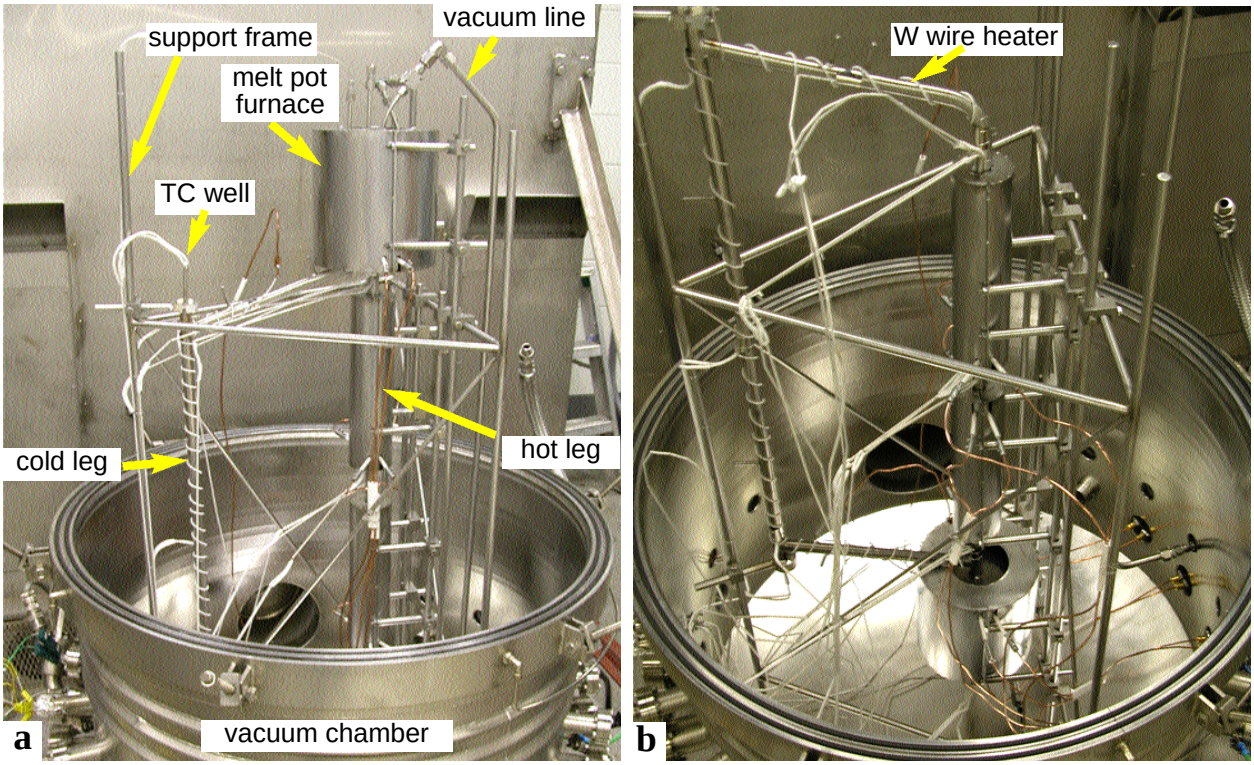

Figure 1. Photographs of (a) the SS loop in the vacuum chamber before bakeout, (b) the inverted SS loop ready for dumping the Li back into the pot.

experiment.[13] To test the planned procedure for running a loop in a vacuum chamber, a type 316 SS loop (~1m tall) was fabricated using the same design as developed for the V-4Cr-4Ti loop. A SS frame was built to hold the loop, 3 Mo wire heating element furnaces (2 hot leg, 1 melt pot) and 17 thermocouples (15 type K, 2 type S), Figure 1a. Each thermocouple (TC) was held in contact with the outside of the tube surface using SS foil and wire. Control and over temperature TCs were used on each furnace and at various locations around the loop. One thermal well was located at the top of the cold leg, Figure 1a, with the tip of the well touching the flowing Li. The chamber was baked out at 150°C for 24h prior to testing the furnaces. (For the V-4Cr-4Ti loop, the bakeout duration will be increased to ~48h to improve the vacuum.) The Li was loaded as sticks into the melt pot before it was welded shut. The Li loading of the loop was accomplished by heating the melt pot (Figure 1a) above the Li melting temperature. A ~3m long W wire with alumina beads was used to heat the cold leg to ~250°C using ~6A to prevent Li from freezing in the cold leg during the filling process. The hot leg furnaces were heated to 600°C before the furnace around the melt pot was turned on. There was some indication (TC variations) of Li melting into the loop when the pot temperature reached >180°C. The loop appeared to fill completely when the pot reached ~360°C.

Lithium flow was maintained for ~48h while the system performance was evaluated. Figure 2 shows the measured temperatures and various estimates of the temperature profile. There was a large, unexpected difference between the TC in the thermal well (TC13) and the TC on the outside of the adjacent tubing (TC10). This was most likely due to a short in the outside TC wire observed on completion of the test. Also, there was a large difference (20-30°C) between the pair of type K and type S thermocouples located at the top and bottom of the hot leg (e.g. TC7 and TC16 in Figure 2). Some of these differences can be attributed to the poor heat conduction in the vacuum and the relatively low thermal conductivity of SS. The differences likely would have been reduced as the system temperature was increased. However, the

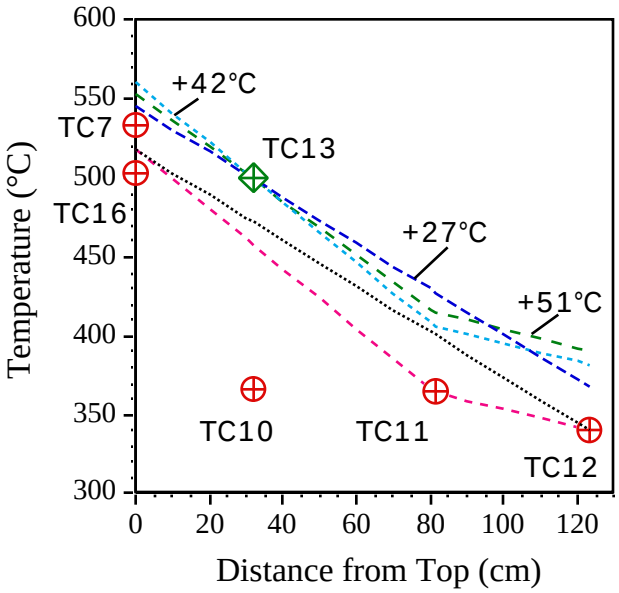

Figure 2. Temperature versus location plot for steady-state loop operation. TC7 and 16 were at the top of the hot leg and TC 10, 11 and 12 were at the top middle and bottom of the cold leg. The measured temperatures are plotted along with several estimates of the profile to estimate the maximum Li temperature.

temperature was not increased above the profile shown in Figure 2 because of the uncertainty of the maximum Li temperature. Because of the TC differences observed and the lack of other thermal wells, the measurement of the Li temperature was not adequate and will be corrected on the V-4Cr-4Ti loop by increasing the number of thermal wells to four (top and bottom of both hot and cold legs).

Two SiC heaters were located on the bottom leg of the loop to provide a “hot spot” test. The heaters were fully energized and the increase in temperature was tracked around half of the loop to measure the Li velocity. Some of these data are shown in Figure 3, which indicated a velocity of ~3.9 cm/s. The hot spot system worked better than expected and will be included in the V-4Cr-4Ti loop

V-4Cr-4Ti loop construction. The V-4Cr-4Ti tubing (19mm OD, 1.6mm wall thickness) has been cut and machined to size and welded, Figure 4a. All of the parts, including the inside of the tubing were acid ($60H_2O$-$30HNO_3$-10%HF) cleaned, acetone wiped and air dried prior to welding. Figure 4b shows a closeup of the nipple at the bottom of the cold leg. This will be cut off to connect a gas line for dumping the loop. Figure 4c shows one of the four thermal wells, also made from V-4Cr-4Ti. The top, bottom and side of the melt pot have been made and the side seam welded, Figure 4d. The only part of the system not made from V-4Cr-4Ti are the five 6.4mm tubes into the top of the melt pot (2 thermal wells, 1 for evacuating the loop and 2 used during dumping the loop). Due to lack of appropriate sized V-4Cr-4Ti tubing, Nb-1Zr tubing was used. The Nb-1Zr should not be in contact with Li during the flowing test and should therefore not affect the results.

To test the quality of the V-4Cr-4Ti tubing, a capsule was made by welding ends onto a length of tubing. Three SS-3 type V-4Cr-4Ti specimens were placed in the capsule. It contained Li for 1000h at 800°C with no leaking observed. The post-exposure Li chemistry has not been checked.

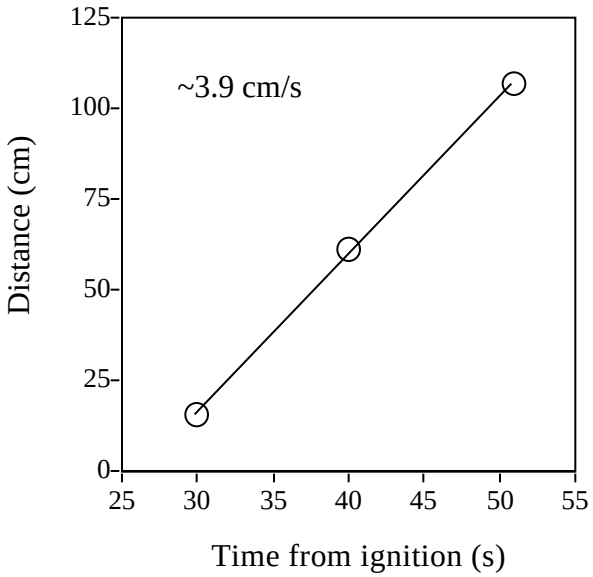

Figure 3. Time versus distance plot for one of the hot spot tests to determine the Li velocity with a peak temperature of 550°C and a 175°C gradient.

Compatibility specimens. As discussed in the previous report,[14] various V-4Cr-4Ti specimens will be used in the specimen chains in the hot and cold leg of the loop. Figure 5a shows a picture of a segment of the specimen chain which includes spacers (with a width similar to the tube ID), SS-3 type tensile specimens and the two layer MHD coating specimen (with a temporary protective covering). The pieces are connected with V-4Cr-4Ti wire. A typical coated specimen is shown in Figure 5b. The central area (arrow) has a ~10μm thick Y_2O_3 coating which is covered by ~10μm of vanadium (central square area). Both coatings were made by physical vapor deposition at Lawrence Livermore National Laboratory. Two batches of coatings were made. The second batch did not produce an optimal composition. One

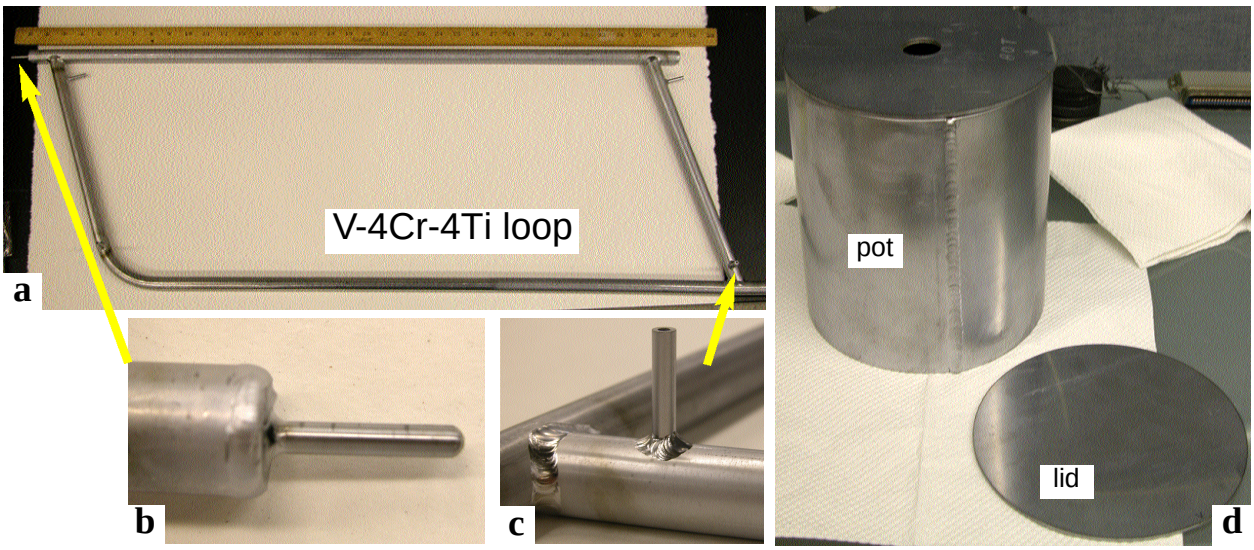

Figure 4. Photographs of (a) the V-4Cr-4Ti loop with closeups of (b) the cold leg nipple and (c) the thermal well at the top of the hot leg and (d) the melt pot and lid before the lid connections were fabricated.

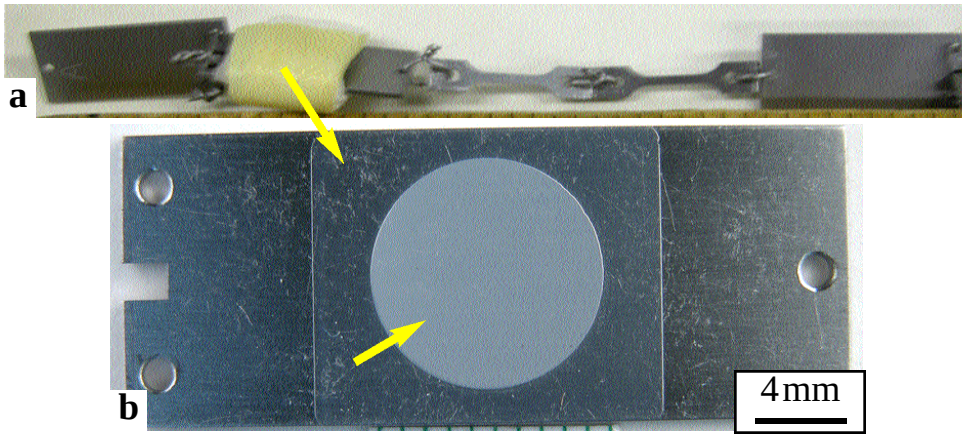

Figure 5. Photograph of examples of V-4Cr-4Ti tab and SS-3 tensile specimens prepared for the loop experiment. The circle (arrow) gives an indication of the PVD oxide (Y_2O_3 or Er_2O_3) coatings that will be applied to some specimens and then overcoated with 10μm of vanadium.

specimen from each batch will be held for characterization. The specimens from the second batch will be placed in the cooler sections of the loop while the coatings with higher quality Y_2O_3 will be placed in the hottest sections of the loop where degradation would be most likely. Post-exposure characterization of the thin V outer layer on these coatings will be one of the critical evaluations for determining compatibility.

References

[1] R. J. Kurtz, K. Abe, V. M. Chernov, D. T. Hoelzer, H. Matsui, T. Muroga, and G. R. Odette, J. Nucl. Mater. 329-333 (2004) 47.
[2] I. R. Kirillov, C. B. Reed, L. Barleon, and K. Miyazaki, Fusion Eng. Des. 27 (1995) 553.
[3] L. Barleon, V. Casal, and L. Lenhart, Fusion Eng. Des. 14 (1991) 401.
[4] S. Malang, H. U. Borgstedt, E. H. Farnum, K. Natesan, and I. V. Vitkovski, Fusion Eng. Des. 27 (1995) 570.
[5] L. Bühler, Fusion Eng. Des. 27 (1995) 650.
[6] A. Y. Ying and A. A. Gaizer, Fusion Eng. Des. 27 (1995) 634.
[7] B. A. Pint, P. F. Tortorelli, A. Jankowski, J. Hays, T. Muroga, A. Suzuki, O. I. Yeliseyeva, and V. M. Chernov, J. Nucl. Mater. 329-333 (2004) 119.
[8] B. A. Pint, J. L. Moser, and P. F. Tortorelli, Fusion Eng. Des. 81 (2006) 901.
[9] Y. Y. Liu and D. L. Smith, J. Nucl. Mater. 141-143 (1986) 38.
[10] I. V. Vitkovsky et al., Fusion Eng. Des. 61-62 (2002) 739.
[11] B. A. Pint, J. L. Moser, A. Jankowski, and J. Hayes, Journal of Nuclear Materials (in press).
[12] B. A. Pint, K. L. More, H. M. Meyer, and J. R. DiStefano, Fusion Sci. Technol. 47 (2005) 851.
[13] B. A. Pint and J. R. DiStefano, Oxid. Met. 62 (2005) 33.
[14] B. A. Pint, S. J. Pawel, and J. L. Moser, DOE-ER-0313/40 (2006) 2.

2.0 CERAMIC COMPOSITE MATERIALS

ANALYZING IRRADIATION-INDUCED CREEP OF SILICON CARBIDE—Y. Katoh, L. L. Snead, and S. Golubov (Oak Ridge National Laboratory)

OBJECTIVE

The objectives of this work were to develop simple models of transient irradiation creep and swelling of silicon carbide, to examine adequacy of the models, and to help defining specific priority objectives of future experiments, in support of resolving critical design issues for silicon carbide-based materials for flow channel insert and other fusion applications.

SUMMARY

Irradiation creep, which is among the major lifetime-limiting mechanisms for nuclear structural materials, is stress-driven anisotropic plastic deformation occurring in excess of thermal creep deformation in radiation environments. In this work, experimental irradiation creep data for beta-phase silicon carbide (SiC) irradiated at intermediate temperatures is analyzed using a rate theory model with an assumed linear-coupling of creep strain rate with the rate of self interstitial atom (SIA) absorption at SIA clusters. The model reasonably explains the experimentally observed time-dependent creep rate of ion-irradiated SiC and swelling evolution of ion- and neutron-irradiated SiC. Bend stress relaxation behavior during irradiation was then simulated using the developed model to confirm agreement with the experimental data obtained by neutron irradiation experiments. Recommended directions of future experiment are provided to further verify and improve the models and assumptions in this work.

PROGRESS AND STATUS

Introduction

Creep deformation and rupture are major lifetime-limiting mechanisms for high temperature materials for structural applications. In nuclear environments, irradiation-induced creep is additive to thermally activated creep deformation [1]. Irradiation creep is anisotropic plastic deformation driven by external or internal stresses, and is induced or enhanced by irradiation in excess of thermal creep deformation. In many cases, irradiation creep is caused by the preferred nucleation of planar defect clusters and/or preferred absorption of supersaturated point defects at edge dislocations [2]. Because irradiation creep is typically not very sensitive to temperature, irradiation creep tends to dominate at lower temperatures. For structural ceramics and ceramic composites for nuclear applications, irradiation creep is one of the most critical unresolved issues [3]. In this work, limited experimental irradiation creep data for beta-phase silicon carbide (SiC) is analyzed using a rate theory model.

Model Description

In mean-field rate theory of defect evolution in irradiated materials, Frenkel defect concentrations are expressed by following equation.

$$\dot{C}_{i,v} = G_{i,v} - \mu_R D_i C_i C_v - D_{i,v} C_{i,v} \sum S^{i,v} \qquad (1)$$

where G is the generation rate, μ_R is the recombination coefficient, D is the diffusivity, S is the sink strength of various extended defects, and subscripts i and v denote self interstitial atom (SIA) and vacancy, respectively. Recombination coefficient is given by $\mu_R = 4\pi r_R/\Omega$, where r_R is the recombination radius and Ω is the atomic volume. Equation (1) assumes $D_i >> D_v$. In SiC, vacancies are practically immobile below ~800ºC, as reported by various fundamental experiments [4,5]. Recent ab-initio calculation studies report minimum migration energies of ~3.5 eV and ~2.4 eV for C and Si vacancies, supporting the extremely limited vacancy mobility at <~800ºC [6]. For intermediate temperature, at which only SIAs are practically mobile, Eq. (1) can be rewritten as

$$\dot{C}_i = G - \mu_R D_i C_i C_v - D_i C_i \sum S_i \quad (2)$$

$$\dot{C}_v = G - \mu_R D_i C_i C_v \quad (3)$$

where $G = G_i = G_v$.

Irradiation-produced defects observed in SiC by transmission electron microscopy after irradiation at <~1000ºC are tiny unidentified defect clusters and dislocation loops. Both types of clusters are believed to be of interstitial-type, because of the very limited mobility of vacancies. For simplicity, all the defect clusters are treated as Frank dislocation loops of interstitial-type here, and the loop number density is assumed to be the temperature-dependent constant. Now, because thermal dissociation of SIA clusters may be inhibited due to very high SIA formation energy (>~6 eV [7]) in SiC, the derivative of the average loop radius rl is determined only by SIA influx and is given by:

$$\dot{r}_l = D_i C_i / b \quad (4)$$

where b is the magnitude of Burgers vector. Additionally, microstructural sinks other than SIA clusters are ignored, because typical mean inter-spacing of SIA clusters are <~10 nm, which is more than one order smaller than typical subgrain sizes in chemically vapor-deposited SiC. Thus, total sink strength for freely migrating SIAs is given as:

$$\sum S_i \approx S_l^i = 2\pi Z_l^i r_l N_l \quad (5)$$

where Z^i_l, taken as 1 in this work, and N_l are loop-interstitial bias factor and loop number density, respectively.

Mechanisms commonly used to explain irradiation creep phenomena of metallic materials are stress-induced preferred loop nucleation or alignment (SIPN), stress-induced preferred absorption of SIAs at dislocations (SIPA), and preferred absorption-enabled glide (PAG) [2,8]. Both SIPN and SIPA require only SIA clusters and migrating SIAs to operate, hence are potential operating mechanisms in SiC. Because there are no gliding dislocations observed in SiC irradiated at relatively low temperatures, PAG can not explain irradiation creep in SiC. Models of SIPN and SIPA both predict linear stress dependence of creep rates for metallic materials, which is in accordance with most experimental observations for metals [2].

In SiC irradiated at <~1000ºC, configurations of SIA clusters have not been characterized sufficiently to discuss kinetic models of irradiation creep [9]. Moreover, because the growth rate of tiny SIA clusters are so slow (cluster sizes remain a few nanometers at 7.7 dpa and 800ºC), it is very difficult to differentiate SIPN and SIPA even if either are the sole operators. However, for either mechanism, the creep rate is believed to be proportional to the total SIA influx to SIA clusters, thus

$$\dot{\varepsilon}_{ic} / \sigma = k_{ic} D_i C_i S_l^i \quad (6)$$

assuming linear stress dependency is maintained, and k_{ic} is a coupling coefficient for creep rate and SIA absorption at SIA clusters.

Analytical Solution

Minimum migration energies for C and Si SIAs in cubic SiC were estimated to be ~0.5 and ~1.4 eV, respectively, by a recent *ab-initio* calculation [6]. Because of the expected high diffusivities (relative to evolutions of other types of defects), the SIA concentration can be treated as in pseudo-equilibrium with

vacancies and other sinks. The C and Si Frenkel defects do not have to be differentiated with this pseudo-equilibrium treatment and vacancy immobility, when antisite defects are neglected. During most of the time of interest (>~10^{-3} dpa), $\alpha C_v >> D_i S_l$ is true, then

$$C_i \approx G/\mu_R D_i C_v \tag{7}$$

$$\dot{C}_V \approx S_l^i G/\mu_R C_v \tag{8}$$

From Eqs. (4), (5), (7), and (8), the following relations are derived.

$$C_i \approx \frac{1}{D_i}\left(\frac{Gb}{9\pi N_l \mu_R t^2}\right)^{1/3} \tag{9}$$

$$C_V \approx \left(\frac{3Gt}{\mu_R}\right)^{2/3}\left(\frac{\pi N_l}{b}\right)^{1/3} \tag{10}$$

$$r_l \approx \left(\frac{3Gt}{\mu_R \pi N_l b^2}\right)^{1/3} \tag{11}$$

The approximated analytical result presented here is consistent with the general analytical solution for the kinetics of low-temperature irradiation processes in metals provided by Golubov [10]. With the analysis presented here, Eqs. (6), (9), and (11) indicate that the irradiation creep rate is proportional to the -1/3 power of time or dose. Additionally, if low temperature swelling of SiC is assumed to be accounted solely by vacancies, Eqs. (10) and (11) imply that irradiation creep rate is in inverse proportion to the square root of swelling. This also suggests that, under a constant stress, a linear compliance that explicitly couples irradiation creep strain and swelling, exists.

Computational Analysis and Comparison with Experiments

In Fig. 1, calculated evolution of SIA absorption rate at SIA clusters, $D_i C_i S^l_i$, is presented. Parameters used for this calculation are listed in Table. 1. The -2/3 power relationship is achieved at a dose of ~10^{-3} dpa, approximately when a recombination-dominant condition ($\alpha C_v >> D_i S^l_i$) is established, and continues until onset of the saturation behavior. A dose of ~10^{-3} dpa is also typical before which SIA cluster nucleation through a homogeneous nucleation process nears completion. The calculation here incorporated cascade re-solution terms for SIA cluster growth and SIA production, which enables the saturation behavior of defect accumulation that is widely observed in experiments. The effect of cascade re-solution becomes apparent between 0.1 and 1 dpa in this calculation, as shown in Fig. 1. Equations (2)-(4) were slightly modified to take the effect of stoichiometric constraint for SIA clusters into consideration. Details of computational method will be published elsewhere [11].

Table 1. Parameters used in calculation

Parameter (*Symbol*)	Value	Unit	Reference
Recombination radius (r_R)	$7.5\text{x}10^{-10}$	m	[12]
Diffusivity pre-exponential for SIA (D^0_i)	$1.58\text{x}10^{-6}$	m^2/s	[12]
SIA migration energy (E^m_i)	0.5	eV	[6]
SIA loop number density (N_l)	$2.2\text{x}10^{25}$ x exp(-0.00404 T)	m^{-3}	[9]
Displacement rate (G)	$1\text{x}10^{-6}$, $1\text{x}10^{-3}$, $3\text{x}10^{-6}$ (n, Si^{2+}, D^+)	dpa/s	-
Fraction of Si displacement to total displacement (f_{Si})	0.24, 0.32, 0.44 (n, Si^{2+}, D^+)	-	[13]

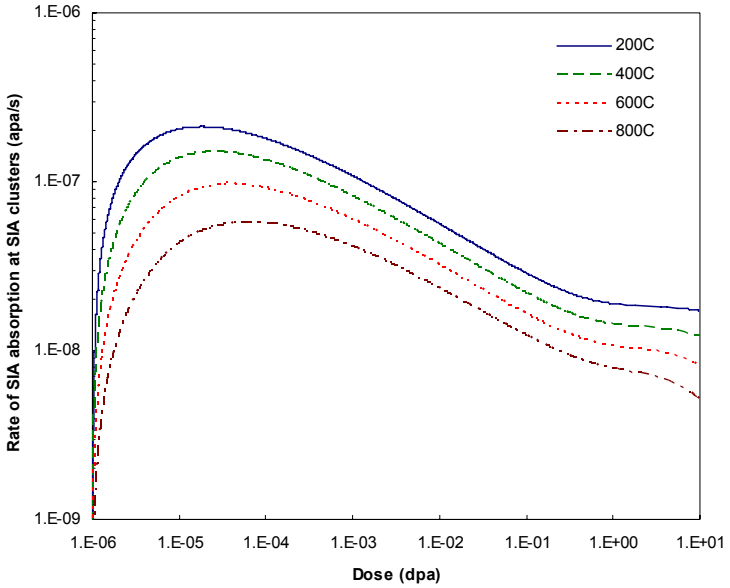

Fig. 1. Calculated dose-dependent evolution of rate of SIA absorption at SIA clusters in beta-SiC at intermediate temperatures.

In Fig. 2, swelling in high-purity, chemically vapor-deposited SiC during Si ion irradiation [14] is plotted against dose. It is seen that the magnitude of swelling approximately follows the 2/3 power law in a broad temperature range below ~800ºC until saturation occurs (<~0.3 dpa). In Fig. 3, dose dependence of swelling in the identical material during neutron irradiation in HFIR [15] is plotted. It is shown that the 2/3 power law also fits the neutron data reasonably at relatively low doses (<~0.1 dpa). These observations support adequacy of the present defect accumulation model.

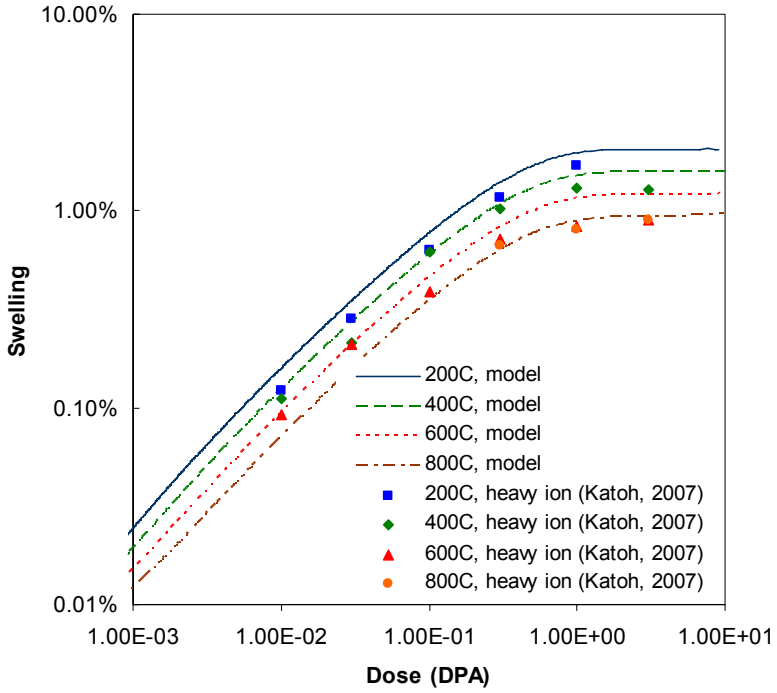

Fig. 2. Dose dependent evolution of swelling in high-purity beta-SiC during heavy ion irradiation: comparison of model and experiment. Experimental data by Katoh [14].

In Fig. 4, calculated irradiation creep strains in SiC during 14 MeV deuteron irradiation are presented as a function of dose, along with experimental data replotted from the torsional irradiation creep data for SCS-6 CVD SiC fibers by Scholz [16]. The creep strain appears to be proportional to approximately 2/3 power of dose, which is in agreement with the analytical model prediction. In this calculation, the coupling coefficient of creep rate with SIA absorption rate at SIA clusters, kic in Eq. (6), was taken to be 3×10^{-3} MPa^{-1} to fit the experimental data, when diffusivity Di is normalized to dpa. Fig. 4 also shows that the relative strains at different irradiation temperatures are in good agreement between experiment and calculation, which further support the model. The discrepancy between experiment and calculation at 800ºC may be due to non-linear stress dependence or slightly anomalous creep behavior recorded only at this temperature in Scholz work.

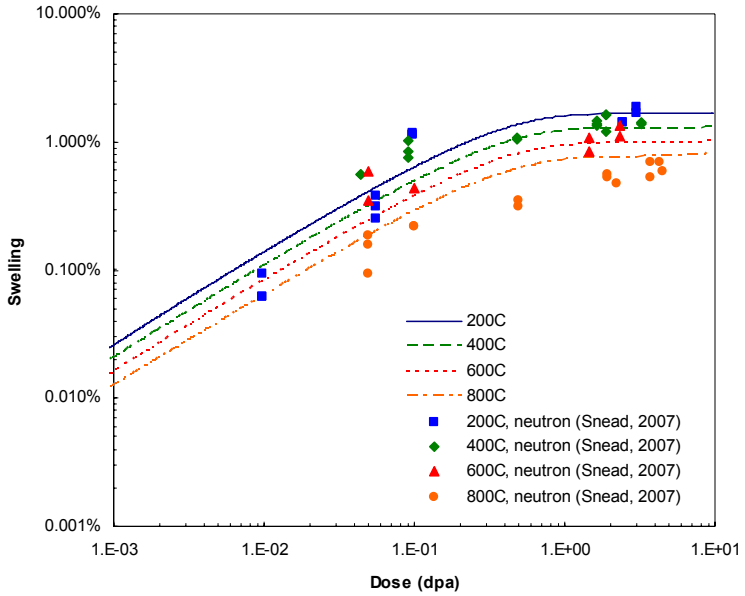

Fig. 3. Dose dependence of swelling in high-purity beta-SiC during neutron irradiation: comparison of model and experiment. Experimental data by Snead [15].

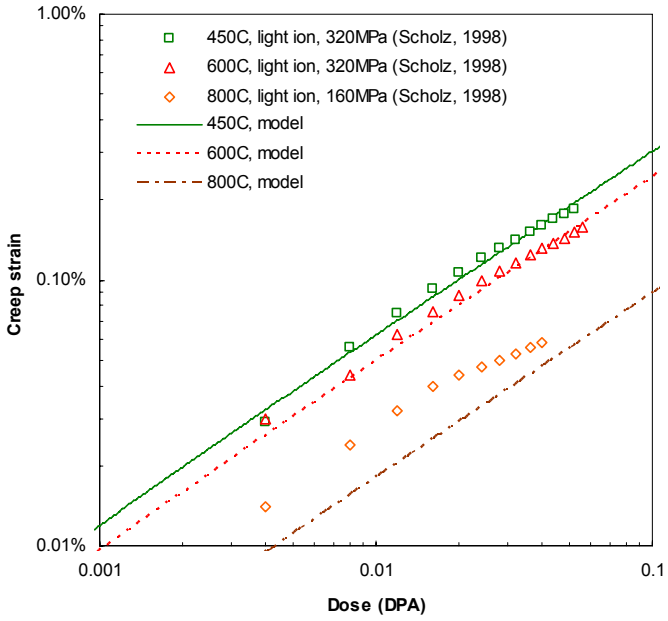

Fig. 4. Dose dependence of creep strain in beta-SiC during light ion irradiation: comparison of model and experiment. Experimental data by Scholz [16].

Analyzing Neutron Irradiation Creep Data

In a companion paper, bend stress relaxation (BSR) irradiation creep experiment was performed using thin strip specimens of high purity CVD SiC [17]. Detailed descriptions of experimental technique development and results are found elsewhere [18]. In Table 2, BSR irradiation creep data for CVD SiC are summarized. Additionally, result from an experiment by Price [19] was interpreted and included. These data are plotted in Fig. 5, in which calculated bend stress relaxation behavior of SiC based on the model described by Eqs. (2)-(6). The coupling coefficient kic was taken to be 3.5×10^{-4} MPa^{-1} to fit the experimental data for the intermediate temperatures (below 800ºC). The fitted coupling coefficient was approximately one order smaller for the neutron-irradiated high purity CVD SiC than for the deuteron-irradiated SCS-6. This difference may be due to the effect of displacement cascade for neutron irradiation, difference in loading mode (flexural in the neutron irradiation vs. torsional shear in the deuteron irradiation), difference in absolute stress levels coupled with potentially non-linear stress dependence of creep rate, and/or difference in material quality. On the other hand, a constant irradiation creep compliance reasonably explain the experimental result at high temperatures (>1030ºC). Obviously, more comprehensive sets of experimental data will be necessary to further examine adequacy of the models and various assumptions involved.

Table 2. Summary of neutron-irradiation creep data

Material	T_{irr} °C	Fluence dpa[1]	Reactor	Initial / final bend stress[2], MPa	Creep strain x10^{-4}	BSR ratio[3] *m*	Ref.
Rohm&Haas CVD SiC	640	3.7	HFIR[4]	87 / 36	1.12	0.42 (+0.03/-0.04)	[18]
	700	0.7		102 / 72	0.63	0.72 (+0.04/-0.06)	
	1030	0.7		86 / 61	0.52	0.73 (+0.04/-0.06)	
	1080	4.2		101 / 8	2.10	0.08 (+0.05/-0.06)	
Rohm&Haas CVD SiC	400	0.6	JMTR[5]	82 / 60	0.41	0.77 (+0.11/-0.19)	[18]
	600	0.2		81 / 57	0.49	0.73 (+0.10/-0.14)	
	600	0.6		81 / 46	0.75	0.58 (+0.10/-0.15)	
	750	0.6		80 / 55	0.53	0.71 (+0.11/-0.15)	
GA CVD SiC	780	7.7	ETR[6]	n/a[7]	n/a	0.36 (±0.03) [8]	[19]
	950	7.7				0.73 (+0.04/-0.06) [8]	
	1130	7.7				0.08 (+0.05/-0.08) [8]	

[1]Displacement per atom. [2]Maximum stress in a flexurally deformed sample. [3]Ratio of final-to-initial stresses. [4]High Flux Isotope Reactor, Oak Ridge National Laboratory. [5]Japan Materials Test Reactor, Japan Atomic Energy Agency. [6]Engineering Test Reactor, Oak Ridge National Laboratory. [7]Not available. [8]Calculated from linear-averaged creep compliance data.

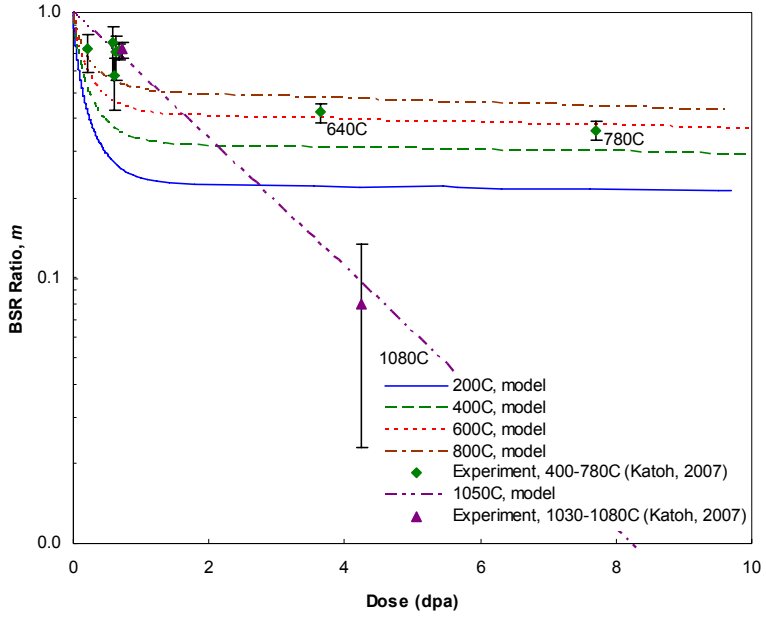

Fig. 5. Dose-dependent evolution of irradiation creep BSR ratio, m, of beta-SiC during neutron irradiation: comparison of model and experiment. Experimental data by Katoh [18] and Price [19].

Conclusions

Simple models of irradiation-induced dimensional instability of silicon carbide at intermediate temperatures were developed based on assumptions of linear-coupling between creep rate and SIA absorption rate at SIA clusters, as well as between swelling and matrix vacancy concentration. The model predicted that both swelling rate and creep compliance are proportional to the -1/3 power of dose under constant temperature and dose rate, until saturation swelling takes place. These predictions are consistent with published experimental data for beta-phase CVD SiC on swelling under neutron and self ion irradiation and on creep under light ion irradiation. Moreover, BSR irradiation creep behavior was simulated using the developed model to confirm a reasonable agreement with the experimental data obtained by neutron irradiation experiments.

To further confirm adequacy of the models and assumptions, and to narrow the ranges of uncertain parameters, it is essential to add credible experimental data on both irradiation creep and swelling, particularly at different temperatures and dose levels within an intermediate temperature (~200 - ~800ºC) / low (~1 dpa)-to-intermediate (~10 dpa) dose regime. It is also necessary that the stress dependence of irradiation creep rate is determined. Moreover, to understand the physical processes of irradiation creep in SiC, configurations of defect clusters and the influence of stress on microstructural development need to be further clarified. Result of this analysis will be utilized to design experimental matrices for future irradiation creep study on silicon carbide presently being planned in US and international fusion advanced materials programs.

References

[1] K. Ehrlich, J. Nucl. Mater. 100 (1981) 149–166.
[2] J. R. Matthews and M. W. Finnis, J. Nucl. Mater. 159 (1988) 257–285.
[3] Y. Katoh, L. L. Snead, C. H. Henager, A. Hasegawa, A. Kohyama, B. Riccardi, and J. B. J. Hegeman, Journal of Nuclear Materials (accepted for publication).
[4] H. Itoh, N. Hayakawa, I. Nashiyama, and E. Sakuma, J. Appl. Phys. 66 (1989) 4529–4531.
[5] A. Kawasuso, H. Itoh, N. Morishita, T. Ohshima, I. Nashiyama, S. Okada, H. Okumura, and S. Yoshida,

Applied Physics A 67 (1998) 209–212.
[6] M. Bockstedte, A. Mattausch, and O. Pankratov, Phys. Rev. B 68 (2003) 205201-1-17.
[7] F. Gao, E. J. Bylaska, W. J. Weber, and L. R. Corrales, Phys. Rev. B 64 (2001) 245208-1-7.
[8] L. K. Mansur, Philos. Mag. A 39 (1979) 497–506.
[9] Y. Katoh, N. Hashimoto, S. Kondo, L. L. Snead, and A. Kohyama, J. Nucl. Mater. 351 (2006) 228–240.
[10] S. I. Golubov, Phys. Met. Metall. 60 (1985) 7–13.
[11] Y. Katoh (to be submitted).
[12] R. A. Johnson, J. Nucl. Mater. 75 (1978) 77–84.
[13] F. Gao and W. J. Weber, Phys. Rev. B 63 (2000) 054101-1-7.
[14] Y. Katoh, H. Kishimoto, and A. Kohyama, J. Nucl. Mater. 307 (2002) 1221–1226.
[15] L. L. Snead, W. Cuddy, D. Peters, Y. Katoh, G. A. Newsome, and A. M. Williams, J. Nucl. Mater. (submitted).
[16] R. Scholz, J. Nucl. Mater. 258–263 (1998) 1533–1539.
[17] Y. Katoh and L. L. Snead, Ceram. Eng. Sci. Proc. 26 (2005) 265–272.
[18] Y. Katoh, L. L. Snead, T. Hinoki, S. Kondo, and A. Kohyama, Journal of Nuclear Materials (accepted for publication).
[19] R. J. Price, Nucl. Tech. 35 (1977) 320–336.

ANISOTROPY IN TENSILE PROPERTIES OF ADVANCED SILICON CARBIDE COMPOSITES—T. Nozawa, Y. Katoh (Oak Ridge National Laboratory), and R. J. Shinavski (Hyper-Therm High-Temperature Composites, Inc.)

OBJECTIVE

The objective of this study is to evaluate the anisotropy in tensile properties of nuclear-grade SiC/SiC composites to provide a basis for the practical component design.

SUMMARY

This study evaluates the anisotropy in tensile properties of satin-woven (S/W) or biaxially braided Hi-Nicalon™ Type-S fiber reinforced chemical-vapor-infiltrated (CVI) SiC matrix composites with multilayered interphase. Results indicate excellent axial and off-axis tensile fracture behaviors for the S/W composites. In contrast, the braided composites failed at unexpectedly lower stresses. The primary cause for this difference was the varied in-plane shear properties, on which off-axis tensile properties significantly depend. Superior in-plane shear properties for the S/W composites were achieved by increasing the volume fraction of transverse fibers normal to the fracture plane. Considering the failure modes depend on the off-axis angle, the anisotropy in proportional limit tensile stress and fracture strength were satisfactorily predicted by a simple stress criterion model. The anisotropy in Young's modulus was well-described by a conventional rule of mixtures for laminates. It is worth noting that specimen size effect on axial and off-axis tensile properties seems very minor for nuclear-grade SiC/SiC composites with rigid CVI-SiC matrix.

PROGRESS AND STATUS

Introduction

Silicon carbide (SiC) ceramics and composites are candidate materials for advanced fission and nuclear fusion applications due to several characteristics such as excellent stability of strength and thermal properties at elevated temperatures, chemical inertness, low radiation-induced activation and low after-heat. Additionally, a crystalline, high-purity, and stoichiometric SiC form such as chemically-vapor-deposited (CVD) SiC provides superior irradiation resistance, e.g., good strength retention [1], improved fracture toughness [2, 3], and moderate thermal transport properties under irradiation [4]. It is now recognized that nuclear-grade SiC/SiC composites reinforced by highly-crystalline and near-stoichiometric "Generation III" SiC fibers, i.e., Hi-Nicalon™ Type-S or Tyranno™-SA, with the high-quality SiC matrix, are similarly radiation-damage resistant [5–7]. Due to the recent advances of composite fabrication techniques and optimization of the fiber/matrix interface, remarkable improvement of the composite performance and reliability under neutron irradiation has been achieved [8].

One of the important design aspects for the use of composites is fiber architecture to ensure the best optimized margins against stresses generated by mechanical loading or thermal expansion in the axial and hoop directions, i.e., anisotropy. Multi-axial fiber reinforcement is often applied to mitigate the issue of anisotropic properties. Historically, studies on anisotropic tensile fracture behaviors of conventional SiC/SiC composites have been conducted [9, 10]. For advanced SiC/SiC composites with rigid matrix such as CVI-SiC, understanding the mechanical contribution from the matrix as well as the fiber should be essential since the rigid SiC matrix enables to transfer load as large as the reinforcing fiber can. Also, the role of the fiber/matrix interface should be emphasized.

Experimental Procedure

Nuclear-grade SiC/SiC composites with different fiber architectures were fabricated by Hyper-Therm High-Temperature Composites, Inc. (Huntington Beach, CA) and their key characteristics are summarized in Table 1. The reinforcement fiber was Hi-Nicalon™ Type-S and the matrix was CVI-SiC. The fiber bundles were biaxially braided for NG1 and NG2, or satin-woven for NG3. The off-axis angle was ±55° for NG1 and

±53° for NG2. A multilayered interface composed of a sequence of pyrolytic carbon (PyC) and CVI-SiC was formed on the fiber. The carbon adjacent to the fiber has a thickness of ~150 nm, while the other 4 surrounding layers have a thickness of ~20 nm. The thickness of the SiC inserts between carbon interlayers was ~100 nm. The density of NG1 braid composites was ~2.9 g/cm^3, while the density of NG2 braid was ~2.7 g/cm^3. Due to the high density of the NG1 braid, the porosity, V_p, of the NG1 braid was quite low, ~9%, although the NG2 composites possess the porosity of ~16%. The density and porosity of the NG3 S/W composites were ~2.7 g/cm^3 and ~16%, respectively. The total fiber volume fraction of 30~40% was designed for each material.

Table 1. Material properties of SiC/SiC composites tested

Material	ID	Loading axis	Density [g/cm^3]	Fiber Volume Fraction	Porosity
NG1 Biaxial braid [±55º]	Braid-35	Transverse	2.87	~0.3	0.09
	Braid-55	Axial	2.83	~0.3	0.08
NG2 Biaxial braid [±53º]	Braid-53	Axial	2.62	~0.3	0.16
NG3 Satin-weave [0º/90º]	S/W-0/90	Axial	2.69	~0.4	0.14
	S/W-45	45º off-axis	2.61	~0.4	0.16

Room-temperature tensile tests were performed following general guidelines of ASTM C1275-00. Two types of tensile specimens: a face-loaded straight bar specimen and an edge-loaded contoured specimen were used (Fig. 1). To investigate the effect of specimen size on tensile properties, the gauge width was varied from 4.0 to 15.0 mm. Sub-sets of tensile tests were conducted accompanied with unloading/ reloading cycles to evaluate the hysteresis response. Tensile strain was measured using a pair of strain gauges bonded in the middle gauge section of the specimen. The length of the stain gauges was 5.0 mm. For off-axis tensile tests, 90°-axis (transverse) and 45°-axis strains as well as 0°-axis (axial) strain were measured to determine the in-plane shear strain. A constant crosshead displacement rate of 0.5 mm/min was applied. Fracture surfaces were observed by the scanning electron microscopy.

In advance of tensile tests, dynamic Young's modulus was measured by the sonic resonance method according to ASTM C1259-01 only for straight bar specimens.

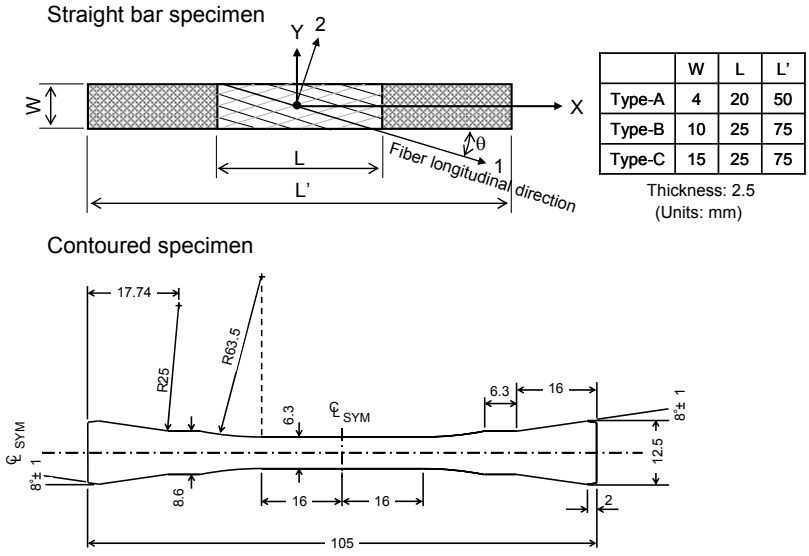

	W	L	L'
Type-A	4	20	50
Type-B	10	25	75
Type-C	15	25	75

Thickness: 2.5
(Units: mm)

Fig. 1. Schematic illustrations of tensile specimens.

Results and Discussion

Tensile fracture behavior

Figure 2 exhibits typical tensile stress-stain curves of the SiC/SiC composites tested. The tensile Young's modulus of the composites was defined as a tangential modulus from the initial linearity. The proportional limit tensile stress (PLS) was defined by the 5% deviation from linearity method. The tensile strength was defined as a failure load divided by the original gauge cross-section. Experimental errors indicated were deviation from the maximum or the minimum due to the scarce of valid tests, while scatter of dynamic Young's modulus means ± one standard deviation. The reduced data were summarized in Table 2.

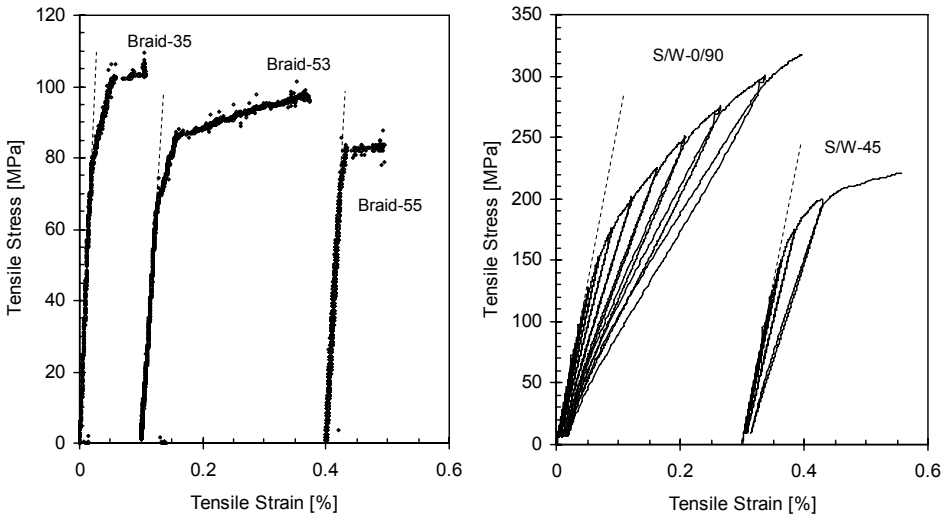

Fig. 2. Typical tensile stress-strain curves of advanced SiC/SiC composites.

Table 2. Tensile properties of advanced SiC/SiC composites

ID	Spec. type (Gauge width)	# of valid tests	Dynamic Young's modulus [GPa]	Tensile Young's modulus [GPa]	PLS [MPa]	Tensile strength [MPa]	Fracture strain [%]
Braid-35	Straight bar (10.0 mm)	3	314 ±1	369 +49/-66	68 +12/-6	105 +2/-1	0.16 +0.09/-0.05
Braid-55	Straight bar (4.0 mm)	3	338 ±6	302 +101/-73	86 +16/-18	87 +15/-19	0.03 +0.02/-0.01
	Contoured (6.3 mm)	4	-	237 +16/-13	79 +8/-8	82 +8/-9	0.04 +0.01/-0.01
	Straight bar (10.0 mm)	4	290 ±19	315 +62/-49	75 +3/-9	78 +6/-7	0.10 +0.15/-0.07
	Straight bar (15.0 mm)	2	282 ±0	395 +9/-9	82 +4/-4	91 +1/-1	0.04 +0.01/-0.01
Braid-53	Straight bar (10.0 mm)	5	218 ±12	174 +88/-55	62 +8/-7	108 +11/-11	0.51 +0.10/-0.24
S/W-0/90	Straight bar (4.0 mm)	9	276 ±9	277 +7/-11	111 +21/-19	346 +67/-50	0.34 +0.05/-0.05
	Contoured (6.3 mm)	4	-	256 +38/-26	114 +7/-10	348 +29/-43	0.62 +0.07/-0.12
S/W-45	Straight bar (4.0 mm)	5	232 ±11	248 +12/-32	136 +10/-9	206 +15/-32	0.33 +0.23/-0.24
	Contoured (6.3 mm)	4	-	232 +18/-32	102 +12/-14	206 +7/-4	0.44 +0.06/-0.07

Satin-woven composites (NG3) show superior tensile fracture behaviors coupled with graceful unloading/ reloading hysteresis curves. The tensile strength of S/W-0/90 was quite high over 300 MPa. Due primary to the anisotropy issue, the S/W-45 failed at a lower fracture stress (~210 MPa) than obtained in the axial tests. For both S/W-0/90 and S/W-45, the considerably high PLS (~130 MPa) was obtained. Meanwhile, NG1 and NG2 braid composites show comparably low tensile strength (~110 MPa) and PLS (~80 MPa). The major difference between NG1 and NG2 composites is the magnitude of failure strain. The failure strain for NG2 was significant (~0.51%), while most of NG1 failed by first matrix cracking at the proportional limit (0.03~0.16%). Although the NG1 braid composites with the dense matrix recorded the highest Young's modulus (~310 GPa), they were within the same magnitude.

It is worth noting that no major size effect seems anticipated in the specimen size range of this study. The effect of specimen size and geometry on axial and off-axial tensile properties for PIP SiC/SiC composites was reported by the authors [11]. The key conclusions of this study are 1) no systematic length, width and thickness effects on axial tensile properties if the fiber volume fraction in the loading direction in a unit structure is unchanged by specimen size, 2) the size dependency of off-axis tensile properties due to the size-relevant change of fracture modes, and 3) very minor effect of specimen geometry. The in-plane shear strength and detachment strength of the low-stiffness PIP-SiC matrix composites are inherently low. Additionally, very narrow specimens show much lower in-plane shear properties due to the size effect. A probable explanation for no major systematic size effect observed for advanced SiC/SiC composites is improved in-plane shear properties of the Generation III dense and rigid matrix composites as discussed later. It is speculated that high load transferability at the fiber/matrix interface can achieve superior in-plane shear properties for any size of specimens.

Figure 3 shows typical tensile fracture surfaces. The figure does not list fracture surfaces of Braid-35 due to the similarity with those of Braid-55. Generally, the fracture plane of the off-axis tensile specimens except for some of the Braid-35 and Braid-55 composites was parallel to the longitudinal fiber direction, although this does not conclude brittle fracture. It is obvious that there exist fiber pullouts on the fracture surface. Specifically blush-like fibers for S/W-45 indicate progressive debonding of transverse fibers normal to the fracture plane. Besides, major cracks propagated within the fiber bundles for Braid-53. These facts promise the in-plane shear as a primary fracture mode in off-axis tension. In contrast, the first matrix cracking behavior seems dominate a failure of NG1 braid composites, the fracture surface of which shows small amounts of very short fiber pullouts embedded in rich SiC matrix, causing a brittle-like fracture. The fracture surface of S/W-0/90 was very fibrous coupled with significant transverse cracks in

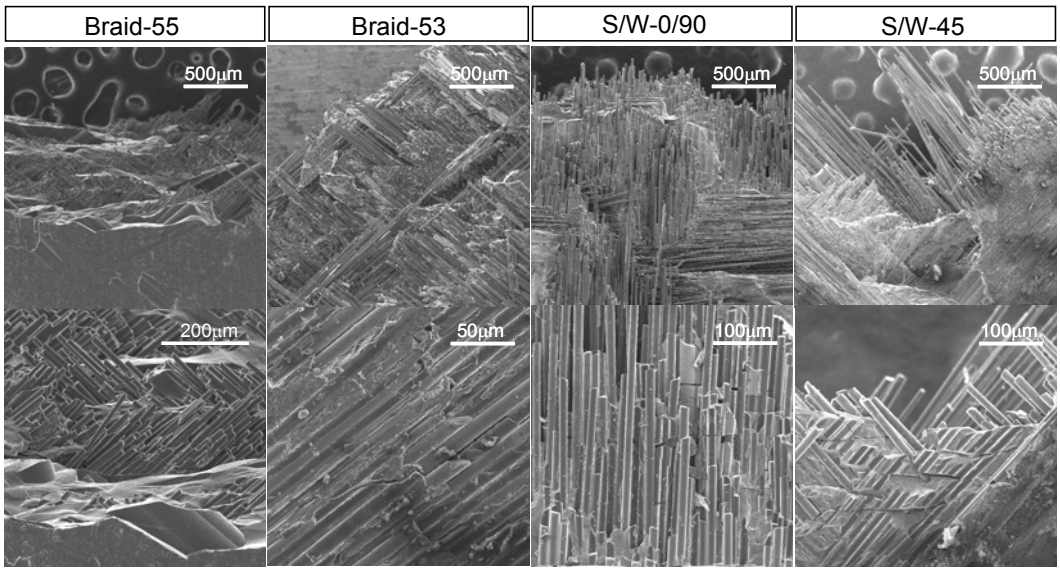

Fig. 3. Typical fracture surface images of SiC/SiC composites.

the 0°- bundles with an average crack spacing of ~25 μm. Similarly, very limited amounts of transverse cracks were observed for S/W-45. However, they were very minor and most of them were localized near the cross sections of the 45°-bundles.

Damage accumulation process

The damage parameter defined in Ref. 12, which is proportional to crack density, was first induced beyond the proportional limit (110~140 MPa) and rapidly increased when the applied stress exceeded ~165 MPa for both S/W-0/90 and S/W-45 (Fig. 4). In contrast, both loop width and inelastic strain index (L) were initiated at the stress of ~165 MPa and they increased monotonically with increasing applied stress. For a [0°/90°] fiber configuration, it is well-known that the damage accumulation first occurs by cracking in the 90°-bundles and then the 90°-bundle cracks extend to form transverse cracks, i.e., matrix cracking (in some paper this is referred to as tunnel cracking), in the 0°-bundles [13,14]. Accordingly, the stress to initiate matrix cracking, σ_{mc}, can be estimated as a stress at L = 0, i.e., σ_{mc} = 165 MPa. Since damages in composites rapidly increase beyond the materials proportional limit, the transverse cracking for S/W-0/90 generally occurred at lower stress than that of undamaged unidirectional (UD) composites (~230 MPa). In contrast, it is speculated that the secondary damage for S/W-45 was caused by the combined effect of in-plane shear and fiber detachments coupled with fiber sliding at the debonded fiber/matrix interface. Therefore, the similar analysis is not presently guaranteed for the off-axis tensile data.

Applying a mean matrix crack spacing of ~25 μm yields an estimated interfacial friction stress of ~100 MPa for S/W-0/90. This is within the same range obtained by the single fiber push-out test for UD Hi-Nicalon™ Type-S/CVI-SiC composites [15]. The high interfacial friction stress may contribute significantly to stress transferring at the interface during fiber pullout process.

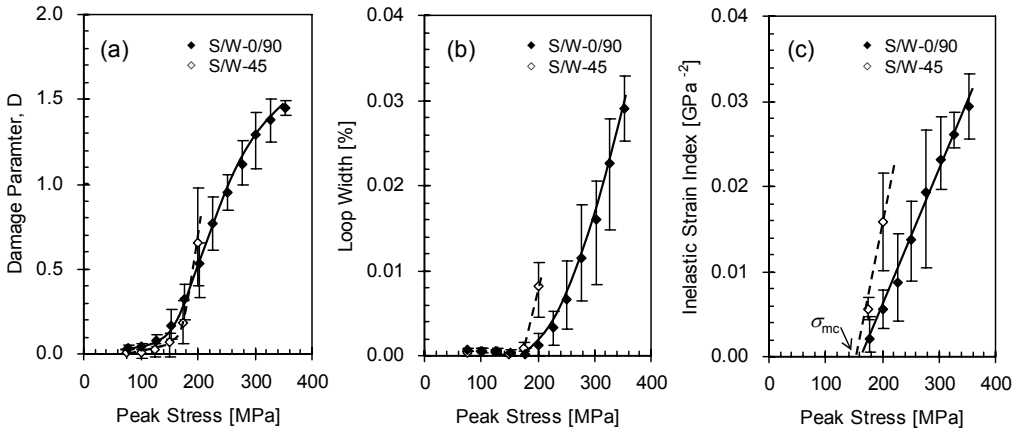

Fig. 4. (a) damage parameter, (b) loop width, and (c) inelastic strain index.

In-plane shear properties

Off-axis tensile tests provide in-plane shear fracture behavior by simple stress conversion [16]. Figure 5 shows in-plane shear stress vs. shear strain curves for S/W-45 and Braid-53. The non-linear segment followed by the initial linearity indicates failure with mixed fracture modes: in-plane shear and fiber detachment coupled with fiber pullouts of transverse fibers. In Fig. 5, the lower proportional limit shear stress (~30 MPa) and shear failure stress (~55 MPa) for Braid-53 were obvious, while the proportional limit shear stress and the shear strength for S/W-45 were ~50 MPa and ~100 MPa, respectively. The in-plane shear properties were slightly improved for braid composites and considerably improved for S/W composites, compared with a proportional limit shear stress of ~15 MPa and a shear failure strength of ~50

MPa for early generation SiC/SiC composites reinforced by Tyranno™-LoxM Si-Ti-C-O fibers with the poor stiffness SiC matrix fabricated by the polymer impregnation and pyrolysis (PIP) process [11].

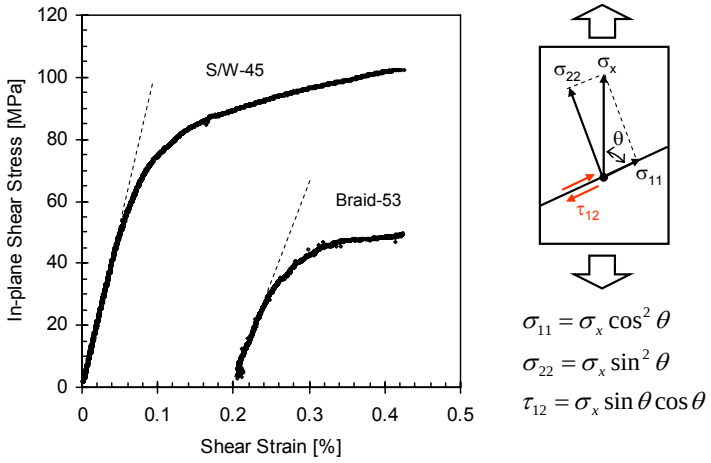

Fig. 5. In-plane shear stress vs. shear strain.

The higher proportional limit shear stress (~55 MPa) and in-plane shear fracture strength (~100 MPa) for S/W-45 resulted in the superior off-axis tensile properties. It is obvious that the contribution from continuous fibers aligned perpendicular to the shear fracture plane is extraordinary for biaxial (including satin-woven) composites. Specifically, the high interfacial friction (~100 MPa) for nuclear-grade SiC/SiC composites can allow significant load transfer via the fiber/matrix interface beyond first in-plane shear cracking. Denk et al. [17] specified the effect of the volume fraction of transverse fibers on in-plane shear strength by Iosipescu shear testing of carbon/carbon composites. A high fiber volume fraction in a unit structure was achieved due probably to the tightly-woven architecture for S/W-45. Therefore, it is reasonable to conclude that S/W-45 with a slightly higher fiber volume fraction of ~40% exhibits the higher in-plane shear properties. Additionally, the pore distribution would affect the in-plane shear data. The braid composites preferably possess pocket pores between fiber bundles however the effect of pocket pores might be minor for the dense NG1 braid composites.

Anisotropy of tensile properties

Continuous fiber reinforcement of the composites provides higher reliability in fracture behaviors as compared with those of brittle ceramics, however, simultaneously imposes anisotropy on material properties. In Figs. 6 and 7, the anisotropy of tensile properties was summarized. For comparison, tensile data of the Generation III SiC/SiC composites in literature were also included.

Figure 6 shows the tensile Young's modulus with respect to the off-axis angle, θ. The Young's modulus of the composites exhibits the maximum at $\theta = 0$ and it tends to decrease with increasing off-axis angle. The anisotropy of the Young's modulus has long been discussed and the composite modulus can be well-described by a rule of mixtures for laminates [20]. Assuming a UD fiber configuration with a fiber volume fraction of 0.3 and varied porosity ranged from 5–20%, an anisotropic change of the Young's modulus can be predicted as shown in Fig. 6. Note that the model assumes columnar pores distributed along the fiber bundles. Analytical results clearly indicate that the Young's modulus decreases with increasing porosity. The data of dense NG1 braid composites agreed with the analytical trend very well, although the moduli for the other composites with a porosity of ~16% did not. Underestimating the porosity effect may result in the lower Young's moduli for the porous composites. Besides columnar pores, there exist pores distributed in pockets at the cross-points of fiber bundles for braid and woven composites.

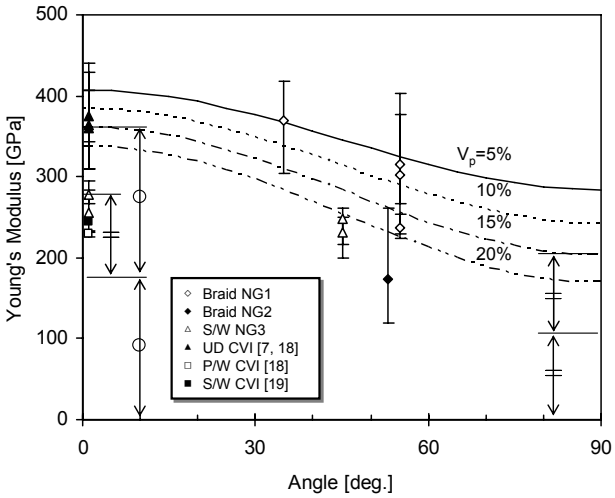

Fig. 6. Anisotropy of Young's modulus. Young's moduli for unidirectional composites with a fiber volume fraction of 30% and varied porosity (V_p = 5~20%) are predicted by a conventional rule of mixtures (solid and broken lines).

Figure 7(a) shows PLS with respect to the off-axis angle. Key crack initiation mechanisms are supposed to be 1) transverse cracking perpendicular to the fiber longitudinal direction, i.e., matrix cracking, 2) in-plane shear cracking within the fiber bundles along the longitudinal fibers, and 3) interlaminar shear cracking along the longitudinal fibers by fiber detachment. For off-axis tension, the applied stress can be separated into three stress elements: tensile stresses in the longitudinal fiber direction, σ_{11} (= $\sigma_x \cos^2(\theta)$), and in the transverse fiber direction, σ_{22} (= $\sigma_x \sin^2(\theta)$), and in-plane shear stress on the plane parallel to the longitudinal fiber direction, τ_{12} (= $\sigma_x \sin(\theta) \cos(\theta)$). For simplicity, we assume a critical stress to initiate matrix cracking, i.e., transverse cracking in 0°-bundles, as σ_{11} = 230 MPa from the result of UD composites

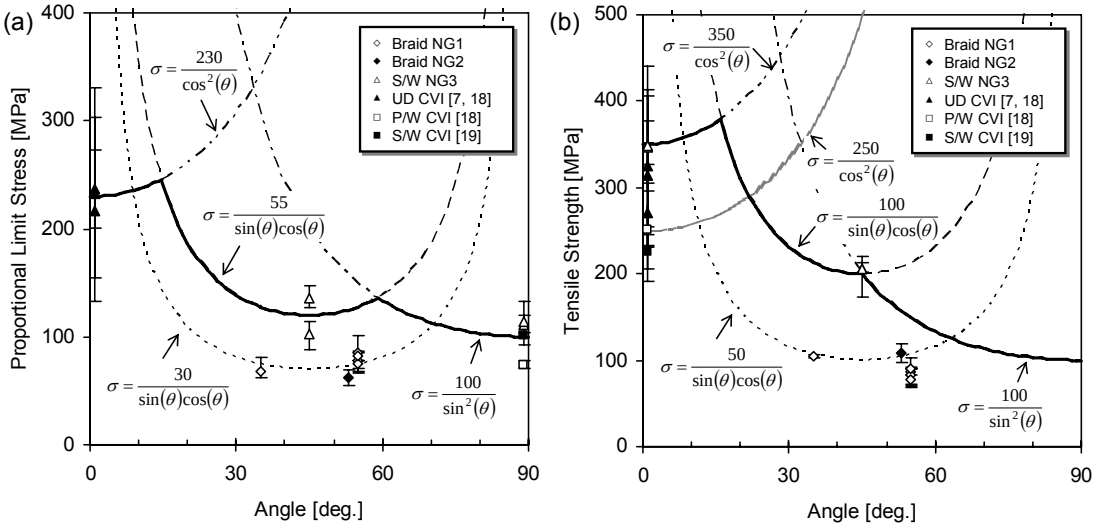

Fig. 7. Anisotropy of (a) PLS and (b) tensile strength. Estimates of PLS and tensile strength are also plotted. The stress criterion for NG3 S/W composites was, for instance, shown as a solid line in the figures.

and a critical detachment stress as σ_{22} = 100 MPa taking a PLS of [0°/90°] composites. A critical in-plane shear stress to induce first cracking is equivalent to a proportional limit shear stress obtained from Fig. 5 (τ_{12} = 30 MPa for NG1 and NG2 vs. τ_{12} = 55 MPa for NG3). Assuming a unique fracture mode operated, stress criterion to determine PLS is therefore drawn as shown in Fig. 7(a). The high PLS for NG3 S/W composites was due to the high proportional limit shear stress to initiate a parallel crack in the fiber bundles. Large scatter of PLS data at θ = 0 seems as a consequence of scattered fiber volume fraction.

Similar to the PLS case, a fracture mechanism anisotropy map for tensile strength can be defined in Fig. 7(b). The critical in-plane shear fracture strengths of 50 MPa for both braid composites, and 100 MPa for NG3, were derived in Fig. 5. The detachment failure strength is assumed to be identical with a detachment initiation stress of ~100 MPa. This is a reasonable assumption since the trans-thickness tensile specimen generally fails without a non-linear damage accumulation stage [21]. Large scatter of tensile strength for UD composites (θ = 0) was due to scatter of the axial fiber volume fraction in the cross-section. It is well-known that the composite fracture strength depends significantly on the axial fiber volume fraction [22]. As infer from Fig. 7(b), there exists the co-operation of multiple failure modes for S/W-45. In contrast, the failure mode of braided composites appears only in-plane shear, although the failure behavior beyond the proportional limit was quite different in each braid composite as discussed.

Acknowledgement

This work was sponsored by the Office of Fusion Energy Sciences, U.S. Department of Energy, under contract DE-AC05-00OR22725 and by the Office of Nuclear Energy Science and Technology, U.S. Department of Energy, under contract DE-AC05-00OR22725 with UT-Battelle, LLC.

References

[1] Y. Katoh and L. L. Snead, J. ASTM Int. 2 (2005) JAI12377.
[2] S. Nogami, A. Hasegawa, and L. L. Snead, J. Nucl. Mater. 307–311 (2002) 1163.
[3] Y. Katoh, private communication.
[4] L. L. Snead, J. Nucl. Mater. 329–333 (2004) 524.
[5] L. L. Snead, Y. Katoh, A. Kohyama, J. L. Bailey, N. L. Vaughn, and R. A. Lowden, J. Nucl. Mater. 283–287 (2000) 551.
[6] J. B. J. Hegeman, J. G. van der Laan, M. van Kranenburg, M. Jong, D. d'hulst, and P. ten Pierick, Fusion Eng. Des. 75–79 (2005) 789.
[7] Y. Katoh, T. Nozawa, L. L. Snead, and T. Hinoki, 12th International Conference on Fusion Reactor Materials, 2005, Santa Barbara, Calif., USA, Journal of Nuclear Materials (accepted).
[8] Y. Katoh, L. L. Snead, C. H. Henager, Jr., A. Hasegawa, A. Kohyama, B. Riccardi, and H. Hegeman, 12th International Conference on Fusion Reactor Materials, 2005, Santa Barbara, Calif., USA, Journal of Nuclear Materials (accepted).
[9] C. Cady, F. E. Heredia, and A. G. Evans, J. Am. Ceram. Soc. 78 (1995) 2065.
[10] T. Nozawa, Y. Katoh, A. Kohyama, and E. Lara-Curzio, 25th Annual International Conference on Advanced Ceramics & Composites, 2001, Cocoa Beach, Fla., USA.
[11] T. Nozawa, Y. Katoh, and A. Kohyama, Mater. Trans. 46 (2005) 543.
[12] E. Vagaggini, J.-M. Domergue, and A. G. Evans, J. Am. Ceram. Soc. 78 (1995) 2709.
[13] Z. C. Xia, R. R. Carr, and J. W. Hutchinson, Acta Metal. Mater. 41 (1993) 2365.
[14] Z. C. Xia and J. W. Hutchinson, Acta Metal. Mater. 42 (1994) 1933.
[15] T. Nozawa, Y. Katoh, and L. L. Snead, 12th International Conference on Fusion Reactor Materials, 2005, Santa Barbara, Calif., USA, Journal of Nuclear Materials (accepted).
[16] W. R. Broughton, Shear, Mechanical Testing of Advanced Fibre Composites, J. M. Hodgkinson (ed.), Woodhead Publishing Limited, Cambridge, England, 2000, 1001–1023.
[17] L. Denk, H. Hatta, A. Misawa, and S. Somiya, Carbon 39 (2001) 1505.
[18] T. Nozawa, unpublished work.
[19] T. Nozawa, Y. Katoh, L. L. Snead, T. Hinoki, and A. Kohyama, 29th International Conference of Advanced Ceramics and Composites, 2005, Cocoa Beach, Fla., USA.

[20] T. Ishikawa, K. Bansaku, N. Watanabe, Y. Nomura, M. Shibuya, and T. Hirokawa, Compos. Sci. Technol. 58 (1998) 51.
[21] Y. Maki, T. Hinoki, and A. Kohyama, 29th International Conference of Advanced Ceramics and Composites, 2005, Cocoa Beach, Fla., USA.
[22] W. A. Curtin, J. Am. Ceram. Soc. 74 (1991) 2837.

FRACTURE STRENGTH AND TIME DEPENDENT PROPERTIES OF 0/90 AND ±55-BRAIDED WEAVE SIC/SIC TYPE-S FIBER COMPOSITES—C. H. Henager, Jr. (Pacific Northwest National Laboratory)[1]

OBJECTIVE

PNNL has performed mechanical property tests on two types of Hi-Nicalon Type-S fiber SiC/SiC composites for the general purpose of evaluating such composites for control rod guide tube applications in the next generation nuclear power (NGNP) high-temperature gas-cooled reactor design. Such composites are also of great interest for fusion applications as well. The mechanical testing consisted of 4-point bend strength, 4-point single-edge notched bend fracture toughness, and 4-point bend slow crack growth testing on both composites from ambient to 1600˚C (1873K). The two composite materials that were tested included a ±55˚-braided-weave composite with Type-S fibers inclined at 55˚ to the principal composite axes to simulate a braided tube architecture and a Type-S 0/90 satin-weave composite as a reference material.

SUMMARY

The use of SiC-reinforced composites for fusion or other nuclear applications will not be restricted to 0/90 aligned fiber applications in all cases. Therefore, it is important to understand the role of fiber orientation in the strength, toughness, and time-dependent strength properties for such materials. The use of high-strength ceramic fibers for composites is predicated on optimizing the strength, fracture resistance, and retained strength in aggressive environments, which argues for the best use of fiber strengths, namely on-axis loading for full load transfer to the high-strength fibers. Evans et al. have developed extensive theoretical treatment of such composites loaded in on-axis orientations [1-3] but relatively few researchers have systematically studied the effects of fiber orientation on composite properties, and none have, to the best of our knowledge, performed any time-dependent testing of off-axis composites.

Although limited work has been performed in off-axis orientations, the research that has been performed gives a solid picture of the effects of such loading on the static strength of composites. Lynch and Evans [4] tested a CMC comprised of Nicalon fibers in a magnesium aluminosilicate (MAS) matrix of boron doped cordierite glass made by Corning Glass. The architecture was a $[0/90^{\circ}]_3$ cross-ply structure and the testing was in tension using specimens cut at 0˚, 30˚, and 45˚ to the weave bias. The 30˚ samples were [30/60˚] in an unbalanced orientation while the 45˚ samples were ±45˚ balanced weave. Kawai et al. tested a unidirectional carbon/epoxy laminate fabricated from a prepreg tape P2053-20 at various off-axis angles and matched these results to a Tsai-Hill model prediction [5]. Govaert et al. investigated unidirectional glass fiber/epoxy composites made by filament winding and using a heated epoxy bath [6]. Both of these materials exhibit good matches to predictions based on existing models.

In all cases, both the static strengths and strains to failure are greatly reduced when off-axis loading is performed on these representative composites. The strength reductions and fracture strains are greatly reduced for unidirectional composites dominated by matrix failures but less so for the woven materials dominated by fiber failure. On the other hand, a reduction in strength of about 70% for the CMC materials suggests that off-axis loading, if and when it should occur represents a serious loss of strength concern. For the case considered here, which is an application of woven SiC-based composites for control rod guide tubes, it is not obvious that on-axis loading can be guaranteed for a woven tubular structure. For that reason a study of the strength and time-dependent strength properties of a prototypical woven architecture that was representative of a braided tube design was performed by the US Department of Energy at Pacific Northwest National Labs (PNNL) in conjunction with Idaho National Lab (INL) and Oak Ridge National Lab (ORNL). This research report covers the work that was performed at PNNL that examined static and time-dependent strengths and crack growth rates in both [0/90˚] woven composites tested on-axis and a ±55˚-braided weave composite designed to represent a tubular composite architecture. Both materials were made with Hi-Nicalon Type-S fibers in a CVI-SiC matrix.

[1]Pacific Northwest National Laboratory (PNNL) is operated for the U.S. Department of Energy by Battelle Memorial Institute under contract DE-AC06-76RLO-1830.

PROGRESS AND STATUS

Introduction

The SiC/SiC materials that were tested at PNNL are 1) a 5-harness satin weave, 8-ply, Hi-Nicalon Type-S fiber composite that was purchased in 2004 from GE Power Systems[2] and 2) A Hypertherm[3] composite purchased in 2006 that is ±55˚ braided weave, 10-ply plate, Hi-Nicalon Type-S fiber composite. Plan view photographs of these materials are shown in Figure 1, which also reveals a major difference between the two composites as a reduced areal fraction of fibers due to the braided weave as compared to the more compact 5-harness satin weave at 0/90. The 5-harness satin weave 0/90 composite from GE Power Systems was manufactured for PNNL in 2002 with a bulk density of 2.69 g/cm^3 and 40% nominal fiber volume fraction and was fabricated using isothermal chemical vapor infiltration (ICVI). A 150-nm thick pyrocarbon (PyC) interface was applied to the Type-S fibers prior to ICVI processing. The Hypertherm materials were also made with Type-S Hi-Nicalon fibers but coated with a 150 nm PyC, (100 nm CVI SiC, 20 nm PyC)$_4$ multi-layer interface applied prior to CVI matrix deposition. These materials had a nominal fiber volume fraction of 30%, a bulk density of 2.9 g/cm^3, and a 380-μm thick outer seal coat of SiC. The composite lay-up was 10-ply of nominally ±45˚ braided tubular weave. PNNL measured the weave angle to be ±55˚ in the flat plate braided weave material.

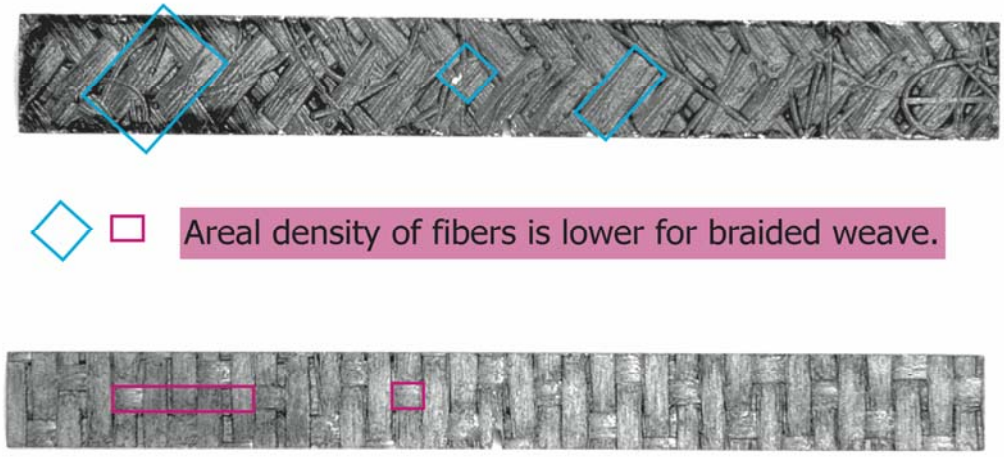

Figure 1. Optical photographs of the two composite materials showing differences in weave architecture and area fraction of fibers. The top image is the ±55˚ braided weave composite and the bottom image is the 0/90 5-harness satin weave composite material.

Mechanical property testing

Composite strength, modulus, proportional limit, and ultimate strain were measured for both materials in 4-point bending per ASTM C-1341 (nominal). The typical sample dimensions and bend fixture dimensions are listed in Table 1. The L/d ratios were 19 for the 0/90 composite and 11.1 for the ±55˚ braid, respectively, which is outside the C-1341 recommended L/d ranges. This might increase the likelihood of shear failures in these materials. The bend data was taken at two strain rates for each material to provide an assessment of slow crack growth in these composites. The 0/90 composite was tested at 6.7 x 10^{-6} and 1 x 10^{-4} s^{-1} strain rates, while the ±55˚ braided composite was tested at 5 x 10^{-6} and 1 x 10^{-3} s^{-1}. The peak load fracture toughness, termed K_Q, using single-edge notched beams (SENB) of each composite material was determined at ambient temperature and also at elevated temperature based on ASTM C-1421 (see Table 1).

[2]http://www.gepower.com
[3]Hypertherm HTC Inc. (Huntington Beach, Calif.)

Time-dependent deformation, or slow crack growth, was also measured for both materials. The PNNL technique for determining slow crack growth parameters for the SiC/SiC composites has been to design a test in the spirit of ASTM C-1465 “Determination of Slow Crack Growth Parameters of Advanced Ceramics by Constant Stress-Rate Flexural Testing at Elevated Temperatures” but using a constant load over a range of test temperatures instead of a constant stress rate. For this time-dependent testing either unnotched bend bars or single-edge-notched bars (SENB) can be used to measure deformation rates. The use of SENB bars suggests that crack propagation rates can be determined using standard methods but since multiple matrix cracking is still observed in these materials at the notch, it becomes problematic to analyze the data for crack growth rates, although this has been attempted with some success [7, 8]. A simpler method is to use the deformation rates as measured by mid-point deflections to determine the composite creep parameters by analogy to the fiber creep parameters since, after matrix cracking has occurred, the fibers are carrying the majority of the load on the composite and it is the thermal creep of the highly stressed fibers that determines the deformation rate of the composite. This work features both the use of unnotched bend bars and SENB held at constant load measured over a temperature range given by the results of the strain-rate dependent strength data.

Table 1. Bend and SENB test specifications

Composite Material-Sample	Fixture[4]		Sample[*]		
	Support Span	Loading Span	Span (L)	Depth[5] (d)	Width (W)
0/90 5-harness satin weave – Flexure	40	20	50	2.1	4
±55˚ braid – Flexure	40	20	50	3.6	4.2
0/90 5-harness satin weave – SENB[6]	40	20	50	5	2.1
±55˚ braid – SENB[7]	40	20	50	6.1	3.6

[4]All dimensions are in mm in Table 1.
[5]Sample surfaces in depth direction were left as received and were not polished.
[6]a/W values were 0.16 for SENB samples.
[7]a/W values were 0.16 for SENB samples.

RESULTS AND DISCUSSION

Rate-dependent bend strength

The bend data are shown in Figure 2 plotted as ultimate bend strength versus temperature for the two strain rates for each material. The difference between the fracture strengths for the fast and slow strain rates is an indication that slow crack growth is occurring in these materials starting at about 1000˚C (1273K). The most likely interpretation of this result is that highly strained fibers are undergoing thermal creep at elevated temperatures and failing by creep cavitation [9-23]. The bend data are summarized in Table 2. When compared to the strength of the 0/90 materials it is seen that the braided weave composite has strengths only 15% of the 0/90 material at ambient temperature but about 53% of the 0/90 material at 1600˚C. This is an interesting comparison. The lack of strength at ambient temperature appears to be slightly more than can be accounted for by simple fiber geometry

due to the off-axis weave, although modeling this behavior still remains to be done. A survey of the literature reveals that in carbon fiber reinforced plastics a strength reduction of about 80% to 90% for ±30˚ fiber orientations was observed, while a study of off-axis loaded ceramic composite materials revealed about a 65% strength reduction for ±30˚ fibers [4, 24]. The lack of sensitivity to elevated temperature strength degradation is likely due to the reduced participation in fiber load sharing relative to the SiC matrix, which is expected to have high resistance to temperature-dependent strength degradation. In other words, the off-axis fiber composite appears to behave more like a monolithic material than a fiber composite and monolithic SiC would exhibit little strength degradation in this temperature range. The high bulk density of 2.9 g/cm^3 and low fiber volume fraction of 30% could contribute to this result.

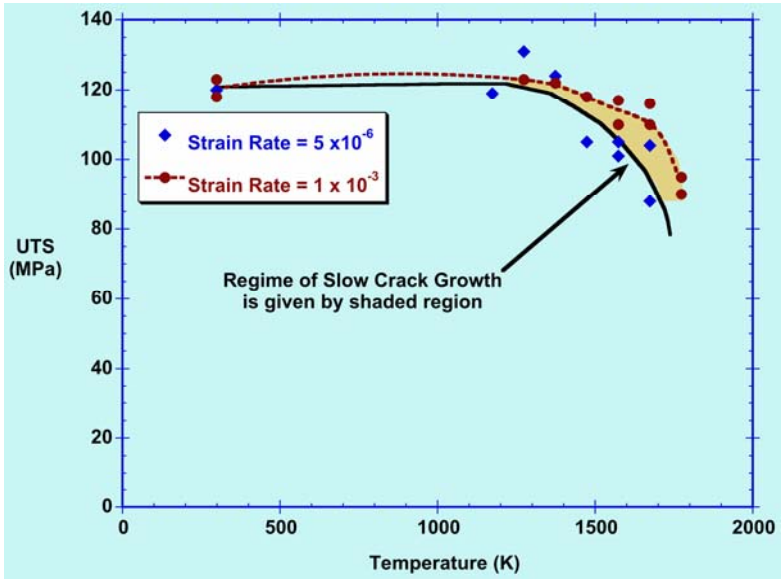

(a)

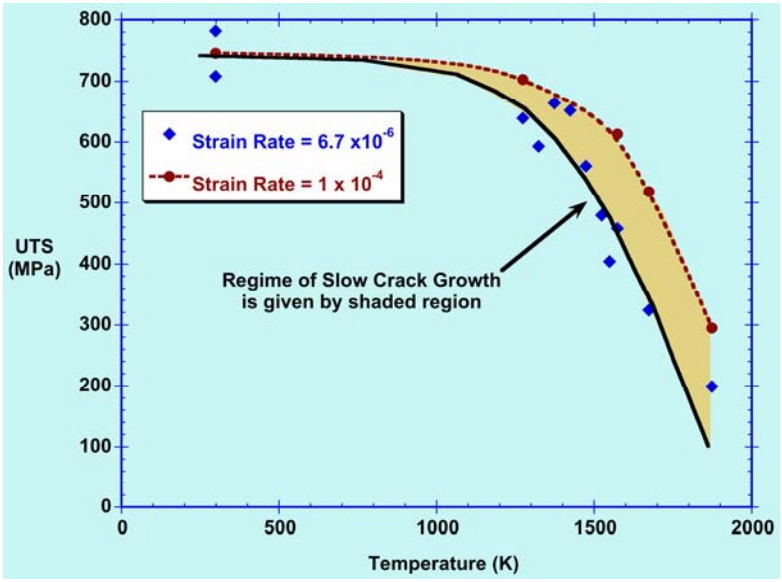

(b)

Figure 2. Ultimate strength (UTS) in bending for (a) Type-S ±55˚ braided composite at two strain rates and (b) Type-S 5-harness satin weave 0/90 composite at two strain rates.

Table 2. Summary of flexure properties[8]

Composite Material	Temperature (K)	Strength (MPa)	Elastic Modulus (GPa)	Proportional Limit Stress[9] (MPa)	Strain to Failure
0/90 5-harness satin weave	25	740	256	115	.008
	1273	703	223	120	.008
	1573	613	192	110	.007
	1673	519	202	100	.006
	1873	295	182	100	.004
±55˚ braid	25	120	155	65	.002
	1273	123	178	60	.002
	1573	114	225	45	.0015
	1673	113	246	40	.002
	1873	104	–	–	–

[8]Data taken from fast strain rate tests at elevated temperatures.
[9]Taken from bend stress-strain curve as first deviation from linearity.

Elastic Modulus in Bending

Representative stress-strain curves in bending are shown in Figure 3 for each type of composite. The linear portion of the initial stress-strain curve was used to compute an elastic modulus in bending for each material, averaging at least two separate stress-strain curves. The 0/90 material has a room temperature modulus of 256 GPa and the ±55˚ braided weave material has a modulus of 155 GPa as shown in Table 2. Values for the elastic modulus for other temperatures are listed in Table 2.

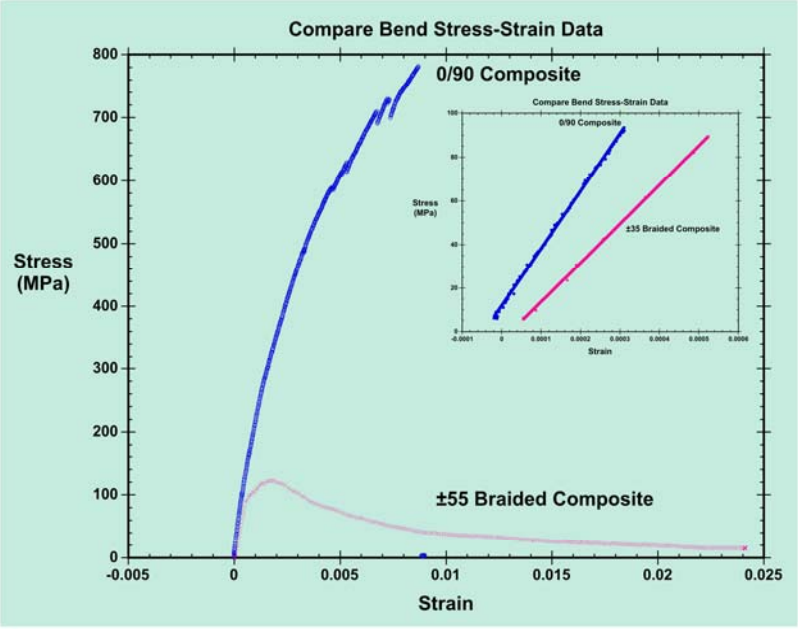

Figure 3. Stress-strain curves in bending for 0/90 and ±55˚-braided composite material at ambient temperature. Inset plot shows linear portions of curves used to calculate bending modulus.

Bend Fracture Photomicrography

Representative fractures are shown in optical micrographs for both 0/90 satin weave and ±55° braided weave materials in Figures 4 to 7. Figure 4 shows typical side views of fractured 0/90 satin weave composite bend bars at the indicated temperature. Some longitudinal splitting along the bar axis is observed and decreasing amounts of fiber pullout are observed with increasing temperature as well as an increased tendency for the fibers to fail within the crack opening region as seen in Figure 5. This pullout length reduction further supports the hypothesis that fibers are failing due to slow crack growth or stress rupture mechanisms. Figure 6 shows similar views for the ±55° braided weave material. Compared to the 0/90 satin weave material the braided weave has less longitudinal splitting during bend testing. Note the 300-μm thick outer layer of SiC on the braided weave material that reduces the fiber volume fraction relative to the 0/90 satin weave material, 30% compared to 40%, respectively. A closer look at the fiber fracture images for the braided weave materials suggests that fibers are failing in bending instead of tension. Figure 7(a) shows broken fibers for the ±55° braided weave material while Figure 7(b) shows broken fibers for 0/90 satin weave material. The fiber fracture surfaces for the braided weave material indicate non-tensile fracture features, while tensile fracture features are readily visible in Figure 7(b) in the form of mirror-mist-hackle regions on the fiber fracture surfaces [25].

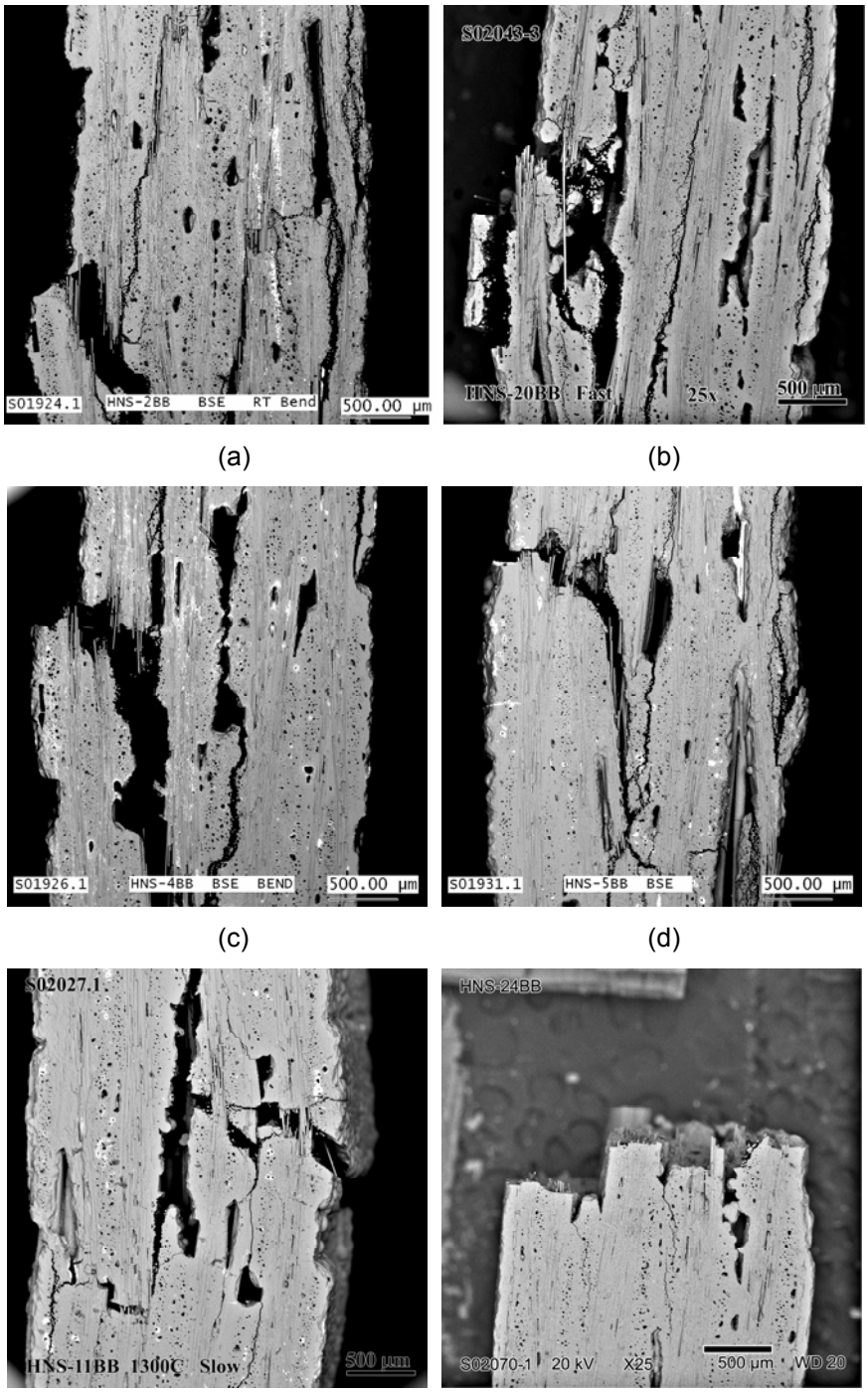

Figure 4. SEM micrographs of bend bars of 0/90 satin weave material after testing in argon at (a) ambient at 6.7 x 10^{-6} s^{-1}, (b) ambient at 1 x 10^{-4} s^{-1}, (c) 1373K at 6.7 x 10^{-6} s^{-1}, (d) 1473K at 6.7 x 10^{-6} s^{-1}, (e) 1573K at 6.7 x 10^{-6} s^{-1}, and (f) 1873K at 6.7 x 10^{-6} s^{-1}.

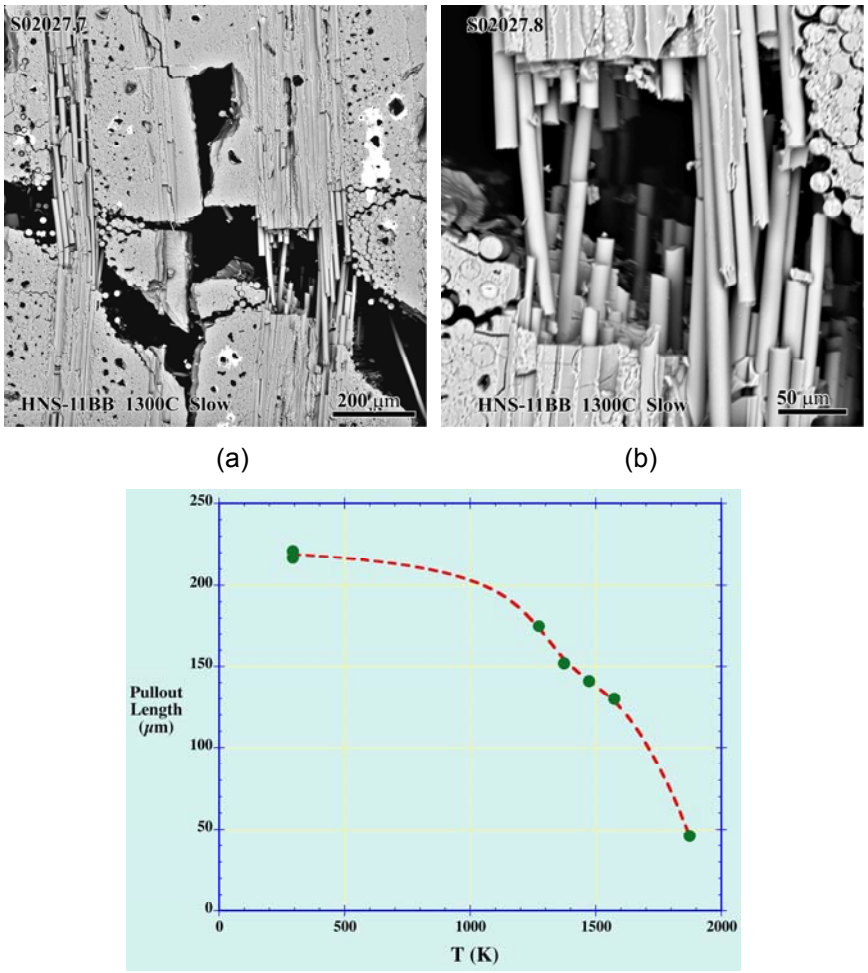

Figure 5. SEM photomicrographs showing fiber failure occurring within the crack opening during bend failure in 0/90 satin weave material at 1573K tested at 6.7 x 10^{-6} s^{-1} in argon in (a) and (b), while in (c) is a plot of fiber pullout lengths as a function of test temperature in argon at 6.7 x 10^{-6} s^{-1}.

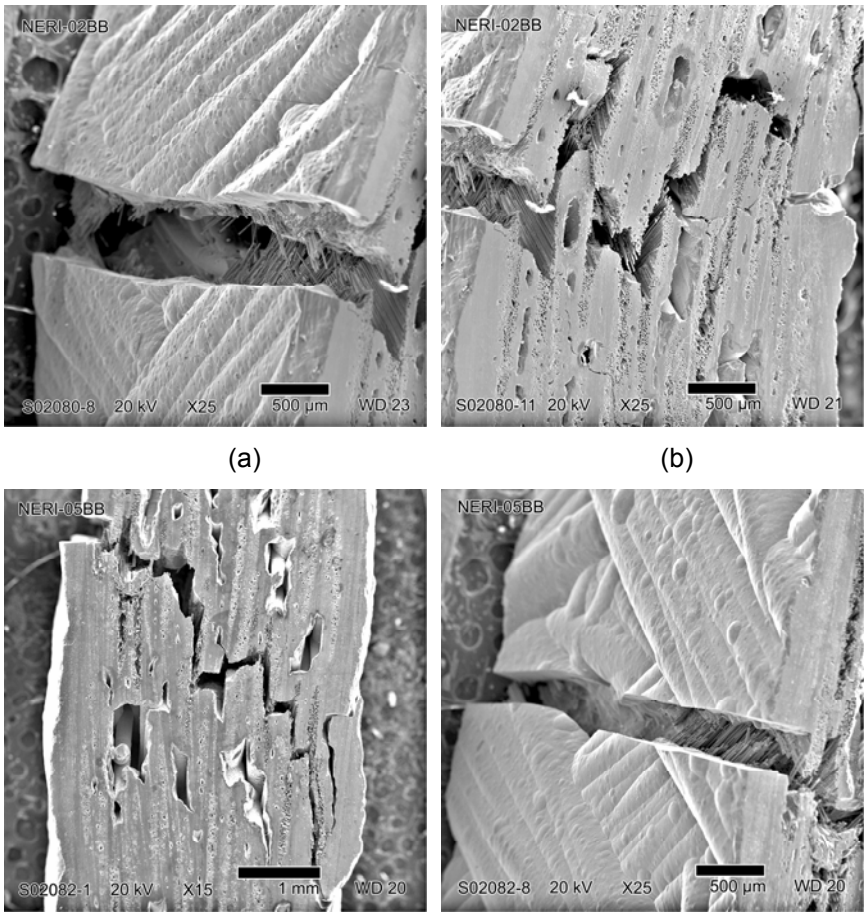

Figure 6. SEM micrographs of bend bars of ±55˚ braided weave material after testing in argon at (a)-(b) ambient at 1.0 x 10^{-3} s^{-1} and (c)-(d) at 1273K at 1.0 x 10^{-3} s^{-1}.

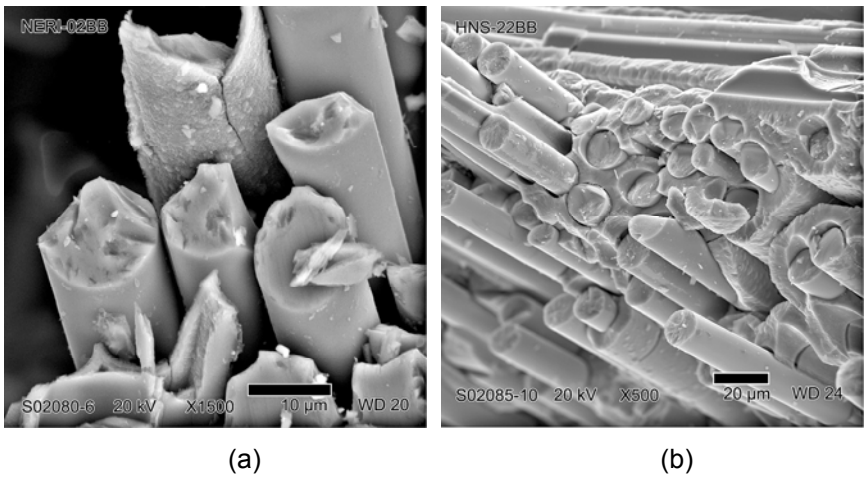

Figure 7. SEM micrographs of failed fibers showing apparent non-tensile fiber failures in (a) for ±55˚ braided weave materials tested at ambient temperature. In (b) is shown a fracture surface of the 0/90 satin weave material tested at 1673K in argon.

Fracture Toughness

The room temperature toughness of the ±55˚-braided materials was determined to be 7.7 MPa√m,

which compares to 23 MPa√m for the 0/90 satin weave materials at room temperature. Again, there is a substantial difference of the 0/90 weave versus the ±55-braided weave. Figure 8 shows the peak load toughness curves for both materials as a function of temperature. Toughness values are listed in Table 3.

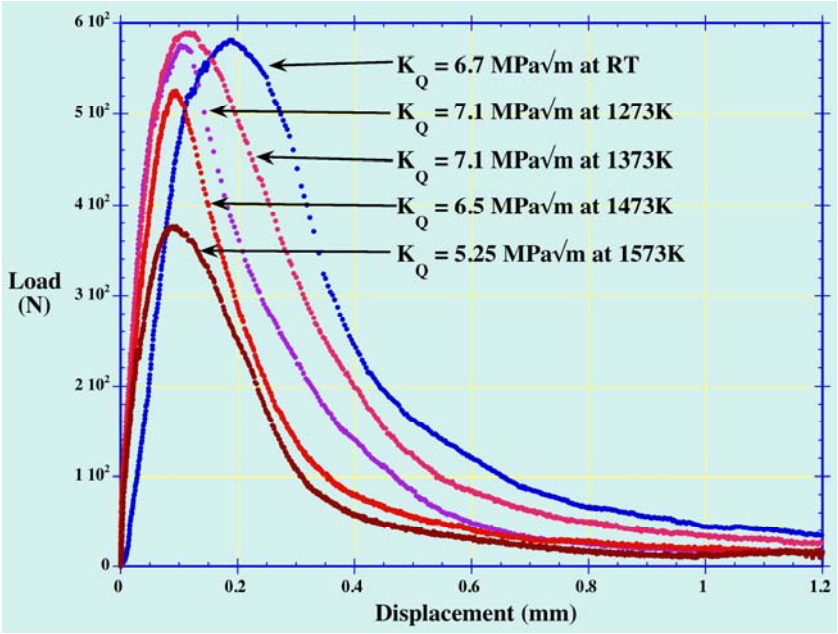

(a)

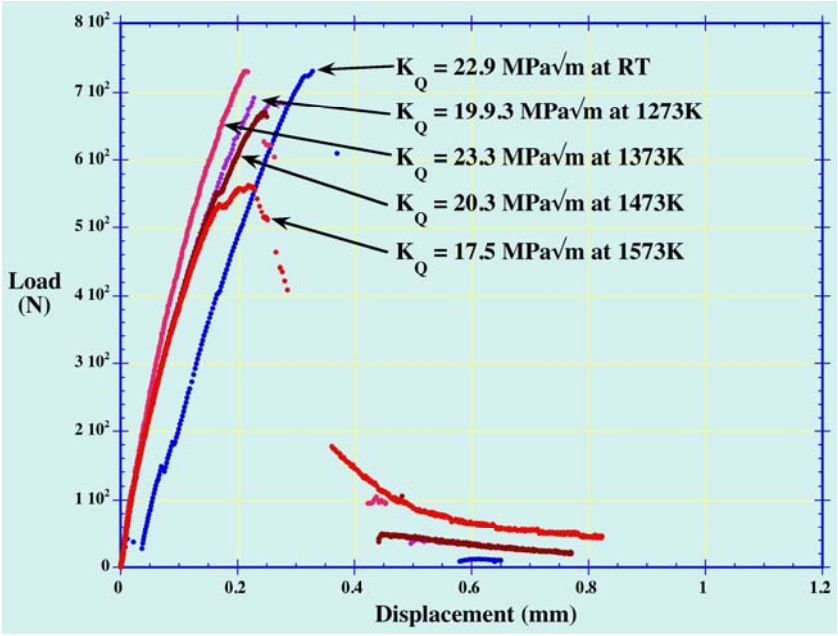

(b)

Figure 8. Load-displacement curves for single edge notch beam samples tested at ambient and indicated temperatures. Peak load fracture toughness reported as K_Q is also indicated.

Table 3. Summary of fracture toughness data

Composite Material	Temperature (K)	Fracture Toughness (MPa√m)
0/90 5-harness satin weave	25	22.9
	1273	19.9
	1373	23.3
	1473	20.3
	1573	17.5
±55° braid	25	7.7[10]
	1273	7.1
	1373	6.8[11]
	1473	6.5
	1573	5.25

[10]Average of three tests.
[11]Average of two tests.

Slow Crack Growth

A type of time-dependent deformation occurs in ceramic composites containing fine-grained or amorphous fibers, such as the Nicalon family of fibers [7, 8, 26]. Composite deformation studies classify these as Type-II composites, which are notch-insensitive materials due to multiple matrix cracking and strong load sharing among fibers. In this case, the SiC-matrix fails in tension by cracking and the load is carried by the Nicalon SiC-fibers, which can then undergo thermal creep deformation at elevated temperatures. The fiber thermal creep process has not been particularly well characterized mechanistically until recently [9, 11] but several groups have performed comprehensive creep studies of the fibers, shown in Table 4, and determined some of the basic creep parameters under either tensile or bending with the bend-stress relaxation technique [9, 10, 21, 23]. A simple characterization of the creep mechanics based on analysis of the best-fit creep equations indicates that fine-grained fiber thermal creep is most likely a grain boundary sliding or viscous flow deformation. This type of deformation is consistent with the low stress exponent and the fractional time-temperature exponent, which typifies a logarithmic creep process that never quite reaches a steady-state process.

The temperature range of interest is determined in this case by the data presented in Figure 2, which shows the temperature region for which time-at-temperature affects the bend strength of the material. For either the 0/90 satin weave or the ±55 braided weave materials this range begins above about 1000°C (1273K) and extends upwards in temperature to the upper use temperature of the material. For the purposes of this study, the upper limit would be established at 1600°C (1873K) but a more practical upper limit is about 1300°C or 1573K since fiber thermal creep is very high at this temperature while the fibers have not started degrading due to thermal processes.

Accordingly, data for the 0/90 satin weave material is shown in Figure 9(a) and that for the ±55 braided weave in Figure 9(b). This data is fit with an equation of the type shown in Table 4 and the subsequent composite time-dependent deformation parameters are determined by curve fitting to the data shown in Figure 9. Comparison of the data with that of the fiber creep data demonstrates the mechanistic similarities that exist and that support the composite fiber creep contention.

This data suggests that the time-dependent deformation characteristics of the 0/90 satin weave and ±55 braided weave materials are similar, which means that the Type-S ceramic fibers are determining the time-dependent deformation of the composites irregardless of their inclination to the crack plane. This finding is supported by the similarity in the time-temperature exponent and activation energies for both materials. It needs to be noted at this point that the loads applied to the ±55 braided weave materials were about one-half of the equivalent loads applied to the 0/90 composite in order to account for their respective fracture toughness levels. This suggests that the PNNL dynamic crack

growth model [7, 8], which has yet to be applied to the inclined fiber composite case, should be able to account for time-dependent crack propagation in the ±55 braided weave composite if the proper geometrical scaling is applied to the crack bridging fibers.

Table 4. Fiber thermal creep and SiC/SiC composite time-dependent data

Fiber type and condition	Creep law[12]	A (MPa^{-1} s^{-1})	n	p	Q (kJ/mol)
Nicalon-CG Thermal Creep	$\varepsilon = A\sigma^n t^p Exp\left(\frac{-Qp}{RT}\right)$	2	1.2	0.4	500 [9, 21]
Hi-Nicalon Thermal Creep	$\varepsilon = A\sigma^n t^p Exp\left(\frac{-Qp}{RT}\right)$	121	1.8	0.58	445-600 [10, 21]
Type-S Thermal Creep	$\varepsilon = A\sigma^n t^p Exp\left(\frac{-Qp}{RT}\right)$	0.7	1.0	0.24 – 0.32	500-700 [10]
0/90 Type-S 5-harness satin weave (bend)	$\varepsilon = A't^p Exp\left(\frac{-Qp}{RT}\right)$	**2090**[13]	**–**	**0.33**	**513**
±55 Type-S braided weave (SENB)	$\varepsilon = A't^p Exp\left(\frac{-Qp}{RT}\right)$	**1972**	**–**	**0.37**	**471**

[12] *s* is stress in MPa, *t* is time in seconds, *Q* is activation energy in kJ/mol, *A* is a constant, and constants *n* and *p* are stress and time-temperature exponents, respectively.
[13] *A'* combines As^n for composites since a constant load was used.

Inclined Fiber Bridging

anical properties between the 0/90 satin weave and ±55˚ braided weave materials indicates strength, toughness, and, fracture surface feature differences, but similar slow crack growth mechanisms. Figure 10 shows the differences observed in bend strength between the two materials as a function of test temperature. Although there are substantial differences in fiber volume fraction and outer seal coat thickness between the two materials that partly account for these differences, one major distinction is that fibers are inclined to the principal axes for the ±55˚ braided weave materials, which acts to reduce fiber load carrying capability, either through decreased strain to failure or other geometrical strength effects. Several researchers have explored mechanics models of such inclined fibers [27-31] and their main findings are summarized here along with an attempt to model the load-displacement curve for an individual inclined fiber in a ceramic matrix for future inclusion into the PNNL dynamic crack bridging model.

Two important issues emerge from this analysis of inclined fibers; first that an additional frictional energy term, so-called snubbing friction, occurs in this problem as the fiber is pulled out and bent near the matrix crack plane [27]. This causes a high friction much as a rope pulled over a curved edge might experience. Second, the matrix acts as an elastic foundation for fiber bending, which modifies conventional bending mechanics in a complex manner, but this problem has been addressed by solid mechanics solutions [30].

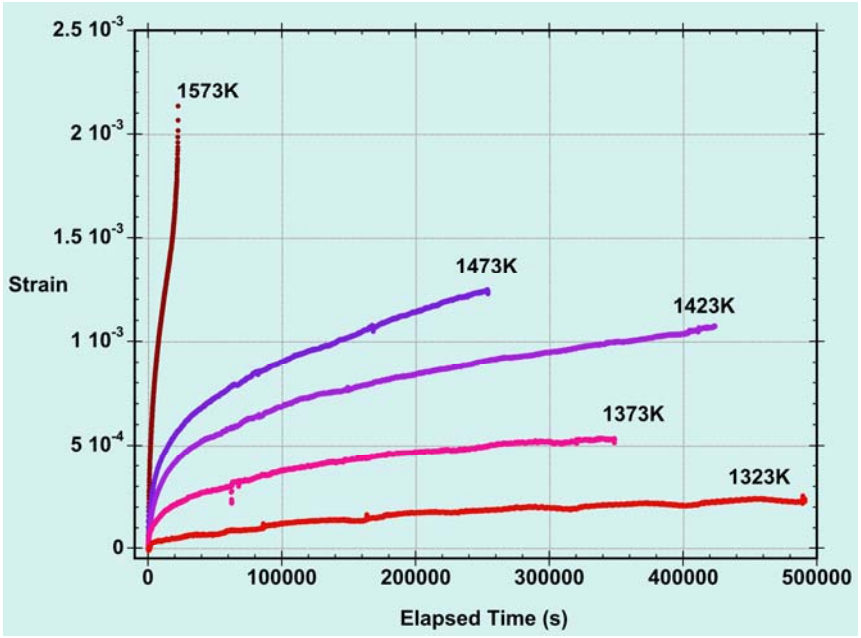

(a)

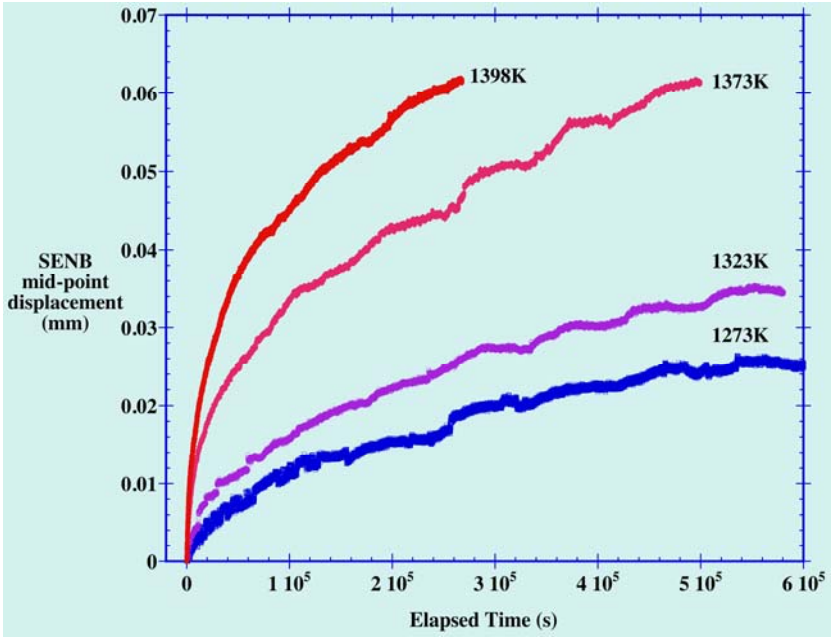

(b)

Figure 9. Strain-time and displacement-time curves for 0/90 satin weave and ±55 braided weave materials at constant load. Shown in (a) are the strain-time plots for 0/90 5-harness satin weave bend bars under constant load for the indicated times, and in (b) are the displacement-time plots for SENB samples held at a load that corresponded to an initial $K_{applied}$ of 5 MPa$\sqrt{m}$ for the indicated time.

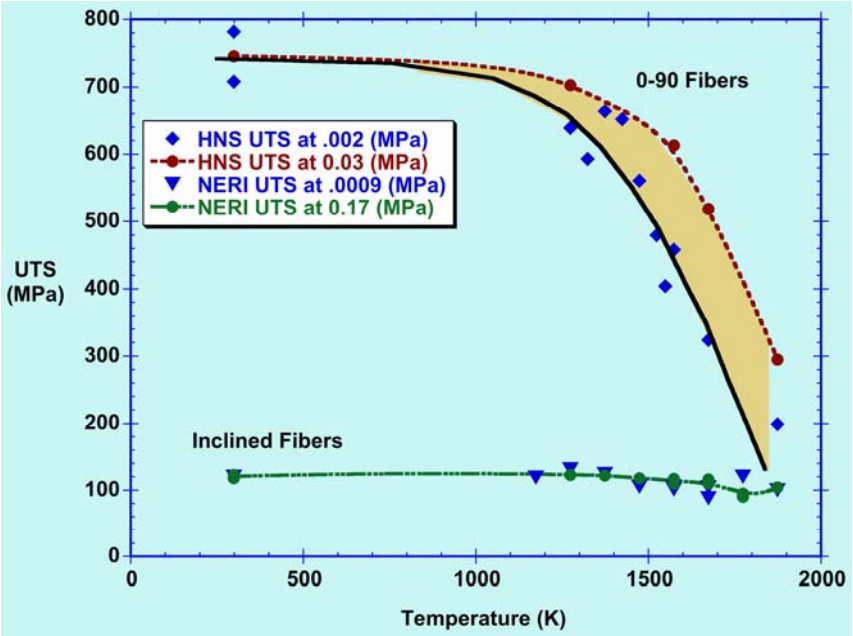

Figure 10. This plot shows the relative strength at ambient temperature and the decrease of strength with test temperature for both composite materials. The ±55˚ braided weave material has a bend strength of only 15% of the 0/90 satin weave material at ambient temperature but this strength difference decreases at elevated temperatures due to enhanced fiber failure seen in the 0/90 composite.

The work of Cox is taken as a starting point for the representation of an inclined fiber in an elastic matrix and snubbing friction is included in the analysis [27]. The force-displacement solution to an inclined bridging fiber is given as two terms, using normalized variables, as

$$W = \frac{\left(\mu_e \left(-\mathrm{Cos}\phi + \mathrm{Cos}(\theta_0 + \phi) + \frac{P\left(\frac{-P\,\mathrm{Cos}\phi + e^{-\frac{\theta_0 \mu_e}{P}} (P\,\mathrm{Cos}\phi - \mu_e \mathrm{Sin}\phi)}{\mu_e} + \mathrm{Sin}(\theta_0 + \phi) \right)}{\mu_e} \right) \right)}{(P^2 + {\mu_e}^2)\,\tau_1} \qquad (1)$$

where W is the fiber deflection, P is the force, ϕ is the inclination angle, θ_0 is the bending angle, μ_e is the snubbing friction term, and τ_1 is the conventional sliding friction term. This equation includes the elastic stretch of the inclined fiber as well as the deformation of the inclined fiber across an interface, such as a crack, due to local bending. The resulting force displacement law is compared to that of a fiber oriented normal to the crack plane using a standard shear-lag fiber model in Figure 11. The Cox inclined bridging law was first calibrated normal to the crack plane to match the Marshall-Cox-Evans law [3] and then angle ϕ was changed to 35˚. This plot shows the displacement for an inclined fiber relative to a normal bridging fiber as a function of applied force. This result indicates that an inclined fiber will be stiffer relative to the normal fiber, thus the composite energy absorption, strength, and toughness will be proportionally reduced because the inclined fibers will fracture sooner than the normal fibers since the inclined fibers cannot tolerate as much crack opening displacement.

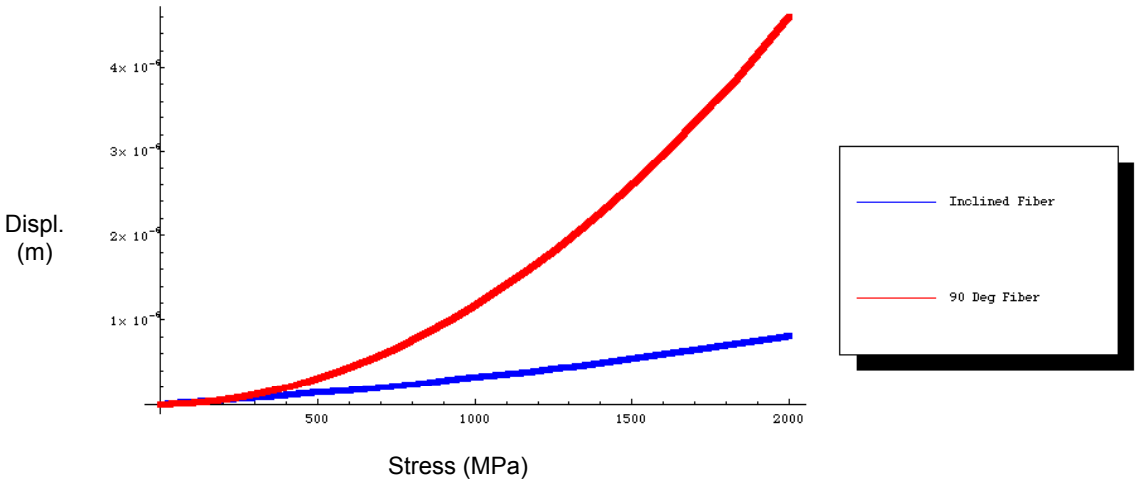

Figure 11. Comparison of stress-displacement laws for an inclined fiber and a normal fiber showing that the inclined fiber appears stiffer relative to the normal fiber. The angle of inclination was set to 90˚ - 55˚ = 35˚ to match the definition of ϕ in Reference [16].

The existence of matrix constraint and snubbing friction suggests that inclined fibers may show telltale fracture surface features of matrix spallation and/or bending failure near the matrix. In Figure 12 indications of this is shown in several SEM micrographs of composite fracture surface features. Figure 12(a) shows slight matrix spallation around a fracture fiber in the 0/90 satin weave material while in Figure 12(b)-(d) much larger regions of matrix spallation can be observed near the inclined fibers in the ±55˚ braided weave material. The inclined fibers also appear to have failed in bending near the region of matrix egress as non-tensile fracture surface features are observed on the fiber fractures. Although not conclusive evidence of the importance of matrix constraint in this problem, these observations substantiate the analysis of Cox and others that such constraints are important considerations in the fracture of inclined fiber composites.

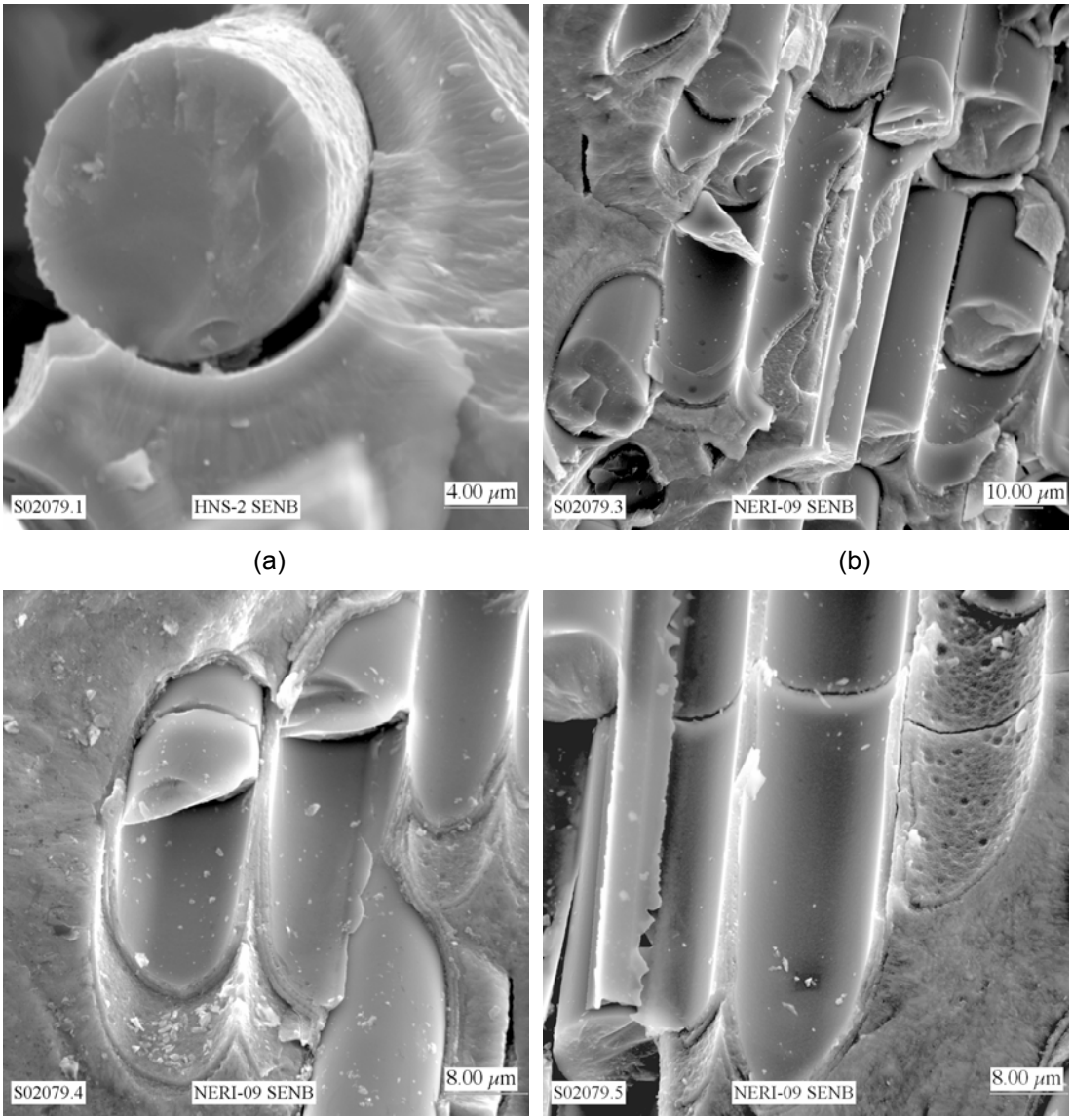

Figure 12. SEM micrographs of composite fracture surfaces showing fiber-matrix constraint and matrix spallation during fracture. In (a) some slight matrix spallation is observed in a 0/90 satin weave material, and in (b)-(d) much larger regions of matrix spallation due to inclined fibers and matrix constraint are observed in ±55° braided weave materials. Note also in (b)-(d) that fibers appear to have failed in bending near matrix egress.

Conclusions

- The following main points summarize the findings of this work:The ±55° braided weave material exhibited only 15% of the average strength and only 30% of the fracture toughness of the 0/90 composite at ambient temperature. These reductions in strength and toughness were greater than typical reductions observed by others for off-axis fiber composites [4-6].
- Both composites were observed to undergo slow crack growth at elevated temperatures with similar activation energies and time-temperature exponents that are consistent with thermal creep of the Type-S bridging fibers.

- The ±55˚ braided weave composite with inclined fibers exhibited fiber fractures and fracture surface features consistent with fibers failing due to bending rather than tension and showing evidence of matrix spallation and snubbing friction effects in the plane of bridged cracks.
- The fiber inclination reduced the fiber participation in energy absorption for the ±55˚ braided weave composite so that it behaved more like a monolithic SiC material compared to the 0/90 composite. This was partly due to composite architectural effects, partly due to fiber inclination, and partly due to non-optimized composite fabrication. The fiber volume fraction was too low and the outer SiC seal coat was too thick.
- The upper use temperature of a Type-S SiC/SiC composite material, regardless of fiber orientation, is limited to about 1300˚C (1573K) due to slow crack growth processes and loss of fiber strength at higher temperatures. This study also documented loss of fracture toughness at and above this temperature.
- Preliminary models of inclined fibers bridging cracks in composites show that inclined fiber bridging must include snubbing friction and fiber bending in addition to elastic stretch. Inclined fibers appear “stiffer” in computed force-displacement laws compared to aligned fibers due to some of these factors.

References

[1] B. Budiansky, A. G. Evans, and J. W. Hutchinson, Int. J. Solids Struct. 32 (1995) 315.
[2] A. G. Evans and F. W. Zok, J. Mater. Sci. 29 (1994) 3857.
[3] D. B. Marshall, B. N. Cox, and A. G. Evans, Acta Metall. 33 (1985) 2013.
[4] C. S. Lynch and A. G. Evans, J. Am. Ceram. Soc. 79 (1996) 3113.
[5] M. Kawai, Y. Masuko, and T. Sagawa, Compos. Part A: Appl. Sci. Manuf. 37 (2006) 257.
[6] L. E. Govaert, H. J. Schellens, H. J. M. Thomassen, R. J. M. Smit, L. Terzoli, and T. Peijs, Compos. Part A: Appl. Sci. Manuf. (Incorporating Composites and Composites Manufacturing) 32 (2001) 1697.
[7] C. H. Henager, C. A. Lewinsohn, and R. H. Jones, Acta Mater. 49 (2001) 3727.
[8] C. H. Henager, Jr., and R. G. Hoagland, Acta Mater. 49 (2001) 3739.
[9] J. J. Sha, J. S. Park, T. Hinoki, and A. Kohyama, Mech. Mater. 39 (2007) 175.
[10] J. J. Sha, J. S. Park, T. Hinoki, and A. Kohyama, Mater. Charact. 57 (2006) 6.
[11] J. A. DiCarlo, H. M. Yun, and J. B. Hurst, Appl. Math. Comput. (New York) 152 (2004) 473.
[12] J. A. DiCarlo and H. M. Yun, in Creep Deformation: Fundamentals and Applications (Proceedings of a Symposium held during the 2002 TMS Annual Meeting), R. S. Mishra, J. C. Earthman, S. V. Raj (eds.) (Minerals, Metals & Materials Society, Warrendale, Pa., 2002) 195.
[13] H. M. Yun and J. A. DiCarlo, Ceram. Eng. Sci. Proc. 20 (1999) 259.
[14] J. A. DiCarlo and H. M. Yun, Adv. Sci. Technol. 22 (Advanced Structural Fiber Composites) 29 (1999).
[15] J. A. DiCarlo and H. M. Yun, Ceram. Trans. 99 (1998) 119.
[16] J. C. Goldsby, H. M. Yun, and J. A. DiCarlo, Scr. Mater. 37 (1997) 299.
[17] J. A. DiCarlo, Ceram. Int. 23 (1997) 283.
[18] R. Bodet and J. Lamon, Silic. Ind. 61 (1996) 23.
[19] H. M. Yun, J. C. Goldsby, and J. A. DiCarlo, Ceram. Trans. 58 (1995) 331.
[20] R. E. Tressler and J. A. DiCarlo, Ceram. Trans. 57 (1995) 141.
[21] J. A. DiCarlo, H. M. Yun, G. N. Morscher, and J. C. Goldsby, Ceram. Trans. 58 (High-Temperature Ceramic-Matrix Composites II) 343 (1995).
[22] H. M. Yun, J. C. Goldsby, and J. A. DiCarlo, Ceram. Trans. 46 (1994) 17.
[23] J.A. DiCarlo, Compos. Sci. Technol. 51 (1994) 213.
[24] M. Kawai and T. Taniguchi, Compos. Part A: Appl. Sci. Manuf. 37 (2006) 243.
[25] N. Lissart and J. Lamon, Acta Mater. 45 (1997) 1025.
[26] R. H. Jones and C. H. Henager, Jr., J. Eur. Ceram. Soc. 25 (2005) 1717.
[27] B. N. Cox, Mech. Adv. Mater. Struct. 12 (2005) 85.

[28] D. D. R. Cartie, B. N. Cox, and N. A. Fleck, Compos. Part A: Appl. Sci. Manuf. 35 (2004) 1325.
[29] W. B. Hillig, J. Mater. Sci. 29 (1994) 419.
[30] W. B. Hillig, J. Mater. Sci. 29 (1994) 899.
[31] C. K. Y. Leung and V. C. Li, J. Mech. Phys. Solids 40 (1992) 1333.

ELECTRICAL CONDUCTIVITY MEASUREMENTS OF SIC-BASED MATERIALS—G. E. Youngblood, E. Thomsen, and G. Coffey (Pacific Northwest National Laboratory)[1]

OBJECTIVE

The primary objective of this fusion materials research effort is to support component design and future testing in the International Thermonuclear Experimental Reactor (ITER).

SUMMARY

We have made electrical conductivity (EC) measurements of several types of 2-dimensional (2D) silicon carbide (SiC) composites using either 2- or 4-probe potentiometric methods. To assess the uncertainty in our transverse EC-measurements for thin disc-shaped composite samples when using a 2-probe method, we have developed a more reliable 4-probe method. At the same time, by comparing 2- and 4-probe measurements, we were able to estimate the error due to contact resistance and assess its effect on previous 2-probe EC measurements. From this analysis, it appears prudent to routinely use the new 4-probe set-up for all transverse EC-measurements of thin SiC-based samples.

PROGRESS AND STATUS

Introduction

SiC/SiC has been proposed as a structural material for the flow channel insert (FCI) component in a U.S. designed test blanket module for ITER. To carry out the required FCI-functions, among other things the SiC/SiC material should exhibit relatively low and uniform transverse electrical conductivity (EC). According to preliminary models, in the envisioned 500-800°C temperature operating range for an FCI these desired EC-values are <20 S/m [1].

In our first report in 2005 [2], for the FCI-application we projected that an architectural or "engineering" design solution would be necessary to achieve the desired low transverse EC (as well as low thermal conductivity) values in conventional 2D-SiC/SiC composite. However, in our next report in 2006 [3], we reported measuring transverse EC-values much lower than expected for such a composite, a so-called "reference" 2D-SiC/SiC made by isothermal chemical vapor infiltration (ICVI). This commercially available composite was made by GE Power Systems using Type S Nicalon™ 5HS woven fabric coated with a relatively thin (110 nm) pyrocarbon (PyC) interphase. Results from previous testing of this SiC/SiC material indicated that its quality was state of the art (e.g., 2.69 g/cc bulk density, 750 MPa and 284 GPa ultimate stress and elastic modulus at RT, respectively, and 27 W/mK TC at RT) [4]. Furthermore, little degradation occurred in this composite after neutron irradiation for doses up to 10 dpa [5]. At 500°C, we measured transverse and in-plane EC-values of ~2 and 400 S/m, respectively for this material. The transverse EC-value of 2 S/m was ~1/10th the FCI-goal. However, this 2D-SiC/SiC is highly anisotropic with in-plane EC-values of ~x200 the transverse EC-values. Such anisotropy in the EC could potentially lead to a MHD pressure drop increase of ~20% along the Pb-Li liquid coolant in an FCI-channel, and is undesirable [6]. Also, this material exhibits about 10% open porosity because of its layered woven fabric pattern and the required open pathways necessary for carrying out the matrix vapor infiltration fill-in process. Nevertheless, if the open porosity could be sealed at the outer surfaces of such a SiC/SiC composite made by conventional ICVI, its properties could meet the requirements desired for the FCI-application.

In general, EC measurements are made using a reliable 4-probe potentiometric method or a less reliable 2-probe method [3]. The 2-probe method is less reliable because EC-values measured by this method include a resistance contribution from the material/electrode contact surfaces in series with the

[1]Pacific Northwest National Laboratory (PNNL) is operated for the U.S. Department of Energy by Battelle Memorial Institute under contract DE-AC06-76RLO-1830.

material resistance that lies between the coincident potential-current probes. If this contact resistance is of the same magnitude or larger than the material resistance, a distinct possibility for thin SiC-based samples, serious errors could occur. Before this study, because of geometric constraints and for convenience, we used a 2-probe method to determine the transverse EC for thin (~2 mm), disc-shaped samples. However, the more reliable 4-probe method was always used to measure the in-plane EC for relatively long bar samples.

At this point, before accepting lower than expected transverse EC-values measured by the 2-probe method for our reference 2D-SiC/SiC, the most important direction for the FCI-application, we sought to carefully reexamine these measurements. To do this we replaced our 2-probe method with a more reliable 4-probe method that would be amenable to measuring the EC across thin disc or plate-shaped SiC materials. At the same time we sought to estimate the level of uncertainty in our previous 2-probe measurements as well as the conditions under which the 2-probe method could still be used with confidence. For instance, a typical minimum resistance value for our reference 2D-SiC/SiC disc samples (2 mm x 7.1 mm dia.) was 20Ω at 800°C. Thus, to reliably keep the error in the 2-probe EC-values <5%, the total contact resistance for both sample-voltage probe interfaces should be <1Ω or <0.8 Ωcm^2 for this composite.

The subject of this report then is the development of a 4-probe potentiometric method for measuring the transverse EC across relatively thin plates of SiC-based or SiC/SiC composite materials, thus eliminating any contact resistance contribution. Also, the efficacy of using either the 2- or 4-probe methods when making these measurements will be assessed.

Experimental Procedure

Materials

We selected two types of SiC-based materials to use during this assessment: a dense high-purity monolithic CVD/b-SiC as a trial material and a relatively dense SiC/SiC composite with uniaxial fiber alignment made by the NITE™ process. Details on the material characteristics as well as results of 4-probe EC measurements made on standard bar-shaped samples of this CVD-SiC material obtained from Rohm and Haas were reported previously [3]. The uniaxial 2D-NITE™ composite was obtained from the Institute of Advanced Energy at Kyoto University [7]. This SiC composite had a density of ~3.0 g/cc and was received in the form of six bars (35.6 x 4.00 x 2.54 mm), three each cut with fibers oriented parallel or perpendicular to the bar lengths, and five discs (10.0 mm dia x 2.0 mm thick) with fibers parallel to the disc surfaces. All surfaces had been machined smooth. This composite contained ~30% Tyranno™-SA fibers coated with a ~500-nm thick PyC interphase. Properties of various forms of monolithic or composite NITE™-SiC are presented elsewhere [8,9]. Note though that the Tyranno-SA™ fiber component contains ~1 wt% alumina, while the NITE-SiC matrix contains ~10 wt% additions of alumina and yttria in mostly crystalline form due to the ~1800ºC sintering temperature. Also note that the PyC interphase makes up ~ 4 vol% overall in these NITE™ samples.

4-Probe and 2-probe EC methods

Our automated EC-measurement system and sample preparation procedures were discussed previously [3]. The new 4-probe configuration for thin disc-shaped SiC samples is depicted in Fig. 1. This configuration has been successfully used in our fuel cell program to determine EC(T) in various atmospheres for several types of ceramic electrode materials [10].

In this new configuration, a small hole (1.5 mm dia x 0.5 mm deep) was bored at the center of each disc face into which potential probes were placed. The potential probes consisted of a gold wire threaded through an electrically insulating alumina thermocouple tube. The thermocouple tube in turn was placed inside a hollow, flat-bottomed alumina push rod, one pair of which was independently spring loaded outside the hot zone. The sample disc faces were prepared in the same manner as for previous 2-probe

set-ups, i.e., a mild HF solution was used to remove any oxide surface layer, and then a Au-film was applied to each face using a SEM vacuum coater. As before, the two current electrodes consisted of gold gauze backed by a gold foil disc that were pressed against the disc faces by the alumina push rods. With this configuration 2-probe or 4-probe resistance measurements (R2 and R4, respectively) could be carried out on the same disc sample by reconnecting the i-v probes externally. The contact resistance Rc was then estimated from Rc = R2 - R4. To do this, R4 must first be prorated for the difference in the disc thicknesses for the 2- and 4-probe configurations. This simple estimate procedure assumes that the resistances are ohmic and that the sample is isotropic in the transverse direction.

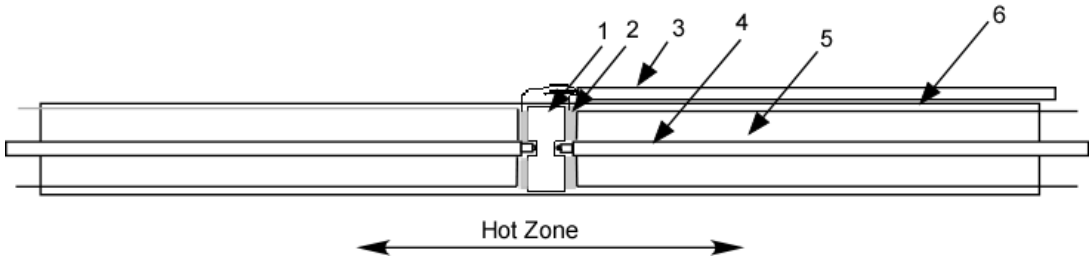

Fig. 1. Sample holder and configuration for 4-probe EC measurements of thin, disc-shaped SiC-type materials. Key: 1. SiC disc-shaped sample (~2 mm x 10 mm dia). 2. Vacuum-evaporated Au film + Au gauze current electrode. 3. Alumina thermocouple tube. 4. Spring loaded thermocouple tube containing independent Au wire voltage and current probes probe. 5. Alumina push rod (10 mm od with 1.6 mm id). 6. Alumina alignment sleeve.

Results and Discussion

Monolithic CVD-SiC

In Fig. 2, the temperature dependent EC(T)-values determined by our new 4-probe set-up for a thin disc sample of CVD-SiC are compared to previously measured values determined using the standard 4-probe method for bar-shaped samples of similar CVD-SiC materials.

The new EC(T)-data shown in Fig. 2 were measured while first increasing temperature to ~800°C, then decreasing temperature to RT and then repeating measurements for a second temperature cycle. The data were reproducible for both cycles, so only the increasing temperature data for the first cycle are plotted. The new data fall within a rather wide range of EC(T)-values measured previously in this laboratory for bar samples of nominally high-purity CVD-SiC from different sources. Apparent activation energies (E_a) were derived from a linear least squares data fit to $EC(T) = ec_0\exp(-E_a/kT)$ in an Arrhenius plot and are given in the legend.

The spread in EC-values for the different, but all nominally high-purity CVD-SiC materials reflects the influence of type and even small amounts of impurity in a temperature range where the electrical conduction is extrinsic for this wide band-gap semi-conducting material. At least the modest agreement of our new 4-probe disc data with previous 4-probe bar data indicated that the new configuration was satisfactory and should provide reliable EC(T)-values.

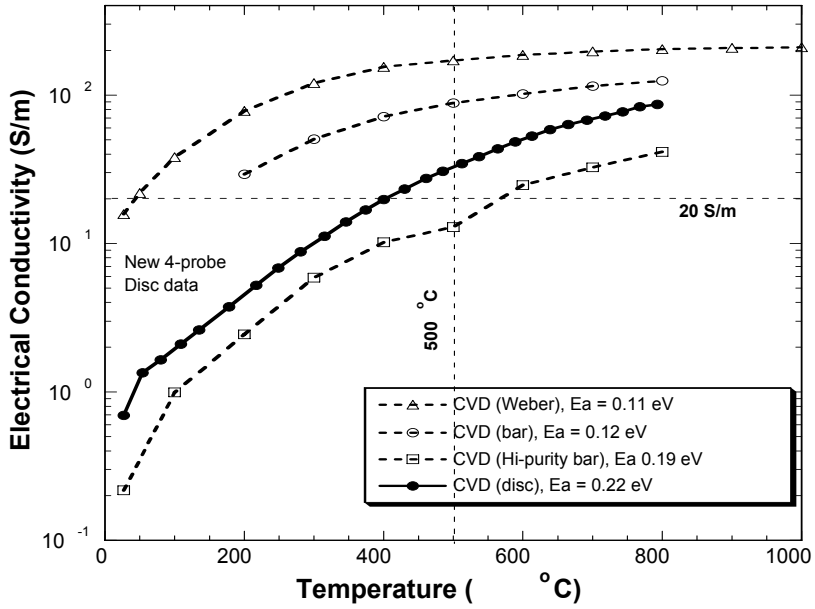

Fig. 2. Electrical conductivity of monolithic CVD-SiC determined by our new 4-probe method for a thin disc-shaped sample (solid symbols) compared to EC(T)-values measured previously on other CVD-SiC bar-shaped samples (open symbols).

Uniaxial 2D-NITE™ SiC/SiC composite

In Fig. 3, measured 4-probe EC(T)-values (solid symbols) for a bar sample of 2D-NITE™ SiC composite with 0º fiber alignment and for a disc sample with 90º fiber alignment are compared to the typical range of EC(T)-values determined for monolithic CVD-SiC (open symbols).

The EC of this 2D-NITE™ SiC/SiC composite is anisotropic with EC-values of ~10^4 or ~300 S/m (a ratio EC(0)/EC(90) of ~30) when the uniaxial fiber alignment is either parallel (0º) or perpendicular (90º) to the current direction, respectively. These EC-values exhibit little temperature dependence and are much greater than the EC-values for high-purity monolithic CVD-SiC.

Similar to the anisotropic reference 2D-SiC/ICVI-SiC, the primary reason that EC(0) >> EC(90) for this uniaxial 2D-NITE™ composite is the dominate contribution of the highly conductive PyC fiber coatings. For the EC(0) case, all the PyC coatings (which make up ~4 % of the total sample volume) are aligned parallel to the current direction. EC-values for PyC coatings have not been explicitly measured, but are expected to lie between 10^4 to 10^6 S/m, the range reported for “soft” amorphous carbon or “hard” crystallized graphite, respectively. A simple parallel conduction model suggests that the coating EC should be ~2 x 10^5 S/m, which appears feasible. Furthermore, the observed temperature independence of EC(0) is characteristic of electronic conduction in graphite. However, the fact that EC-values for the NITE (90) sample are > 4-6 times the EC-values for CVD-SiC suggests that the NITE™ matrix SiC itself has higher EC-values than nominally pure CVD-SiC. We plan to test this possibility by measuring EC on a monolithic NITE™-SiC sample.

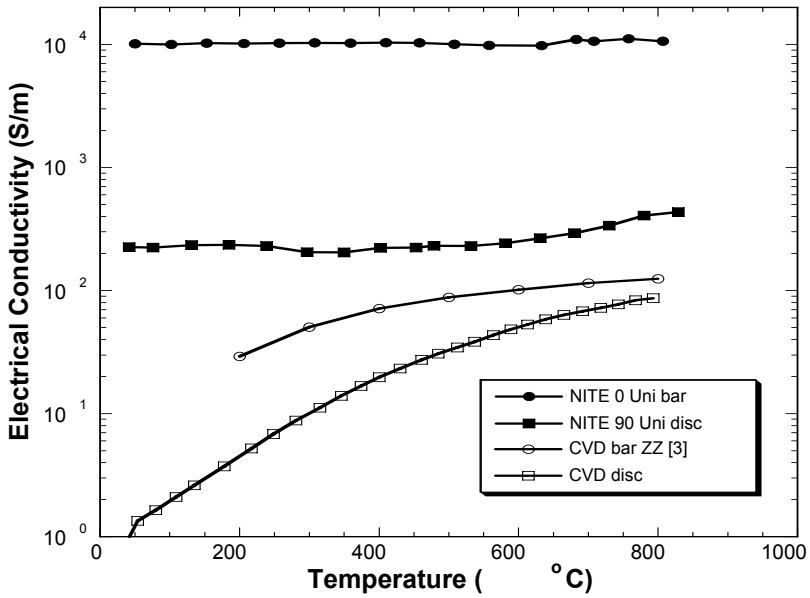

Fig. 3. Electrical conductivity of a uniaxial 2D-NITE™ SiC/SiC composite with either 0º or 90º fiber alignment compared to typical EC(T)-values for monolithic CVD-SiC all measured using 4-probe methods.

Contact resistance estimates

Qualitative estimates of the contact resistances were made for the 4-probe NITE™ 90 and CVD disc configurations at 200 and 500ºC and are given in Table 1.

From Table 1, a qualitative estimate of Rc for the 2-probe configuration with a smooth, pure CVD-SiC surface in contact with a thin gold metal film is ~10Ω or ~9.2 Ωcm^2. In contrast, Rc for a smooth NITE-SiC/SiC surface in contact with gold metal is only ~1.2Ω or ~0.95 Ωcm^2. Such relatively high Rc-values in comparison to the measured 4-probe R4-values result in large error factors for the corresponding 2-probe configurations.

Table 1. Qualitative estimates of the contact resistance for different types of disc-shaped SiC samples

Material	**Disc thick**	**Temp (ºC)**	**R2 (Ω)**	**R4 (Ω)**	**Rc (Ω)***	**Error Factor***
CVD	2.49 mm	200	20.1	6.2	13.9	x2.2
"	"	500	9.41	1.07	8.3	x7.8
NITE-90 uni	2.00	200	1.20	0.11	1.09	x10
"	"	500	1.38	0.12	1.26	x11
2D-SiC/SiC ref	2.20	200	1378	nm	est 10	~0.007
" "	"	500	107	nm	est 10	0.10
" "	"	800	16.3	nm	est 10	x1.6

*Rc = R2 – R4 and Error Factor = Rc/R4.

The magnitude of the contact resistance, in general, is quite variable since it depends upon so many factors, primarily the mating surface roughness (the actual contact area between flat surfaces of dissimilar materials) as well as contact pressure, temperature, mode of electrical conduction between dissimilar materials, etc. [11]. Therefore, the following analysis is qualitative.

The difference between the Rc-values for the CVD and NITE-90 2-probe set-ups can be explained by considering the types of mating dissimilar materials for each of these cases. Apparently, for the interface between a highly conductive metal and only a moderately conductive semi-conductor, as we prepared them, Rc was rather high. For the NITE-90 configuration, the SiC surface is interspersed with numerous highly conductive PyC coating intersections, which dramatically reduces the Rc magnitude. Nevertheless, the error factor is still quite large for this set-up. Because of the apparently large error factors and the uncertainty connected with making Rc corrections, 2-probe measurements are deemed unacceptable for determining EC for the CVD-SiC and 2D-NITE SiC/SiC materials. Only 4-probe EC-measurements should be used for disc samples of SiC-based materials with relatively high EC.

At the bottom of Table 1, error factor estimates expected at three temperatures (200, 500 and 800ºC) for the case of measuring the transverse EC for our reference 2D-SiC/ICVI-SiC using a 2-probe set-up are added. This SiC/SiC composite had a dense CVD-SiC seal coat (~0.1 mm thick); so the actual contact surfaces for our reference 2D-SiC/SiC set-up likely were similar to those encountered in our 2-probe CVD-SiC set-up. Therefore, Rc was estimated to be ~10Ω for all temperatures. For this after the fact case, the error factor exceeds 10% only when the temperature exceeds 500ºC. Thus, only for a limited low temperature range where the EC-values are fairly low would the 2-probe method yield acceptable EC-values. In fact, the influence of contact resistance may explain why an analysis of the transverse EC(T)-values for the reference 2D-SiC/SiC did not yield a typical Arrhenius temperature dependence.

From this analysis of measured and expected relatively large contact resistances for various 2-probe configurations, it appears prudent to routinely use the new 4-probe set-up when determining the transverse EC of thin disc-shaped samples of SiC-type materials from now on. As a final note, contact resistance itself may not be bad. In the FCI-application, a contact resistance between the Pb-Li coolant and the extensive surface of a SiC/SiC insert may be beneficial in reducing the MHD-induced electrical currents.

Conclusion

Making EC(T)-measurements of most thin samples of SiC-type materials using a 2-probe method is unreliable due to inherent relatively large and highly variable contact resistances. To overcome this problem, a more reliable 4-probe potentiometric method was designed and assessed. Previously reported transverse EC-values for 2D-SiC/SiC need to be corrected.

Future Work

Our previous transverse EC(T) measurements for several types of 2D-SiC/SiC composites will be redone using the more reliable 4-probe method.

References

[1] N. B. Morley et al., Current understanding of feasibility of SiC/SiC composites for flow channel inserts in Dual Coolant Pb-17Li blankets, presented at TBM meeting, June 4, 2004, UCLA.
[2] G. E. Youngblood, R. J. Kurtz, and R. H. Jones, Development of SiC/SiC for Application as a Flow Channel Insert, Fusion Materials Semiannual Progress Report for period ending December 31, 2004, DOE-ER-0313/37, 3–8.
[3] G. E. Youngblood, E. Thomsen, and G. Coffey, Electrical Conductivity of SiC/SiC, Fusion Materials Semiannual Progress Report for period ending December 31, 2005, DOE-ER-0313/39, 46–51.
[4] G. E. Youngblood and R.H. Jones, Characterization of a 2D-SiC/SiC composite made by ICVI with Hi-Nicalon™ Type S fabric, Fusion Materials Semiannual Progress Report for period ending June 30, 2003, DOE-ER-0313/34, 34–40.
[5] T. Hinoki et al., The effect of high dose/high temperature irradiation on high purity fibers and their silicon carbide composites, J. Nucl. Mater. 307–311 (2002) 1157–1162.
[6] S. Smollentsev, UCLA, Los Angeles, private communication.
[7] J-S. Park, Kyoto University, Kyoto, Japan, private communication.

[8] J. S. Park et al., Tailoring the microstructure of hot-pressed SiC by heat treatment, J. Nucl. Mater. 329–333 (2004) 558.
[9] Y. Katoh, A. Kohyama, T. Nozawa, and M. Sato, SiC/SiC composites through transient eutectic-phase route for fusion applications, ibid. 587.
[10] G. Hsieh, T. O. Mason, and L. R. Pederson, Experimental limitations in impedance spectrometry, effect of reference electrode geometry/position, Solid State Ionics 96(3–4) (1990) 153.
[11] N. Ben Jemaa, J. L. Quffelec, and D. Travers, Electrical contact resistance study of cleaned and corroded materials, Meas. Sci. Technol. 1 (1990) 282.

SWELLING OF NUCLEAR GRAPHITE AND HIGH QUALITY CARBON FIBER COMPOSITE UNDER VERY HIGH IRRADIATION TEMPERATURE—L. L. Snead, T. D. Burchell, and Y Katoh (Oak Ridge National Laboratory)

OBJECTIVE

The objective of this work is to define the thermophysical property changes of high quality graphite materials under high temperature neutron irradiation.

SUMMARY

The purpose of this experiment was to evaluate the dimensional change of newly proposed nuclear graphite material following high-temperature irradiation, and to compare the measured swelling with the historic nuclear graphite H-451. Over the irradiation temperature range studied (~850-1475°C) and neutron dose range (~1.78, ~5.25 and 8.73 x 10^{25} n/m^2 (E>0.1 MeV)) the UCAR PCEA and SGL NBG-10 candidate nuclear graphite had similar densification to that of Great Lakes Carbon nuclear graphite H-451. In this temperature and dose range all materials remained in the densification stage. Additionally, the effect of high-temperature irradiation on the dimensional stability of high-quality carbon fiber composites was investigated. A high thermal conductivity three dimensional carbon fiber composite, FMI-222, and a very high thermal conductivity one dimensional carbon fiber composite MKC-1PH, were studied. Results indicate that a greater than anticipated dimensional change occurs for these composites. Moreover, the dimensional stability of the 3-D composite appears to be a strong function of the sample size chosen, raising the question of the appropriate size sample to use to determine irradiation-induced dimensional change for these materials.

PROGRESS AND STATUS

Introduction

Fusion reactors have and continue to use nuclear graphite and carbon fiber composite at higher temperatures than typically considered for previous generations of nuclear reactors. This article reports on data generated in the METS (Mapping Elevated Temperature Swelling) capsule irradiated in the High Flux Isotope Reactor (HFIR) at the Oak Ridge National Laboratory. This set of capsules is unique in that it was designed to achieve, extremely high irradiation temperatures (800-1500°C.) This temperature range includes and well exceeds the design temperature for both core graphite and control rod materials for the NGNP. The primary purpose of the experiment was to determine the irradiation-induced dimensional change of two graphite materials recently produced to mimic the historic nuclear graphite H-451. A secondary purpose was the evaluation of very high performance (i.e., high thermal conductivity) carbon fiber composites for which there are only limited performance data.

Experimental

The METS capsules were irradiated in the flux trap region of HFIR to doses of ~1.78,~5.25 and 8.73 x 10^{25} n/m^2 (E>0.1 MeV, ~ 2.4, 7, and 11.6 dpa respectively.) A depiction of a METS capsule taken prior to assembly is shown in Fig. 1. Each capsule contained ten sub-capsules, individually containing many specimens. The specimens were nominally 5.8 mm in diameter with varied thicknesses. The samples were loaded in contact with a high-purity POCO AXF-5Q graphite holder, and the capsule environment was high purity argon. For the three highest temperature sub-capsules a molybdenum sleeve was used external to the graphite holder to increase the gamma heating. On both ends of the sub-capsule cylinders were threaded graphite caps that included eight wells each containing a melt-block. An end of view of the melt block holder is shown in Fig. 2. The melt blocks were pure materials or binary alloys specifically blended to achieve a select melting temperature. For a given sub-capsule the design temperature was achieved by varying the gas gap between the outside of the sample holder and

the inner diameter of the capsule containment. The maximum sub-capsule irradiation temperature was then determined by viewing the melt-wires following irradiation. The melt-blocks were arrayed to compensate for either an overestimation or underestimation of the true temperature of the sub-capsules. Typical intervals between melt-blocks were ~20-40°C. A temporal variation in temperature within a sub-capsule is expected due to the radiation-induced dimensional change of the POCO AXF-5Q holder, thus changing the gap between the sample holder and capsule containment. No change in temperature due to variation in reactor power was expected due to the exceptionally steady power history of the HFIR reactor during the irradiations.

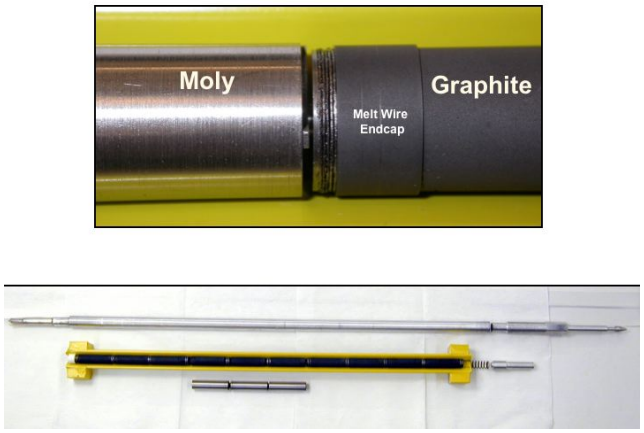

Fig. 1. Photograph of METS capsule components.

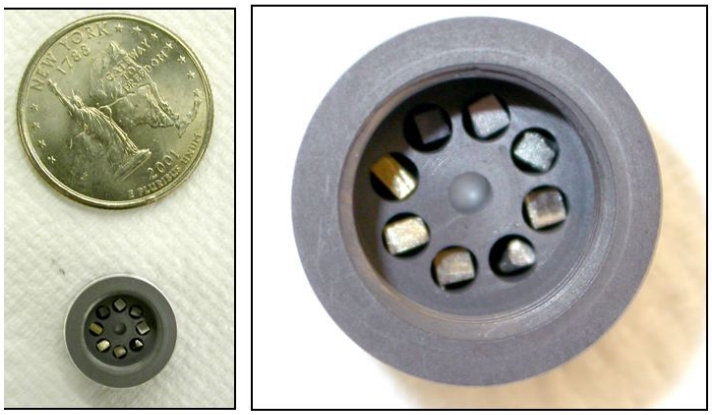

Fig. 2. End on view of melt block holder.

Materials for this study (see Table 1) included three nuclear graphite materials and two high-quality carbon fiber composites. All materials were machined in cylinders of 5.8 mm diameter of varied lengths (approximately 3 mm). The nuclear graphite H-451, a near-isotropic, medium size grain graphite previously manufactured by Sigri Great Lakes Carbon, was included as a standard for comparison. The two other graphite materials are NBG-10 manufactured by SGL and PCEA manufactured by UCAR. All graphite materials were machined with the cylindrical axis parallel to the extrusion direction. The carbon fiber composites were manufactured by Fiber Materials

Incorporated (FMI-222) and Mitsubishi Kasei (MKC-1PH). The FMI-222 material is a three dimensional, balanced weave, composite utilizing P-55 pitch based fibers and a mesophase pitch matrix. The thermal properties of this composite are near isotropic. The MKC-1PH is also based on a pitch fiber (K-139) and a mesophase pitch matrix, though has a 1-dimensional architecture

Table 1. Properties of material studied

Designation	Manufacturer	Architecture	Constituents	Grain or cell size	Density (g/cc)
SGL NBG-10	Sigri Carbon	graphite	Pitch Coke Extruded Graphite Near Isotropic	1.6 mm (Max)	1.8
PCEA	Graftech	graphite	Petroleum Coke Extruded Graphite Near Isotropic	0.8 (Max.)	1.79
H-451	Great Lakes Carbon	graphite	Coal tar pitch binder. Petroleum pitch impregnation. Petroleum Coke.	0.5 (Mean)	1.76
FMI-222	Fiber Materials Incorporated	3-D Balanced Weave Composite	Amoco P-series Pitch Fiber. Pitch Derived Matrix.	0.7 mm	1.96
MKC-1PH	Mitsubishi Kasei	1-D Composite	K-139 Pitch Based Fiber, Pitch Derived Matrix.	n/a	1.93

yielding highly anisotropic thermal properties. The cylindrical axis of the MKC-1PH was parallel to the fiber axis.

Dimensional and mass measurements were taken on each sample before and after irradiation. A calibration-certified micrometer was used to measure the thickness and diameter. Three measurements of thickness and four of diameter were taken and averaged. Accuracy of determining the change in thickness and diameter was limited by the smallness of the sample and the statistical variation in repeated measurements.

Results

The effects of irradiation on the sample thickness and diameter for the UCAR, Sigri, and H-451 nuclear graphites are given in Figs. 3 and 4, respectively. Error bars shown (Figs. 3 and 4) for irradiation temperature, determined by evaluation of the melt-blocks and the calculated change due to the sleeve dimensional change, are included in the figures. It is noted that the scatter in the dimensional change data is approximately 0.5 %. This is in part due to the error associated with the measurement itself, and in part due to the limited size of the sample. The sample thickness and diameter were typically 3.0 and 5.8 mm, respectively. These dimensions are small when considering the grain size of the nuclear graphite and the unit cell size of the FMI-222 composite. Specifically, the maximum grain size for the NBG-10 materials is approximately 1.6 mm. [1] The unit cell size for the FMI-222 composite is approximately 0.7 mm. Given the intrinsic anisotropic swelling behavior of graphite combined with the small ratio of sample size-to-grain size statistical scatter would be expected for dimensional change. Such a scatter in as-irradiated dimensional change for nuclear graphite is common in the literature. It is noted that the thickness measurements were quite accurate (<0.1% error) and repeatable. However, the diameter measurements were less repeatable. This was especially true for the FMI-222 composites, which became distinctly out-of-round due to irradiation.

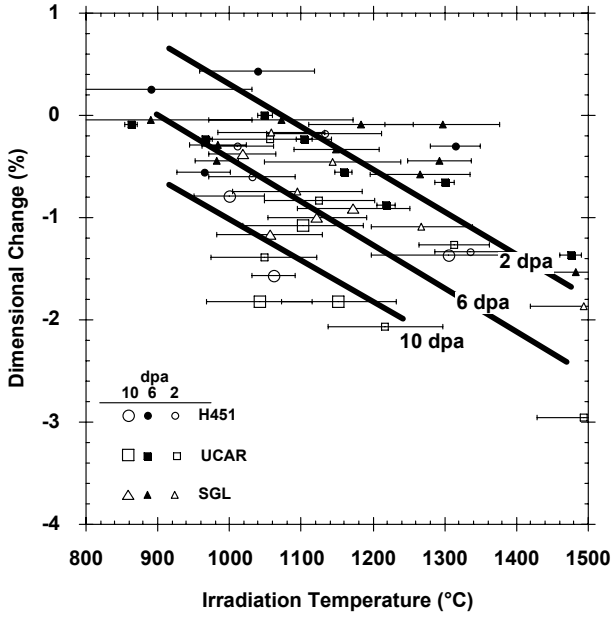

Fig. 3. Effect of irradiation on thickness of graphite materials.

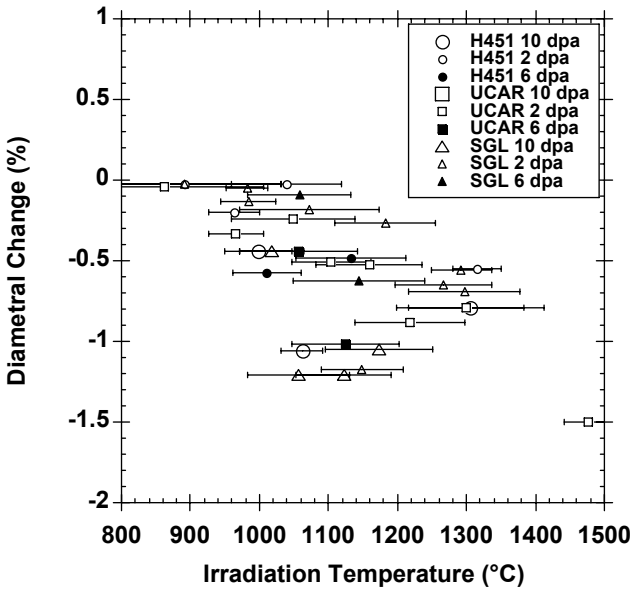

Fig. 4. Effect of irradiation on sample diameter of graphite materials.

The irradiation-induced dimensional change for the FMI-222 and MKC-1PH composite are shown in Figs. 5 and 6, respectively. The data plotted in Figs. 5 and 6 are limited to the 2.4 dpa irradiation. As seen from the figures the amount of swelling for the composite materials at the 2.4 dpa level was substantial. For all irradiation conditions the gross dimensional change caused the FMI-222 material to become friable. This was especially the case for the higher dose irradiations. Given the condition of the samples, and the gross dimensional change occurring, the dimensional changes for doses higher than 2.4 dpa were not considered meaningful.

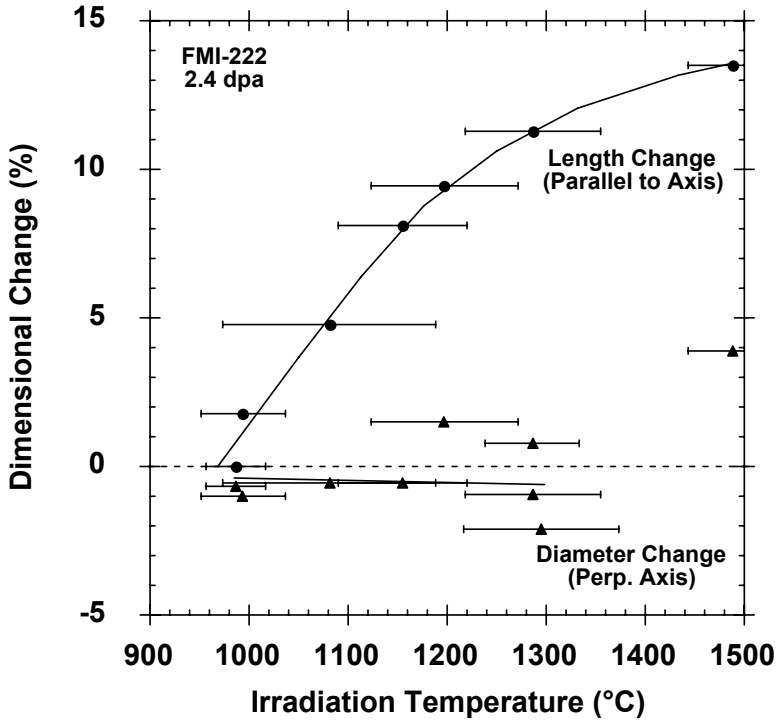

Fig. 5. Effect of irradiation on dimensional change of FMI-222 composite.

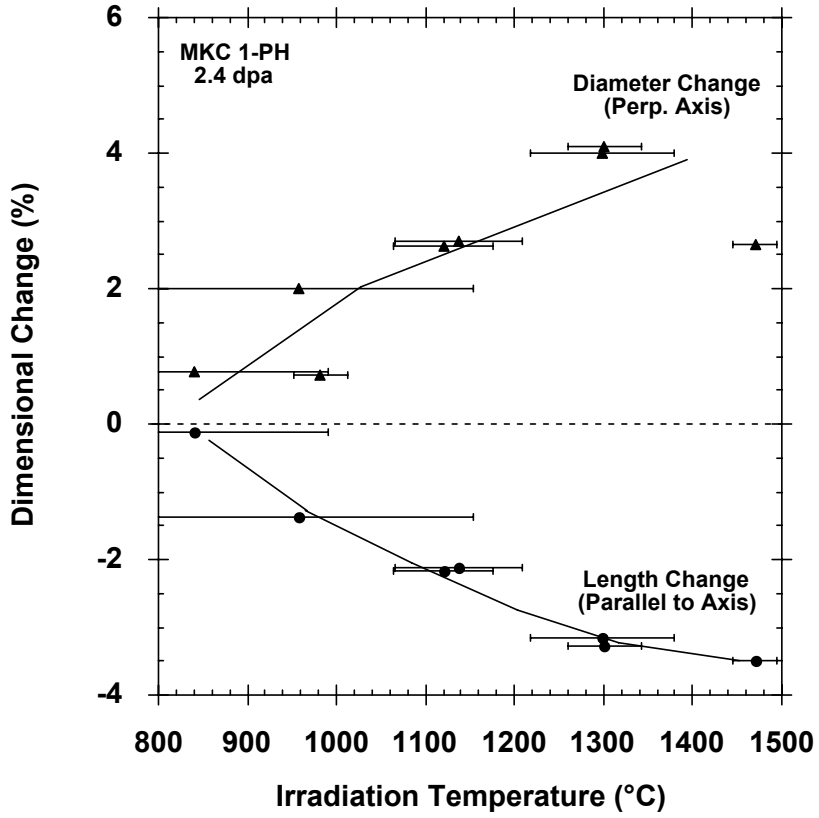

Fig. 6. Effect of irradiation on dimensional change of MKC-1PH composite.

Discussion

Radiation damage in graphite occurs when energetic particles, such as fast neutrons, impinge on the crystal lattice and displace carbon atoms from their equilibrium positions, creating a lattice vacancy and an interstitial carbon atom. The displaced carbon atoms recoil through the lattice and produce other carbon atom displacements in a cascade effect. The cascade carbon atoms tend to be clustered in small groups of 5-10 atoms and it is generally satisfactory to treat the displacements as if they occur randomly. However, not all of the carbon atoms remain displaced. The displaced carbon atoms diffuse between the graphite layer planes in two dimensions and a high proportion of them recombine with lattice vacancies. Others coalesce to form linear molecules, which in turn may form the nucleus of a dislocation loop, essentially a new graphite plane. Interstitial clusters, on further irradiation, may be destroyed by impinging neutrons or energetic displaced carbon atoms (irradiation annealing). Adjacent lattice vacancies in the same graphite crystal basal plane are believed to collapse parallel to the basal plane, thereby forming sinks for other vacancies that are increasingly mobile above 600°C, and hence can no longer recombine and annihilate interstitials. The lattice strain that results from displacement damage causes significant structural and property changes in the graphite.

A principal result of the carbon atom displacements discussed above is crystalline dimensional change. Interstitial defects will cause crystallite growth perpendicular to the layer planes (c-axis direction), whereas coalescence of vacancies will cause a shrinkage parallel to the layer planes (a-axis direction). The damage mechanism and associated dimensional changes are illustrated in Fig. 7.

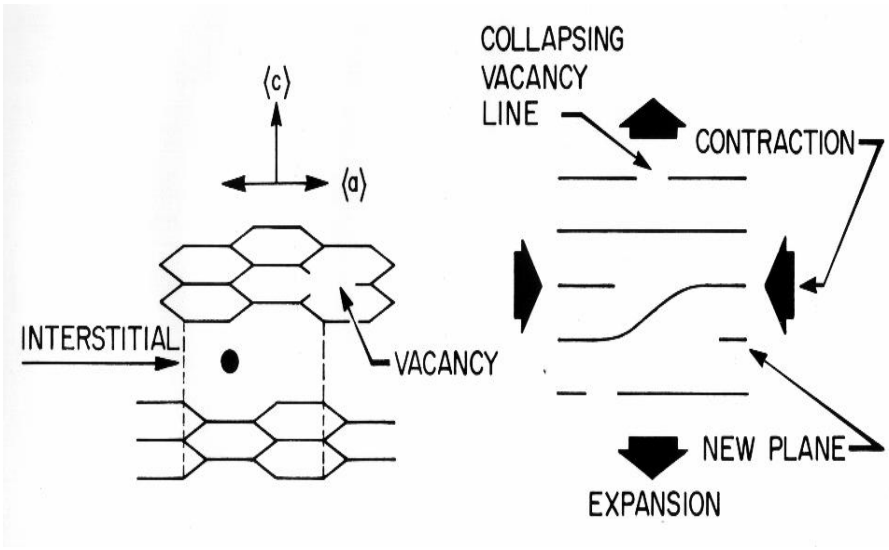

Fig. 7. Neutron irradiation damage mechanism in graphite showing the induced crystal dimensional changes.

Polygranular graphite exhibits a polycrystalline structure, usually with significant texture resulting from the method of forming during manufacture. Consequently, structural and dimensional changes in polygranular graphite are a function of crystallite dimensional change and the graphite texture. In polygranular graphite, thermal shrinkage cracks (formed during manufacture) that are preferentially aligned in the crystallographic a-direction initially accommodate the c-direction expansion, so mainly a-direction contraction is observed. Hence, the graphite undergoes net volume shrinkage. This behavior is illustrated with data from grade H-451 graphite, an extruded grade used in the Fort St. Vrain HTGR. As seen in Fig. 8, H-451 exhibits volume shrinkage behavior at irradiation temperatures of 600 and 900°C. With increasing neutron dose

(displacements), the incompatibility of crystallite dimensional changes leads to the generation of new porosity, and the volume shrinkage rate falls, eventually reaching zero. The graphite then begins to swell at an increasing rate with increasing neutron dose because of the combined effect of c-axis growth and new pore generation. The graphite thus undergoes a volume change "turnaround" into net growth which continues until the generation of cracks and pores in the graphite, due to differential crystal strain, eventually causes total disintegration of the graphite (Fig. 8).

At low irradiation temperatures, typically < 300°C, volume growth may be observed initially, followed by the rapid onset of volume shrinkage [2] [3] . The low dose volume swelling has been attributed to the relaxation of fabrication stresses [3] [4] [5] . With increasing dose the volume shrinkage behavior would be expected to turnaround to net swelling [5] .

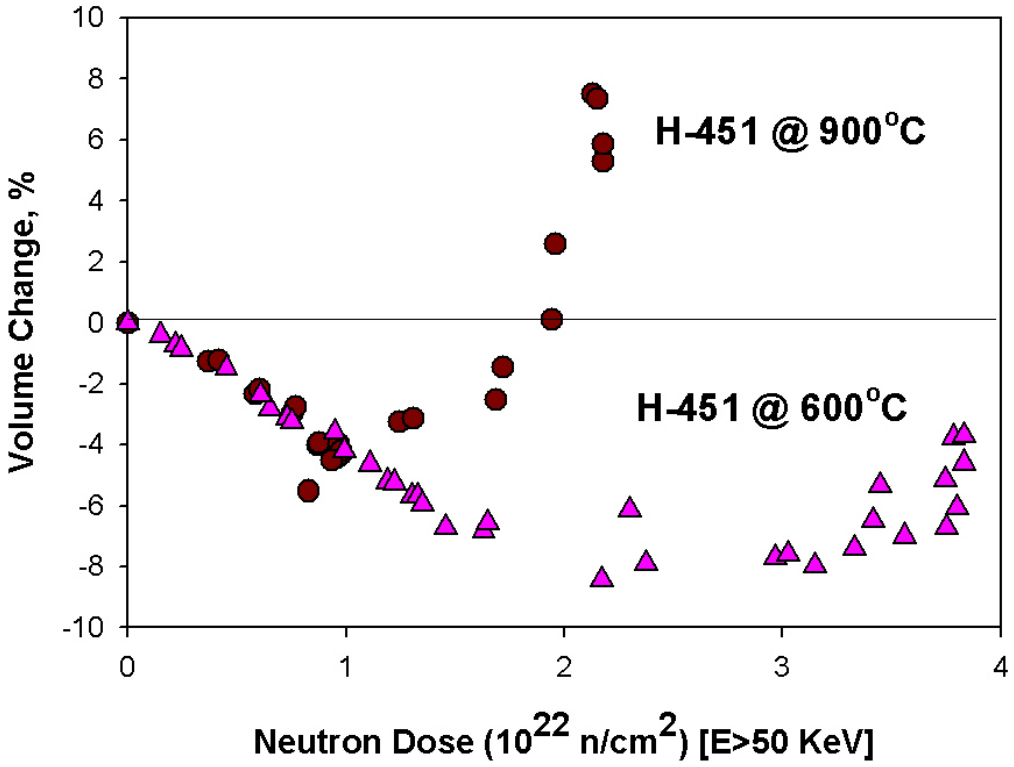

Fig. 8. Irradiation-induced volume changes for H-451 graphite at two irradiation temperatures [6].

As H-451 graphite is an extruded material, and thus the filler coke particles are preferentially aligned in the extrusion axis (parallel direction). Consequently, the crystallographic a-direction is preferentially aligned in the parallel direction and the a-direction shrinkage is more apparent in the parallel (to extrusion) direction, as indicated by the parallel direction dimensional change data in Figs. 9 and 10. The dimensional and volume changes are greater at an irradiation temperature of 600°C than at 900°C, i.e., both the maximum shrinkage and the turnaround dose are greater at an irradiation temperature of 600°C. This temperature effect can be attributed to the thermal closure of internal porosity aligned parallel to the a-direction that accommodates the c-direction swelling. At higher irradiation temperatures a greater fraction of this accommodating porosity is closed and thus the shrinkage is less at the point of turnaround.

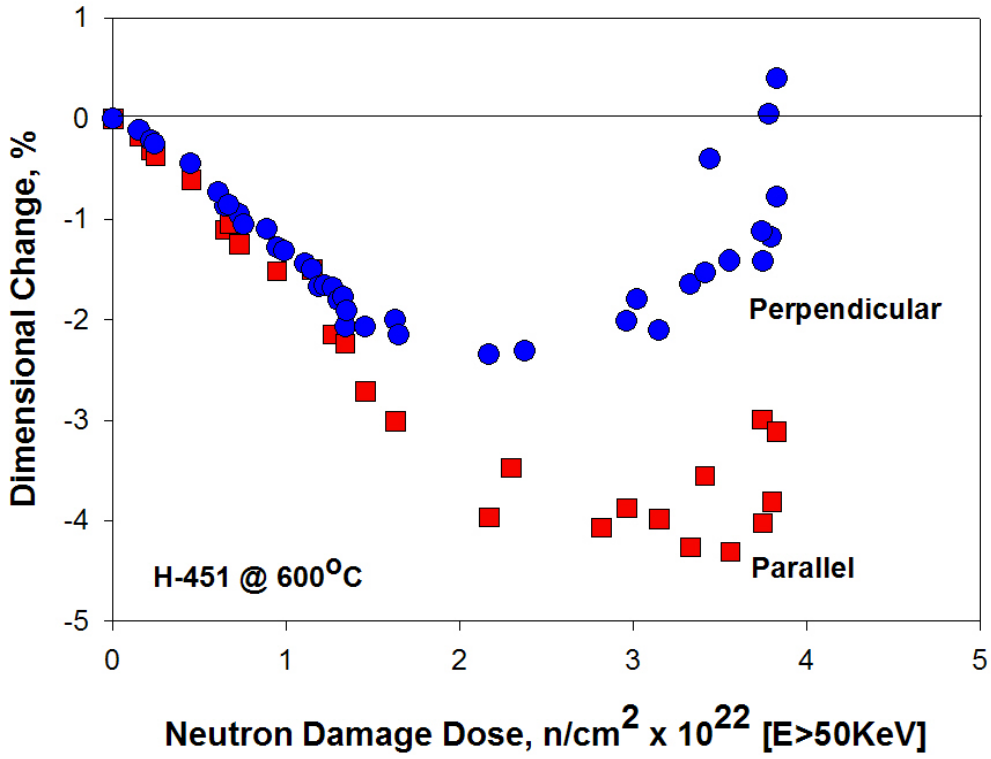

Fig. 9. Dimensional change behavior of H-451 graphite at an irradiation temperature of 600°C [6].

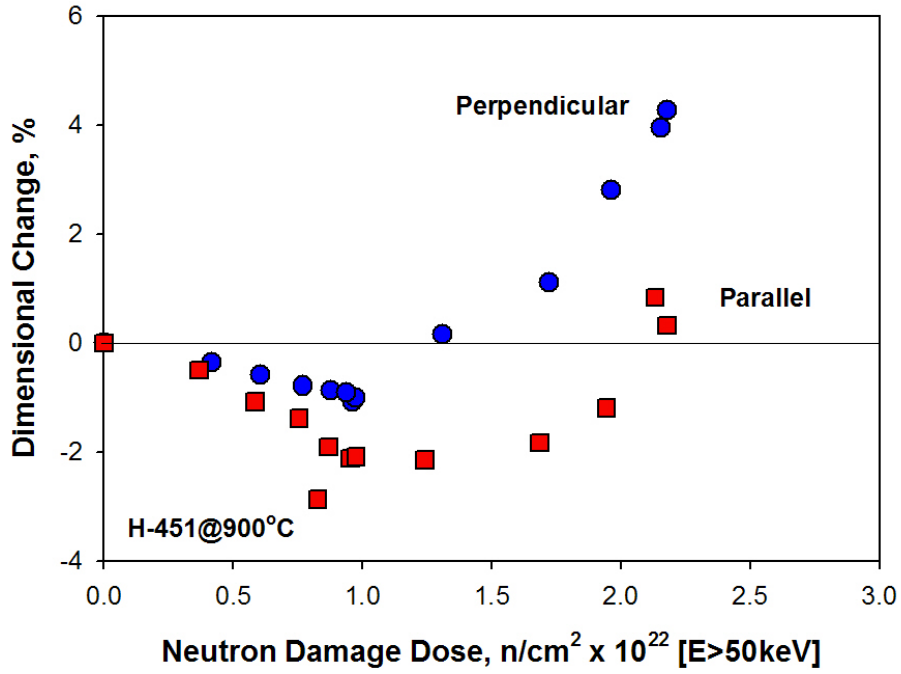

Fig. 10. Dimensional change behavior of H-451 graphite at an irradiation temperature of 900°C [6].

Limited work has been carried out on the dimensional stability of H-451 graphite at the very high temperatures of the current work. The work of Engle[7] provides data over the temperature range of 550-1350°C for both H-451 and H429 materials in a dose range relevant for discussion. Figure 11 gives a set of dimensional change curves for H-451 measured both perpendicular and parallel to the extrusion direction. This data was taken from the trend curves of Engle's data for a dose of to 2 x 10^{25} n/m^2 (E>0.1 MeV). From this figure a clear trend towards greater densification of higher irradiation temperatures is observed, along with a difference in swelling behavior for directions perpendicular and parallel to the extrusion direction. The data for dimensional change in the direction parallel to extrusion of Fig. 11 is compared to the 2.4 dpa data of Fig. 3, and are seen to be in general agreement. To summarize the behavior of the nuclear graphite studied here, within experimental error, the dimensional change for the UCAR PCEA and SLG NBG-10 are similar to the standard nuclear graphite H-451, whose swelling is consistent with previous data at similar irradiation temperatures. This is true for the ~ 2.4 dpa dose level. Limited, higher dose data (~ 6dpa) on H-451 is available from the Engle[7] report, which is also consistent with the present work.

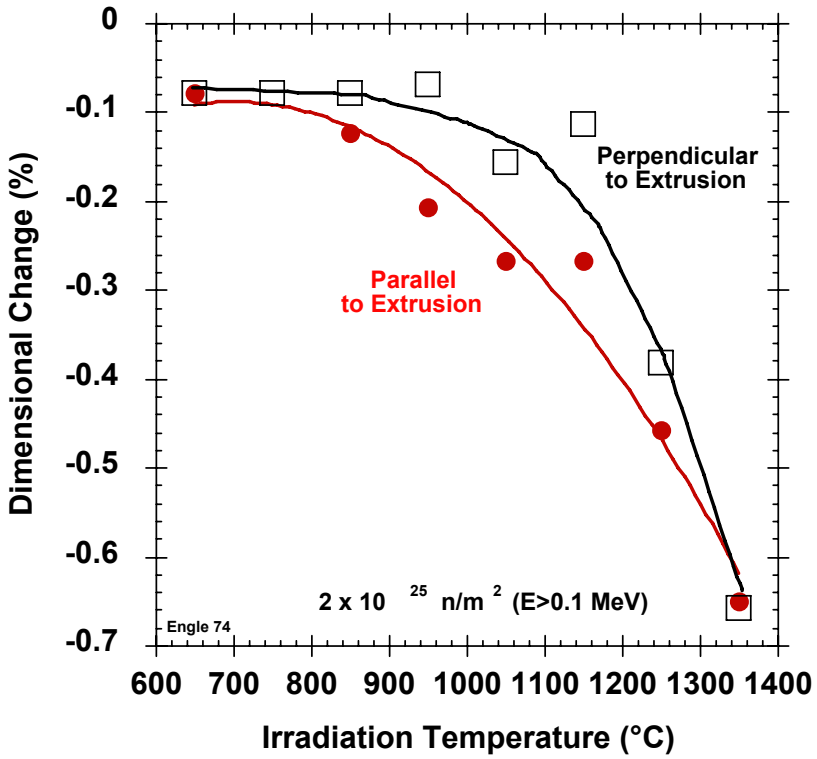

Fig. 11. Dimensional change for H-451 irradiated to 2.4 x 10^{25} n/m^2(E>0.1 MeV) as a function of temperature [7].

The physical processes leading to the irradiation-induced anisotropic dimensional changes for graphite crystals and non-isotropic graphite (discussed previously) also explain the dimensional change in composite materials. In Fig. 7, the anisotropic dimensional change is explained by irradiation-created interstitials forming new planes between the existing basal planes leading to swelling perpendicular, and shrinkage parallel to these planes. The same process applies to graphitic carbon fiber, though the microstructure of the fibers differ from pyrolytic or nuclear

graphites in that the basal planes tend to form circumferentially around the fiber axis. By applying the graphite crystal swelling mechanism to the core-sheath microstructure typical of a graphite fiber (see Fig. 12) the as-irradiation dimensional change for graphite fibers would be for diameteral swelling and axial shrinkage. The matrix of the carbon fiber composite will behave in a fashion similar to graphite.

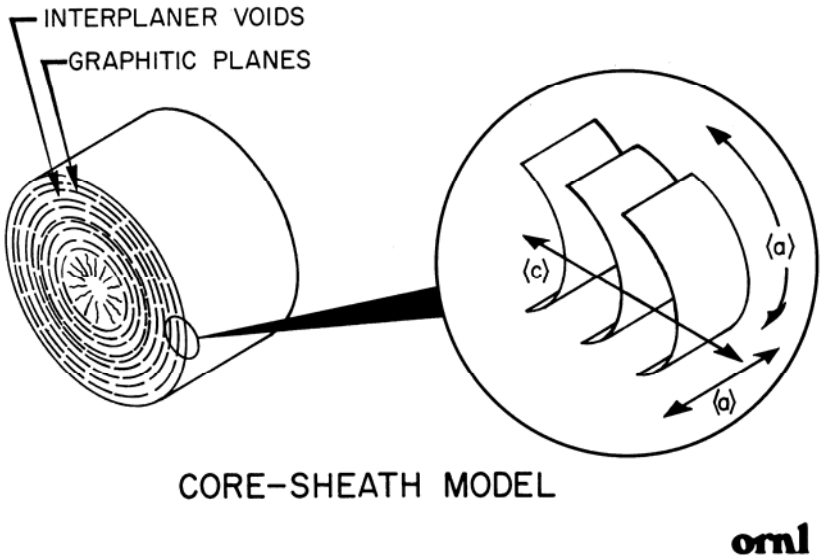

Fig. 12. Schematic representation of graphite fiber.

Figure 13 shows the dimensional change behavior of 1, 2 and 3 directional composites replotted from the literature. [8] In this example, solid cylinders were irradiated at 600°C to doses ranging from 0-5 dpa and the resulting diameter and length measured. The behavior of each material can be explained by the accepted theory for dimensional change in graphite after taking into account the individual fiber architectures, and by observing that a graphite fiber, PAN based in this example, is basically a filament of circumferential or radial basal planes running parallel to the fiber axis. The irradiation induced dimensional change of such a fiber is therefore to shrink in length and grow in diameter, as observed for the unidirectional composite of Fig. 5. At doses less than 1 dpa the dimensional change is relatively minor for the unidirectional composite of Fig. 13. As the dose is increased, the direction perpendicular to the fiber axis is more or less unchanged while a significant shrinkage along the direction parallel to the fiber axis occurs. At about 2 to 3 dpa swelling in the composite occurs in the perpendicular direction. The random fiber composite of Fig. 13 has a random orientation of chopped PAN fibers in the plane perpendicular to the cylindrical axis. The specimen diameter shows practically no change perpendicular to the fiber axis to about 4.5 dpa, though exhibits ~ 2% shrinkage parallel to the fiber axis. The 3-D balanced PAN weave fiber has essentially isotropic shrinkage to a dose of ~ 2 dpa, at which point the diameter of the fibers and hence the sample begin to swell.

Also given in the 3-D composite plot in Fig. 14 is the radiation induced dimensional change behavior parallel to the fiber axis of an Amoco P55 pitch fiber composite (the FMI-222 material of the present study.) This material was processed in an identical manner to the PAN fiber composite. From the plot it appears that the pitch fibers, and thus the composite, undergoes slightly less shrinkage, possibly due to the higher fiber crystallinity. This hypothesis is also supported by the observation that fibers with higher final heat treatment temperatures tend to exhibit less dimension change and is also consistent with the observation that elevating the heat treatment temperature of graphite reduces the irradiation induced shrinkage.

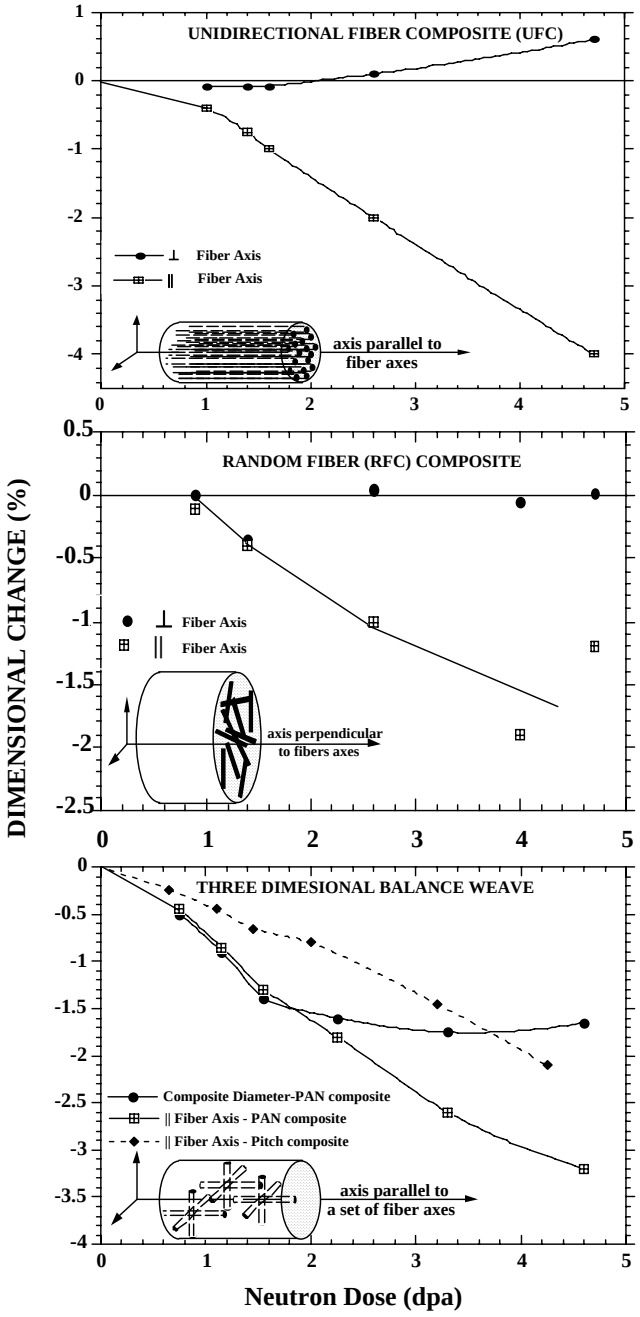

Fig. 13. As-irradiated dimensional changes for carbon fiber composites of varied architectures. Irradiation temperature of 600°C [8].

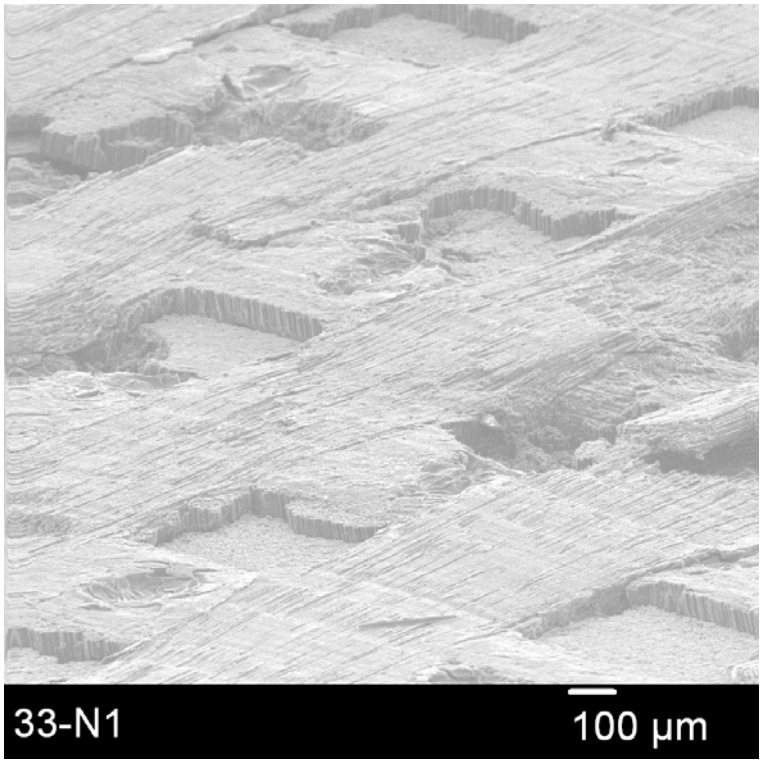

Fig. 14. SEM image of top surface of a FMI-222 composite following irradiation to 980°C, 2 dpa.

The composite materials investigated in this study underwent gross dimensional change, unexpected given the sparse elevated temperature data in the literature. The data shown in Figs. 5 and 6 are limited to the lowest dose capsules in part due to the gross dimensional change present, and in part due to their friable nature following irradiation. The FMI-222, a nearly isotropic orthogonal weave pitch-fiber composite with equivalent fiber volume fraction in the x, y, and z directions underwent positive dimensional change (swelling) parallel to the cylindrical axis of the sample which increased with increasing temperature. This material has entered into the swelling regime for these dose and temperature conditions. The magnitude of swelling was in excess of 10% at the highest temperatures studied at the 2 dpa dose level. This is in contrast to FMI-222 swelling data reported by Burchell [8] and Snead [9] also for HFIR irradiation, though at lower irradiation temperature. Specifically, a contraction of 0.6 % is interpolated from the data of Burchell for FMI-222 irradiated at 600°C to an equivalent fluence as the data of Fig. 5. Snead [9] reports on an 800°C irradiation to a substantially higher dose (7.7 x 10^{25} n/m^2) than the Fig. 5 dose (~2.4 x 10^{25} n/m^2.) In that case the material underwent a contraction of 3.6%. However, Snead [9] reported contraction along the length of a bend-bar (2.3 x 6 x 30 mm.) It was also noted in this work that the width and thickness direction exhibited swelling. Specifically, swelling parallel to the width direction (6 mm) was 1.4% and swelling parallel to the thickness direction (2.3 mm) was 5.9 %. The overall dimensional effects were related to the effect of (measured) gross changes in dimension of fiber bundles noting that gaps were evident on the surface of the bend bars. Figure 14 shows and example of the top surface of an FMI-222 composite irradiated in the present work to 980°C, 2.4 dpa. This composite underwent very low swelling. By inspection of the sample surface the contraction of the fiber tows below the free surface of the sample is evident. However, there is evidence from this micrograph that some of the fibers (particularly at the tow edge) have not withdrawn into the sample. This is evidence of shear within the fiber bundle as opposed to the tow-matrix interface. This observation is evidence of the large stresses that must be building in the composite under irradiation. The fact that the bundles are not failing at the tow-matrix interface also supports the prior finding that, at least in the initial

period of gross dimensional change, the load carrying capacity of the composite has not been degraded. In fact, previous measurement of FMI-222 irradiated to a dose of ~ 7.7×10^{25} n/m2 (E>0.1 MeV) at 800°C, described a 54% increase in strength. [9]

Figure 15 compares the surface morphology of FMI-222 irradiated in previous work with that of the present. Figure 15(c) and 15(d) show side views of two samples from the present study. Specifically, Fig. 15(c) shows a sample which exhibited very small (~0.5%) swelling with a sample exhibiting > 10% swelling parallel to the cylindrical axis. By inspection of Figs. 15(b) and 15(d), it is apparent that gross changes in the fiber bundle length (and diameter) have occurred, leading to gaps at the free surfaces. Given these gross changes it is speculated that, for this nearly isotropic composite, the difference between the observed contraction parallel to the bend bar axis, and swelling in the smaller thickness and width directions, is attributed solely sample size effects. For the samples of this study, for which there are approximately 4 unit cells to the thickness, the constraint is limited leading to exaggerated apparent swelling.

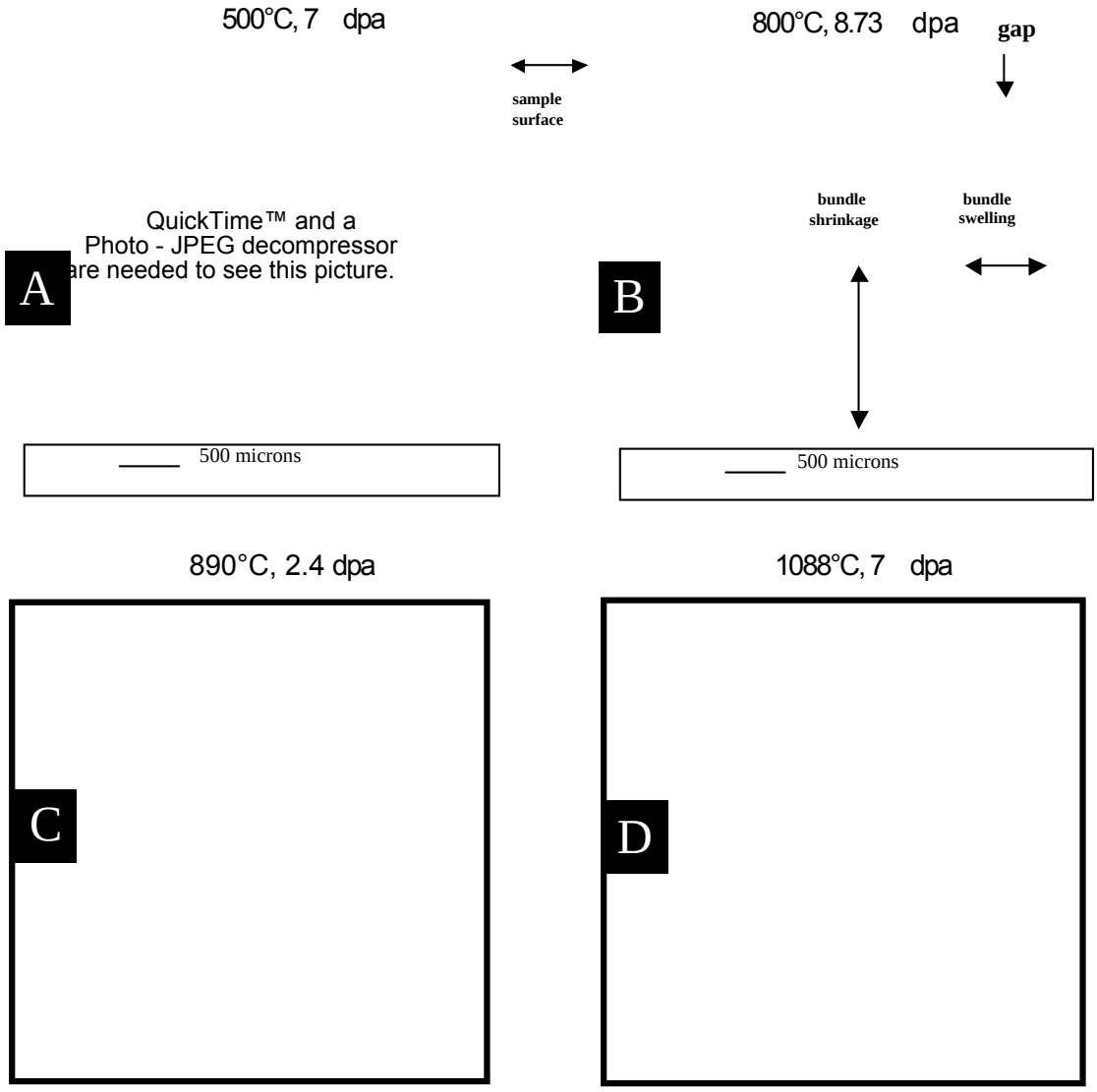

Fig. 15. SEM image of side surface of FMI-222: (A) 500°C, 6 dpa 800°C dpa [9], 500°C, 7.7 dpa 800°C dpa [9], (C) 890°C, 2 dpa (this study), and (D) 1088°C, 6 dpa (this study).

The behavior of the FMI-222 balanced weave composite is in contrast to the unidirectional MKC-1PH of Fig. 6. The unidirectional composite behavior is as explained by the upper plot of Fig. 13, swelling perpendicular to the unidirectional fibers' axis, and shrinking parallel to the fiber axis. This data compares favorably with the data of Eto [10] for the irradiation of MKC-1PH at 1000°C to a dose equivalent to the dose of Fig. 6 (~2.2 x 10^{25} n/m^2 , E>0.1 MeV). In this case, the MKC composite underwent a 0.97-2.11% contraction parallel to the fiber axis. This is in good agreement with the data presented in Fig. 6.

Conclusions

Over the irradiation temperature range studied (~850-1475°C) and neutron dose range (2-10 x 10^{25} n/m^2 (E>0.1 MeV)) the UCAR PCEA and SGL NBG-10 candidate nuclear graphites had similar densification to that of Great Lakes Carbon Nuclear Graphite H-451. In this temperature and dose range all materials remained in the densification stage exhibiting higher densification with increased irradiation temperature and dose. Swelling for high-quality unidirectional and three-dimensional composites at the same irradiation temperature and dose range have been found to be several percent, and in the case of the 1-1-1 balanced weave material the swelling for the small samples studied was found to be quite large (>10%) even for the lowest dose studied. It is speculated that the large dimensional change observed for the three-dimensional composite is in part attributed to the geometry of the sample raising the question as to the appropriate sample size required to obtain relevant design data.

Acknowledgements

This work is sponsored by the U.S. Department of Energy, Office of Nuclear Energy Science and Technology and Office of Science Fusion Energy Sciences under contract DE-AC05-00OR22725 with Oak Ridge National Laboratory, managed by UT-Battelle, LLC. The authors would like to thank Katey Lenox, Joel McDuffee, Bob Sitterson, and Dennis Heatherly who were involved in design and construction of the irradiation capsules and Marie Williams who carried out the SEM imaging.

References

[1] B. Tahon and F. Gerstgrasser, "Nuclear Graphite Grades," presented at the Generation IV Reactors International Forum, Knutsford, Cheshire, United Kingdom, September 7, 2004.
[2] J. W. H. Simmons, Radiation Damage in Graphite, Pergamon Press, Vol. 102, First Ed., 1965.
[3] R. E. Nightingale, Nuclear Graphite, Academic Press, 1962.
[4] C. R. Kennedy, "TSX Graphite for Extended use in the N-Reactor," 1985.
[5] T. D. Burchell and A. J. Wickham, "The Dimensional Change in Pile Grade A Graphite Irradiated in CEGB Magnox Power Reactors," Proceedings of the CARBON '87, 18th Biennial Conference on Carbon, 1987.
[6] T. D. Burchell, Proceedings of Carbon '02, Beijing China, 2002.
[7] G. B. Engle et al., "Development status of near-isotropic graphites for large HTGRs," General Atomics (1974) 73.
[8] T. D. Burchell, Materials Properties Data for Fusion Reactor Plasma Facing Carbon-Carbon Composites, in Physical Processes of the Interaction of Fusion Plasmas with Solids, Plasma-Materials Interactions, W. O. Hofer and J. Roth (eds.), Academic Press (1996) 341.
[9] L. L. Snead, T. D. Burchell, and A. L. Qualls, J. Nucl. Mater. 321 (2003) 165.
[10] M. Eto et al., J. Nucl. Mater. 212–215 (1994) 1223.

ACCUMULATION OF THERMAL RESISTANCE IN NEUTRON IRRADIATED GRAPHITE MATERIALS—L. L. Snead (Oak Ridge National Laboratory)

OBJECTIVE

The objective of this work is to define the thermophysical property changes of high quality graphite materials under high temperature neutron irradiation.

SUMMARY

A nuclear graphite, H451, and two high thermal conductivity graphite composites have been irradiated in the temperature range of 310-710°C in the High Flux Isotope Reactor and their thermal conductivities monitored in-situ. Data were measured continuously up to a fast neutron dose of approximately 1 x 10^{25} n/m^2 (E>0.1 MeV.) Data is interpreted in terms of the added thermal resistance and materials compared on this basis. Following this analysis it is shown that for the three materials studied, which have significantly different initial thermal conductivity values, the accumulation of thermal resistance is greater for the materials with lower initial thermal conductivity. Given that vacancies dominate phonon scattering at these irradiation temperatures and dose levels, these data clearly indicate that materials of higher perfection have a slower rate of stable vacancy accumulation during irradiation.

PROGRESS AND STATUS

Introduction

The physical processes governing the thermal conductivity of graphite, as well as the mechanisms responsible for the radiation-induced degradation in thermal conductivity, have been well established[1,2] . For all but the poorest grades of carbon, thermal conductivity is dominated by phonon transport along the graphite basal planes and is reduced by scattering obstacles such as grain boundaries, lattice defects, inclusions, and composite interfaces. For graphite with the largest crystallites, i.e., pyrolitic or natural flake graphite, the in-plane room temperature thermal conductivity approaches 2000 W/m-K [3] . The same mechanisms governing intrinsic and radiation-degraded thermal conductivity of graphite hold true for carbon carbon composites.

The thermal conductivity of graphite-based materials can be written as a summation of the thermal resistances due to scattering obstacles[1,4]:

$$(1) \quad K(x,T)= \alpha\,(x)\bullet(1/K_u + 1/K_{GB} + 1/K_{RD})^{-1}$$

where the term α (x) is a coefficient which includes terms due to orientation (with respect to the basal plane or composite orientation (x)), porosity and some other minor contributors. The first two terms inside the parentheses are the contributions to the thermal conductivity due to the Umklapp scattering ($1/K_u$) and the grain boundary scattering ($1/K_{GB}$) respectively. The grain boundary phonon scattering ($1/K_{GB}$) dominates thermal resistance at low temperatures and is insignificant above a few hundred degrees Celsius, depending on the perfection of the graphite. For the irradiation temperature of this study (>310°C), the grain boundary term can therefore be neglected. Umklapp scattering, or phonon-phonon scattering, dominates thermal conductivity at higher temperatures and scales nearly as T^2 [2] The Umklapp scattering therefore defines the upper limit in thermal conductivity for "perfect," non-irradiated, graphite. Following Taylor's analysis [5] the Umklapp-limited thermal conductivity of the graphite crystal is ~ 2200 W/m-K at room temperature, which is not far removed from the best pyrolytic graphite and vapor grown carbon fibers. For later comparison, the Umklapp thermal resistance ($1/K_u$) at 310 and 710°C is .0012 and .0019 m-K/W, respectively.

The third term in Equation (1), K_{RD}, is the contribution to the thermal resistance in the basal plane due to defect scattering. Following neutron irradiation, various types of stable defects will be produced depending on the irradiation temperature. These defects are very effective in scattering phonons and in practical terms for nuclear application of graphite quickly becomes the dominant term in equation (1). While many types of defects have been identified in graphite, at irradiation temperatures less than ~650°C, only simple defects are found in significant quantities. It has been further shown[6] that at an irradiation temperature near 150°C, the defect which dominates the thermal resistance is the single lattice vacancy. For temperatures from ~150-1000°C small vacancy loops also become important. Kelly attributes all thermal conductivity degradation to vacancy and small interstitial complexes for irradiation temperatures less than 650°C.[1,7] Of significance is that the number of vacancies surviving for a given neutron irradiation dose is a strong function of irradiation temperature, with greater vacancies surviving at lower irradiation temperatures. This is in part the reason why thermal conductivity degradation is greater for low-temperature irradiation.

It is worth noting that even for the maximum dose of the present study (about 2 displacements per atom; dpa) the material was undergoing volumetric shrinkage.[8-10] At several times the dose of this study both graphite and graphite fiber composite would move into a swelling phase leading to significant disruption of grain boundaries and composite fiber interfaces. For materials entering into the phase of volumetric expansion Equation 1 would be difficult to apply due to scattering at newly created internal interfaces. This is not the case for the data of this paper as only minimal change in the internal interfaces of these materials are expected.

There have been a few studies aiming to develop dose-temperature algorithms for thermal conductivity degradation of carbon fiber composites and graphite utilizing semi-empirical approaches. [11-13] Numerous algorithms based on particular graphite data have also been generated for specific reactor applications. However, these algorithms had limited basis in the physics of phonon scattering and added little into the physical insight of the processes involved. Their primary purpose was to provide tools to reactor designers and in that way proved useful. Moreover, standard practice for comparing irradiation performance of various grades of graphite has been to report thermal conductivity normalized to non-irradiated conductivity. In the early graphite literature an example of this is the work of Kelly [6,14] on pyrolytic graphite, where the metric for comparing the effect of irradiation temperature on conductivity was the “fractional change in thermal resistance,” defined as $(K_{non\text{-}irr}/K_i)$-1. Similarly, Burchell uses [15] “fractional reduction in thermal conductivity,” defined as $1-(K_{non\text{-}irr}/K_i)$. Both of these simple metrics have been effectively used to compare irradiation effects in one graphite type, or among very similar materials. Over the past decade it has become common practice to compare the degradation of various graphite and composite materials as a ratio of the irradiated to non-irradiated values, $K_i/K_{non\text{-}irr}$. [16-19] .

Recently, a variant of the simple metrics discussed above, based on Equation 1, has been applied to a number of ceramic materials. Specifically, Snead[20] discusses a “thermal defect resistance approach” to compare the efficiency of neutron irradiation in degrading thermal conductivity of dissimilar ceramics and similar ceramics with a range in thermal conductivity. The thermal defect resistance term is simply found by combining the Umklapp and grain boundary phonon scattering terms of Equation 1 (yielding $1/K_{non\text{-}irr}$) and solving for the irradiation induced term $1/K_{RD}$. In this way it was shown (for monolithic ceramics[20]) that the accumulation of thermal defect resistance ($1/K_{RD}$) at low neutron dose does not scale proportionally for many ceramics for 60°C neutron irradiation (in other words the ratio of the change in thermal resistance to the change in neutron fluence is less than unity.) This implies significant defect mobility and vacancy annihilation for irradiation near room temperature. Moreover, it was shown that the accumulation of thermal defect resistance for similar materials (e.g., sapphire and high-purity polycrystalline alumina) was similar even though the non-irradiated conductivities were significantly different. This last finding suggests that by mapping the thermal defect resistance for a specific material, such as alumina, the thermal conductivity as a function of irradiation

temperature and neutron dose can be predicted for any high quality alumina independent of the non-irradiated thermal conductivity.

The purpose of this paper is to apply the simple thermal defect resistance approach to a few graphite materials of differing initial thermal conductivities to determine the predictive capability of this method, and to gain insight into the accumulation rate of phonon scattering defects in graphite materials as a function of neutron dose and irradiation temperature.

Experimental

Materials for this study (see Table 1) include a nuclear graphite and two high-quality carbon fiber composites. The nuclear graphite was the near-isotropic, medium size grain H451 previously manufactured by Sigri Great Lakes Carbon. The carbon fiber composites were manufactured by Fiber Materials Incorporated (FMI-222) and Mitsubishi Kasei (MKC-1PH.) The FMI-222 material is a three dimensional balanced weave composite utilizing P-55 pitch based fibers and a mesophase pitch matrix. The thermal properties of this composite are isotropic. The MKC-1PH is also based on a pitch fiber (K-139) and a mesophase pitch matrix, though has a 1-dimensional architecture yielding highly anisotropic thermal properties. The MKC-1PH was studied in the high conductivity direction only. Figure 1 gives a plot of thermal conductivity as a function of temperature (in the high conductivity direction where applicable) for the three materials.

Table 1. Properties of Material Studied

Designation	Manufacturer	Architecture	Constituents	Grain or Cell Size	Density (g/cc)
H451	Great Lakes Carbon	graphite	Coal tar pitch binder. Petroleum pitch impregnation. Petrolium Coke.		1.76
FMI-222	Fiber Materials Incorporated	3-D Balanced Weave Composite	Amoco P-series Pitch Fiber. Pitch Derived Matrix.		1.96
MKC-1PH	Mitsubishi Kasei	1-D Composite	K-139 Pitch Based Fiber, Pitch Derived Matrix.	n/a	1.93

Fig.1. Non-irradiated thermal conductivity as a function of temperature.

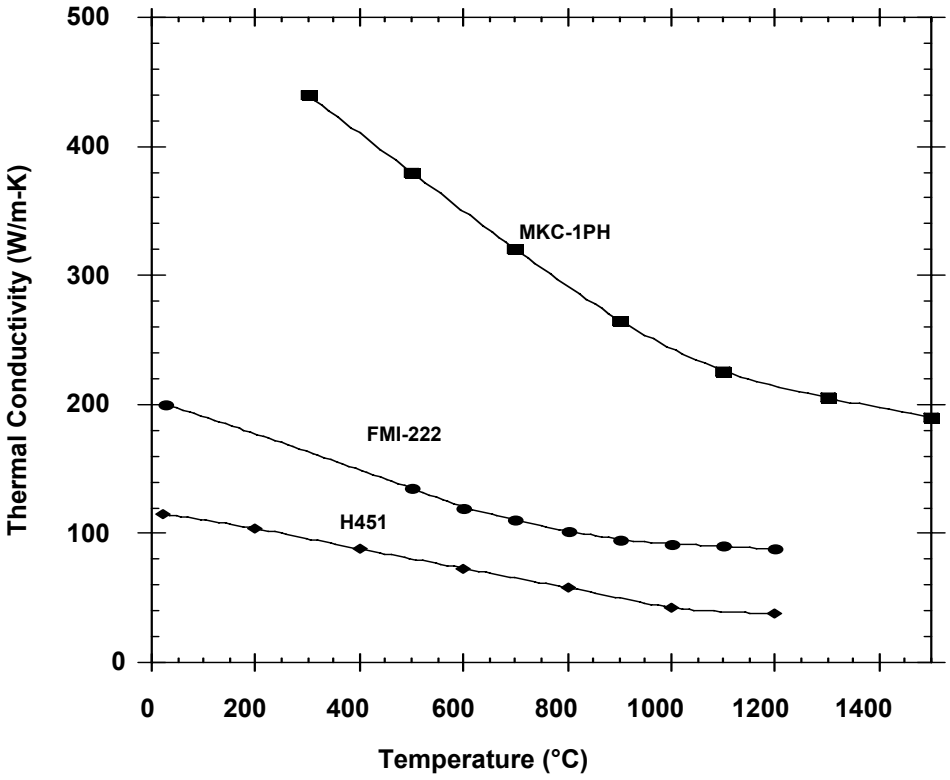

Cylindrical samples were machined from the graphite materials to a diameter of 6 mm and 12 mm length. Following machining shallow pilot holes were drilled 0.76 mm deep into the center of both ends of the sample and one end was brazed to a vanadium heat sink. Very small (0.5 mm) stainless steel sheathed Type N thermocouples were brazed into the pilot holes. A representation of a single vanadium heat sink including two mock samples is given in Figure 2. Holders were then stacked within a cylindrical aluminum tube, cleaned, and baked at 200°C in vacuum to drive off moisture. The tube was then filled with a high-purity helium cover gas and welded shut.

Fig.2. Mock-up of samples bonded to vanadium heat sink.

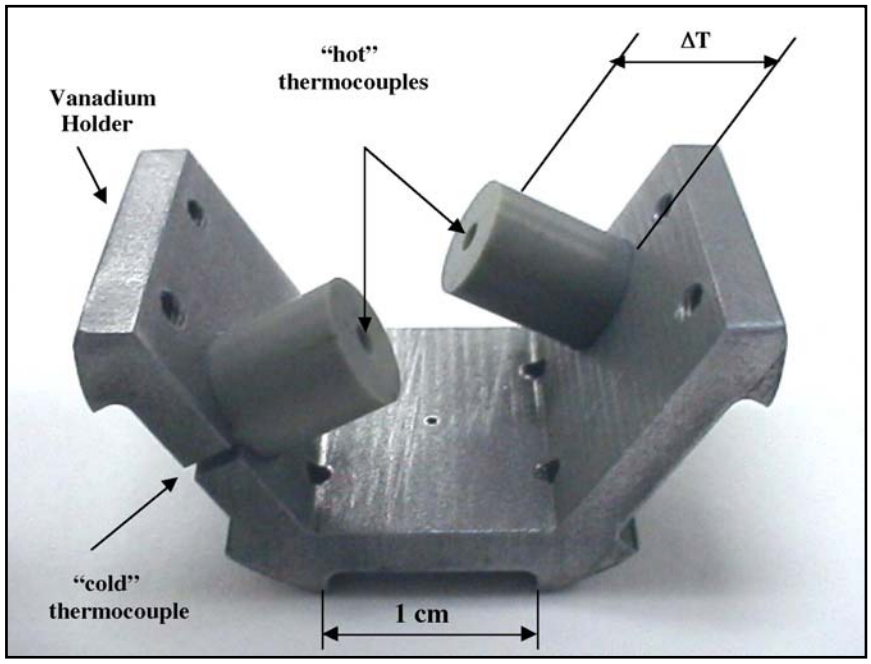

Irradiation was carried out in the Removable Beryllium position of the High Flux Isotope Reactor. The peak flux for this position is approximately 6 x 10^{18} n/m^2-s (E>0.1 MeV.) These experiments were carried out for a total of two ~ 22 day cycles. The total fluence and carbon dpa of a complete HFIR cycle are ~1.14x10^{25} n/m^2 (E>0.1 MEV) and 1.5 dpa, respectively. A high-purity variable sweep gas mixture of argon and helium, along with a gas gap between the heat-sink and the aluminum holder, defined the irradiation temperature of the sample. In addition to the thermocouples bonded to the samples, thermocouples were bonded to each heat sink and monitored continuously. These thermocouples were used to continuously vary the argon/helium sweep gas to maintain a constant heat sink temperature. The basic concept of this experiment is to constrain the nuclear heat generated within the cylindrical sample to one-dimensional heat flow along the axis of the sample into the heat sink. The gamma heating intrinsic to the reactor core provides the uniform volumetric heat source to the sample. With this technique there are two ways the thermal conductivity can be found. The most straightforward is to use the gamma heating, sample density, distance between thermocouple junctions, and the measured temperature difference between the thermocouples (about 30°C.) A three-dimensional finite element heat transport code was used to incorporate end effects and the presence of the thermocouples. This method yielded a reasonable approximation for thermal conductivity for the

samples. A simple 1 one-dimensional heat flow calculation also agreed well with the three-dimensional calculation. However, an error caused by uncertainty in the local gamma heating (possibly significant) and the distance between thermocouples (small) is additive and unknown. For this reason a more straightforward method for calculating thermal conductivity was selected. Specifically, the thermal conductivity as a function of temperature of each sample measured prior to capsule assembly. The thermal conductivity at the start of the irradiation period was assumed to be the same as the pre-irradiation value and thus fixed. With this assumption the thermal conductivity as a function of time in reactor is inferred directly from the change in the temperature difference between the paired (hot-side and cold-side) sample thermocouples. Implied in this assumption is that gamma heating remained constant throughout the period of irradiation. The operating performance of the High Flux Isotope Reactor, as seen in numerous instrumented capsules, suggests that the gamma heat flux for the central portion of the core (where these samples were located) is fairly constant as a function of core life. The reactor power was extremely constant throughout this particular experiment.

Results

The in-situ thermal conductivity, measured as a function of time in the HFIR core, is shown in Figures 3, 4, and 5. In these figures data are plotted every fifteen minutes (actual measurement were taken on the order of every few seconds.) Approximately 524 hours into the irradiation a data discontinuity is observed. This discontinuity marks the end of one irradiation cycle and the start of the following cycle. The period of refueling between cycles was approximately one week and is omitted from the plot. In Figure 3 the degradation of H451 thermal conductivity for irradiation temperatures of 430 and 710°C is provided. These irradiation temperatures are mean values of the hot-side and cold-side thermocouples at the middle of the irradiation period. As the irradiation progressed the temperature difference between the thermocouples increased by as much at 20°C (due to the degrading thermal conductivity.) Considering this along with the small change in temperature between the braze joint and the hot-side thermocouple, the irradiation temperatures quoted from here forward are considered approximations within ~ 30°C. From figure 3, it is clearly seen that the lower temperature irradiated graphite (430°C) begins irradiation at a higher value of thermal conductivity though rapidly degrades such that its thermal conductivity is less than the H451 material irradiated at 710°C. By the end of 1000 hours of irradiation the thermal conductivity of the H451 irradiated at 430°C has been reduced from ~ 80 to ~ 30 W/m-K while the sample irradiated at 710°C has been reduced from about 65 to 40 W/m-K.

An experimental artifact of this work was thermocouple failure. While it is easily shown that thermocouple de-calibration due to nuclear transmutations would not become significant for several cycles, outright thermocouple failure did occur. This failure was presumably due to failure of the magnesium oxide insulation between the thermocouple wires and the thermocouple sheath. This failure is attributed to the extremely small insulating gap required for these 0.5 mm diameter sheathed thermocouples. Thermocouple deterioration and failure, which occurred for about 30% of thermocouples, occurred rapidly, and was preceded by a period of noisy data. An example of this is shown for the 710°C irradiated FMI-222 composite of Figure 4 at approximately 200 hours into the irradiation. Prior to complete thermocouple failure the data is observed to become noisier. After this point the data was considered unreliable and is left off the plot. In some cases outright failure of the thermocouple attributed to shorting of the thermocouple to the outer sheath occurred.

Fig. 3. Thermal Conductivity Reduction of H451 graphite.

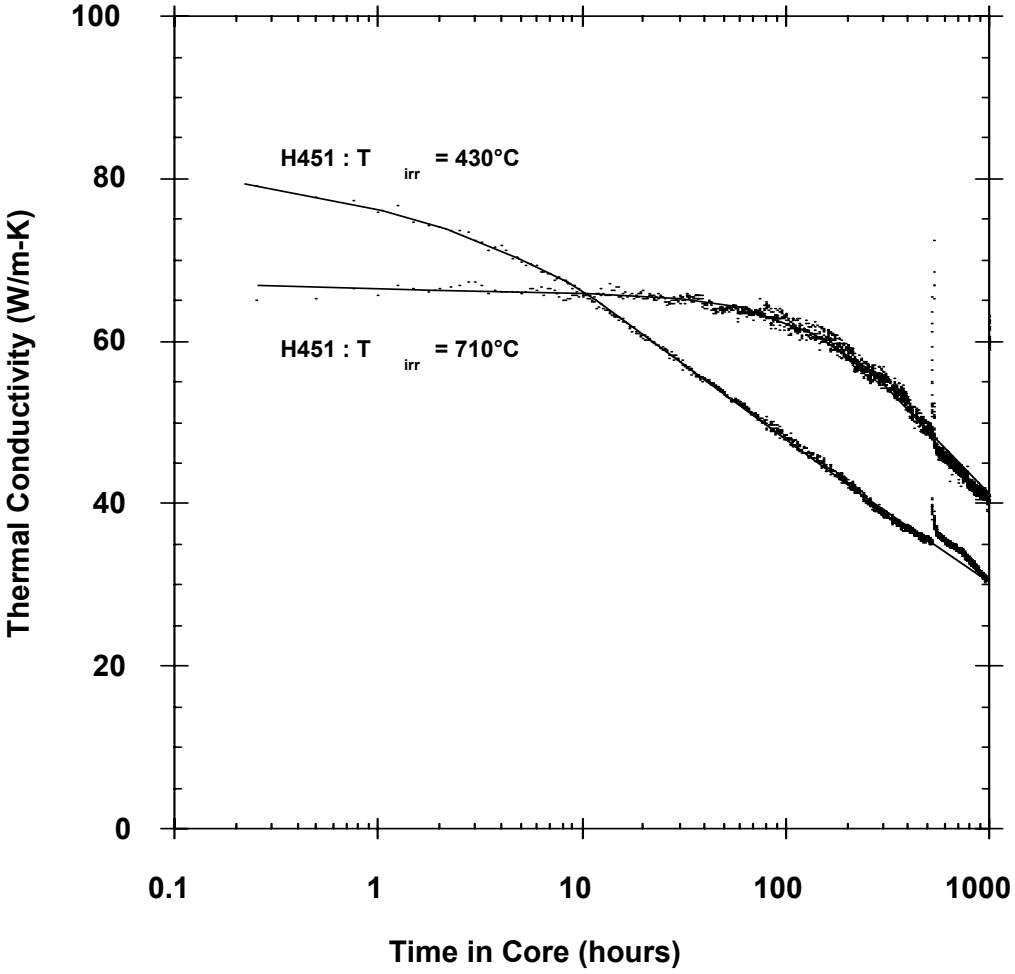

Fig. 4. Thermal conductivity reduction of FMI-222.

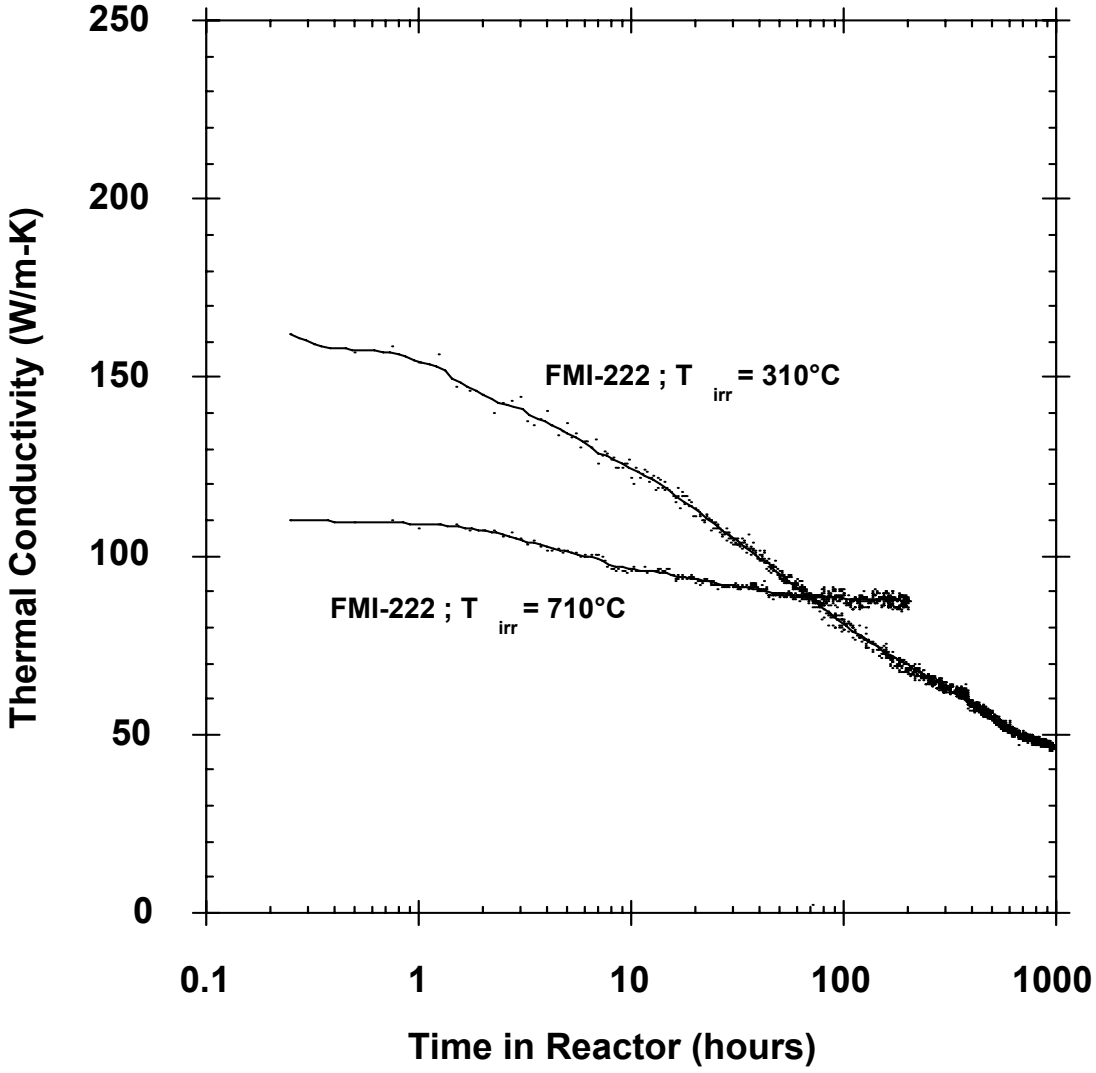

Fig. 5. Thermal conductivity reduction of materials irradiated at 310-430°C.

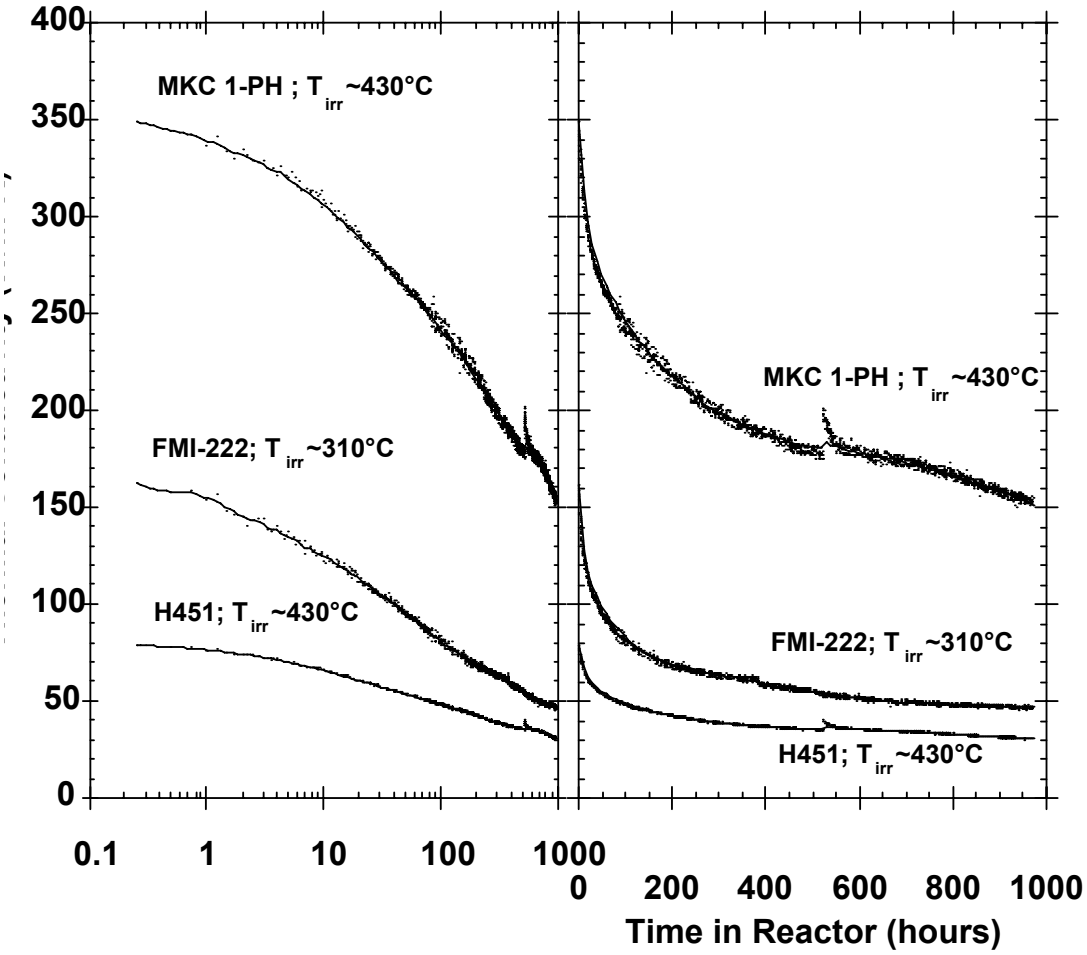

The data of Figure 5 gives a relative comparison of the reduction in thermal conductivity for the materials studied at irradiation temperatures of 310-430°C. It is noted that for 1000 hours in core the total displacement dose to these materials was approximately 2 x 10^{25} n/m^2 (E>0.1 MeV.) The maximum dose of this study does not quite reach thermal conductivity saturation. However, by inspection of the rightmost curve of figure 5, which gives the same data plotted on a linear time scale, saturation thermal conductivity has nearly been achieved.

Discussion

Unfortunately, ex-situ (post-irradiation) thermal conductivity data to precisely compare to results of this work do not exist. However, similar dose and irradiation temperature data do exist for the H451 graphite. In comparing to the data of figure 3, Price[21] carried out H451 irradiation at 600°C which resulted in a thermal conductivity reduction at the irradiation temperature from ~ 75

(non-irradiated) to ~ 32 W/m-K for a dose of 2.2 x 10^{25} n/m^2 (E>0.18 MeV.) This is about twice the highest dose of this study and is in general agreement with the extrapolated values of the 430 and 710°C data of figure 3. Engle[22] derives a set of thermal conductivity curves for H451 as a function of dose and irradiation temperature. Extrapolating the Engle data to the 710°C thermal conductivity curve of Figure 3, the data corresponding to 100 hours in core is ~65 W/m-K while the 1000 hour value is ~ 42 W/m-K. Both of these values are in agreement with the 710°C curve of Figure 3. There is very limited data for the composite materials, though Burchell's[15] data on FMI-222 thermal conductivity degradation for an ~ 600°C irradiation to twice the dose of the present study are in general agreement with the extrapolated data of Figure 4. The unidirectional composite MCK-1PH was irradiated by Bonal[18] at the same temperature of this study. His measured thermal conductivity for the irradiation dose of 1.1 x 10^{25} n/m^2 (E>0.1 MeV) was 120 W/m-K, which is consistent with the extrapolated MKC-1PH data of Figure 5.

The data on thermal conductivity reduction plotted in Figures 3-5 indicate an approximately linear degradation of thermal conductivity as a function of log time. This is the case for all but the first few hours of irradiation. All data from this study are replotted in terms of thermal defect resistance in Figures 6-8. In Figure 6, the build-up of thermal defect resistance ($1/K_i$, assuming α of unity) for the nuclear graphite H451 is depicted for irradiation temperatures of 430 and 710°C. At 430°C a rapid increase followed by a leveling of to an apparently constant accumulation rate. In contrast, the H451 irradiated at 710°C has a lower accumulation of thermal defect resistance and enters into the linear accumulation regime more rapidly. It is interesting to note that the levels of thermal defect resistance for both irradiation temperatures quickly dominate the thermal resistance due to phonon scattering. As discussed previously, the Umklapp thermal resistance is 0.0012 and 0.0019 at 300 and 700°C, respectively. The equivalent thermal defect resistance occurs just a few hours into irradiation for H451 irradiated at 300°C and at about 200 hours in reactor for the H451 irradiated at 700°C.

Figure 7 gives the thermal defect resistance for the FMI-222 composite irradiated at 310 and 710°C. As with the lower temperature irradiated H451 graphite, the 310°C irradiated FMI-222 composite exhibits a sharp initial rise in thermal defect resistance followed by a gradual decline into a linear accumulation regime. Unlike H451 irradiated at 710°C, the FMI-222 also exhibits an initial sharp increase. Unfortunately, the data for the FMI-222, 710°C at >200 hours becomes noisy and cannot be used to determine the behavior in the linear accumulation regime.

Of interest in comparing the curves of Figures 6 and 7 are the relative levels of thermal defect resistance accumulation for the two materials. A straightforward comparison is complicated due to the difference in irradiation temperatures (i.e., 310-v-430°C at the low end of the irradiation temperatures), though it is clear that the accumulation rate is substantially higher for the H451 graphite even when considering the differing irradiation temperatures. This point is reinforced by inspection of Figure 8, which gives a comparison of the low temperature irradiations for all three materials of this study. Clearly, the magnitude of the initial rise in thermal defect resistance is greater for the lower thermal conductivity materials. The thermal defect accumulation rate of the linear accumulation regime is difficult to compare, though from the data presented in Figure 8 there appears to be a weak dependence of the accumulation rate on the material. It appears as if there may be a tendency for the lower thermal conductivity materials to have a somewhat higher linear accumulation rate (the slope of the right side of the curves of Figure 8.)

Fig. 6. Accumulated thermal defect resistance of H451.

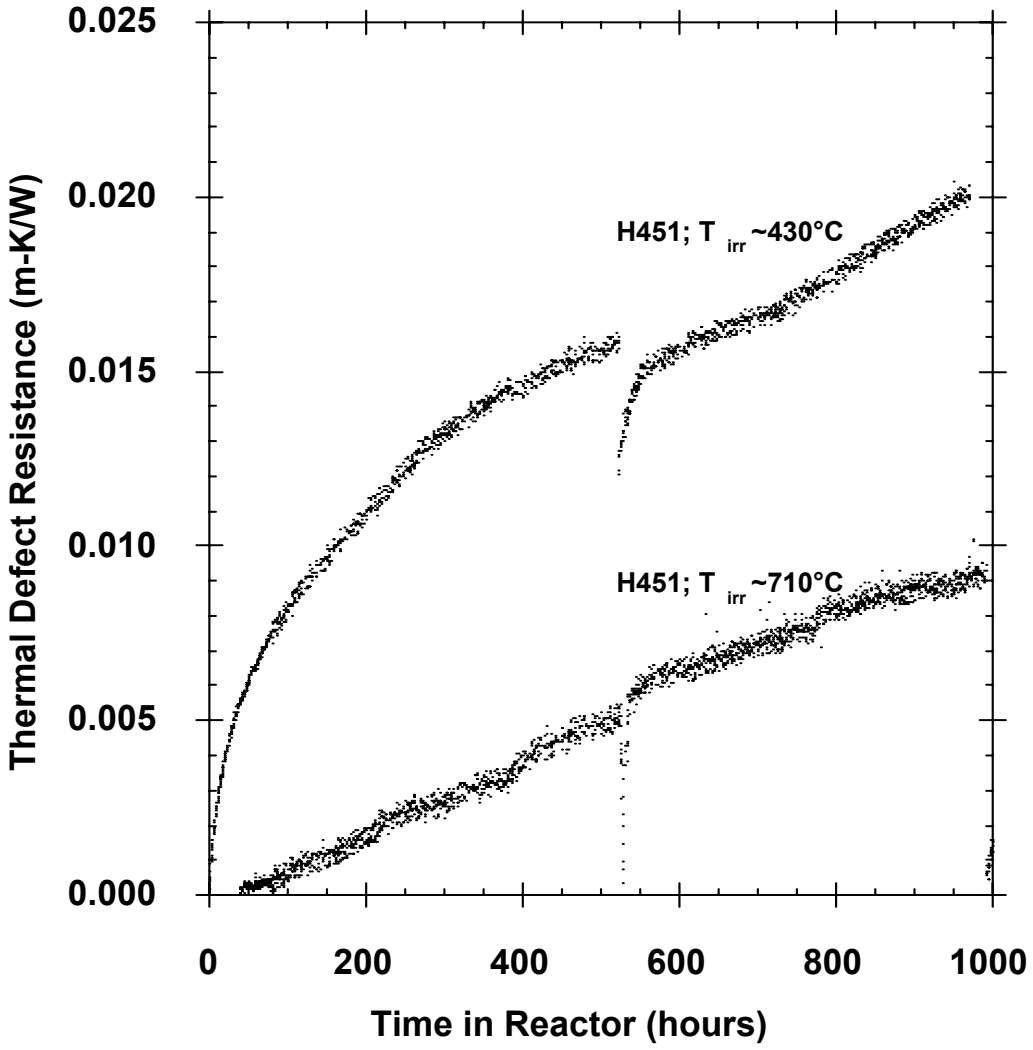

Fig. 7. Accumulated thermal defect resistance of FMI-222.

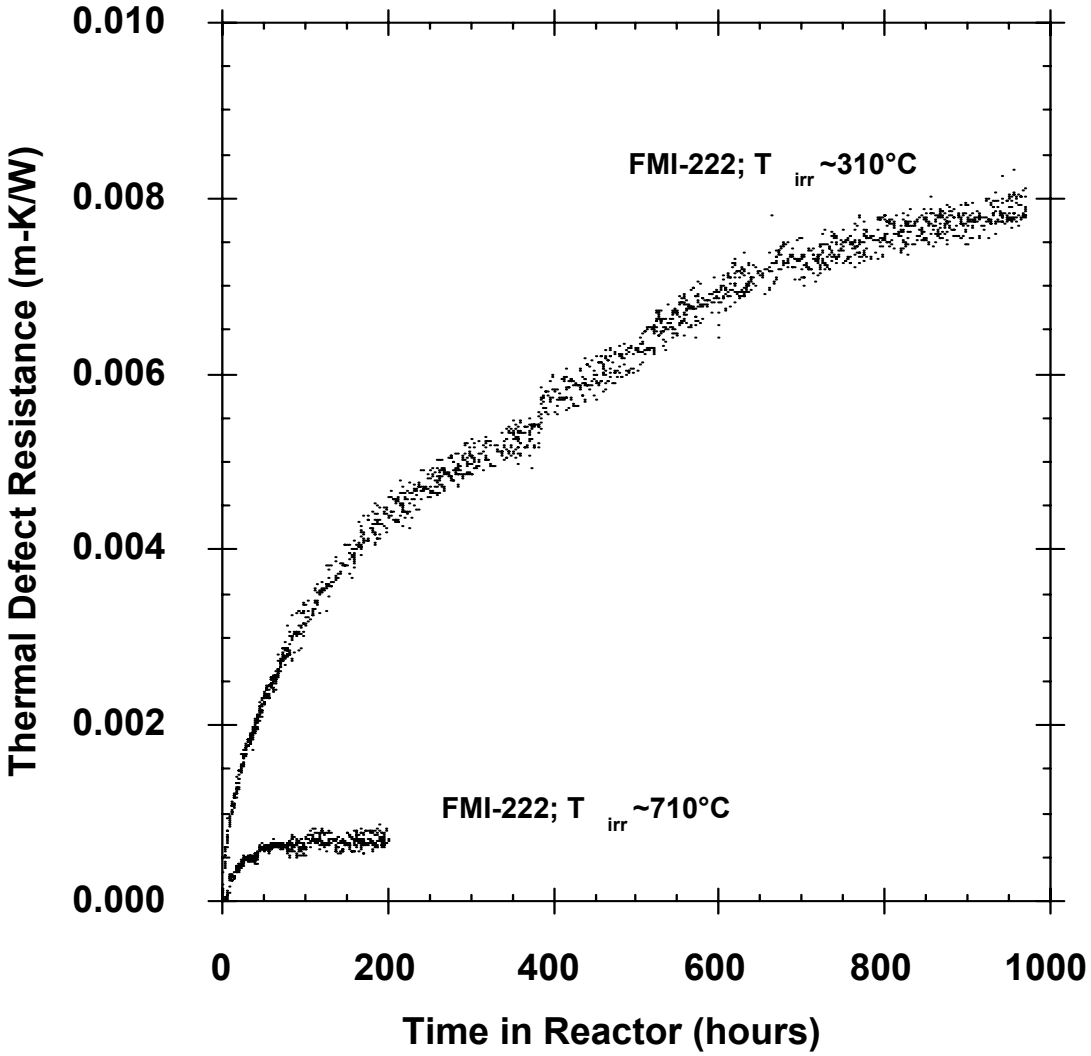

Fig. 8. Comparison of thermal defect resistance for materials irradiated at 310-430°C.

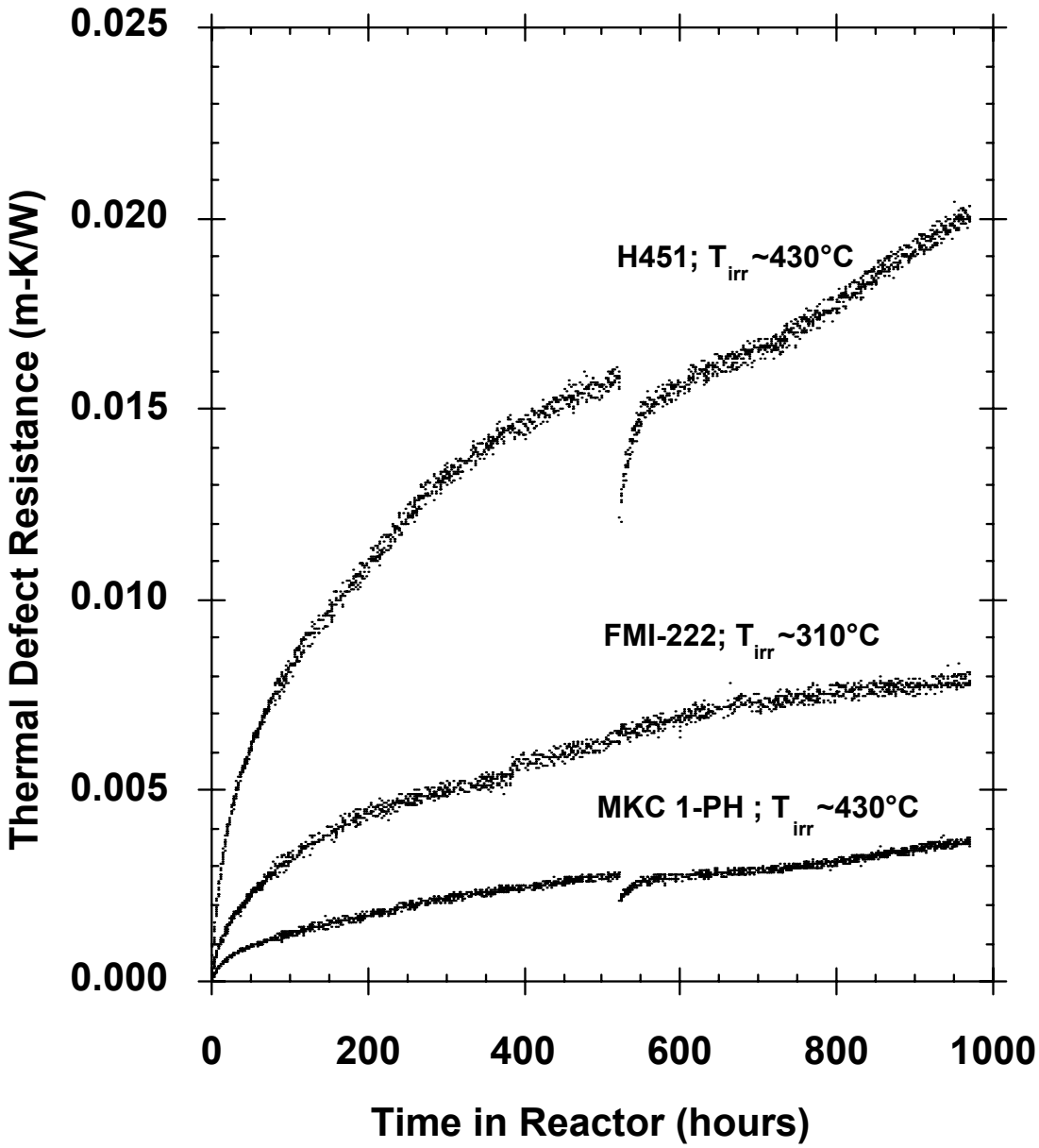

An obvious benefit from generating thermal conductivity data in the manner of this work (in-situ) is the large number of data points taken on a single sample. However, by analyzing literature data from post-irradiation measurement of thermal conductivity the same basic trends discussed in the previous paragraphs are observed. [16,17,19] As example, Wu[17] has reported on thermal conductivity reduction for a range of graphite materials irradiated at temperatures similar to the present study. The Wu data span three decades of fluence corresponding to about 30 minutes to a few days of irradiation in the present work. By plotting the Wu data in terms of thermal defect resistance the initial buildup, and the transition to a lower accumulation rate, is clearly seen. Moreover, the reduced accumulation rate for materials with higher initial thermal conductivity is also seen. Additionally, work by Kelly[23] on nuclear graphite materials (Pile Grade A and Gilsocarbon) in the as-produced and 3400°C annealed (thus increasing crystallite size and thermal conductivity) clearly indicates higher defect resistance accumulation for the pre-annealed, higher thermal conductivity materials.

As mentioned in the introduction, it has been previously shown that for ceramics such as alumina the accumulation of thermal defect resistance upon irradiation does not depend strongly on the initial conductivity (hence crystalline perfection) of the alumina studied. The high purity polycrystalline alumina accumulated thermal defect resistance at approximately the same rate as single crystal alumina (sapphire) even though the thermal conductivities ranged from 18 W/m-K (polycrystal) to 42 W/m-K (single crystal.) It is apparent that graphite does not behave in this manner.

The behavior of the thermal defect accumulation in graphite discussed above can be explained in terms of accumulation of simple defects during irradiation. As mentioned in the introduction, the primary defects responsible for thermal conductivity reduction at these irradiation temperatures are lattice vacancies and simple complexes of interstitials and vacancies. In the work by Taylor[6] the actual concentration of vacancies was calculated based on phonon transport theory and a experimental program of irradiation and annealing. In this way Taylor determined the concentration of vacancies for pyrolytic graphite irradiated at ~450°C to a fluence about twice that of the present study to be ~0.49%. The vacancy concentrations for the lower temperature irradiations in the Taylor study were considerably higher due to the reduced mobility of migrating defects suppressing the annihilation of defects produced following a fast neutron-induced cascade. Moreover, the interstitial defect contribution was shown by Taylor to be insignificant above ~ 300°C. Kelly[1] and others have concluded that the thermal resistance due to vacancies is directly proportional to vacancy concentration. The thermal defect resistance plots (Fig. 6-8) could then be considered to be directly proportional to the vacancy concentrations of the material. However, this assumes an accumulation of a single type (size) of vacancy complex.

The fact that the initial accumulation of thermal defect resistance is considerably higher for materials with lower initial thermal conductivity can be attributed to migration of interstitials and annihilation of vacancies following the atomic displacement cascade. It is reasonable to assume that materials with lower conductivity possess lower crystalline perfection and smaller crystallites and that this retards the migration of interstitials. Limiting the migration of interstitials would lead to less recombination and a higher saturation vacancy concentration. The reason for the transition to a linear accumulation of thermal defect resistance (cf figures 6-8) is less clear. As the irradiation dose increases the increased defect density will have the effect of both increasing the probability of annihilation of newly produced defects and increasing the complexity of the defects formed (ie larger, more stable vacancy loops.) The relative effectiveness of vacancies and loops on the thermal defect resistance can be described as follows: [1]

$$1/K_{RD} = (\alpha(x)/\Delta[\beta S_v^2 C_V + \Delta(C_{v\ loop}/r_o)] \quad (2)$$

where $1/K_{RD}$ and $\alpha(x)$ are as in Equation (1), Δ is a numerical constant dependent on temperature, and S and S_v are constants. The defect variables are the defect radius r_o, and the

vacancy and vacancy loop concentrations C_V and $C_{v\ loop}$, respectively. As discussed by Kelly[1] , the vacancy term in Figure 2 dominates thermal defect resistance below the 650-900°C irradiation temperature with the loop term dominating at an irradiation temperature of 1350°C.

A more detailed study of the nature and density of the vacancy complexes would be beneficial. However, it is interesting to note that in the classic work by Henson [24] the concentrations of the various defects prevalent for irradiation in the 300-650°C irradiation temperature range were determined as a function of neutron fluence. For the Pile Grade A nuclear graphite of Henson's study the concentration of free vacancies accumulated in the same fashion as described in the present work. Moreover, other properties primarily affected by point-defect or simple defect clusters exhibit the same rapid rise and transition to linear accumulation. Specifically, the stored energy (Wigner energy, E_w) resulting from low temperature neutron irradiation exhibits such behavior. In fact, Bell[25] has shown that the Wigner energy for low irradiation dose levels is directly proportional to the thermal defect resistance through the relationship $E_w = 6.25\ (K_o/K_i - 1)_{30°C}$, or in terms of the thermal defect resistance $E_w = 6.25\ (1/K_{RD})_{30°C}$. As pointed out by Kelly[1], the thermal defect resistance at low irradiation temperature is directly proportional to the vacancy concentration (also for low neutron dose.) The same is true for the accumulation of stored energy. Similarly, the elastic modulus of graphite, (which is dominated by the C44 elastic constant and related to the ability of graphite planes to shear over one another) is primarily affected by simple defect production. Such a correlation between elastic modulus change and thermal transport is to be expected. As pointed out by Taylor[5] , the thermal transport in the basal plane can be directly related to the elastic constants C11 and C66. As with the stored energy, the rapid rise and deceleration of the change in elastic modulus is similar to the accumulation in thermal defect resistance shown here.

The previous discussion has avoided dealing with the material dependent constant □(x). This parameter, typically attributed to the porosity and other factors which increase the effective phonon path length through graphite, is generally in the range of 5-15 for nuclear graphite and is less for materials with higher thermal conductivity. It is not clear to the author the best way to determine such a factor for a composite system where the thermal conduction is not necessarily equally shared between the fiber and matrix. However, finessing this question in no way alters the conclusions regarding the accumulation of thermal defect accumulation put forward. In fact, given that the constant is certainly lower for the composite materials as compared to the nuclear graphite H-451, the behavior of the accumulation of thermal defect resistance would be even more exaggerated than described above.

Conclusions

This work gives the first high-dose, in-situ, measurement of thermal conductivity for graphite materials. The data have been interpreted in terms of a thermal defect accumulation leading to the following conclusions which are reinforced by measurements in the literature taken by post-irradiation measurement of thermal conductivity. The thermal defect accumulation rate exhibits a significant, prompt rise rapidly making a transition to a lower, linear, accumulation rate. The initial accumulation of thermal defect resistance is related to the initial perfection of the material, with lower initial thermal conductivity materials exhibiting a larger initial accumulation rate. The behavior of the accumulation of thermal defect resistance is consistent with the dose behavior of the elastic modulus and stored energy, both of which are directly related to the simple point defect accumulation.

Acknowledgements

This work is sponsored by the U.S. Department of Energy, Office of Nuclear Energy Science and Technology and Office of Science Fusion Energy Sciences under contract DE-AC05-00OR22725 with Oak Ridge National Laboratory, managed by UT-Battelle, LLC. The authors would like to thank Katey Lenox, Joel McDuffee, Bob Sitterson, and Dennis Heatherly who were involved in design and construction of the irradiation capsule.

References

[1] B. T. Kelly, The Thermal Conductivity of Graphite, In Chemistry and Physics of Carbon; P. L. Walker, Ed., Marcel Dekker, Inc., New York, 1969, Vol. 5, pp 119.
[2] B. T. Kelly, Physics of Graphite, Applied Science Publishers, London, 1981.
[3] A. DeCombarieu, J. Phys. (France), *28*, (1968) 931.
[4] R. Taylor, K. E. Gilchrist, L. J. Poston, Carbon, *6*, (1968) 537.
[5] R. Taylor, Phil. Mag, *13*, (1966) 157.
[6] R. Taylor, B. T. Kelly, K. E. Gilchrist, J. Phys. Chem. Solids, *30*, (1969) 2251.
[7] J. W. H. Simmons, Radiation Damage in Graphite, First ed. International Series of Monographs in Nuclear Energy, Pergamon Press, 1965, Vol. 102.
[8] L. L. Snead, T. D. Burchell, A. L. Qualls, J. Nucl. Mat., *321*, (2003) 165.
[9] L. L. Snead, Fusion Energy Applications, In Carbon Materials for Advanced Technologies, T. D. Burchell, Ed., Elsevier Science Ltd, Kidlington, Oxford, England, 1999, pp 389.
[10] C. R. Kennedy, E. M. Woodruff, "Irradiation Effects on the Physical Properties of Grade TSX Graphite," Westinghouse Hanford Company, 1989.
[11] V. Barabash, L. L. Snead, J. Nucl. Mat, *329-333*, (2004) 860.
[12] L. L. Snead, T. D. Burchell, "Reduction in Thermal Conductivity Due to Neutron Irradiation", 22nd International Conference on Carbon, 1995, San Diego, CA. pp 774-775.
[13] L. Binkele, J. Non-Equilib. Thermodyn., *3*, (1978) 257.
[14] B. T. Kelly, Carbon, *9*, (1971) 783.
[15] T. D. Burchell, W. P. Eatherly, J. P. Strizak,. "The effect of neutron irradiation on the structure and properties of carbon-carbon composite materials", Effects of Radiation on Materials, 16th International Symposium, ASTM STP 1175, (1994) 1266-1282.
[16] L. L. Snead, T. D. Burchell, J. Nucl. Mat., *224*, (1995) 222.
[17] C. H. Wu, J. P. Bonal, B. Thiele, J. Nucl. Mat., *212-215*, (1994) 1168.
[18] J. P. Bonal, C. H. Wu, J. Nucl. Mater., *228*, (1996) 155.
[19] B. A. Thiele et. al. "Effect of Neutron Irradiation on thermal conductivity of carbon/carbon fiber materials at 400 and 600°C in the fluence range of 1E22 to 1E24/m2", Proc. 16th Int. Symp. on Effects of Radiation on Materials,. ASTM-STP 1175 D Gelles, T Nanstad, E Little, editors, (1992) 1302-1314.
[20] L. L. Snead, S. J. Zinkle, D. P. White, J. Nucl. Mat, *340*, (2005) 187.
[21] R. J. Price, "Thermal Conductivity of Neutron-Irradiated Reactor Graphites," General Atomics, 1974.
[22] G. B. Engle et. al. "Development status of near-isotropic graphites for large HTGR's," General Atomics, 1974. 73
[23] B. T. Kelly, P. Schofield, R. G. Brown, Carbon, *28*, (1990) 155.
[24] R. W. Henson, A. J. Perks, J. W. H. Simmons, Carbon, *6*, (1968) 789.
[25] J. C. Bell et. al., Phil. Trans. Roy. Soc., *A254*, (1962) 361.

3.0 FERRITIC/MARTENSITIC STEELS AND ODS STEELS

APPLICATION OF THE MASTER CURVE TO INHOMOGENEOUS FERRITIC/MARTENSITIC STEEL—M. A. Sokolov (Oak Ridge National Laboratory) and H. Tanigawa (Japan Atomic Energy Agency)

OBJECTIVE

In this study, extensive fracture toughness characterization of the IAE heat of F82H steel was performed using 1T C(T), 0.4T C(T), and 0.18T C(T). The objective of this study was to examine the application of the master curve methodology to the transition fracture toughness of this ferritic/martensitic steel.

SUMMARY

A total of 53 specimens of F82H steel have been tested in the transition region, 27 1T C(T), 19 0.4T C(T) and 7 0.18T DC(T). The results of this study showed that the scatter of fracture toughness for a 25 mm plate of F82H-IEA steel was larger than anticipated by the conventional master curve analysis. Several other types of analysis that are the advanced extensions to the conventional master curve method were applied to theses data. It was shown that the random inhomogeneity analysis provides a better description of the data scatter for F82H steel, than does the conventional master curve analysis or any other analyses. At the same time, the T_o values derived using the conventional and random inhomogeneity analyses are quite similar.

PROGRESS AND STATUS

Introduction

Recent advances in fracture toughness have led to employment of Weibull statistics to model scatter of fracture toughness in the transition region of low-alloyed reactor pressure vessel steels. This methodology, proposed by K. Wallin [1,2], uses a concept of the universal temperature dependence of fracture toughness in the transition region, the so-called “master curve.” The current physical background for this methodology suggests that it is applicable to a wide variety of ferritic bcc steels, including tempered ferritic-martensitic steels. These steels are structural material candidates for fusion reactors, yet the transition fracture toughness data for this class of steels are rather sparse.

In this study, three sizes of fracture toughness specimens of F82H steel were tested to verify the master curve concept. Specimens were tested at several temperatures in the transition region and at least four specimens were tested at each temperature allowing for application of the Weibull statistic/master curve analysis procedure. The largest specimens were 1T C(T) compact specimens. Broken halves of 1T C(T) specimens were later used to machine and test smaller, 0.4T C(T) and 0.18T DC(T) size specimens which could be more suitable for irradiation experiments.

The reduced-activation ferritic-martensitic (RAFM) steel F82H is a primary candidate low-activation material for fusion applications, and it is being investigated in the joint U.S. Department of Energy-Japan Atomic Energy Agency (DOE-JAEA) collaboration program. The F82H alloy (Fe-8Cr-2W-V-Ta) was developed by JAEA and NKK Corporation, Kawasaki, Japan and provided to participants in the International Energy Agency (IEA) round-robin tests. Material used for the IEA round robin tests was melted in two 5 metric-ton heats (heat #9741 and #9753). All fracture toughness specimens were taken from 25-mm plates 31W-29 and 31W-3 from heat #9753. These plates were EB- and TIG-welded, respectfully, followed by post weld heat treatment. All specimens were machined in the L-T orientation such that the crack would propagate in the transverse orientation.

Testing and analysis procedures

The fracture toughness tests were conducted in accordance with the ASTM E 1921-05 Standard Test Method for Determination of Reference Temperature, T_o, for Ferritic Steels in the Transition Range. The specimens were fatigue precracked to a ratio of the crack length to specimen width (a/W) of about 0.5. The unloading compliance method was used for measuring crack growth. Specimens were tested in the laboratory on a 98-kN (22-kip) capacity servohydraulic machine. An outboard clip gage was used to measure load-line displacement. The broken specimens were examined with a calibrated measuring optical microscope to determine the initial and final crack lengths.

The following is a brief description of the master curve methodology. More details can be found in Ref. [3] for example. Values of J-integral at cleavage instability, J_c, were converted to their equivalent values in terms of stress intensity factor K_{Jc} by the following equation:

$$K_{Jc}=\sqrt{J_c\frac{E}{1-\nu^2}} \tag{1}$$

where E is Young's modulus and v=0.3 is Poisson's ratio.
The master curve methodology imposes two validity criteria to qualify K_{Jc} data. A K_{Jc} datum would be considered invalid if this value exceeded the $K_{Jc(limit)}$ requirement of E 1921:

$$K_{Jc(limit)}=\sqrt{\frac{Eb_o\sigma_{YS}}{30(1-\nu^2)}} \tag{2}$$

where b_o is the in-plane size of the remaining ligament of the specimen and σ_{ys} is yield strength of the material. If the measured value exceeds the validity limit, it is considered an invalid value and replaced (censored) with the $K_{Jc\ (limit)}$ value for T_o calculation. A noticeable number of specimens (14 out of 53) in this study violated this requirement. The second validity requirement limits the amount of stable crack growth prior to cleavage instability. A K_{Jc} datum was considered invalid if the test terminated in cleavage after more than $0.05b_o$ or 1 mm, whichever is smaller, of slow-stable crack growth. Several specimens in this study violated this requirement. The same specimens violated the requirement by Eq. 2 and were censored by the procedure described above for T_o calculation.

All K_{Jc} data were converted to 1T equivalence, $K_{Jc(1T)}$, using the weakest-link size adjustment procedure of E1921:

$$K_{Jc(1T)}=20+\left[K_{Jc(xT)}-20\right]\left(\frac{B_{xT}}{B_{1T}}\right)^{1/4} \tag{3}$$

The distribution of fracture toughness values is described by the three-parameter Weibull cumulative probability function:

$$P_f=1-\exp\left[-\left(\frac{K_{Jc}-20}{K_o-20}\right)^4\right] \tag{4}$$

where two parameters are fixed to 4 and 20 MPa√m, respectfully. Thus, only the scale parameter, K_o, needs to be determined. K_o is determined using the maximum likelihood function

L. The censored likelihood function, *L*, is the product of the probability density function and survival function [3]. The probability density function, *f*, for the master curve distribution function is given by:

$$f\left(K_{Jc}\right)=\frac{dP}{dK_{Jc}}=\frac{4\left(K_{Jc}-20\right)^{4-1}}{\left(K_o-20\right)^4}\exp\left[-\left(\frac{K_{Jc}-20}{K_o-20}\right)^4\right] \tag{5}$$

The master curve survival function is given by:

$$S\left(K_{Jc}\right)=\exp\left[-\left(\frac{K_{Jc}-20}{K_o-20}\right)^4\right] \tag{6}$$

Thus, the censored likelihood function, *L*, can be expressed as:

$$L=\prod_{i=1}^{N} f_i^{\delta_i}\times S_i^{1-\delta_i}=\prod_{i=1}^{N}\frac{4\left(K_{Jc(i)}-20\right)^{3\delta_i}}{\left(K_o-20\right)^{4\delta_i}}\cdot\exp\left(-\left\{\frac{K_{Jc(i)}-20}{K_o-20}\right\}^4\right) \tag{7}$$

where δ_i= 1.0 if the $K_{Jc(i)}$ datum is valid or zero if datum is invalid and censored. The master curve temperature dependence is described as:

$$K_{Jc(med)}=20+\left(K_o-20\right)\left(\ln 2\right)^{1/4}=30+70\exp\left[0.019\left(T-T_o\right)\right] \tag{8}$$

where T_o is the reference fracture toughness transition temperature that corresponds to the temperature at which $K_{Jc(med)}$ =100MPa$\sqrt{m}$. The T_o is determined using the multi-temperature equation from E1921 by inserting the master curve dependence, Eq. (8), into Eq. (7) and solving it for $\partial\ln(L)/\partial T_o=0$:

$$\sum_{i=1}^{N}\delta_i\frac{\exp\left[0.019\left(T_i-T_o\right)\right]}{11+77\exp\left[0.019\left(T_i-T_o\right)\right]}-\sum_{i=1}^{N}\frac{\left(K_{Jc(i)}-20\right)^4\exp\left[0.019\left(T_i-T_o\right)\right]}{\left\{11+77\exp\left[0.019\left(T_i-T_o\right)\right]\right\}^5}=0 \tag{9}$$

where T_i= test temperature corresponding to $K_{Jc(i)}$ value.

It is firmly stated in the E1921 standard that this methodology should be applied to the transition fracture toughness data as close as possible to K_{Jc} level of 100MPa$\sqrt{m}$. Moreover, the E1921 requires that only fracture toughness data within -50°C≤ T_o ≤50°C should be used for final T_o calculation using Eq. 9.

Results and Discussion

A total of 53 specimens of F82H steel have been tested in the transition region, 27 1T C(T), 19 0.4T C(T) and 7 0.18T DC(T). One 0.4T compact specimen tested at -20°C did not cleave as that test was stopped when the clip gage ran out of measuring range. Final stress intensity factor converted from the J-integral value at the end of the test was higher than the $K_{Jc\ (limit)}$ value; thus it was treated as an invalid specimen. All data are summarized in Table 1. The reference fracture toughness transition temperature, T_o, for this data set is determined to be -105°C and standard deviation σ=3.4°C. Figure 1 illustrates the 1T size-adjusted fracture toughness data vs. test temperature, with the master curve and the 5% and 95% tolerance bounds from this analysis added. The first observation of these data is that this material exhibited a very high scatter of

fracture toughness data in the transition region. Sixteen out of 53 fracture toughness values or 30% are outside 5% and 95% tolerance bounds. For example, at -20°C measured fracture toughness values of F82H varied from 84 to 497 MPa√m. At same time, the scatter of fracture toughness within data sets for larger or smaller specimens appears to be similar. It indicates that size adjustment procedure by Eq. 3 works well for these data.

Since there were replicate tests performed at several temperatures, it was decided to determine median fracture toughness values at each of these temperatures and than compare how well those median values follow the master curve, Fig. 2. On this plot, the solid line is the master curve and each data point represents the median fracture toughness at the given temperature. Number in parentheses is the ratio of total number of tested specimens to the number of valid K_{Jc}.

Table 1. Fracture toughness data of the IAE heat of F82H steel

I.D.	Size	Test T °C	σ_y MPa	K_{Jc} MPa√m	K_{Jc}^{1T} MPa√m	$K_{Jc\ (limit)}$ MPa√m	δ_i
M10	1T	-20	537	88.6	88.6	311	1
5_10	1T	-20	537	416.7	416.7	311	0
M7	1T	-20	537	395.6	395.6	311	0
5_12	1T	-20	537	524.2	524.2	311	0
M8	1T	-50	550	128.4	128.4	316	1
5_5	1T	-50	550	114.6	114.6	316	1
5_4	1T	-50	550	146.7	146.7	316	1
5_7	1T	-50	550	94.6	94.6	316	1
5_8	1T	-50	550	412.4	412.4	316	0
M2	1T	-70	560	136.9	136.9	320	1
M5	1T	-70	560	117.1	117.1	320	1
5_6	1T	-70	560	122.1	122.1	320	1
M6	1T	-70	560	137.4	137.4	320	1
M3	1T	-70	560	127.3	127.3	320	1
M4	1T	-70	560	129.0	129.0	320	1
M1	1T	-70	560	113.8	113.8	320	1
5_11	1T	-100	575	111.7	111.7	326	1
5_1	1T	-100	575	96.6	96.6	326	1
5_9	1T	-100	575	173.4	173.4	326	1
5_2	1T	-100	575	96.4	96.4	326	1
5_3	1T	-100	575	131.5	131.5	326	1
3-16	1T	-40	546	87.3	87.3	314	1
3-13	1T	-40	546	80.2	80.2	314	1
3-17	1T	-60	555	86.2	86.2	318	1
3-14	1T	-60	555	87.2	87.2	318	1
3-18	1T	-80	564	99.7	99.7	322	1
3-15	1T	-80	564	81.1	81.1	322	1
52-1	0.4T	-50	550	124.5	103.2	209	1
52-2	0.4T	-50	550	322.9	261.1	204	0
m71	0.4T	-20	537	347.7	280.8	204	0
m72	0.4T	-20	537	414.6	333.9	208	0
56-3	0.4T	-100	575	81.0	68.6	214	1
56-2	0.4T	-100	575	161.3	132.5	211	1
58-4	0.4T	-100	575	92.9	78.0	218	1
58-3	0.4T	-100	575	135.1	111.5	211	1
58-2	0.4T	-100	575	116.8	96.9	217	1
58-1	0.4T	-100	575	225.5	183.4	217	0
56-1	0.4T	-50	550	306.0	247.5	207	0

Table 1. Fracture toughness data of the IAE heat of F82H steel (continued)

I.D.	Size	Test T	σ_y	K_{Jc}	K_{Jc}^{1T}	$K_{Jc\ (limit)}$	δ_i
		°C	MPa	MPa√m	MPa√m	MPa√m	
56-4	0.4T	-50	550	359.1	289.6	212	0
59-1	0.4T	-50	550	393.0	316.9	206	0
59-2	0.4T	-50	550	340.6	275.0	204	0
59-4	0.4T	-50	550	394.4	318.0	207	0
59-3	0.4T	-50	550	335.9	271.6	209	0
510-1	0.4T	-165	612	56.1	48.7	211	1
510-2	0.4T	-165	612	40.9	36.7	225	1
510-3	0.4T	-165	612	37.9	34.3	220	1
HM1	0.18T	-140	597	107.6	77.2	153	1
HM2	0.18T	-140	597	111.1	79.5	155	1
HM3	0.18T	-140	597	91.0	66.3	155	1
HM5	0.18T	-140	597	98.1	71.0	153	1
HM6	0.18T	-140	597	84.7	62.2	149	1
HM8	0.18T	-140	597	48.7	38.8	154	1
HM9	0.18T	-140	597	101.2	73.0	145	1

values at the given temperature. Remarkably, the median fracture toughness values are following the master curve trend very well within the wide temperature range studied.

Larger than expected scatter indicates a potential for inhomogeneity of fracture toughness properties of this F82H plate. Scanning electron-microscopy (SEM) has been performed to examine the fractured surfaces of the broken specimens. All specimens failed by cleavage; no evidence of intergranular fracture was observed on the fractured surfaces.

D. Gelles performed metallographic and SEM examination of broken specimens from this study [4,5]. Among other observations, metallographic carbide etchant revealed larger particles dispersed through the thickness of the plate. The particles were found to be rich in Ta and O. Nevertheless, size distribution measurements did not indicate any inhomogeneity in distribution through the thickness of the plate. However, in the course of examination [5], it became apparent from the spatial distribution that the particles tended to clump, but clumping was generally restricted to the center of the plate.

H. Tanigawa et al. [6] investigated inclusions formed in the plates of F82H steel by SEM and transmission electron microscopy (TEM) equipped with EDS. Analyses by SEM and TEM for the plates revealed that Ta does not form MX precipitates, but instead, it forms composite Al_2O_3 – Ta(V,Ti)O oxide, or single phase Ta(V)O oxide. The composite inclusions are rather dominant in the plate obtained from the bottom of the ingot, but not in the plate from the middle of the ingot. SEM observations by Tanigawa et al. [6] of broken specimens from this study also revealed that composite oxide tended to be observed at the crack-initiation site of broken specimens.

Despite some extensive microstructural investigations [4-6] of the F82H steel, including broken specimens from this study, it remains difficult to draw a strong link between distribution of these composite oxides and the inhomogeneity of fracture toughness.

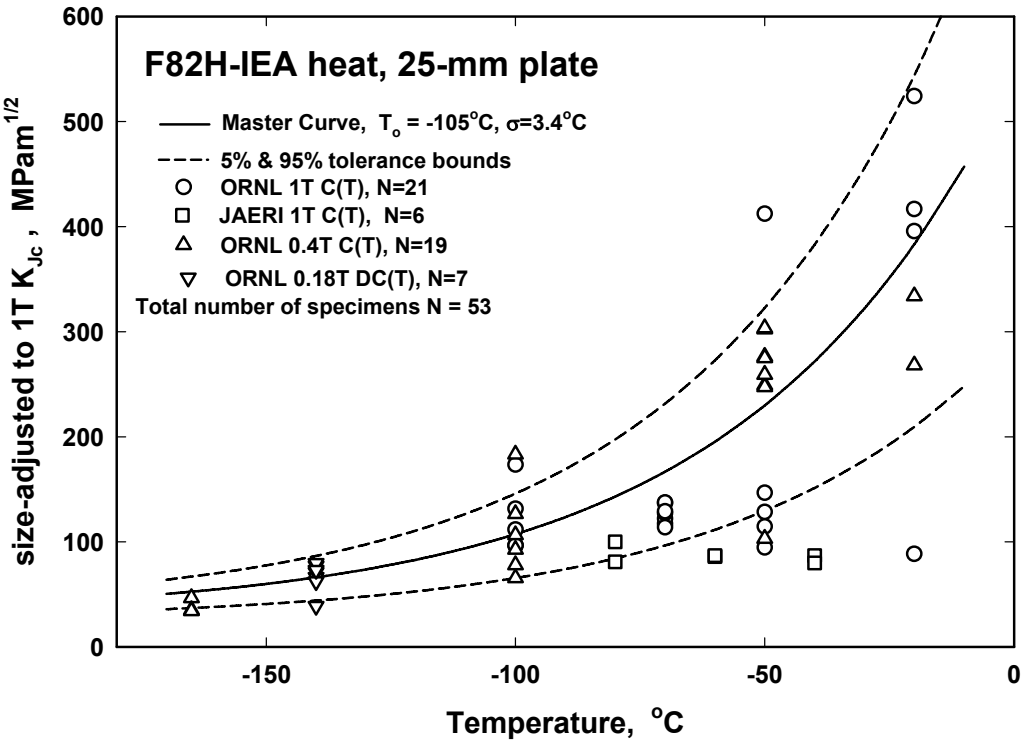

Fig. 1. Scatter of F82H-IAE fracture toughness data relative to the conventional master curve and 5% & 95% tolerance bounds.

Bimodal Master Curve Analyses of Fracture Toughness Data

The large scatter in fracture toughness data required a reconsideration of the application of the conventional master curve approach as in Eqs. 4-9. One way of doing it is to assume that our data consist of two combined master curve distributions. In this case, the total cumulative probability distribution can be expressed as a bimodal distribution of the form [7]:

$$P_f = 1 - p_1 \cdot \exp\left[-\left(\frac{K_{Jc} - 20}{K_{o1} - 20}\right)^4\right] - (1 - p_1) \cdot \exp\left[-\left(\frac{K_{Jc} - 20}{K_{o2} - 20}\right)^4\right] \quad (10)$$

where K_{o1} and K_{o2} are the scale parameters for the two distributions and p_1 is the probability of the toughness belonging to distribution 1. In the case of multi-temperature data set like in the present work, K_{o1} and K_{o2} should be expressed in terms of reference fracture toughness temperatures, T_{o1} and T_{o2}. While the Eq. 10 appears to be a simple modification of Eq. 4, there is a key difference in them. There are three parameters need to be determined in the bimodal distribution function, Eq. 10, compared to only one in the conventional master curve analysis, Eq. 4. As such, a larger number of specimens needs to be tested to perform the bimodal analysis

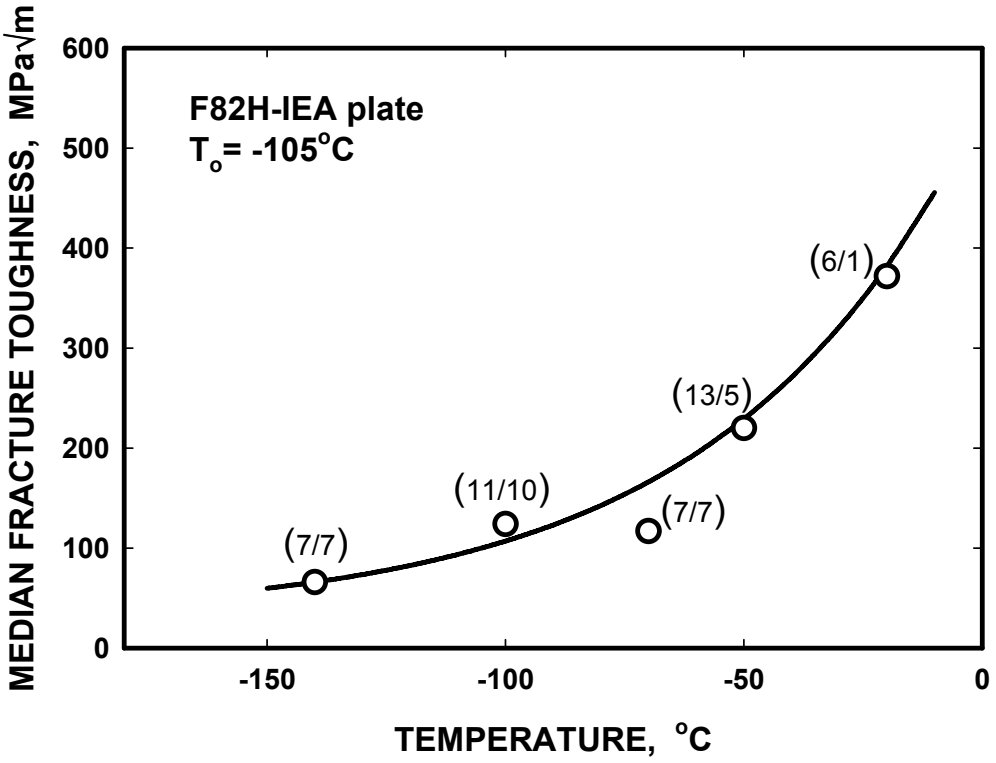

Fig. 2. Median fracture toughness values of F82H plate at different temperatures. The solid line is the master curve. Number in parentheses is the ratio of total number of tested specimens to the number of valid K_{Jc} values at the given temperature.

compared to the conventional master curve analysis. The general form of the likelihood function will remain the same as in Eq. 7, however, the probability density and the survival functions have the following forms in the bimodal analysis [7]:

$$f_c = 4\cdot p_1 \cdot \frac{(K_{Jc}-20)^3}{(K_{o1}-20)^4}\exp\left[-\left(\frac{K_{Jc}-20}{K_{o1}-20}\right)^4\right] - 4\cdot(1-p_1)\cdot\frac{(K_{Jc}-20)^3}{(K_{o2}-20)^4}\cdot\exp\left[-\left(\frac{K_{Jc}-20}{K_{o2}-20}\right)^4\right]$$

$$S_c = p_1\cdot\exp\left[-\left(\frac{K_{Jc}-20}{K_{o1}-20}\right)^4\right] + (1-p_1)\cdot\exp\left[-\left(\frac{K_{Jc}-20}{K_{o2}-20}\right)^4\right] \qquad (11)$$

Application of the bimodal analysis gives the following results for the present data of F82H plate: p_1=0.63, T_{o1} = -80°C, and T_{o2} = -120°C, Fig. 3. The bimodal analysis provides slightly better description of scatter in toughness data that the conventional master curve analysis. This bimodal analysis was originally suggested by Wallin to characterize fracture toughness data of heat-affected zone (HAZ) of welds [7]. In the case of HAZ, any given result may be affected by location of the crack tip in the specimen. There might be a potential for some specimens to have crack tip near base metal rather than HAZ and thus justifying the bimodal distribution of data. Yet, the cause for bimodal distribution of fracture toughness in the F82H plate remains unclear. Figures 4a and 4b are the Weibull plots of F82H plate data at -100°C and -50°C, respectfully. The solid lines correspond to the conventional master curve analysis and the dashed lined correspond to the bimodal analysis. These plots do not provide any additional evidence that the bimodal analysis lines follow the data more closely than the conventional master curve analysis.

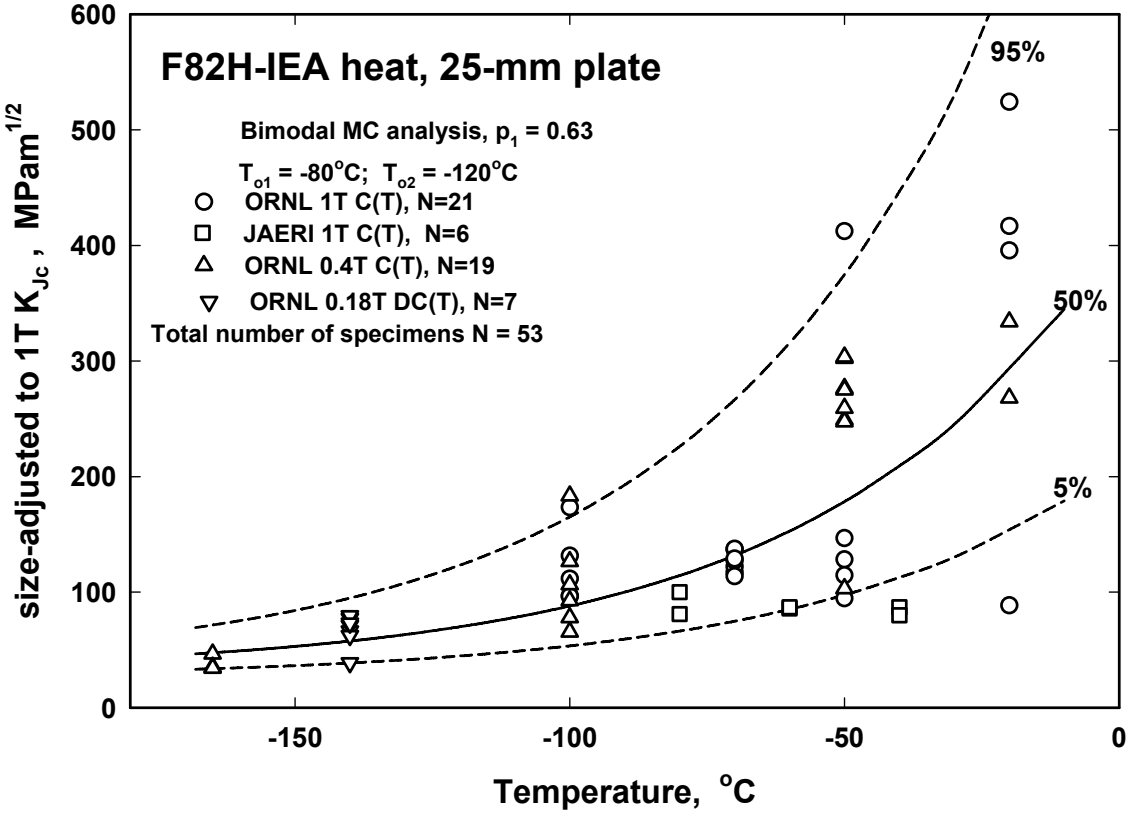

Fig. 3. The bimodal master curve analysis of the F82H plate fracture toughness data.

a)

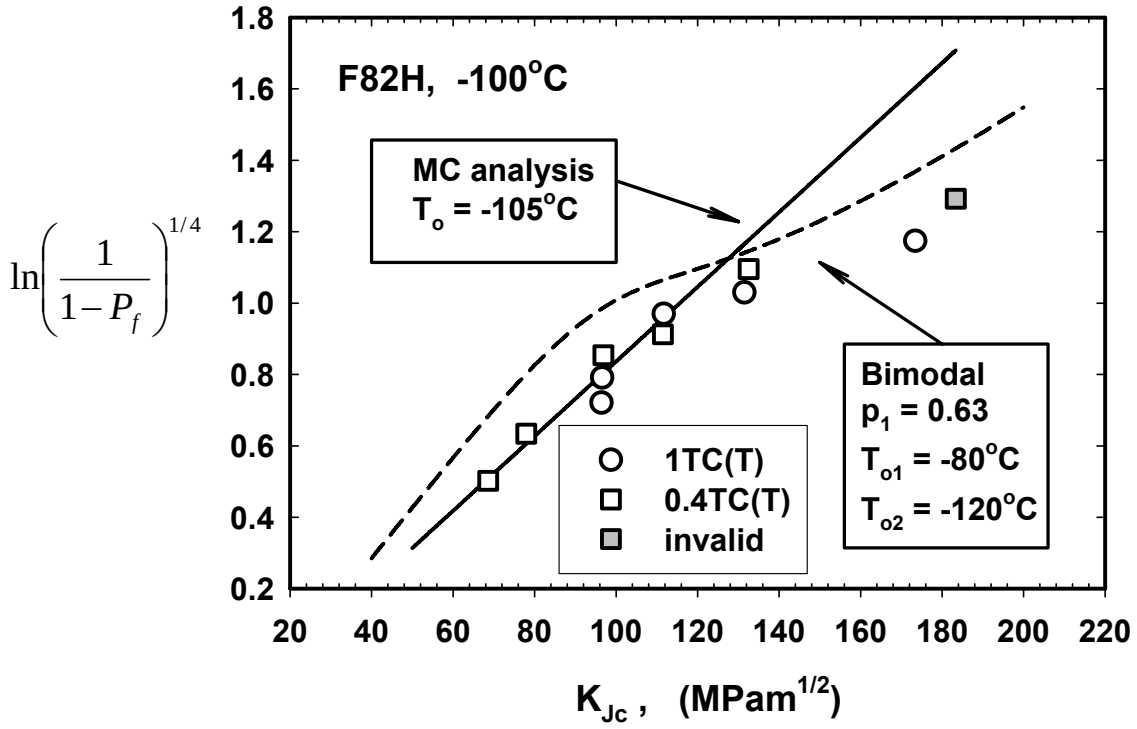

b)

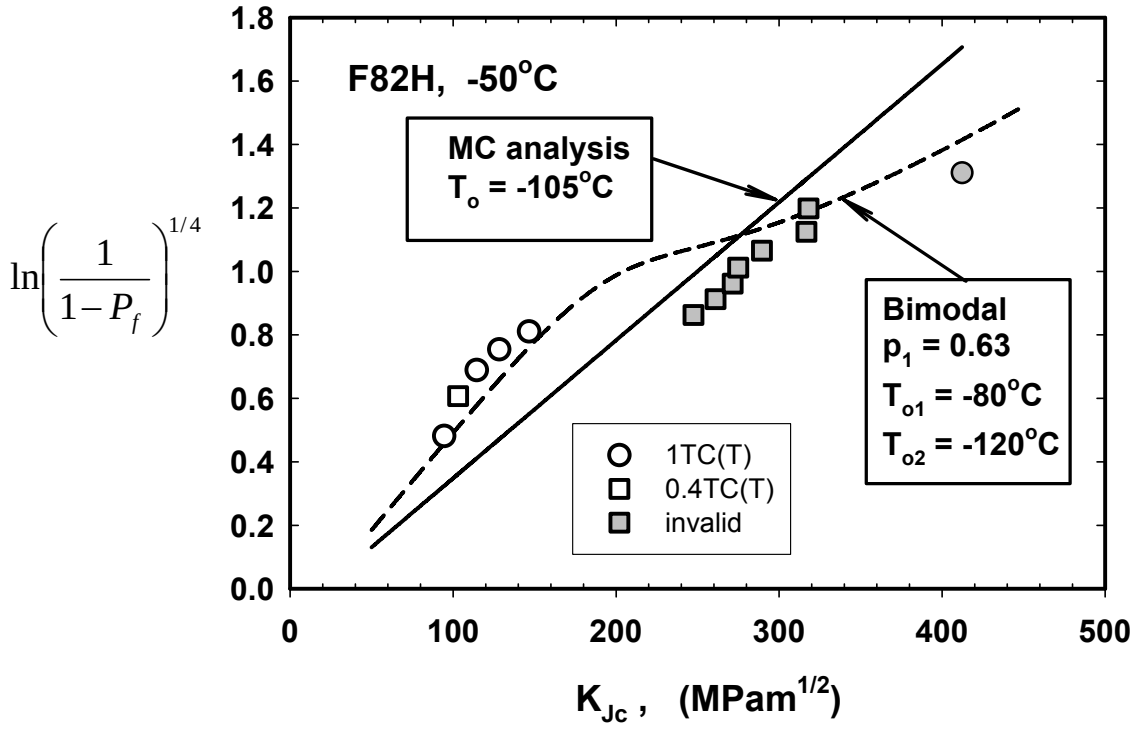

Fig. 4. Comparison of the bimodal and conventional master curve analyses of F82H fracture toughness data at -100°C (a) and -50°C (b).

Random Inhomogeneity Analysis of Fracture Toughness Data

In the previous section, the assumption was made that the present fracture toughness data might consist of two populations. However, the bimodal analysis did not noticeably improve description of the scatter of fracture toughness data. Thus, the next logical step is to assume that we are dealing with an inhomogeneous dataset.

Wallin suggested [7] a simple engineering method, the single point estimation, to examine this assumption. In this method, individual T_o estimates are determined from all non-censored size-adjusted K_{Jc} values:

$$T_{oi} = T_i - \frac{\ln\left(\frac{K_{Jc\,i} - 30}{70}\right)}{0.019} \tag{12}$$

The single point T_o value (T_{osp}) is then estimated as follows [8]:

$$T_{oSP} = \frac{\sum_{i=1}^{r} T_{o\,i}}{r} - 4\ ^{o}C \tag{13}$$

where r is the number of non-censored (valid) results as defined above and the standard deviation becomes:

$$\sigma_{T_{o\,SP}} = \sqrt{\frac{\sum_{i=1}^{r} T_{oi}^2 - \frac{\left(\sum_{i=1}^{r} T_{oi}\right)^2}{r}}{r} - \left(21^{o}C\right)^2} \tag{14}$$

Application of the single point estimate method to the current data set resulted in T_{oSP} = -84°C and σ_{ToSP}=24°C. The T_{oSP} estimate is 21°C higher than the T_o value from the conventional master curve analysis. More importantly, there is a significant difference in the standard deviation estimates. The standard deviation from the single point method is several times more that from the conventional master curve analysis. This is a strong indication that this data set is inhomogeneous. As such, the maximum likelihood method for random inhomogeneity case as suggested by M. Scibetta [8] can be applied to the data analysis. In this method, the value of T_o becomes a random variable in the inhomogeneous dataset. Then, the probability density function for T_o is:

$$f_T = \frac{1}{2\sqrt{\pi}\cdot\sigma_{T_{oRI}}} \exp\left[-\frac{\left(T_o - T_{oRI}\right)^2}{2\sigma_{T_{oRI}}^2}\right] \tag{15}$$

where T_{oRI} and σ_{ToRI} are an estimate of the fracture toughness transition temperature from the random inhomogeneity analysis and its standard deviation, respectively. The local conditional density and survival probabilities at T_o, f_{To} and S_{To}, are the same as in conventional master curve methodology, Eqs. 5 and 6. Then, the total density and survival probabilities are:

$$f = \int_{-\infty}^{\infty} f_T \cdot f_{T_o} \cdot dT_o \quad and \quad S = \int f_T \cdot S_{T_o} \cdot dT_o \tag{16}$$

The parameters T_{oRI} and σ_{ToRI} are then solved by maximizing:

$$\ln L = \sum_{i=1}^{N} \left[\delta_i \cdot \ln(f_i) + (1 - \delta_i) \cdot \ln(S_i) \right] \tag{17}$$

Application of this random inhomogeneity analysis yielded T_{oRI}=-93°C and σ_{ToRI}=26.3°C. Note that the absolute value from this analysis is similar to the T_o estimate of -105°C from the conventional master curve analysis. The main difference comes in the standard deviation values. The standard deviation from the random inhomogeneity analysis provides a more realistic scatter band for these data. Five out of 53 fracture toughness values or 9.5% are outside 5% and 95% tolerance bounds compared to 16 data points (30%) in the case of the conventional master curve analysis. Figure 5 illustrates the master curves (50%) and 5% and 95% tolerance bounds from the random inhomogeneity and the conventional analyses.

In addition to the present data, G. Odette et al. assembled a large database of fracture toughness of F82H from different sources [9] including most of data from this study. All data were constraint adjusted by a procedure developed at UCSB. There were a total of 219 data points in the UCSB database. The conventional master curve T_o value for this large constraint adjusted dataset of F82H was determined to be -103°C [9]. This corresponds well with T_o value (-105°C) from this study. As in the case of the present study, there was a large number of data points (55 out of 219, 24%) outside 5% and 95% tolerance bounds, see Fig. 6. This provides another argument in favor of the inhomogeneity of fracture toughness of F82H steel. On the other hand, there were only 16 data points (or 7.3%) outside 5% and 95% tolerance bounds derived in this study by the random inhomogeneity analysis.

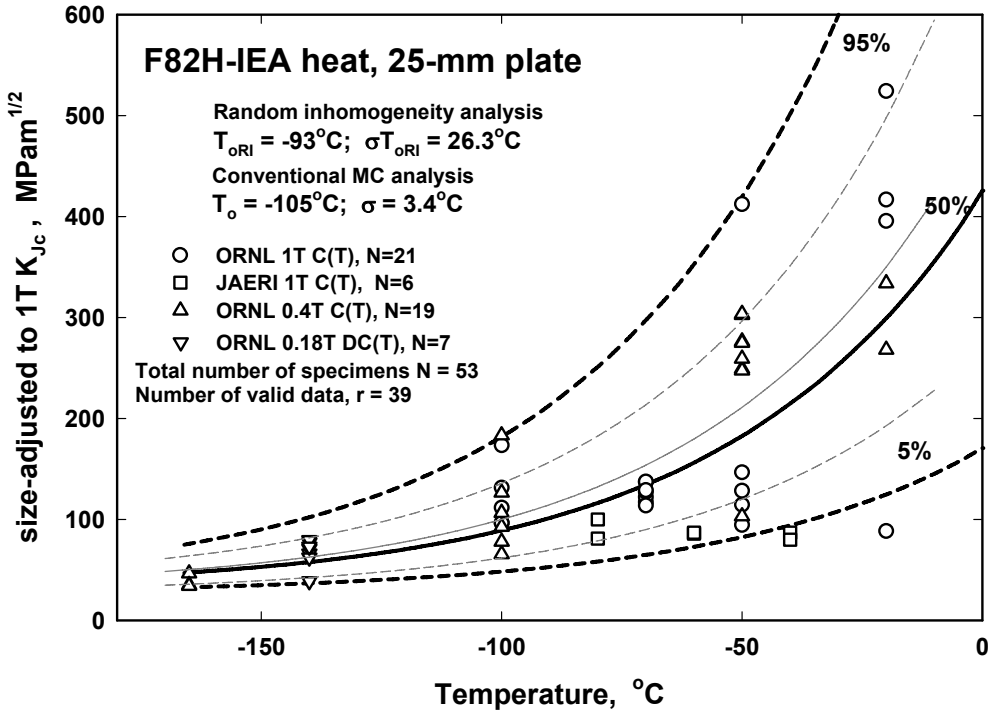

Fig. 5. Comparison of random inhomogeneity analysis (heavy lines) and conventional master curve analysis (light lines) of F82H data.

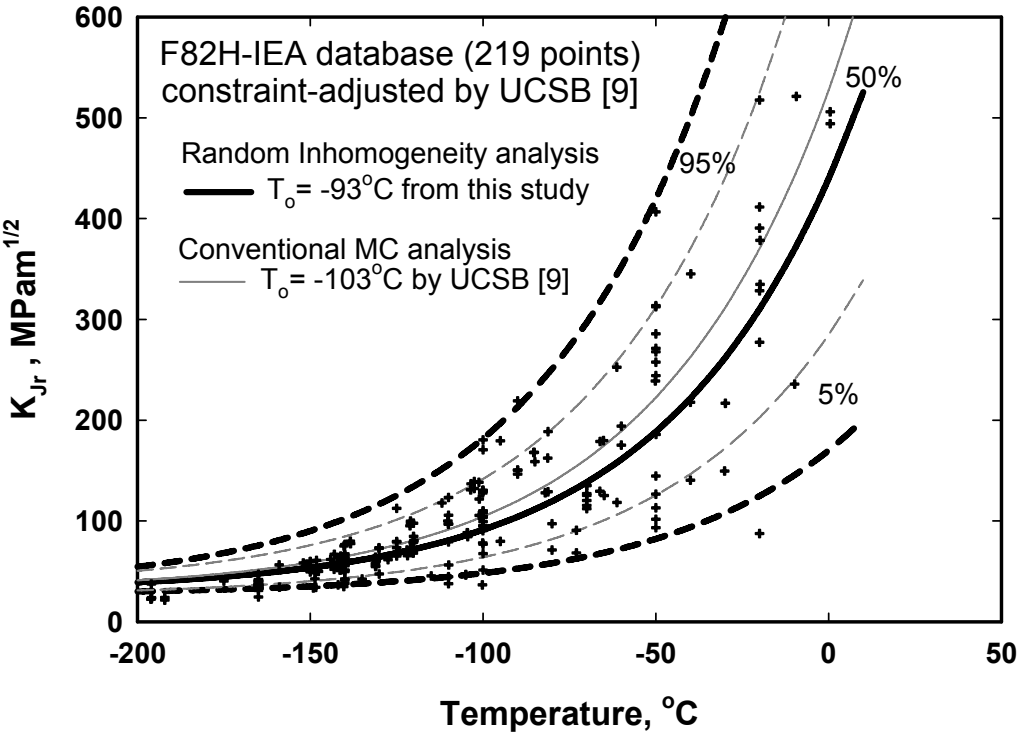

Fig. 6. Application of random inhomogeneity analysis from the present study to a large constraint-adjusted UCSB database [9] of fracture toughness data on F82H. Solid lines are the master curves (50%), dashed lines are 5% and 95% tolerance bounds. Heavy lines are the random inhomogeneity analysis; the light lines are the conventional master curve analysis.

Clearly, the scatter in the transition fracture toughness of F82H-IEA steel is somewhat higher than expected by the conventional master curve analysis. The random inhomogeneity analysis provides a better description of the same scatter. Notably, the T_o values derived by both analyses are similar, the main difference comes in values of the standard deviation. This has an important practical application for use of the small specimens for post-irradiation characterization of this steel. The random inhomogeneity analysis requires a relatively large number of data points. At the same time, only a small number of small size specimens can be irradiated in test reactors. The result is that researchers are forced to determine the irradiated T_o values for candidate fusion materials using only few specimens. It appears from the analysis of data in this study that this practice provides a reasonable estimate of irradiated T_o values, but it is not able to address the issue of proper description of the scatter in the transition fracture toughness.

Conclusion

The results of this study showed that the scatter of fracture toughness for a 25 mm plate of F82H-IEA was larger than anticipated by the conventional master curve analysis. The random inhomogeneity analysis provides a better description of the data scatter for F82H steel, than does the conventional master curve analysis. At the same time, the T_o values derived using the conventional and random inhomogeneity analyses are quite similar. It appears from the analysis of data in this study that small number of sub-sized specimens used for irradiation studies could provide a reasonable estimate of irradiated T_o values, but they may not able to address the issue

of proper description of the scatter in the transition fracture toughness of irradiated F82H-IAE steel.

Acknowledgements

This research was sponsored by the Office of Fusion Energy Sciences, U.S. Department of Energy, under Contract DE-AC05-00OR22725 with UT-Battelle, LLC. Authors would like to thank M. Scibetta from SCK-CEN, Belgium, for his assistance with random inhomogeneity analysis of the data.

References

[1] K. Wallin, Eng. Fract. Mech. 19 (1984) 1085.
[2] K. Wallin, Eng. Fract. Mech. 22 (1985) 149.
[3] J. G. Merkle, K. Wallin, and D. E. McCabe, Technical Basis for an ASTM Standard on Determining the Reference Temperature, T_o, for Ferritic Steels in the Transition Range, NUREG Report NUREG/CR-5504 (1998).
[4] D. S. Gelles and M. A. Sokolov, Fusion Materials Semiannual Progress Report for Period Ending June 30, 2003, DOE/ER-0313/34.
[5] D. S. Gelles and M. A. Sokolov, Fusion Materials Semiannual Progress Report for Period Ending December 31, 2003, DOE/ER-0313/35.
[6] H. Tanigawa, A. Sawahata, M. A. Sokolov, R. L. Klueh, and A. Kohyama, Mater. Trans. 3 (2007).
[7] K. Wallin, Eng. Fract. Mech. 71 (2004) 2329.
[8] M. Scibetta, SCK-CEN, private communication, 2005.
[9] G. R. Odette, T. Yamamoto, H. Kishimoto, M. A. Sokolov, P. Spatig, W. J. Yang, J.-W. Rensman, and G. E. Lucas, J. Nucl. Mater. 329–333 (2004) 1243.

MECHANICAL PROPERTIES AND MICROSTRUCTURE OF THREE RUSSIAN FERRITIC/MARTENSITIC STEELS IRRADIATED IN BN-350 REACTOR TO 50 dpa AT 490°C—A. M. Dvoriashin, S. I. Porollo, Yu. V. Konobeev (State Scientific Centre of Russian Federation, The Institute for Physics and Power Engineering), N. I. Budylkin, E. G. Minonova, A. G. Ioltukhovskiy, M. V. Leonteva-Smirnova (State Scientific Centre of Russian Federation), A. A. Bochvar (All-Russia Research Institute of Inorganic Materials (VNIINM), Moscow, Russia), and F. A. Garner (Pacific Northwest National Laboratory)[1]

OBJECTIVE

The object of this effort is to assess the mechanical and microstructural behavior of Russian ferritic-martensitic steels during neutron irradiation in order to better predict how to improve the radiation performance of advanced steels required for fusion energy systems.

SUMMARY

Ferritic/martensitic (F/M) steels are being considered for application in fusion reactors, intense neutron sources, and accelerator-driven systems. While EP-450 is traditionally used with sodium coolants in Russia, EP-823 and EI-852 steels with higher silicon levels have been developed for reactor facilities using lead-bismuth coolant. To determine the influence of silicon additions on short-term mechanical properties and microstructure, ring specimens cut from cladding tubes of these three steels were irradiated in sodium at 490°C in the BN-350 reactor to 50 dpa.

Post-irradiation tensile testing and microstructural examination show that EI-852 steel (1.9 wt% Si) undergoes severe irradiation embrittlement. Microstructural investigation showed that the formation of near-continuous χ-phase precipitates on grain boundaries is the main cause of the embrittlement.

PROGRESS AND STATUS

Introduction

Ferritic/martensitic (F/M) steels are used in various fast reactor facilities and are considered as candidate materials for application in fusion reactors, intense neutron sources and accelerator-driven systems. Their advantages over other structural materials are higher resistance to void swelling, lower irradiation creep rate, and relatively low induced radioactivity compared to most austenitic alloys. It is known, however, that one of the shortcomings of F/M steels is their tendency to develop low-temperature irradiation embrittlement.

EP-450 is a typical 12% Cr steel commonly used for nuclear applications in Russia and other former Soviet countries with properties similar to Western 12% Cr steels [1]. Two Russian F/M steels designated EP-823 and EI-852 were developed specially for reactor facilities with lead-bismuth coolant [2]. The corrosion resistance of these steels in the coolant was obtained primarily by a higher content of silicon. To elucidate the influence of silicon additions on short-term mechanical properties and microstructure, three F/M steels EP-450, EP-823 and EI-852 with different contents of silicon were irradiated in the form of fuel cladding tubes in the BN-350 fast reactor in Kazakhstan.

[1]Pacific Northwest National Laboratory (PNNL) is operated for the U.S. Department of Energy by Battelle Memorial Institute under contract DE-AC06-76RLO-1830.

Experimental Procedure

Materials

The chemical composition of F/M steels EP-450, EP-823 and EI-852 and the sizes (diameter and thickness) of cladding tubes from which ring specimens for mechanical tests were cut are shown in Table 1.

Table 1. Composition of steels EP-450, EP-823 and EI-852 (wt %)

Steel	Tube size, mm	Content, wt %						
		C	Mn	Si	P	S	Cr	Ni
EP-450	6.0×0.3	0.13	0.32	0.18	0.023	0.006	13.28	0.22
EP-823	7.0×0.3	0.18	0.6	1.05	0.012	0.008	11.40	0.70
EI-852	7.0×0.3	0.13	0.52	1.9	0.014	0.012	12.85	0.22

Content, wt %							
Mo	Nb	V	W	Ti	Al	B	N
1.5	0.45	0.28	-	-	-	0.004	0.040
0.67	0.20	0.40	0.65	0.03	0.030	0.004	0.040
1.66	-	-	-	-	0.014	-	0.034

The heat treatment for the EP-450 tubes consisted of quenching from 1050°C followed by tempering at 780°C for 1 h. The EP-823 tubes were normalized at 1050°C and aged at 740°C for 1.5 h. The EI-852 steel was aged at 850°C for 0.5 h but no normalization or tempering was used.

Ring specimens of 2 mm length were cut from these tubes for measurements of mechanical properties and additional rings of 4 mm length were cut for electron microscopy. These rings were irradiated in flowing sodium in a special fuel assembly in the BN-350 fast reactor. This assembly used short fuel pins in the bottom of the assembly, which allowed heating of the specimens in the upper part of the assembly to 490±10°C. The neutron fluence was 1.12×10^{22} n/cm^2 (E>0.1 MeV) corresponding to 50 dpa (NRT) at 1.47×10^{-7} dpa /s.

Mechanical properties of both non-irradiated and irradiated 2 mm specimens were measured using a standardized Russian ring-pull test (see Refs. 3 and 4 for details) in a shielded tensile testing machine at test temperatures ranging from 20°C to 700°C. The pre-test aging time for the specimens at any test temperature was 20 min. Two or three separate specimens were tested at any given test temperature. Fractography of fracture surfaces was not conducted so no determination of fracture mode was made.

Disks of 3 mm diameter were punched from the 4 mm rings and prepared using the two-jet "TENUPOLE" polishing technique with an electrolyte of 5% $HClO_4$ + 95% acetic acid. The microstructure was observed using a JEM-100CX electron microscope operating at 100 kV and equipped with a lateral goniometer.

Results

Measured mechanical properties of unirradiated and irradiated F/M steels EP-450, EP-823 and EI-852 at various test temperatures are shown in Figs. 1 and 2. The mechanical properties of the three unirradiated steels are similar, namely, up to the test temperature of 500°C the ultimate strength decreases rather smoothly, but at higher temperatures, it falls sharply, accompanied by a rise in total

elongation. Of the three steels investigated, EI-852 in the unirradiated condition had the lowest strength and the highest ductility.

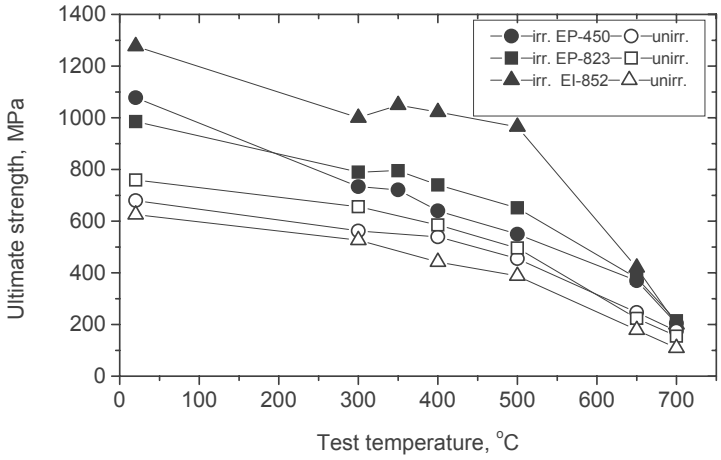

Fig. 1. Ultimate strength of both unirradiated and irradiated steels EP-450, EP-823, and EI 852 versus test temperature.

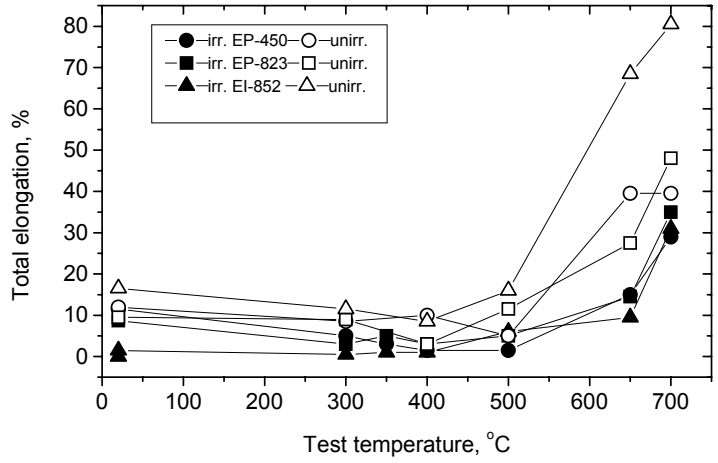

Fig. 2. Total elongation of both unirradiated and irradiated steels EP-450, EP-823, and EI 852 versus test temperature.

Neutron irradiation resulted in a significant change of mechanical properties, expressed primarily in hardening. At room temperature the ultimate strength increment equals 649 MPa for EI-852, 398 MPa for EP-450 and 225 MPa for EP-823. With increase of test temperature, the difference in strength between unirradiated and irradiated steels becomes smaller and at a test temperature of 700ºC the difference almost disappears.

The ductility of the irradiated steels vs. test temperature is more complicated. In the range 300-500ºC the total elongation ε_t of EP-450 and EP-823 decreases with increasing test temperature, reaching 1.5% for EP-450 and 3.0% for EP-823, and then sharply rises. In contrast, EI-852 at room temperature has low ε_t values (0 to 1.5%) and, in the range 300-400ºC, the ductility is consistently lower compared with those of EP-450 and EP-823 steels.

The initial microstructures of EP-450 and EP-823 steels were similar and consisted of ferrite grains and tempered martensite grains. Carbide precipitates of type $M_{23}C_6$ were observed on grain and subgrain boundaries of the tempered martensite grains. In the ferrite grains, fine needle precipitates of M_2X type were observed. The microstructure of unirradiated steel EP-852 was observed to consist of ferrite grains only, with $M_{23}C_6$ precipitates uniformly distributed in the grains.

Irradiation at 490°C to 50 dpa has resulted in the formation of voids in all three steels at relatively low concentration ($<10^{18}$ m^{-3}) with diameters up to 20 nm. The distribution of voids in the steels was found to be non-uniform. Voids in ferrite grains, as a rule, were adjacent to precipitates. In grains of tempered martensite, voids were located primarily on subgrain boundaries. After irradiation, the phase structure of the steels has changed, with both sizes and concentration of $M_{23}C_6$ increased, needle precipitates in ferrite grains of EP-450 and EP-823 dissolved, and new radiation-induced phases formed, as shown in Figs. 3 and 4.

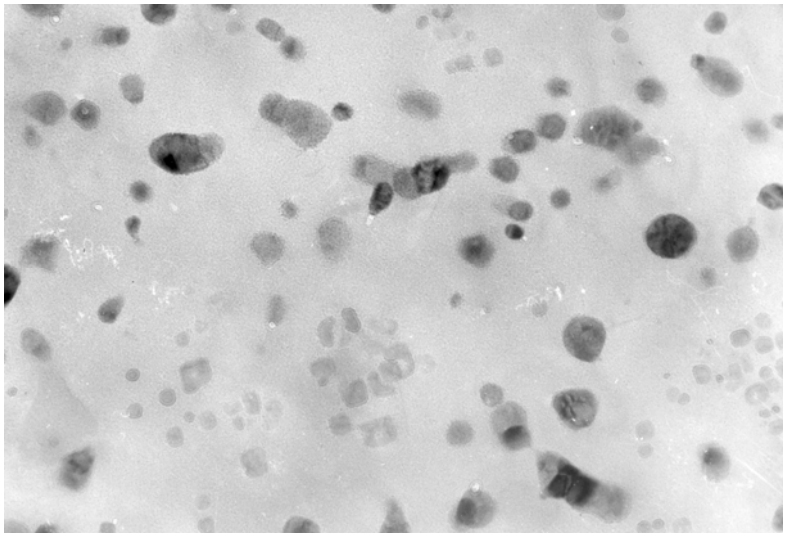

Fig. 3. Bright-field image of microstructure of ferrite grains of irradiated EP-450 at 490°C and 50 dpa.

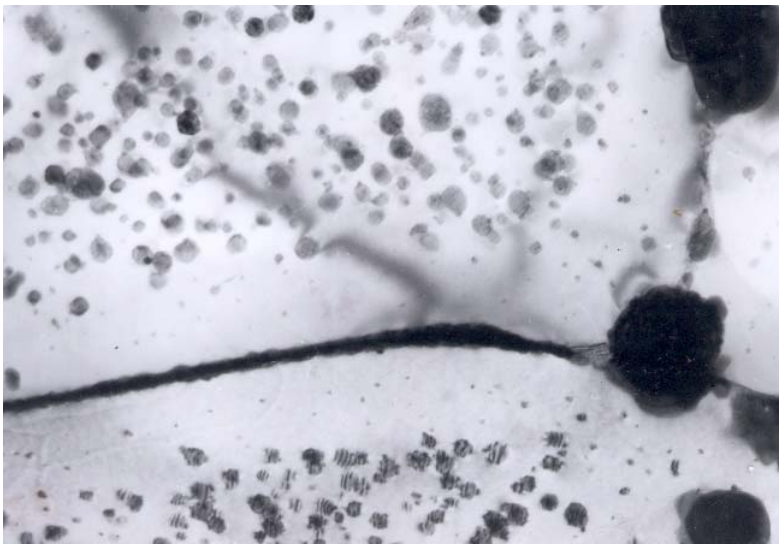

Fig. 4. Bright-field image of zone denuded of χ-phase precipitates in irradiated EP-450 at 490°C and 50 dpa.

Micro-diffraction analysis of precipitates formed during irradiation has shown that in EP-450 new precipitates are the α' and χ phases. In EP-823 and EI-852 only χ phase has formed. The mean size, concentration, and volume fraction of radiation-induced phases are shown in Table 2.

Table 2. Mean size, concentration and volume fraction of phases formed under irradiation

Steel	Phase	Mean size, nm	Concentration, 10^{21} m^{-3}	Volume fraction, %
EP-450	χ	40	0.8	4
	α'	20	1.0	1
EP-823	χ	50	0.8	5
EI-852	χ	36	3.0	12

As shown in Table 2, χ-phase (an intermetallic phase known to be rich in Si) is the major irradiation-induced phase increasing progressively with silicon content. Note that the volume fraction of χ-precipitates in EI-852 reaches 12 %.

There is a significant difference in the spatial distribution of χ -precipitates in the various alloys. In EP-450 and EP-823, these precipitates are rather uniformly distributed within grains, although at grain boundaries a precipitate-denuded zone of ~300 nm width (Fig. 4) is observed. In contrast, the χ-precipitates in EI-852 have formed both in the grain interior as well as on grain boundaries, with these precipitates forming continuous chains on and near the boundaries (see Fig. 5).

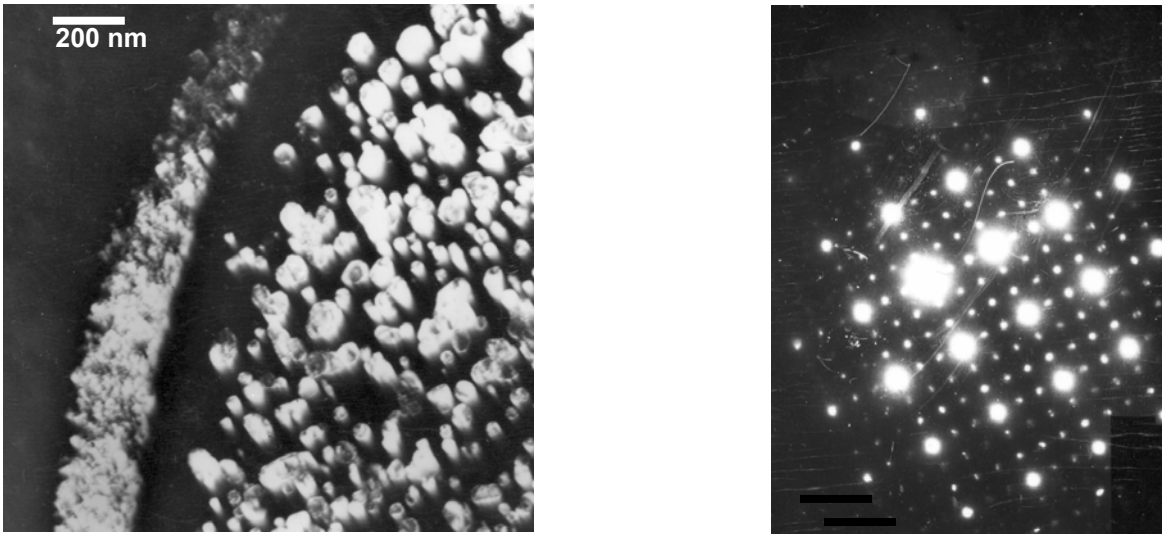

Fig. 5. Dark-field image of χ-phase reflection at grain boundary separated by precipitate-denuded zone from precipitation in the matrix (a) and diffraction pattern of χ-precipitates (b) of EI-852 at 490°C and 50 dpa.

Discussion

As mentioned above, F/M steels EP-823 and EI-852 were developed as materials capable of withstanding corrosion in Pb-Bi coolant [2]. The resistance to corrosion was achieved mainly by increased silicon content compared with that of EP-450 steel. Such compositional modifications might

be used for fusion applications and therefore it is of interest to compare the effect of neutron irradiation on these three steels.

In all three steels, the void concentration was very low after irradiation to 50 dpa, irrespective of chemical composition and heat treatment. This observation confirms the generality of data showing a high resistance of F/M steels to swelling determined, most probably, by the crystallographic properties of the Fe-Cr bcc matrix.

It should be noted that, in spite of their distinctive chemical compositions, the mechanical properties of EP-450 and EP-823, both before and after irradiation, are similar. Both steels demonstrated rather high strength and ductility at all test temperatures. In contrast, EI-852 experiences much greater hardening and embrittlement following irradiation, and in some cases its ductility is essentially zero.

These data confirm previously published results on the irradiation hardening and embrittlement of the two Si-modified F/M steels when irradiated in the BR-10 and BOR-60 fast reactors at temperatures of 350 to 680ºC [5, 6]. One of these studies showed that formation of χ-precipitates at higher irradiation temperatures contributes to ductility reduction [6].

Analyzing the relationship between microstructure and radiation-induced changes of mechanical properties, one can conclude that severe embrittlement of EI-852 steel is caused not only by the greater degree of precipitation of χ-phase in the matrix and therefore higher matrix strengthening, but also arises due to the near-continuous precipitation of χ-phase on grain boundaries. This conclusion is in agreement with results of Refs. [7, 8] that show that the formation of χ-phase in ferritic and martensitic steels during either aging or irradiation, results in ductility reduction as revealed in both tensile and impact mechanical tests. In the other two F/M alloys, the matrix is also hardened by precipitation, albeit to a lower level, but the precipitate-denuded zones near grain boundaries may allow enough grain boundary sliding during deformation to preserve some ductility. Therefore it appears that ~1 wt% Si is probably an upper limit for alloys developed for corrosion resistance in Pb-Bi coolant.

Conclusions

The changes in mechanical properties and microstructure of F/M steels EP-450, EP-823, and EI-852 following irradiation in the BN-350 reactor at 490°C to 50 dpa can be summarized as follows:

1. All three steels are very resistant to swelling at these irradiation conditions, with voids occasionally observed at very low concentrations.

2. Irradiated EP-450 and EP-823 containing 0.18 and 1.05 wt% of silicon, respectively, demonstrate good mechanical properties both before and after irradiation. Steel EI-852 with 1.9 wt% silicon, however, hardens to a higher level and develops severe irradiation embrittlement.

3. The embrittlement of EI-852 steel by radiation is caused not only by a higher level (volume fraction of 12%) of Si-rich χ-phase precipitates inside grains, but especially by the near-continuous formation of χ-phase on grain boundaries. This latter microstructural feature probably precludes grain boundary sliding that can occur in the precipitate-denuded zones maintained in the other two alloys.

4. Increasing silicon additions appear to offer no large influence on the void swelling of the Russian F/M steels at these irradiation conditions, but the silicon content must be limited to ~1% in order to preserve sufficient post-irradiation ductility.

Acknowledgements

This work was supported by the Russian Foundation for Basic Research under the Project # 04-02-17278. F. A. Garner's participation was funded by the USDOE, Offices of Fusion Energy and Advanced Fuel Cycle Initiative.

References

[1] R. L. Klueh and D. R. Harries, High Chromium Ferritic and Martensitic Steels for Nuclear A.
[2] A. E. Rusanov, V. M. Troyanov, Yu. S. Belomytzev, A. A. Smirnov, G. A. Yachmenev, R. H. Gibadullin, V. N. Sugonyaev, and V. M. Pykhtin, Proceedings of the Conference on Heavy Metal Liquid Coolants in Nuclear Technology (October 5–9, 1998, Obninsk, Kaluga Region, Russia), Vol. 2, 1999, 633–639.
[3] Ring-Pull Test Standard 086-288-99, Dimitrovgrad, Russia, State Scientific Centre, Research Institute of Atomic Reactor, 1999 (in Russian).
[4] O. Yu. Makarov, V. I. Prokhorov, A. V. Goryachev, V. P. Smirnov, L. A. Egorova, E. P. Kaplar, and K. V. Lyutov, Proceedings of the 6th Russian Conference on Reactor Material Science (September 11-15, 2000, Dimitrovgrad), Vol. 2, Part 2, 2001, 209–220.
[5] A. G. Bespalov, S. I. Porollo, Yu. V. Konobeev, V. A. Rudenko, V. S. Khabarov, and S. V. Shulepin, Proceedings of the Conference on Heavy Metal Liquid Coolants in Nuclear Technology (October 5–9, 1998, Obninsk, Kaluga Region, Russia), Vol. 2, 1999, 640–647.
[6] S. I. Porollo, A. M. Dvoriashin, Yu. V. Konobeev, and F. A. Garner, J. Nucl. Mater. 329–333 (2004) 314–318.
[7] Y. Hosoi, N. Wade, T. Urita, M. Tanino, and H. Komatsu, J. Nucl. Mater. 133–134 (1984) 337–342.
[8] Y. Kohno, A. Kohyama, and D. S. Gelles, J. Nucl. Mater. 179–181 (1981) 725–727.

4.0 COPPER ALLOYS

5.0 REFRACTORY METALS AND ALLOYS

6.0 AUSTENITIC STAINLESS STEELS

INFLUENCE OF CARBON ADDITION ON NEUTRON-INDUCED VOID SWELLING OF Fe-15Cr-16Ni-0.25Ti MODEL ALLOY—N. Sekimura, T. Okita (University of Tokyo), and F. A. Garner (Pacific Northwest National Laboratory)[1]

OBJECTIVE

The objective of this effort is to determine experimentally those environmental and compositional variables that determine the radiation-induced evolution of microstructure, physical and mechanical properties, and the dimensional stability of austenitic steels.

SUMMARY

Addition of 0.05 wt% C to a model Fe-15Cr-16Ni-0.25Ti quaternary model alloy leads to a reduction in neutron-induced swelling at 430ºC. The transient regime of swelling is prolonged by carbon addition, most strongly at lower dpa rates. Contrary to the swelling behavior observed in carbon-free Fe-15Cr-16Ni and Fe-15Cr-16Ni-0.25Ti model alloys irradiated in the same experiment, Fe-15Cr-16Ti-0.25Ti-0.05C does not exhibit a strong dependence of swelling on dpa rate. It appears that carbon's role, while not yet well-defined, operates via a solute-based or TiC complex mechanism rather than by a precipitate-based mechanism. A model is proposed whereby carbon stabilizes loop microstructures against unfaulting, where unfaulting is known to be a prerequisite to formation of the glissile dislocation network needed to establish a high swelling rate. This stabilization is proposed to counteract the tendency of loop unfaulting to occur more strongly at low dpa rates.

PROGRESS AND STATUS

Introduction

In an earlier series of reports by Okita and coworkers it was shown that two simple, annealed austenitic model alloys, ternary Fe-15Cr-16Ni and quaternary Fe-15Cr-16Ni-0.25Ti, when irradiated in the Materials Open Test Assembly in the Fast Flux Test Facility (FFTF-MOTA) during irradiation Cycles 11 and 12 at ~430ºC exhibited a very strong influence of dpa rate on void swelling (1-3). While the eventual steady state swelling rate of ~1%/dpa was unaffected by dpa rate, the transient regime was strongly affected, with a progressive shortening of the transient duration as the dpa rate decreased, as shown in Fig. 1. At 430ºC the addition of titanium did not change the swelling significantly but there were relatively strong changes in the size distributions and densities of both Frank loops and voids. Boron additions to the ternary alloy also did not alter the total swelling significantly, but did the void density somewhat (4).

The counterintuitive dependence of swelling on dpa rate observed in these model alloys was shown to be mirrored in other published neutron experiments conducted on more complex commercial alloys (5-13). A similar dependence of swelling on dpa rate over a wider range of temperatures was also observed in ion irradiations studies conducted on the same ternary alloy used in the FFTF-MOTA study (14,15).

Okita and coworkers showed that the increased delay in swelling with increasing dpa rate arose primarily from the increased density of smaller Frank faulted loops that developed at higher dpa rates (1-3). The smaller loops and consequently denser loop ensembles formed at higher dpa rates appeared to be more resistant to unfaulting and subsequent formation of a glissle dislocation network, a condition thought to be critical to the development of a high swelling rate.

[1]Pacific Northwest National Laboratory (PNNL) is operated for the U.S. Department of Energy by Battelle Memorial Institute under contract DE-AC06-76RLO-1830.

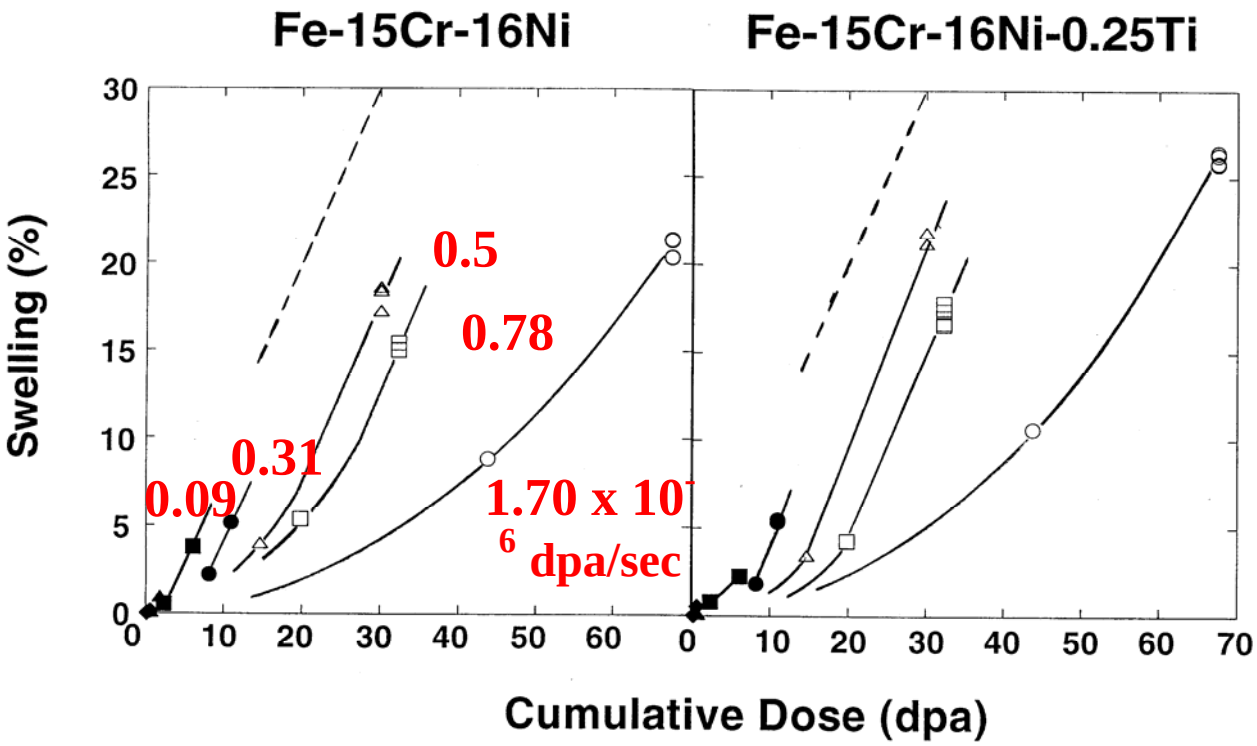

Fig. 1. Swelling of simple model f.c.c. Fe-Cr-Ni alloys in FFTF-MOTA at ~430ºC, as observed by Okita and coworkers (1), showing that the transient regime of swelling increases progressively as the dpa rate increases (1-3).

Also contained in the FFTF-MOTA experiment was Fe-15Cr-16Ti-0.25Ti-0.05C (wt %), also in the annealed condition and irradiated side-by-side with the ternary and quaternary alloys. Examination of the carbon-added alloy in the current study allows the possibility for investigation of possibly synergistic effects of two important variables, dpa rate and carbon level. This paper addresses the influence of carbon additions on the swelling of this alloy series as observed in specimens irradiated in FFTF Cycles 11 and 12.

Some indication of the complex and interactive microstructural consequences of carbon and titanium additions on void swelling in this alloy series was observed in earlier papers by Sekimura and coworkers that presented results from an irradiation series conducted in FFTF Cycle 10 and/or Cycle 11(16,17). Whereas this earlier Cycle 10 study focused on a range of irradiation temperatures, 430-600ºC, at only one dpa rate, the current study conducted in Cycles11-12 focused only on irradiation conducted only at ~430ºC.but at seven dpa rates.

Experimental Procedure

Relatively pure Fe-15Cr-16Ni, Fe-15Cr-16Ni-0.25Ti and Fe-15Cr-16Ni-0.25Ti-0.05C (wt %) with no added solute were prepared by arc melting from high purity Fe, Ni, Cr and Ti. The alloys were rolled to sheets of 0.25 mm thickness, cut into 3 mm diameter disks and then annealed for 30 minutes at 1050°C in high vacuum. The final compositions of the three alloys, as measured by the broad-beam EDS technique in a JOEL scanning electron microscope, are presented in Table 1.

Table 1. Composition in wt% of alloys as determined by broad-beam EDS analysis

Alloy	C	Ti	Si	Mn	P	S	Cr	Ni	Fe
Fe-15Cr-16Ni	0.012	---	0.004	0.003	----	0.01	16.03	15.01	bal
Fe-15Cr-16Ni-0.25Ti	0.017	0.28	---	0.01	---	0.0	16.04	15.46	bal.
Fe-15Cr-16Ni-0.25TI-0.05C	0.052	0.27	---	---	---	---	16.00	15.48	bal

Sets of identical specimen groups were placed in sealed, helium-filled packets at each of seven different axial positions of the Materials Open Test Assembly (MOTA), ranging from below the core to above the core of the Fast Flux Test Facility (FFTF). The packets each contained four identical side-by-side specimens of each of the three alloys. The three alloys were located side-by-side in the same packet, with the total of twelve specimens occupying only 3.0 mm axial height. Two or more identically-loaded packets were placed in each MOTA capsule, with the dpa rate of each capsule dependent on its axial location in MOTA.

With the exception of the below-core capsule, the temperatures in MOTA capsules were actively controlled to ±5°C of the nominal target, although the nominal target temperatures varied a little from capsule to capsule.

The first irradiation sequence proceeded in Cycle 11 of MOTA-2A for 2.59×10^7 sec, and a subset of specimen packets was then removed. The other packets continued in Cycle 12 of MOTA-2B for another 1.71×10^7 sec. The dpa rates in the various capsules ranged from 8.9×10^{-9} to 1.7×10^{-6} dpa/sec. The dpa levels attained by the specimens varied from 0.23 to 43.8 dpa in Cycle 11 and an additional 0.24 to 24.0 dpa in Cycle 12. Table 2 summarizes the irradiation conditions for the fourteen combinations of temperature, dpa and dpa rate.

The starting and post-irradiation densities were measured using an immersion density technique known to be accurate to ±0.2 % change in density. In some cases it was not possible to clearly identify and retrieve all four specimens, but in general there were at least two identical specimens measured from each capsule. Determination of microstructural evolution in the specimens using a transmission electron microscope has been completed for the ternary and quaternary alloys (1-3), but has not been fully completed for the carbon-doped alloy from Cycle 12. Both the recently measured density change data and the earlier microscopy data are presented in Fig. 2.

Results

Figure 2 presents some limited microscopy of the three model alloys at the two highest dpa levels attained in this experiment. Although Ti addition to the ternary alloy does not significantly change the overall swelling, it does significantly coarsen the void ensemble. Addition of carbon to the quaternary alloy clearly reduces the swelling, however, leading to a lower mean void size in particular. These micrographs illustrate that electron microscopy is not suitable for accurate swelling determinations at such high swelling values with high levels of void intersection with the foil surface. The use of density change measurements to determine the swelling is necessary for accurate swelling values in excess of 5-10%.

It is considered to be particularly important that no significant precipitation was observed by microscopy as a result of carbon addition at these high swelling levels, implying that most of the carbon was retained in solution or existed as sub-visible clusters of TiC.

There are a number of major results observed in the swelling behavior when carbon was added to the quaternary alloy. First, the maximum swelling at the highest dose level and 430ºC is reduced from ~26%

Table 2. Irradiation conditions in FFTF Cycles 11 and 12 (MOTA-2A and MOTA-2B). Note that in three of the seven cases the specimens irradiated in both cycles did not experience conditions completely identical with those of single cycle packages.

Dose Rate, dpa/sec		Dose, dpa		Temperature, C		Symbols
# 11	#12	#11	#11 & #12	#11	#11 & #12	
1.7 x 10^{-6}	1.4 x 10^{-6}	43.8	67.8	427	408	▼
7.8 x 10^{-7} *1	9.5 x 10^{-7}	20.0 *1	32.4	390	387	▲
5.4 x 10^{-7}	8.4 x 10^{-7}	14.0	28.8	430	424	◆
8.2 x 10^{-7}	-----	21.1	-----	430	-----	■
3.2 x 10^{-7} *2	3.5 x 10^{-7}	8.22 *2	13.1	373	373	●
3.1 x 10^{-7} *3	3.0 x 10^{-7}	8.05 *3	11.1	411	410	▷
1.5 x 10^{-7}	1.3 x 10^{-7}	3.87	6.12	430	431	◁
9.1 x 10^{-8}	2.1 x 10^{-7}	2.36	6.36	430	431	▽
4.6 x 10^{-8}	4.2 x 10^{-8}	1.18	1.91	434	437	△
2.7 x 10^{-8}	6.6 x 10^{-8}	0.71	1.87	434	437	◇
1.4 x 10^{-8}	1.4 x 10^{-8}	0.37	0.61	436	444	□
8.9 x 10^{-9}	2.2 x 10^{-8}	0.23	0.61	436	444	○

Note: The swelling data of the underlined irradiation conditions come from TEM observation, while the others are density measurements.

*1: 6.0 x 10^{-7} dpa/sec and 15.6 dpa for #11 in 2 Cycle irradiation specimens
*2: 2.7 x 10^{-7} dpa/sec and 6.90 dpa for #11 in 2 Cycle irradiation specimens
*3: 2.2 x 10^{-7} dpa/sec and 5.69 dpa for #11 in 2 Cycle irradiation specimens

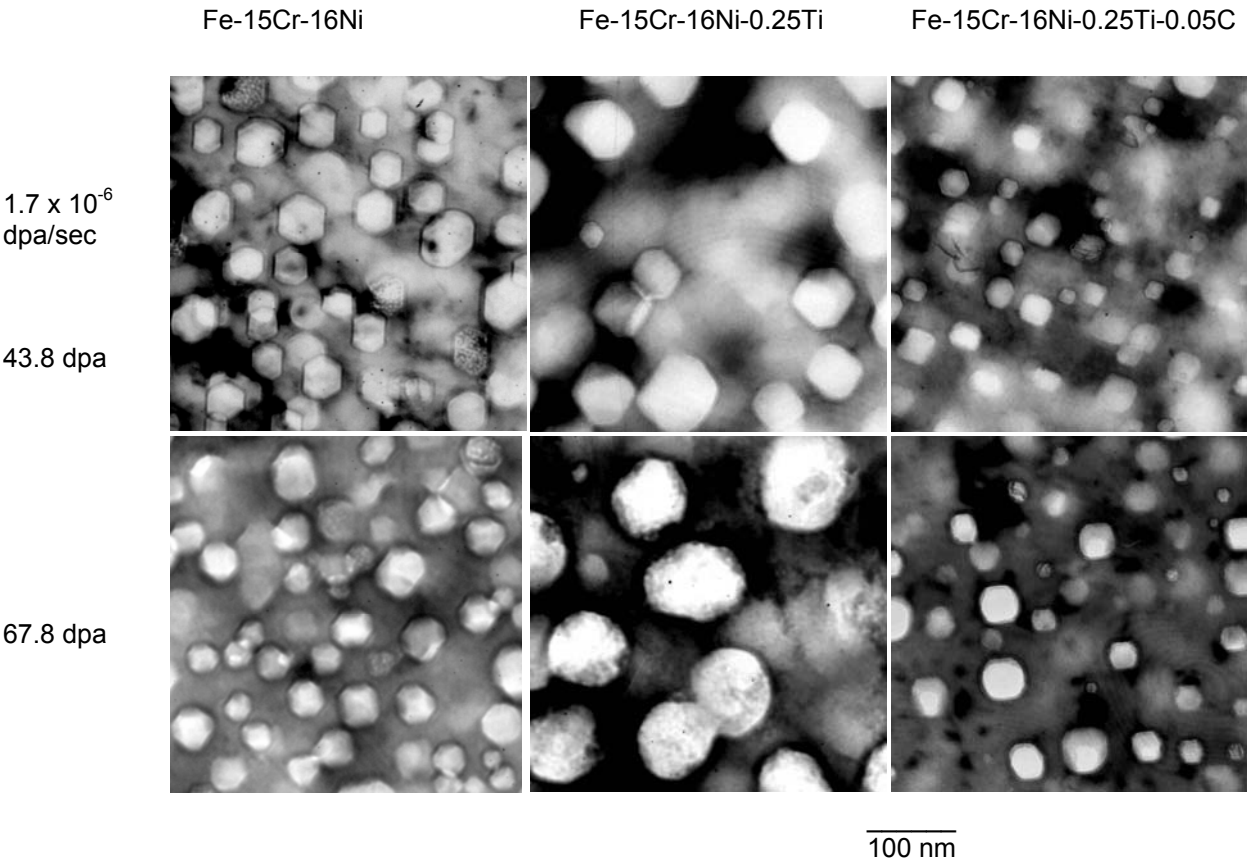

Fig. 2. Void microstructures observed in the three model alloys irradiated in this experiment at ~430ºC for the two highest dpa rates.

to ~15%, as shown in Fig. 3. Second, the trends of microscopy determinations of swelling agree reasonably well with values and trends of density determinations. Third, and most importantly, the swelling of the carbon-added alloy at ~430ºC appears to show no obvious influence of the dpa rate whereas the swelling behavior of the carbon-free ternary and quaternary alloys shown in Fig. 1 exhibits a very pronounced dependence on dpa rate. Finally, it is particularly noteworthy that the carbon-added alloy never reached the terminal swelling rate of ~1%/dpa observed in the carbon-free alloys at most lower dpa rates. The swelling rate was still increasing at the end of the experiment, never exceeding ~0.3%/dpa. This implies that the transient regime is still in progress.

As was observed earlier in the simple ternary and quaternary alloys, the range of swelling between identical specimens irradiated side-by-side is relatively small, especially at higher dpa exposures, indicating the overall reproducibility of the swelling phenomenon. However, when the data at lower dpa and dpa rates are examined more closely, a somewhat larger amount of scatter is observed in the swelling values, with some measurements indicating that a net densification may have occurred.

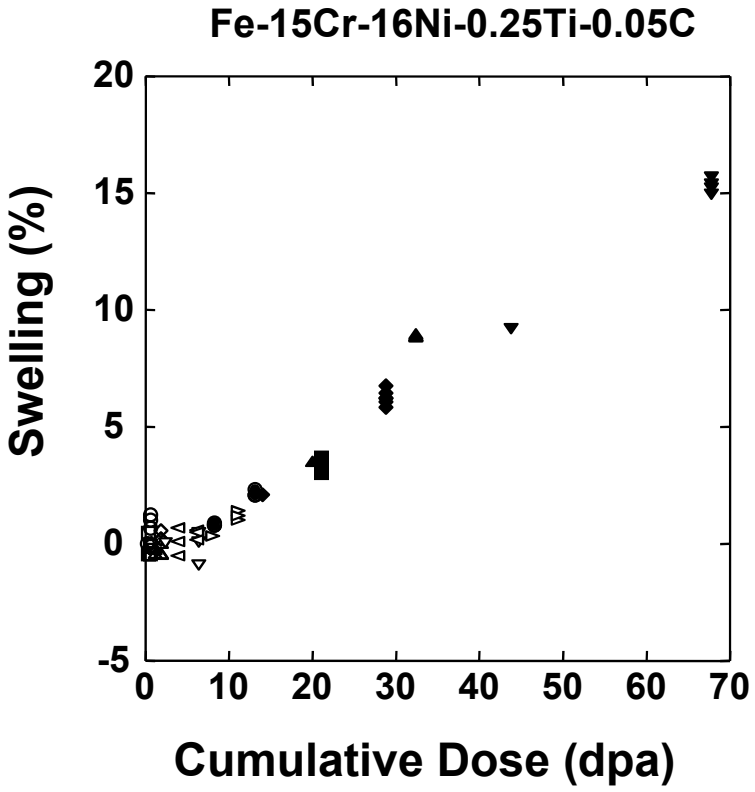

Fig. 3. Swelling of simple model f.c.c. Fe-15Cr-16Ni-0.25Ti-0.05 irradiated in FFTF-MOTA Cycles 11 and 12 at ~430ºC, showing that the swelling is relatively independent of dpa rate. There were two to four identical specimens for each irradiation condition. See Table 2 for symbol identification of dpa rates and reactor cycles for each data point.

Discussion

A minor complication of this experiment was the fact that while the target capsule temperatures were maintained within ±5ºC they varied somewhat (373-444ºC) from capsule to capsule as shown in Table 2. In earlier papers on the carbon-free alloys Okita and coworkers addressed the possibility that variations in capsule target temperatures might obscure or overwhelm the effect of differences in dpa rate (2). However, it was easy to group the various data sets into groups such that two or more capsules operated at nearly identical temperatures but at greatly different dpa rates. In each group the strong effect of dpa rate was obvious and overwhelmed any effect of temperature differences.

There are five major features of these results. First, carbon addition clearly delays somewhat the onset of swelling in Fe-15Cr-16Ni-0.25Ti at ~430ºC. Second, carbon addition suppresses the early termination of the transient regime, especially at lower dpa rates where the carbon-free alloys exhibited very short durations of the transient. Third, the carbon-induced suppression looks to be less effective at higher dpa rates. Fourth, the addition of carbon introduces more specimen-to-specimen scatter than observed in the carbon-free alloys at low dpa and dpa rates. Finally, there does not appear to be any significant precipitation of titanium carbides, at least in the higher dose and dose rate specimens.

The latter observation was confirmed at comparably high dpa rates in the results of the earlier Cycle 10 and/or Cycle 11 study of Sekimura and Ishino (16,17). They showed that TiC precipitates were only occasionally present after irradiation at ~430ºC but were not a dominant feature of the microstructure in carbon-bearing specimens. Therefore, a direct precipitate role in the swelling behavior can not be invoked and we must assume that a large fraction of the carbon must still have been in solution or existed in sub-visible TiC clusters, at least at the higher dpa rates.

Based on the current results alone, however, it can not be assumed that precipitation did not occur at the lower dpa rates, since no microscopy was performed at the lower dpa conditions. Kawanishi and Ishino, however, conducted similar irradiations on Fe-15Cr-16Ni-0.3Ti-0.06C alloys at lower doses and dpa rates in the JOYO fast reactor at ~400ºC (18,19). They showed that carbon additions led to a longer transient regime of swelling and that visible TiC carbide precipitates were not formed during irradiation.

Microstructural observations of the carbon-free alloys irradiated in both Cycle 11 and Cycle 12 specimens showed that the flux sensitivity of the transient regime arose primarily from the flux sensitivity of Frank loop evolution (1-3). Higher dpa rates produced higher densities of smaller loops which were more resistant to unfaulting and network formation, thereby delaying the development of a dislocation network. Attainment of a glissile dislocation network was found to be coincident with the termination of the transient regime in these carbon-free alloys (1-3).

In the Sekimura and Ishino studies the loop microstructure could not be accurately assessed because an off-normal shutdown and cool-down sequence occurred in Cycle 10 and resulted in addition of a dense population of small Frank loops in all alloys studied (16,17).

Kawanishi and Ishino, however, showed that the addition of carbon and titanium significantly altered the faulted loop morphology, producing highly irregular-shaped or “crenulated” loops. Carbon addition also changed the loop distribution such that their interaction and unfaulting was delayed (18,19). Kawanishi and Ishino also noted that TiC complexes form easily and act to retard loop unfaulting.

Garner and Gelles demonstrated that sub-visible precipitates or complexes encountered by growing loops in carbon-containing alloys create the irregular boundaries characteristic of “crenulated” loops. They also demonstrated that the irregular periphery of such loops indeed changes the growth rate and stability of individual loops and loop ensembles (20).

While the above arguments appear to be plausible at 430ºC over the investigated rates of dpa rates, the swelling behavior observed in Cycle 10 by Sekimura and Ishino (Fig. 4) indicates that carbon also suppresses swelling at higher temperatures, even though the effect of titanium on swelling becomes stronger with increasing temperature (16,17). Remember that these specimens were identical to those of the current experiment. Note that in agreement with the current study the influence of Ti addition was very small at ~430ºC, but increased at higher temperatures.

Garner compiled a summary of data examining the effect of carbon on swelling of commercial austenitic stainless steels (21). At temperatures near 430ºC the effect of carbon is usually to delay or reduce swelling, but at higher temperatures the effect is reversed to produce increased swelling. This latter behavior is not observed in the simple model alloys shown in Figs. 3 and 4. In commercial alloys the presence of other solutes leads to significant precipitation of carbides and intermetallic phases at higher temperatures, while such precipitation can not occur in the model alloys.

Redistribution of carbon during irradiation frequently produces a small net densification in irradiated stainless steels (21). It appears in this study that densification occurs during irradiation in this experiment but densification does not require discrete precipitates to form. Associated with this densification appears to be a somewhat larger amount of data scatter in identical specimens than observed in carbon-free alloys.

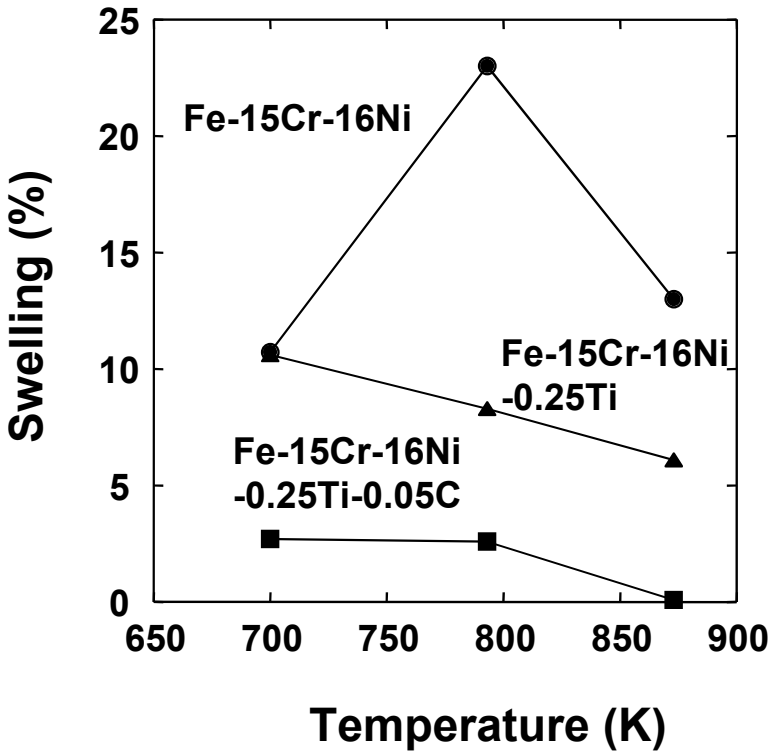

Fig. 4. Cavity volume fraction determined by Sekimura and Ishino using microscopy of three simple austenitic alloys after irradiation in FFTF-MOTA-2A at three different temperatures. In the first publication the dpa level was estimated to be ~36 dpa, but the reported doses in the second reference were reevaluated to be ~43 dpa at all three temperatures (16,17).

Conclusions

The addition of 0.05% carbon to Fe-15Cr-16Ni-0.25Ti leads to a reduction of neutron-induced swelling at ~430ºC, with the reduction being largest when the irradiation is conducted at relatively low dpa rates. Another consequence of carbon addition is that the strong influence of the dpa rate observed in the carbon-free alloy completely disappears in the carbon-doped alloy.

Earlier discussions of the effect of dpa rate to determine the onset of swelling at high rate focused on the effect of dpa rate to influence the development of a glissile dislocation microstructure by stabilizing or destabilizing Frank loop ensembles against unfaulting.
Carbon appears to stabilize loop microstructures against unfaulting, thereby possibly counteracting the tendency of loop unfaulting to occur strongest at lower dpa rates. It is speculated that perhaps this mechanism accounts for the disappearance of the dose rate effect in carbon-bearing alloys.

It appears that carbon's role, while not yet well-defined, operates via a solute-based or TiC complex mechanism rather than by a precipitate-based mechanism.

Acknowledgements

This work was supported by Monbusho, the Japanese Ministry of Education, Science and Culture under the FFTF-MOTA collaboration and the JUPITER program (Japan-USA Program for Irradiation Testing for Fusion Research), and the U.S. Department of Energy, Office of Fusion Energy, under Contract DE-AC06-76RLO 1830 at Pacific Northwest National Laboratory.

References

[1] T. Okita, N. Sekimura, F. A. Garner, L. R. Greenwood, W. G. Wolfer, and Y. Isobe, Proceedings of the 10th International Conference on Environmental Degradation of Materials in Nuclear Power Systems –Water Reactors, 2001, issued on CD format, no page numbers. NACE International, E. P. Ford, G. Was, and J. L. Nelson (eds.). Also in Fusion Materials Semiannual Progress Report for Period Ending June 30, 2001, Vol. 30, 148–164.
[2] T. Okita, N. Sekimura, T. Sato, F. A. Garner, and L. R. Greenwood, J. Nucl. Mater. 307–311 (2002) 322–326.
[3] T. Okita, W. G. Wolfer, F. A. Garner, and N. Sekimura, Philos. Mag. 85(18) (2005) 2033–2048.
[4] T. Okita, W. G. Wolfer, F. A. Garner, and N. Sekimura, J. Nucl. Mater. 329–333 (2004) 1013–1016.
[5] J. L. Seran and J. M. Dupouy, Effects of Radiation on Materials, 11th International Symposium, ASTM-STP 782, H. R. Brager and J. S. Perrin (eds.), American Society for Testing and Materials, 1982, 5–16.
[6] J. L. Seran and J. M. Dupouy, Proceedings of the Conference on Dimensional Stability and Mechanical Behavior of Irradiated Metals and Alloys, Vol. 1, BNES, 1983, 25–28.
[7] G. M. Bond, B. H. Sencer, F. A. Garner, M. L. Hamilton, T. R. Allen, and D. L. Porter, Proceedings of the 9th International Conference on Environmental Degradation of Materials in Nuclear Power Systems–Water Reactors, 1999, 1045–1050.
[8] F. A. Garner, N. I. Budylkin, Yu. V. Konobeev, S. I. Porollo, V. S. Neustroev, V. K. Shamardin, and A. V. Kozlov, Proceedings of the 10th International Conference on Environmental Degradation of Materials in Nuclear Power Systems–Water Reactors, 2003, 647–656.
[9] F. A. Garner and M. B. Toloczko, J. Nucl. Mater. 251 (1997) 252–261.
[10] V. S. Neustroev, V. K. Shamardin, Z. E. Ostrovsky, A. M. Pecherin, and F. A. Garner, Effects of Radiation on Materials, 19th International Symposium, ASTM-STP 1366, M. L. Hamilton, A. S. Kumar, S. T. Rosinski, and M. L. Grossbeck (eds.), American Society for Testing and Materials, 2000, 792–800.
[11] O. P. Maksimkin, K. V. Tsai, L. G. Turubarova, T. Doronina, and F. A. Garner, J. Nucl. Mater. 329–333 (2004) 625–629.
[12] O. P. Maksimkin, K. V. Tsai, L. G. Turubarova, T. A. Doronina, and F. A. Garner, accepted by Journal of Nuclear Materials (Proceedings of ICFRM-12).
[13] F. A. Garner and B. J. Makenas, Paper A302-PV1 in Proceedings of Fontevraud 6 International Symposium on Contributions to Materials Investigations to Improve the Safety and Performance of LWRs, SFEN French Nuclear Energy Society, 2006.
[14] T. Okita, N. Sekimura, T. Iwai, and F. A. Garner, Proceedings of the 10th International Conference on Environmental Degradation of Materials in Nuclear Power Systems–Water Reactors, 2001, issued on CD format, no page numbers. NACE International, E. P. Ford, G. Was, and J. L. Nelson (eds.).
[15] T. Okita T. Sato, N. Sekimura, T. Iwai, and F. A. Garner, accepted by Journal of Nuclear Materials (Proceedings of ICFRM-12).
[16] N. Sekimura and S. Ishino, J. Nucl. Mater. 179–181 (1991) 542–545.
[17] N. Sekimura, K. Hamada, and S. Ishino, Effects of Radiation on Materials: 16th International Symposium, ASTM STP 1175, A. S. Kumar, D. S. Gelles, R. K. Nanstad, and E. A. Little (eds.), American Society for Testing and Materials, 1994, 992–1000.
[18] H. Kawanishi and S. Ishino, J. Nucl. Mater. 155–187 (1988) 806–809.
[19] H. Kawanishi and S. Ishino, J. Nucl. Mater. (1991) 534–537.
[20] F. A. Garner and D. S. Gelles, J. Nucl. Mater. (1988) 286–309.
[21] F. A. Garner, Chapter 6: Irradiation Performance of Cladding and Structural Steels in Liquid Metal Reactors, Vol. 10A of Materials Science and Technology: A Comprehensive Treatment, VCH Publishers, 1994, 419–543.

THE SYNERGISTIC INFLUENCE OF TEMPERATURE AND DISPLACEMENT RATE ON MICROSTRUCTURAL EVOLUTION OF ION-IRRADIATED Fe-15Cr-16Ni MODEL AUSTENITIC ALLOY—T. Okita, T. Sato, N. Sekimura (Department of Quantum Engineering and Systems Science, University of Tokyo, Japan), T. Iwai (Research Center for Nuclear Science and Technology, University of Tokyo, Japan), and F. A. Garner (Pacific Northwest National Laboratory)[1]

OBJECTIVE

The object of this effort is to determine the influence of atomic displacement rate on the swelling of austenitic stainless steels.

SUMMARY

An experimental investigation of microstructural evolution has been conducted on Fe-15Cr-16Ni irradiated with 4.0 MeV nickel ions. Irradiations proceeded to dpa levels ranging from ~0.2 to ~17 dpa at temperatures of 300, 400, 500 and 600°C at displacement rates of 1 x 10^{-4}, 4 x 10^{-4} and 1 x 10^{-3} dpa/sec. The swelling was found to monotonically increase with decreases in dpa rate at every irradiation condition studied.

The earliest and most sensitive component of microstructure to both temperature and especially displacement rate was found to be the Frank loops. The second most sensitive component was found to be the void microstructure, which co-evolves with the loop and dislocation microstructure.

PROGRESS AND STATUS

Introduction

The experiment described in this paper is one of two companion experiments using identical specimens directed toward the study of the dependence of void swelling on displacement rate. The other experiment proceeded at seven different neutron-induced dpa rates between 8.9 x 10^{-9} to 1.7 x 10^{-6} dpa/sec in FFTF-MOTA at ~400°C [1, 2]. In that experiment, the swelling of Fe-15Cr-16Ni was found to monotonically increase with decreases in dpa rate at every irradiation condition studied. The experiment described in this paper focused on the same model alloy using ion irradiation at four different temperatures and three different displacement rates between 1 x 10^{-4} and 1 x 10^{-3} dpa/sec.

Experimental Procedure

The model austenitic alloy, ternary Fe-15Cr-16Ni, was prepared by arc melting from very pure Fe, Ni and Cr. The alloy was rolled to sheets of 0.2 mm thickness. Afterward, standard 3 mm microscopy disks were then punched and annealed for 30 minutes at 1050°C in a very high vacuum. The chemical composition of the alloy in wt% is Fe-15.01Cr-16.00Ni-0.012C-0.0008Si-0.0007Mn-0.0007P-0.007S and <0.0007Mo.

Irradiation proceeded with 4.0 MeV Ni^{3+} ions in the High Fluence Irradiation Facility (HIT) operated by the University of Tokyo and located at Tokai-Mura, Japan. No gas atoms were preinjected or simultaneously injected. Two or three specimens were observed at every irradiation condition.

The four irradiation temperatures and three dpa rates chosen are listed in Table 1. Note that the trend with respect to dpa rate was established only at the lower two dpa levels. For the highest dpa level, 16-18 dpa, irradiation proceeded only at 4 x 10^{-4} dpa/sec.

---

[1]Pacific Northwest National Laboratory (PNNL) is operated for the U.S. Department of Energy by Battelle Memorial Institute under contract DE-AC06-76RLO-1830.

Table 1. Irradiation conditions and microstructural data of Fe-15Cr-16Ni

Temperature (C)	dpa*	dpa/sec*	Dislocation loop density (m^{-3})	Cavity density (m^{-3})	Swelling (%)
300	0.17	1.0×10^{-4}	4.93×10^{22}	5.75×10^{21}	0.0060
		4.0×10^{-4}	4.51×10^{22}	5.40×10^{21}	0.0053
		1.0×10^{-3}	4.12×10^{22}	4.12×10^{21}	0.0045
	1.6	1.0×10^{-4}	9.89×10^{22}	5.19×10^{22}	0.038
		4.0×10^{-4}	8.32×10^{22}	4.52×10^{22}	0.032
		1.0×10^{-3}	7.40×10^{22}	4.42×10^{22}	0.020
	18.0	4.0×10^{-4}	1.01×10^{23}	5.23×10^{22}	0.042
400	0.18	1.0×10^{-4}	1.44×10^{22}	1.02×10^{21}	0.0071
		4.0×10^{-4}	1.10×10^{22}	8.90×10^{20}	0.0055
		1.0×10^{-3}	9.23×10^{21}	7.25×10^{20}	0.0048
	1.3	1.0×10^{-4}	6.10×10^{22}	5.92×10^{21}	0.054
		4.0×10^{-4}	5.20×10^{22}	5.76×10^{21}	0.037
		1.0×10^{-3}	2.18×10^{22}	4.55×10^{21}	0.022
	16.2	4.0×10^{-4}	8.90×10^{22}	9.90×10^{21}	0.054
500	0.17	1.0×10^{-4}	2.94×10^{21}	3.95×10^{21}	0.030
		4.0×10^{-4}	2.59×10^{21}	3.07×10^{21}	0.019
		1.0×10^{-3}	2.06×10^{21}	2.24×10^{21}	0.011
	1.7	1.0×10^{-4}	2.09×10^{22}	4.08×10^{21}	0.55
		4.0×10^{-4}	1.56×10^{22}	3.49×10^{21}	0.35
		1.0×10^{-3}	1.07×10^{22}	2.92×10^{21}	0.17
	16.4	4.0×10^{-4}	1.14×10^{22}	3.18×10^{21}	1.23
600	0.16	1.0×10^{-4}	6.76×10^{20}	1.92×10^{21}	0.015
		4.0×10^{-4}	6.08×10^{20}	1.62×10^{21}	0.018
		1.0×10^{-3}	7.21×10^{20}	1.23×10^{21}	0.0095
	1.5	1.0×10^{-4}	5.01×10^{20}	2.42×10^{21}	0.20
		4.0×10^{-4}	8.53×10^{20}	2.09×10^{21}	0.072
		1.0×10^{-3}	7.49×10^{20}	1.97×10^{21}	0.061
	17.0	4.0×10^{-4}	8.98×10^{20}	1.93×10^{21}	1.27

*Dpa rates and dpa levels are defined at the depth at which microscopy was performed.

The damage vs. depth profile was calculated using the TRIM code [3] and is shown in Fig. 1. After irradiation the specimens were electrochemically thinned to reach a depth of 600 to 700 nm. This depth was chosen to avoid a strong influence of the "injected interstitial" effect [4, 5] and the implanted nickel and also to minimize the influence of the specimen surface. The uncertainty in depth was 10% at most, yielding a dpa and dpa rate uncertainty of ~10%, much smaller than the differences in the three dpa rates employed. Analysis of the loop microstructure by the dark field weak-beam method was conducted using a JEOL 200CX electron microscope operating at 200 KeV.

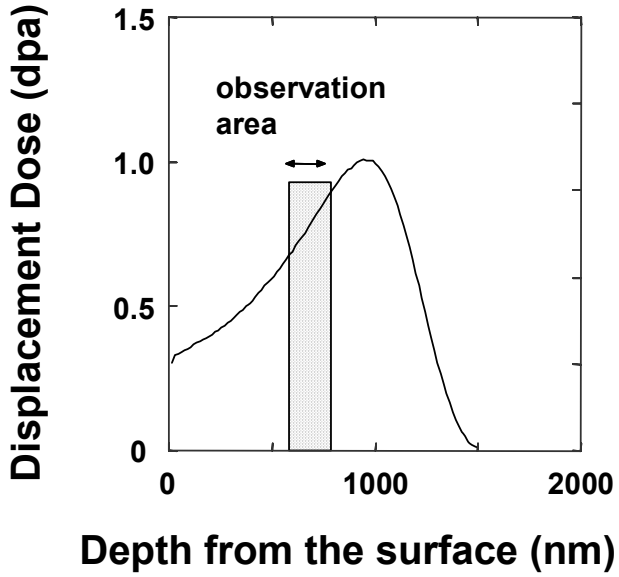

Fig. 1. Depth distribution of ion-induced damage as calculated by the TRIM code, showing a nominal 1.0 dpa maximum with the range of depths chosen for observation by microscopy.

Results

In general, the radiation-induced microstructures were dense, especially at the lower temperatures, but rather simple, being comprised primarily of Frank interstitial loops, some unfaulted perfect loops, some network dislocations, and faceted voids. The density and diameter of the cavities and loops observed in the experiments are summarized in Table 1.

As shown in Fig. 2 the swelling of Fe-15Cr-16Ni increases as the atomic displacement rate is lowered at all three irradiation temperatures studied. While swelling appears to increase with increasing temperature, it is significant to note that swelling occurs at 300°C, a temperature normally thought to preclude swelling in austenitic stainless steels.

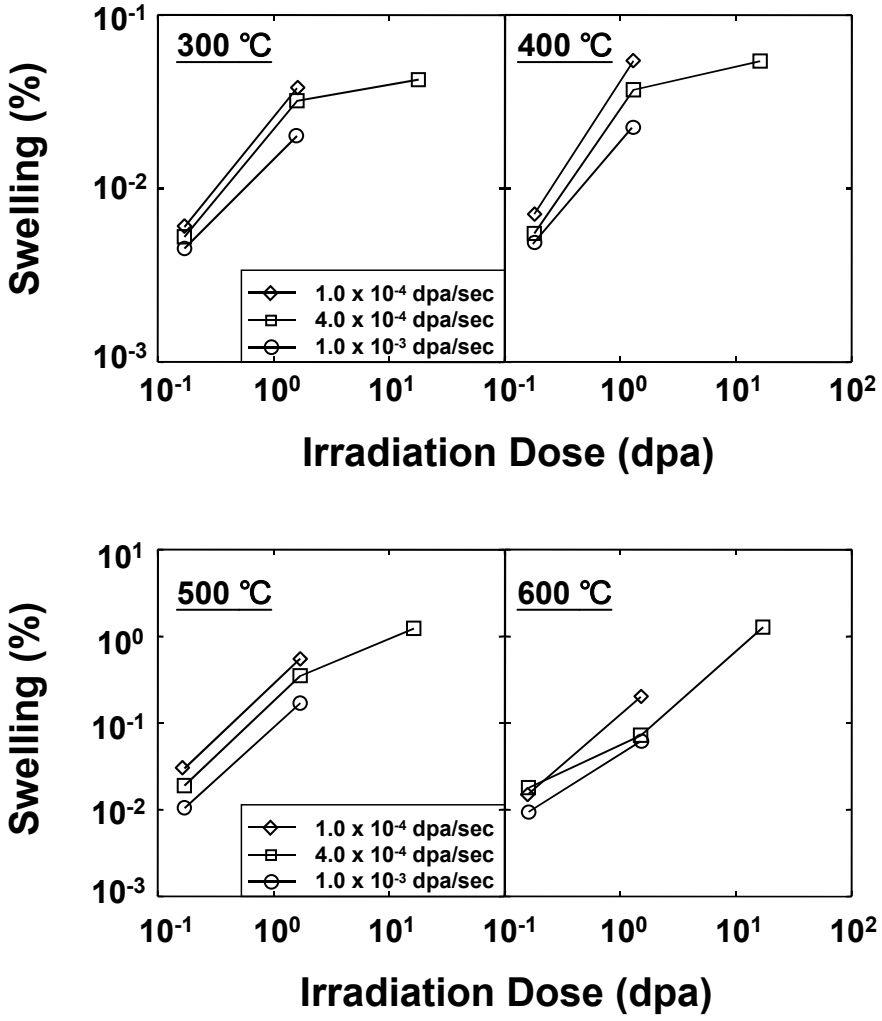

Fig. 2. Dependence of ion-induced swelling of annealed Fe-15Cr-16Ni on temperature, dpa and dpa rate.

Figure 3 shows that the cavity density increased somewhat as the dpa rate decreases, although the cavity density also increases as the irradiation temperature falls. At a given dpa level the Frank loop density also increased with decreasing temperature and decreasing dpa rate, as shown in Fig. 4.

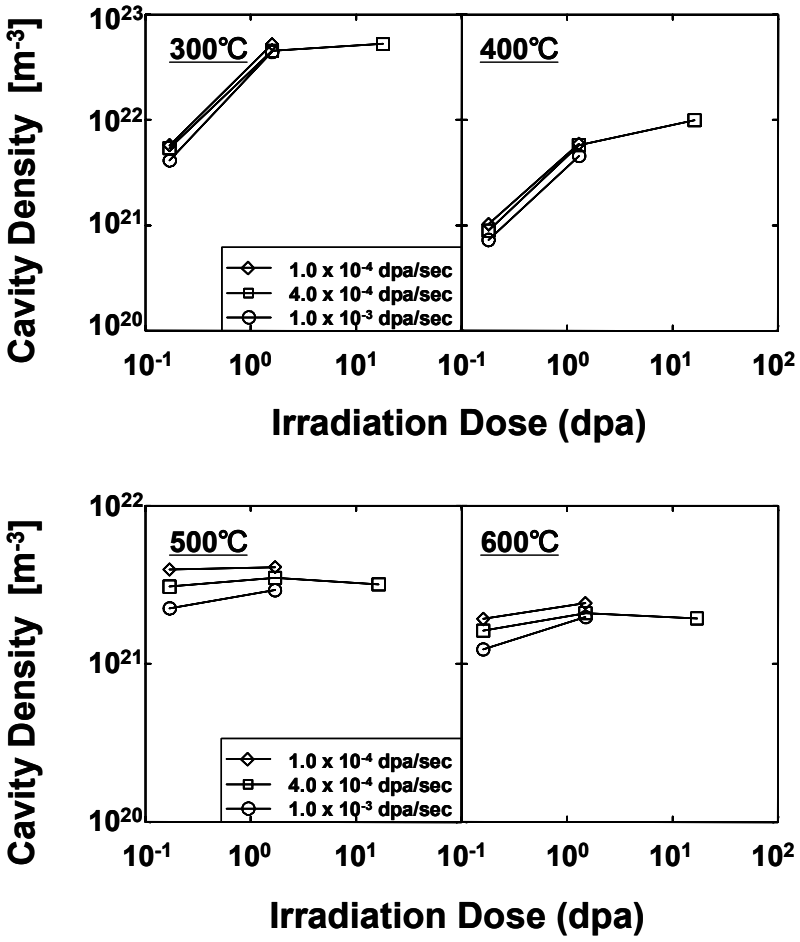

Fig. 3. Dependence of cavity density of annealed Fe-15Cr-16Ni on temperature, dpa and dpa rate.

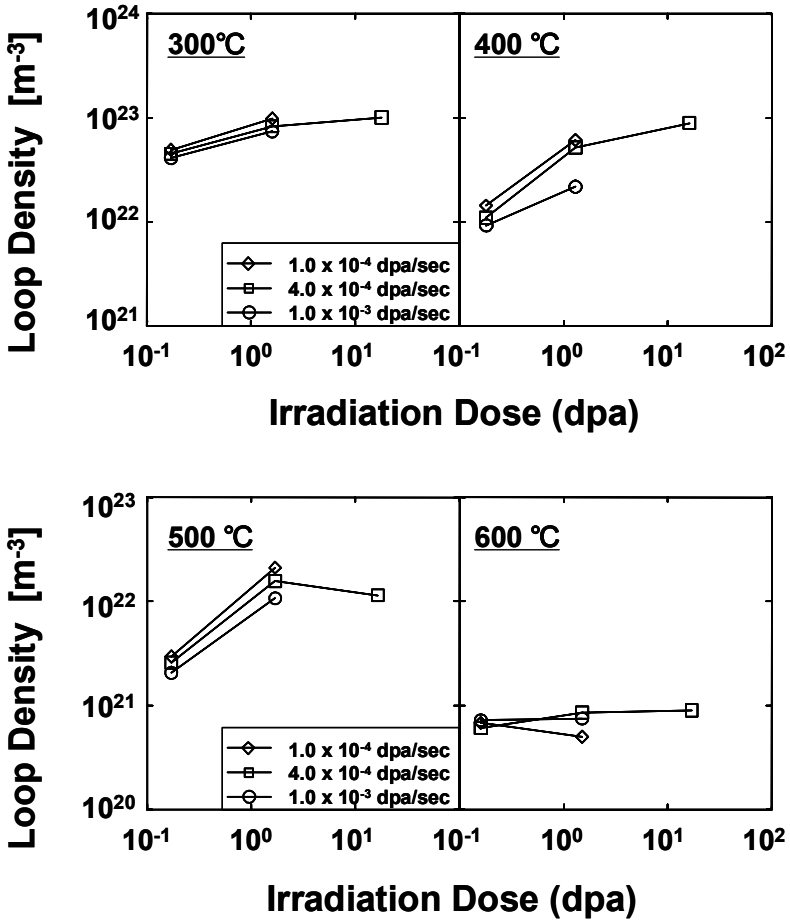

Fig. 4. Dependence of loop density of annealed Fe-15Cr-16Ni on temperature, dpa and dpa rate.

Discussion

The most significant observation from this study is that swelling can occur at temperatures as low as 300°C, even in the absence of injected gases. This result agrees with the results of recent studies on various commercial stainless steels [6-11]. The second important observation is that void swelling was accelerated at lower dpa rates at every temperature studied, and in a manner similar to that of the companion irradiation study using fast neutrons at ~400ºC [1, 2].

When comparing the results of the ion and neutron studies at 400ºC, it is apparent that the level of swelling obtained at a given dpa level at the very high ion-induced dpa rates is less than that obtained at lower neutron-induced dpa rates, suggesting that dpa rate effects operate regardless of bombarding particle. It must also be recognized, however, that ion-induced swelling tends to be additionally retarded by the combined influence of the surface and the injected interstitial, even when steps are taken to minimize these influences.

The swelling levels attained in this ion experiment have not yet reached sufficiently high levels where it can be determined if changes in dpa rate are expressed primarily in the duration of the transient regime of swelling, as clearly observed in the neutron experiment. However, the ion experiments allow us the opportunity to test the conclusion of the neutron study concerning the origin of the transient shift. In the

neutron study, it appeared that the primary flux sensitivity was expressed in the evolution of the Frank loop population and its subsequent unfaulting. At all the neutron-induced dpa rates studied, however, most of the loops had already unfaulted and network formation was well in progress at even the lowest dpa levels studied. In the ion experiment, however, the specimens at the lowest dpa levels still retained most of the Frank loops and a glissile dislocation microstructure was not available to terminate the transient regime.

The loop population at the two lower ion doses decreased with increasing temperature. As shown in Fig. 5, at 16.2 dpa and 400ºC the loop density at 4.0 x 10^{-4} dpa/sec has almost reached saturation at a level consistent with (dpa rate)$^{0.5}$ extrapolation of the ~400ºC neutron data and the models of Watanabe et al. [12] and Muroga and co-workers [13]. At 1.0 x 10^{-4} dpa/sec saturation consistent with this model was reached by ~1 dpa, however, indicating that the saturation dose increases with increasing dpa rate. As the saturated loop density increases with increasing dpa rate, the size of the loops decreases.

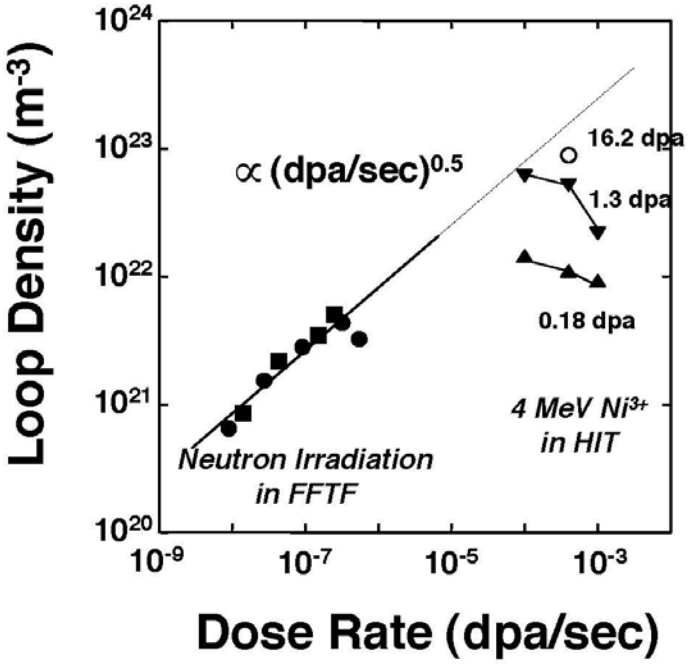

Fig. 5. Dependence of loop density on dpa rate to the 1/2 power, as observed at 400ºC in this experiment and in the companion FFTF experiment. Note that the ion-induced loop density moves toward the trend line of the neutron data with increasing dpa, indicating that saturation of ion-induced loops requires relatively large dpa levels. The dose at which saturation occurs, however, increases with increasing dpa rate.

When the results of the two companion studies are combined, it appears that the earliest and most sensitive components of microstructure to both temperature and, especially, displacement rate are the Frank loops, whose rate of unfaulting appears to be dependent on size and determines when the glissile dislocation network starts to evolve. The second most sensitive component was found to be the void microstructure, which co-evolves with the loop and dislocation microstructure. It should be noted, however, that loop-dominated microstructures can still allow void formation, but that the growth rate of these voids is restrained until a glissile dislocation microstructure develops. Based primarily on various neutron and some earlier ion experiments, the flux dependence is manifested primarily in the duration of the transient regime of swelling and not in the steady-state swelling rate.

There are several consequences to these findings. First, most high exposure data are generated in high-flux reactors such as FFTF, guaranteeing that swelling predictions based on these data will significantly

under-predict swelling in lower-flux devices or lower-flux positions. Second, the use of ion bombardment studies conducted at greater than reactor-typical dpa rates will further under-predict swelling under reactor-relevant conditions.

Conclusions

Over the range of 300-600ºC, the ion-induced void swelling of model Fe-15Cr-16Ni increases as the dpa rate decreases, in agreement with the results of a companion neutron irradiation study on this alloy at ~400ºC. This observation is consistent with a growing body of evidence that void swelling of commercial austenitic alloys increases strongly at lower dpa rates, primarily by earlier unfaulting of larger Frank loops produced at lower density.

Acknowledgements

This work was supported by Monbusho, the Japanese Ministry of Education, Science and Culture under the FFTF-MOTA collaboration and the JUPITER program (Japan-USA Program for Irradiation Testing for Fusion Research), and the US department of Energy, Office of Fusion Energy under Contract DE-AC06-76RLO 1830 at Pacific Northwest National Laboratory.

References

[1] T. Okita, N. Sekimura, F. A. Garner, L. R. Greenwood, W. G. Wolfer, and Y. Isobe, Proceedings of the 10th International Conference on Environmental Degradation of Materials in Nuclear Power Systems —Water Reactors, 2001, NACE International, issued on CD format.
[2] T. Okita, N. Sekimura, T. Sato, F. A. Garner, and L. R. Greenwood, J. Nucl. Mater. 307–311 (2002) 322–326.
[3] J. P. Biersack and L. G. Haggmark, Nucl. Instrum. Methods 174 (1980) 257.
[4] F. A. Garner, J. Nucl. Mater. 117 (1983) 177–197.
[5] E. H. Lee, L. K. Mansur, and M. H. Yoo, J. Nucl. Mater. 85&86 (1979) 577–581.
[6] V. S. Neustroev, V. K. Shamardin, Z. E. Ostrovsky, A. M. Pecherin, and F. A. Garner, International Symposium on Contribution of Materials Investigation to the Resolution of Problems Encountered in Pressurized Water Reactors, September 14–18, 1998, Fontevraud, France, French Nuclear Energy Society, pp. 261–269.
[7] V. S. Neustroev, Z. E. Ostrovskiy, and V. K. Shamardin, Proceedings of the 7th Russian Conference on Reactor Material Science, September 8–12, 2003, Ministry of the Russian Federation for Atomic Energy, pp. 152–167, in Russian.
[8] O. P. Maksimkin, K. V. Tsai, L. G. Turubarova, T. Doronina, and F. A. Garner, J. Nucl. Mater. 329–333 (2004) 625–629.
[9] O. P. Maksimkin, K. V. Tsai, L. G. Turubarova, T. Doronina, and F. A. Garner, Journal of Nuclear Materials Proceedings of ICFRM-12 (submitted).
[10] S. I. Porollo, Yu. V. Konobeev, A. M. Dvoriashin, A. N. Vorobjev, V. M. Krigan, and F. A. Garner, J. Nucl. Mater. 307–311 (2002) 339–342.
[11] F. A. Garner and M. B. Toloczko, J. Nucl. Mater. 251 (1997) 252–261.
[12] H. Watanabe, A. Aoki, H. Murakami, T. Muroga, and N. Yoshida, J. Nucl. Mater. 155–157 (1988) 815–822.
[13] T. Muroga, H. Watanabe, and N. Yoshida, J. Nucl. Mater. 174 (1990) 282–288.

.

MEASUREMENT OF HELIUM GENERATION IN AISI 304 REFLECTOR AND BLANKET ASSEMBLIES AFTER LONG-TERM IRRADIATION IN EBR-II—F. A. Garner, B. M. Oliver, L. R. Greenwood (Pacific Northwest National Laboratory),[1] D. L. Porter (Idaho National Laboratory), and T. Allen (University of Wisconsin)

OBJECTIVE

The object of this effort is to determine whether potential variations in He/dpa ratio participated significantly in development of void swelling in a data base on AISI 304 stainless steel where relatively large variations in dpa rate were thought to primarily determine the duration of the transient regime of swelling.

SUMMARY

Five hexagonal ducts constructed from AISI 304 stainless steel in the annealed state were removed from rows 8-14 of the EBR-II fast reactor after many years of irradiation to study the effect of atomic displacement rate on void swelling. For this objective it was important to ensure that the observed differences in void swelling were not strongly influenced by variations in helium/dpa ratio. The two major contributions to helium production arise from the nickel and boron content of the steel. However, the boron content was unspecified and therefore unknown, but it was determined from an unirradiated archive duct by converting a well-defined fraction to helium and then measuring the helium content using isotopic dilution mass spectrometry. The same technique was used to measure the total helium in the irradiated duct specimens. After separating the boron contribution from the total measured helium it was possible to determine the contribution from various fast and thermal neutron interactions with the other major elements in the steel and compare the helium generation with predicted values. One important conclusion of the study is that the range of He/dpa ratios over the five subassemblies was not very large, allowing the observed changes in swelling to be attributed primarily to variations in displacement rate and temperature.

PROGRESS AND STATUS

Introduction

Far from the active core regions of a small fast reactor it becomes somewhat more difficult to calculate the helium generation in stainless steel components of the reflector and blanket regions. This is particularly true for components that served many years in EBR-II while the core and reflector regions underwent many modifications, or for components which were moved and sometimes rotated during their lifetime.

In an experiment directed toward determination of the effect of displacement rate on void swelling of annealed AISI 304 stainless steel, it was important to ensure that observed differences in void swelling were primarily in response to displacement rate and not other important variables such as the helium/dpa ratio that might exhibit time-dependent or position-dependent variations [1-3]. Helium is well known to accelerate the nucleation of voids and shorten the transient regime of swelling. However, since there are helium sources associated with both low energy and high energy neutrons, one can not confidently assume that lower flux regions with their inherently softer spectra will lead to consistent decreases or increases in helium generation per dpa. As the high energy source of helium declines the low energy source tends to increase and the net change can move in either direction.

[1]Pacific Northwest National Laboratory (PNNL) is operated for the U.S. Department of Energy by Battelle Memorial Institute under contract DE-AC06-76RLO-1830.

Rather than relying only on calculations of expected helium content for such complicated histories, the helium content was measured directly using an isotopic dilution mass spectrometry method known to be very accurate. Since some significant fraction of the helium in these relatively soft spectral regions arises from transmutation of boron it was necessary to determine the unknown boron content using an archive duct of the same heat of steel.

Experimental Details

The width of the face of these hexagonal ducts is 2.9 cm and the duct is 1 mm thick. Four of the five ducts employed in this study were constructed from the same heat of steel designated 772864 and were irradiated for the majority of their lifetime in rows 8, 9, and 10 of EBR-II, as schematically shown in Fig. 1. The two ducts that were irradiated in row 10 were on opposite sides of the core. The fifth duct was much older and spent most of its residence time in Row 14 but was constructed from an earlier different heat of steel prepared to the same specification but without an available archive, but analyses conducted after irradiation showed that the composition of the two heats was quite similar, as shown in Table 1.

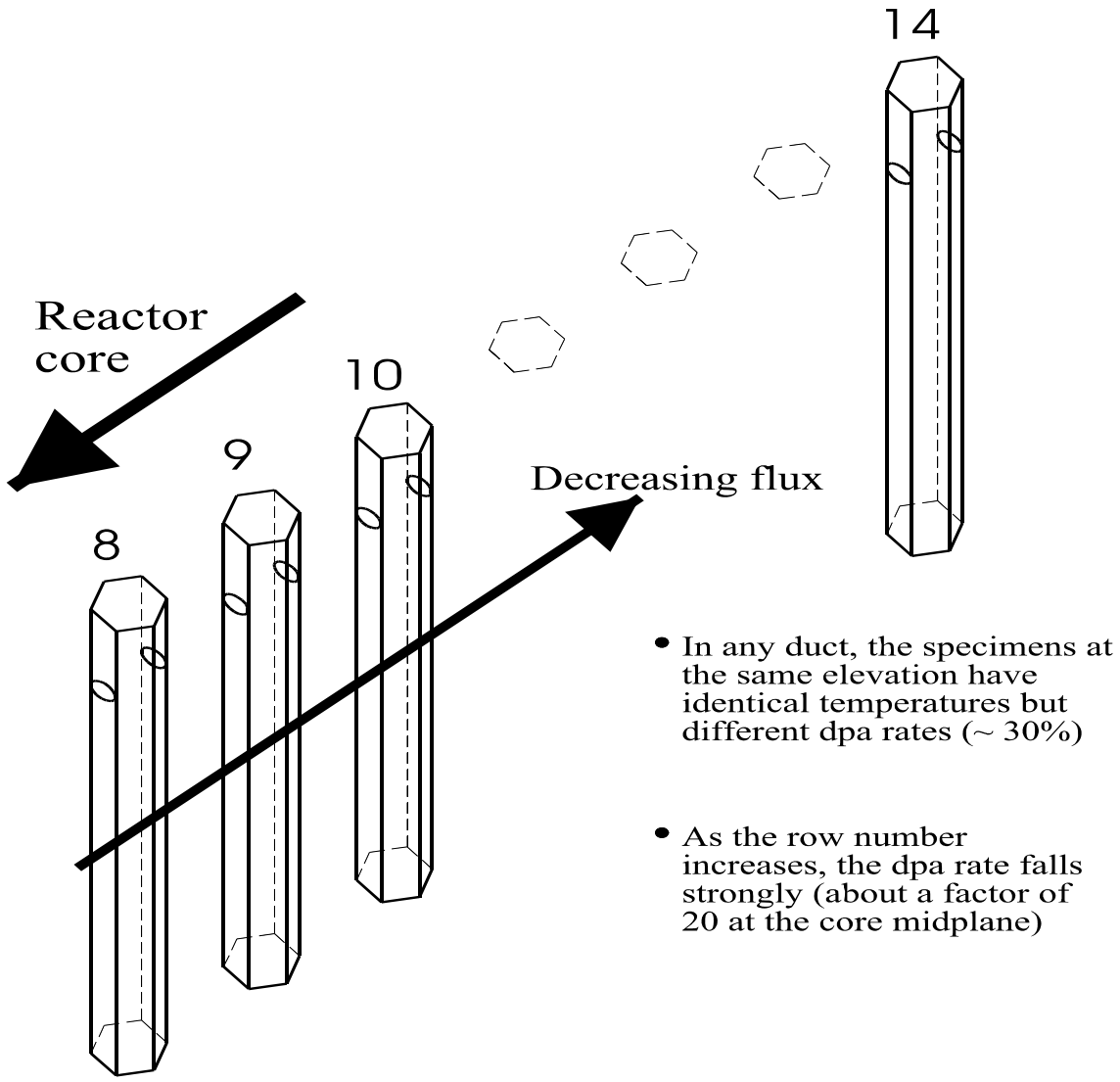

Fig. 1. Schematic representation of flux-effects experiment in EBR-II.

Table 1. Composition of heat 772864 in wt%

	N_2	Mn	Cr	Ni	Co	Cu	Si	Mo	Nb	P	C	S
Vendor Specification for Row 14 duct	----	0.8	18.56	9.05	----	----	0.51	----	----	0.027	0.07	0.003
Measurements at EBR-II on other ducts	0.05	0.832	----	8.20	0.016	0.02	----	0.011	0.001	----	----	----

---- = not specified or measured

As shown in Table 2 and also Fig. 2 these ducts remained in the reflector and blanket regions of EBR-II for different periods spanning many years, with only the two row 10 ducts remaining in the same position and orientation throughout their residence. However, while the row 10 ducts (U9007 and U9009 at 32 and 27 dpa, respectively) were not moved, the core, reflector and blanket regions underwent many significant modifications during this period. During the Liquid Metal Reactor Program the core was expanded to include many lower worth assemblies, with many changes made from run-to-run.

Table 2. Run history and temperature assignments

Assembly	EBR-II Row	MWD in this Row*	Time Fraction	dpa (max)	Temperature Assignment**
U9007	10	187,505	1.00	32.0	average
U9009	10	184,463	1.00	27.0	average
U8972	9	91,166	0.41	33.0	time average
	15	133,785	0.59	1.4	in row 9 only
U9807	8	60,165	0.36	32.0	time average
	16	107,495	0.64	0.9	in row 8 only
U1603	8	5,951	0.02	2.4	time average
	14	348,584	0.98	7.6	in row 14 only

*MWD = megawatt-days

**Temperatures are not relevant to helium production or retention. See references 1 and 3 for details.

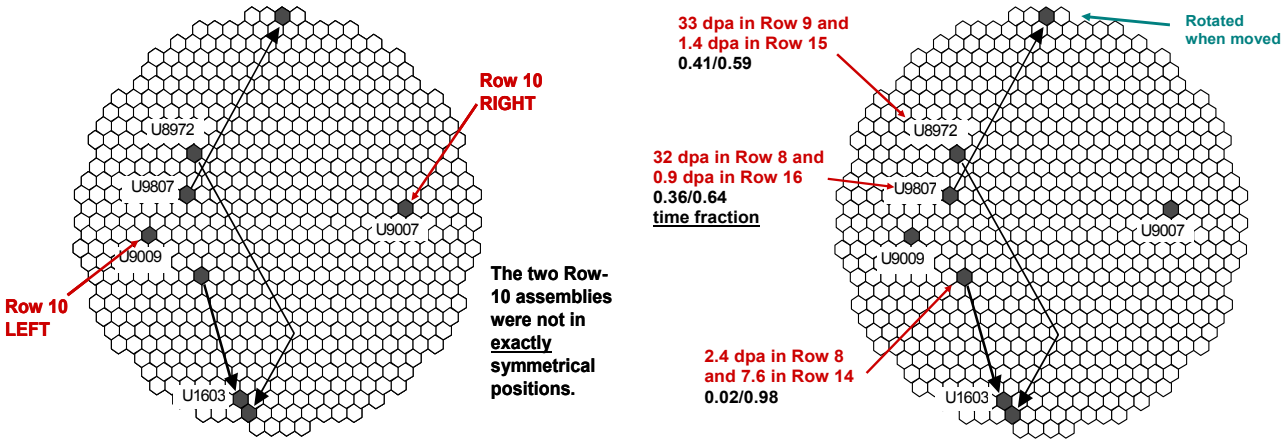

Fig. 2. Schematic representation of assembly location and dose history.

Twenty 2.0 cm diameter specimens spanning a large axial range about the core center-plane were removed from each of the inboard and outboard faces of each duct. The faces examined were defined by the orientation and row where the majority of the dose was accumulated, with inboard-outboard defined relative to the core centerline to maximize the dose difference. The average density of each 2.0 cm disk was measured using an immersion density technique and the results are reported elsewhere [1-3]. After density measurements were completed, smaller specimens averaging ranging from ~2 to ~4 mg were produced from five of the twenty disks from each of the inboard and outboard sides of each duct and used for determination of helium content. A total of 40 specimens were measured, taken from two opposing flats of each assembly.

The time-averaged values of temperature and dpa relevant to each duct and individual specimen were determined at the EBR-II facility of Argonne National Laboratory. These calculations are reported in [3] and the dpa and methods of temperature assignments are shown in Table 2.

An archive duct of the production heat used for ducts in rows 8-10 was obtained and a ~30 mg sample was cut from one of the faces of the duct. For the helium analyses, specimens were prepared from each supplied sample by sectioning using small diagonal cutters. Before each use, the cutters were cleaned by wiping several times with a dry paper wipe. Prior to analysis, each specimen was cleaned in acetone and air-dried. The mass of each specimen was then determined using a calibrated microbalance traceable to the National Institute of Standards and Technology (NIST). Mass uncertainty is estimated to be ±0.002 mg. Sample etching to remove at least 0.013 mm was performed to remove sufficient material to avoid errors associated with α-recoil across specimen surfaces, or surface contamination. Two separate measurements were made on specimens cut from each sample.

Helium analyses were conducted using isotope-dilution gas mass spectrometry following vaporization in a resistance-heated tungsten-wire crucible in one of the helium mass spectrometer system's high-temperature vacuum furnaces [4]. The absolute amount of ^{4}He released was measured relative to a known quantity of added ^{3}He "spike." Each helium spike was obtained by expanding and partitioning a known quantity of gas through a succession of calibrated volumes [5]. Additionally, the mass spectrometer was calibrated for mass sensitivity during each series of runs by analyzing known mixtures of ^{3}He and ^{4}He.

The results of the gas analyses are presented in Figs. 3 and 4 as gas concentrations in atomic parts per million (10^{-6} atom fraction). Conversion from total gas atoms released to gas concentration was based on a calculated value of 1.097×10^{22} atoms/gram for the 304 stainless steel material. It should be noted, however, that this conversion value, and the gas concentrations obtained using it, are not very sensitive to small changes in material composition. Uncertainty in the individual helium analysis results,

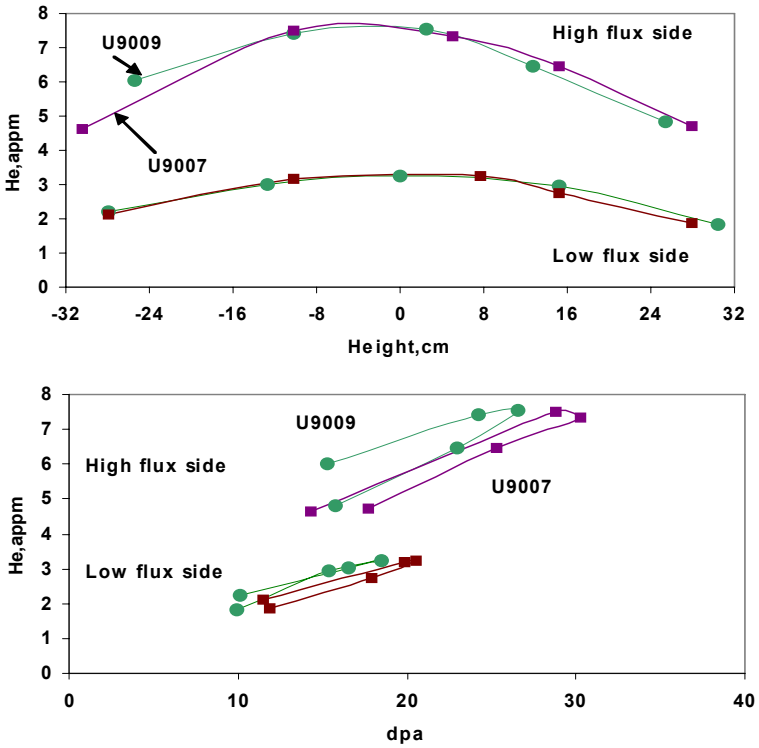

Fig. 3. Helium measurements of the two row 10 assemblies vs. axial location and dpa level. Note the very clear separation in generation rate between the low and high flux sides.

determined from the cumulative uncertainties in the sample mass, the isotope ratio measurement, and the spike size, is estimated to be ~1%.

The boron content in the hex-can sample was determined using a method similar to neutron activation. The sample was exposed to a known dose of thermal neutrons in order to convert a known fraction of the ^{10}B isotope to helium via the ^{10}B (n,α) ^{7}Li reaction. After irradiation, the helium generated was measured in several smaller specimens (~3.5 mg) cut from the sample, and used to determine the boron content, assuming an isotopic abundance of 19.9% for ^{10}B. Neutron dosimetry samples, in the form of a well characterized Al-^{6}Li alloy wire, were included in the irradiation assembly to accurately determine the thermal neutron fluence via the ^{6}Li (n,α) ^{3}H reaction. The thermal neutron cross sections for the ^{10}B and ^{6}Li samples are well known.

The irradiation of the archive specimens was conducted in the research reactor at McMaster University in Canada. The irradiation time and thermal fluence were 160 hours and 2.04 x 10^{19} n/cm^2, respectively. The thermal-to-fast neutron ratio in this spectrum was approximately six, ensuring that >99% of the helium was generated from the boron with no significant amount of helium generated from the major elements, Ni, Fe, Cr, etc.

Results and Discussion

As discussed in references 1 and 2 there was a very clear and consistent effect of flux on void swelling in AISI 304 stainless steel at every temperature studied, providing that some other unrecognized variable did not contribute strongly. For void swelling the helium generation rate is known to often be a strong

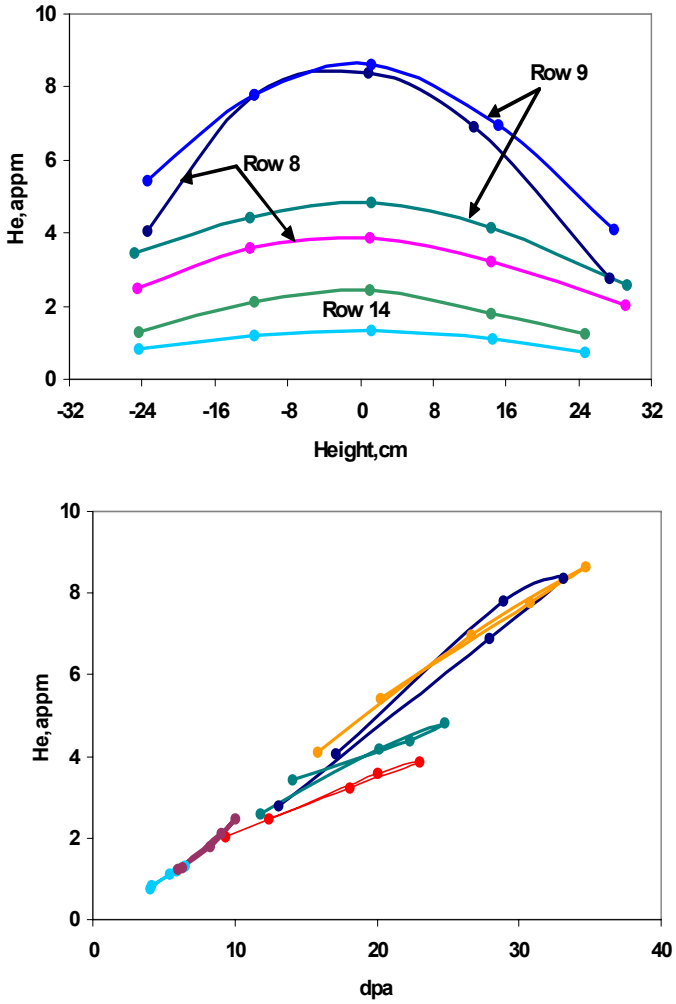

Fig. 4. Helium measurements on assemblies in rows 8, 9, and 14 vs. axial location and dpa level. Higher levels of helium are reached on the inboard face compared to the outboard face.

contributor to the onset of swelling, especially when the steel initially resists swelling [6]. While annealed 304 stainless steel is known not to be very resistant to swelling [6,7], it was prudent to check the possibility that the helium/dpa generation rate might be varying strongly. After measuring the total helium content the first step in assessing its origin lies in the determination of the boron content. The natural boron content in the archive samples was determined in this study to be 1.4 wt. ppm, corresponding to 0.25 wt. ppm ^{10}B, or 1.4 appm ^{10}B) with an uncertainty calculated to be about ± 3%. Therefore, even at complete burnup the maximum helium arising from the ^{10}B source could not exceed 1.4 appm. Most measured helium levels are significantly larger, at minimum a factor of ~2 higher, indicating that the primary helium contributions at higher exposures came from Ni, Fe and Cr.

The results of the helium measurements on the irradiated specimens are shown vs. both position and vs. dpa in Figs. 3 and 4. Note that the two row 10 assemblies have remarkably similar profiles even though the total exposures of the two assemblies are ~16% different. The helium generation rate per dpa on the high flux side of the row 10 assemblies is measurably larger than that of the low flux sides. There is also some small variation in total helium generation between the upper and lower portions of the row 10

assemblies with slightly more helium produced in the lower portion of the assembly. This difference is not so pronounced in the other assemblies and may reflect some influence of their movement during residence. For all subassemblies, however, the He/dpa ratio is relatively independent of axial location as shown in Fig. 5.

When all He concentration data are plotted vs. dpa, it is seen in Fig. 6 that the helium generation rate averages about ~0.25 appm/dpa. While some assemblies lie above or below this average rate, the variations are not large enough or systematic enough to significantly impact the conclusion of a strong dependence of dpa rate on swelling. Together with the finding that the total helium concentration never exceeds 10 appm this allows us to conclude that the range of He/dpa ratios over the five subassemblies is not very large, allowing the observed changes in swelling to be attributed primarily to variations in displacement rate and temperature, with helium playing at most a second-order role.

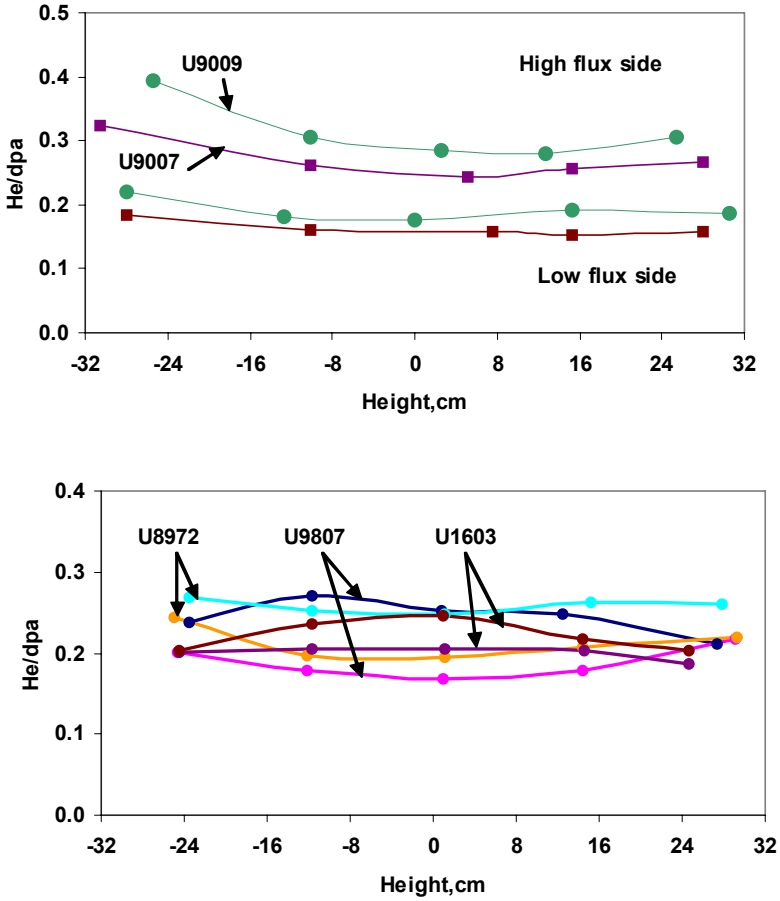

Fig. 5. Helium/dpa ratios of assemblies in row 10 (top) and rows 8, 9 and 14 (bottom) vs. axial location.

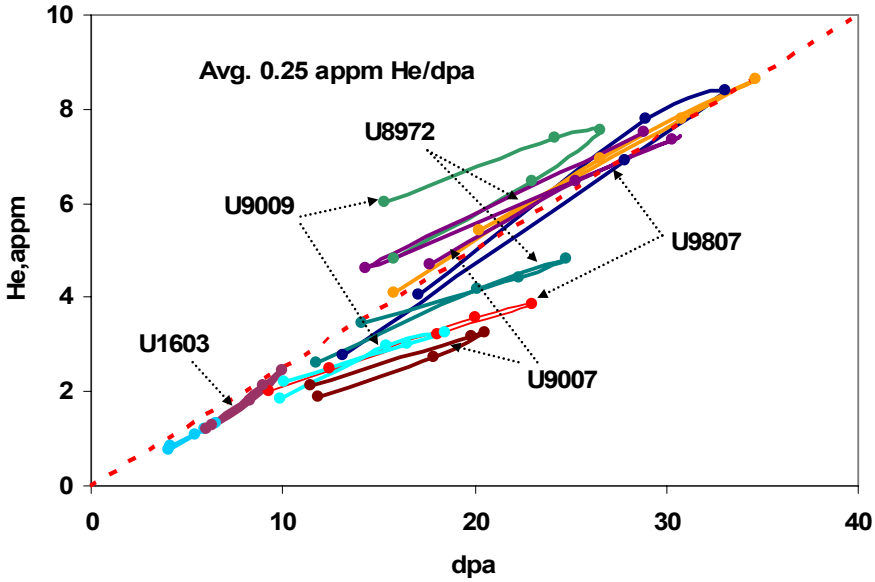

Fig. 6. Compilation of helium measurements for all assemblies vs. dpa level, showing an average generation rate of ~0.25 appm/dpa.

When the components have experienced a complicated history in neutron flux-spectra the need for measurements of time-integrated helium generation can be demonstrated using calculated flux-spectra that were available early in the life of EBR-II. Detailed flux-spectra derived from the EBR-II reactor low power dosimetry run designated 78C were available for comparison [8] and the total integrated time were used to make comparisons between 78C-based calculations and our measurements. However, the core has undergone numerous changes in local experimental loading over the lifetime of these assemblies. With exception of U1603 (in the core from run 25 to 170), all assemblies were put into reactor during runs 95-118, and stayed through runs 166-170. During the lifetime of these assemblies EBR-II underwent significant expansion to accommodate a growing number of experimental subassemblies. This expansion tended to reduce the local neutron flux over time.

As shown in Fig. 7 the 78C-based predictions of dpa are indeed significantly larger than those calculated for the mid-point of the assemblies, with the magnitude of over-prediction increasing strongly at lower row numbers. Note that significantly more helium was measured in row 10 than was predicted. Figure 8 shows that the predicted helium for row 8 is also significantly lower than measured in row 8, but also for rows 9 and 14.

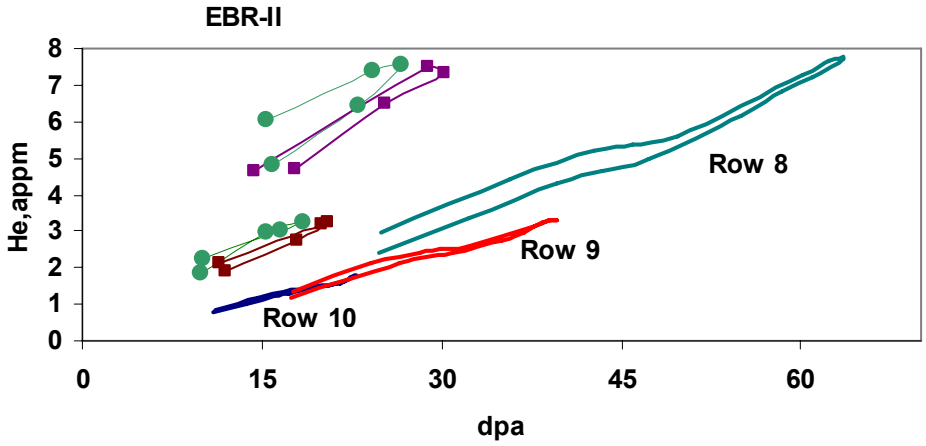

Fig. 7. Comparison of measured values of helium for the two row 10 assemblies vs. predicted values (calculated at assembly center) for rows 8, 9 and 10. Note that the measured values of helium for row 10 assemblies are significantly larger than predicted.

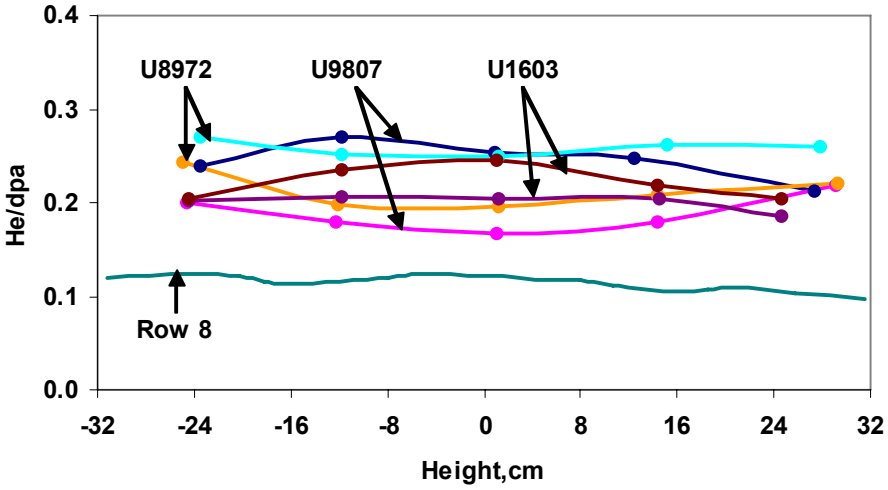

Fig. 8. Comparison of measured values of helium/dpa vs. axial location for assemblies in rows 8, 9 and 14 vs. prediction for Row 8. Note that significantly more helium is generated in row 8 than was predicted.

This apparently contradictory set of conclusions is a reflection of the fact that helium is generated primarily by nickel in a Fe-Cr-Ni alloy, but there are two competing reactions [9-14]. The first helium contribution arises from a high-energy reaction (n, α) with threshold energy of ~1 MeV. As the core expanded the average neutron flux and energy both tended to decrease in the reflector region. On the other hand the low-energy two-step ^{58}Ni (n, γ) ^{59} Ni (n, α) ^{56}Fe reaction sequence increases in importance in softer spectra and dominates the helium production in this experiment. In addition the ^{10}B (n,α) ^{7}Li reaction also becomes more important in softer spectra.

These Run 78C predictions confirm two aspects of the measured behavior**.** First, Fig. 7 shows that there is indeed a tendency for slightly higher helium generation rates in the lower portion of the core compared

to the upper portion. Second, Fig. 8 shows that the He/dpa rate is relatively constant along the axial direction of a given assembly, both in agreement with the results of the current study.

Conclusions

The helium generated in AISI 304 stainless steel during irradiation in the EBR-II fast reactor is a sensitive function of neutron flux-spectra. When the flux-spectra vary over the residence time of a long-lived component it becomes more difficult to predict the accumulated helium, especially when the time history of the component is complicated and when the components reside in the blanket and reflector regions of the reactor.

In such cases the helium is best measured using techniques such as isotope-dilution gas mass spectrometry. If it is desirable to predict the relative contributions of high-energy (n, α), low energy ^{58}Ni (n, γ) ^{59}Ni (n, α) ^{56}Fe and low energy ^{10}B (n,α) ^{7}Li reactions, then the detailed composition of the steel must be known. When the boron concentration has not been measured then the ^{10}B (n,α) ^{7}Li reaction can be used with archive material to determine its concentration and contribution to helium production. In a complicated time-history experiment where it was important to know the relative roles of He/dpa ratio and dpa rate, it was demonstrated in this report that the He/dpa ratio did not vary strongly among the experimental samples and was most likely only a variable of second-order importance compared to the effect of dpa rate on void swelling of AISI 304 stainless steel.

References

[1] G. M. Bond, B. H. Sencer, F. A. Garner, M. L. Hamilton, T. R. Allen, and D. L. Porter, Void Swelling of Annealed 304 Stainless Steel at ~370-385°C and PWR-Relevant Displacement Rates, 9th International Conference on Environmental Degradation of Materials in Nuclear Power Systems—Water Reactors, 1999, 1045–1050.
[2] F. A. Garner, D. J. Edwards, S. M. Bruemmer, S. I. Porollo, Yu. V. Konobeev, V. S. Neustroev, V. K. Shamardin, and A. V. Kozlov, Recent Developments Concerning Potential Void Swelling of PWR Internals Constructed from Austenitic Stainless Steels, Proceedings of Fontevraud 5, Contribution of Materials Investigation to the Resolution of Problems Encountered in Pressurized Water Reactors, September 23–27, 2002, paper #22, on CD.
[3] F. A. Garner, M. L. Hamilton, D. L. Porter, T. R. Allen, T. Tsutsui, M. Nakajima, T. Kido, T. Ishii, Determination of Damage Rate Dependence of Void Swelling of Solution-Annealed 304 Stainless Steel Using Irradiated EBR-II Reflectors (in preparation).
[4] B. M. Oliver and H. Farrar, Mass Spectrometer System to Determine Very Low Levels of Helium in Small Solid and Liquid Samples, J. Vacuum Sci. Technol. A4 (1986) 1740.
[5] B. M. Oliver, J. G. Bradley, and H. Farrar, Helium Concentration in the Earth's Lower Atmosphere, Geochimica Cosmochimica Acta 48 (1984) 1759.
[6] F. A. Garner, Chapter 6: Irradiation Performance of Cladding and Structural Steels in Liquid Metal Reactors, Materials Science and Technology: A Comprehensive Treatment, Vol. 10A Nuclear Materials, B. R. T. Frost (ed.), VCH Publishers, 1994, 419–543.
[7] F. A. Garner and D. L. Porter, A Reassessment of the Swelling Behavior of AISI 304L Stainless Steel, International Conference on Dimensional Stability and Mechanical Behavior of Irradiated Metals and Alloys, Brighton, England, 1983, 41–44.
[8] F. C. Franklin, E. R. Ebersole, and R. R. Heinrich, Analysis of EBR-II Low-Power Dosimetry Run 78C, Argonne National Laboratory Report, Vol. ANL-77-76, 1977.
[9] L. R. Greenwood, F. A. Garner, and B. M. Oliver, Helium Generation Rates in Isotopically Tailored Fe-Cr-Ni Alloys Irradiated in FFTF/MOTA, J. Nucl. Mater. 191–194 (1992) 1051–1055.
[10] F. A. Garner, L. R. Greenwood, and D. L. Harrod, Potential High Fluence Response of Pressure Vessel Internals Constructed from Austenitic Stainless Steels, Sixth International Symposium on Environmental Degradation of Materials in Nuclear Power Systems—Water Reactors, San Diego, Calif., 1993, 783–790.
[11] L. R. Greenwood, F. A. Garner, and B. M. Oliver, An Assessment of the Ni-59 Isotopic Tailoring

Technique to Study the Influence of Helium/dpa Ratio, J. Nucl. Mater. 212–215 (1994) 492–497.
[12] F. A. Garner, L. R. Greenwood, and B. M. Oliver, A Reevaluation of Helium/dpa and Hydrogen/dpa Ratios for Fast Reactor and Thermal Reactor Data Used in Fission-Fusion Correlations, ASTM STP 1325, Effects of Radiation on Materials: 18th International Symposium, American Society of Testing and Materials, R. K. Nanstad, M. L. Hamilton, F. A. Garner, and A. S. Kumar (eds.), 1999, 794–807.
[13] F. A. Garner, B. M. Oliver, and L. R. Greenwood, The Dependence of Helium Generation Rate on Nickel Content of Fe-Cr-Ni Alloys Irradiated at High dpa Levels in Fast Reactors, J. Nucl. Mater. 258–263 (1998) 1740–1744.
[14] F. A. Garner and L. R. Greenwood, Survey of Recent Developments Concerning the Understanding of Radiation Effects on Stainless Steels Used in the LWR Power Industry, 10th International Conference on Environmental Degradation of Materials in Nuclear Po1wer Systems—Water Reactors, 2003, 887–909.

LOW-TEMPERATURE MECHANICAL PROPERTIES OF Fe-0.06C-18Cr-10Ni-0.4Ti AUSTENITIC STEEL DETERMINED USING RING-PULL TENSILE TESTS AND MICROHARDNESS MEASUREMENTS—V. S. Neustroev, E. V. Boev (Research Institute of Atomic Reactors, Dimitrovgrad, Russia), and F. A. Garner (Pacific Northwest National Laboratory)[1]

OBJECTIVE

The object of this effort is to determine the mechanical behavior of austenitic stainless steels during neutron irradiation, using techniques frequently employed in Russia but not commonly applied in the USA.

SUMMARY

Irradiated austenitic stainless steels removed from Russian water-cooled VVERs experience irradiation temperatures and He/dpa conditions that are very similar to steels to be used in ITER. Data are presented on the radiation hardening of the Russian analog of AISI 321 at 0.2 to 15 dpa in the range of 285 to 320°C. The Russian variant of the ring-pull tensile test was used to obtain mechanical property data. Microhardness tests on the ring specimens provide useful information throughout the deformed regions, but at high hardening levels caution must be exercised before application of a widely accepted hardness-yield stress correlation to prediction of tensile properties. Low-nickel austenitic steels are very prone to form deformation martensite, a phase that increases strongly with the larger deformation levels characteristic of microhardness tests, especially when compared to the 0.2% deformation used to define yield stress.

PROGRESS AND STATUS

Introduction

Light water-cooled power reactors and first generation fusion devices such as ITER share certain similarities with respect to the environmental conditions experienced by the major structural materials, which are austenitic stainless steels. These conditions are relatively low operating temperatures, water-cooling, relatively high helium/dpa ratios and relatively low dpa rates compared to those of typical fast reactors. In Russia and the USA attention is now directed toward low-temperature irradiation-hardening, low-temperature void swelling and void-induced embrittlement of PWR and VVER-1000 austenitic internals [1-4].

Experimental Procedure

Test specimens were cut from thin-wall instrument guide tubes located in fuel assemblies of several VVER-1000 reactors after 3-4 years of irradiation to doses of 0.2 to 15 dpa in the range of 285 to 320°C [5]. Dpa levels were calculated using the standard NRT formulism and temperatures were assumed to be that of the local water temperature, an assumption that is appropriate for thin-wall tubes with water on both sides. The temperature is known within ±2 ºC.

The tubes were constructed from Fe-0.06C-18Cr-10Ni-0.4Ti steel (Russian analog of AISI 321) in the austenized state (1050ºC, 30 min, AC) and were 12.6 mm in diameter with wall thickness of 0.8 mm. The specimens were cut to produce rings of 3 mm length. The rings were deburred, cleaned and lightly polished prior to testing.

Note that the Russian variant of the ring-pull test involves no local reduction in the ring diameter to produce thin gauge sections as frequently employed in other studies [6-8]. This standardized test [9,10] is frequently employed in the states of the former Soviet Union and allows tests to be performed on irradiated tubes without expensive mechanical or electrical machining. Results of other studies using this test technique have recently been reported [11,12].

[1]Pacific Northwest National Laboratory (PNNL) is operated for the U.S. Department of Energy by Battelle Memorial Institute under contract DE-AC06-76RLO-1830.

Mechanical properties on both irradiated and unirradiated specimens were determined via tensile tests and microhardness measurements conducted on the ring-shaped specimens. Tensile tests were conducted at temperatures between 20 and 800ºC, but microhardness measurements were conducted only at 20ºC. The tensile test proceeded with a deformation rate of ~1 mm/min. Figure 1 shows the geometry of this test configuration. The measurement error of mechanical properties via this test is estimated at ~5%.

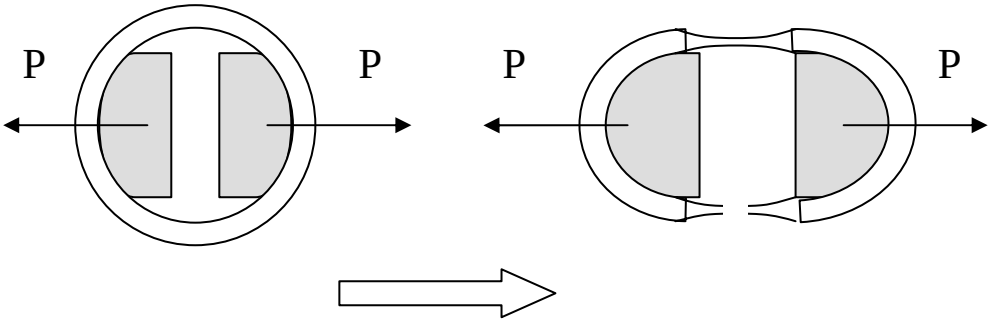

Fig. 1. Schematic diagram showing loading and testing of tube rings in a ring-pull test. Note that two regions on opposite sides of the tube are being deformed, but only one will fail and terminate the test. The non-failed ligament can be used to measure the approach to failure along the full length of the ligament. P indicates the force applied to separate the two mandrels in side the ring.

Microhardness was measured remotely using ring specimens mounted on a mandrel. A standard diamond pyramid indenter was forced into a specimen using 100g load and the microhardness calculated from the size of the indentation. The measurement error of the microhardness is estimated at ~2%.

Results

Figure 2 presents the yield stress measured at 20^{o}C for the irradiation temperature range 285 to 320^{o}C as a function of dpa. The measured yield stress increase was approximated by a formula used by Kalinin and coworkers to process data for ITER application [13].

$$\Delta\sigma = A\sqrt{1 - e^{(-Kt/D_0)}} \qquad (1)$$

Factor A characterizes the saturation level of yield stress increase in MPa. The factor D_o describes the duration of the transient regime and Kt is the damage dose, where the latter two parameters are both in dpa. In this data set D_o at 20ºC is 4.7 dpa, independent of irradiation temperature over this limited range. The factor A is 600 MPa for tests conducted at 20ºC.

A similar dependence (Fig. 3) was obtained for microhardness. Factor A at 20ºC in this case is equal to 230 kg/mm^2 when factor D_o was chosen to be 4.7 dpa to match that of the yield stress increase. The ratio between saturation levels of increases in yield stress and microhardness at damage doses of about 9-15 dpa was found to be 2.61.

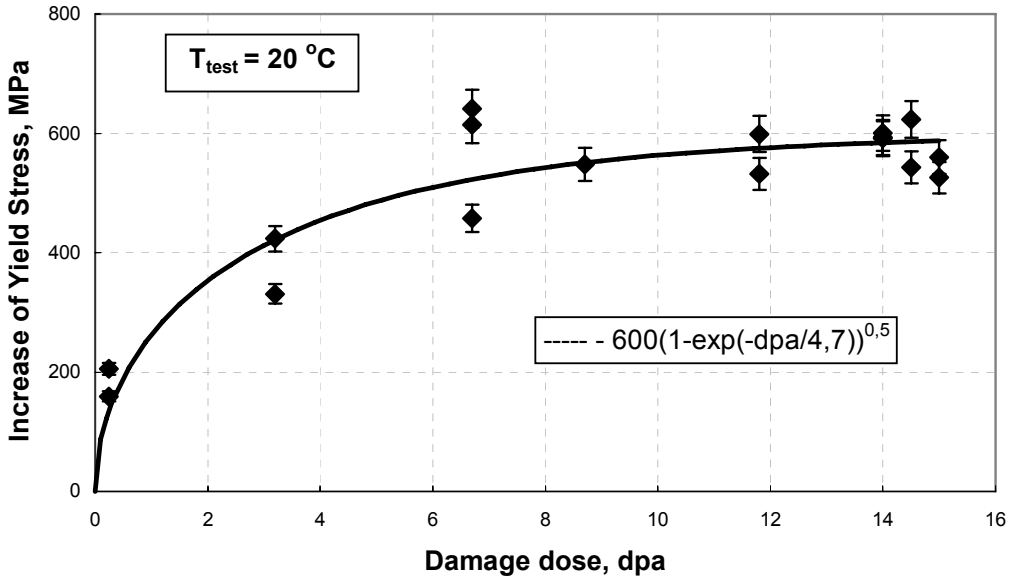

Fig. 2. Dose dependence of yield stress increase.

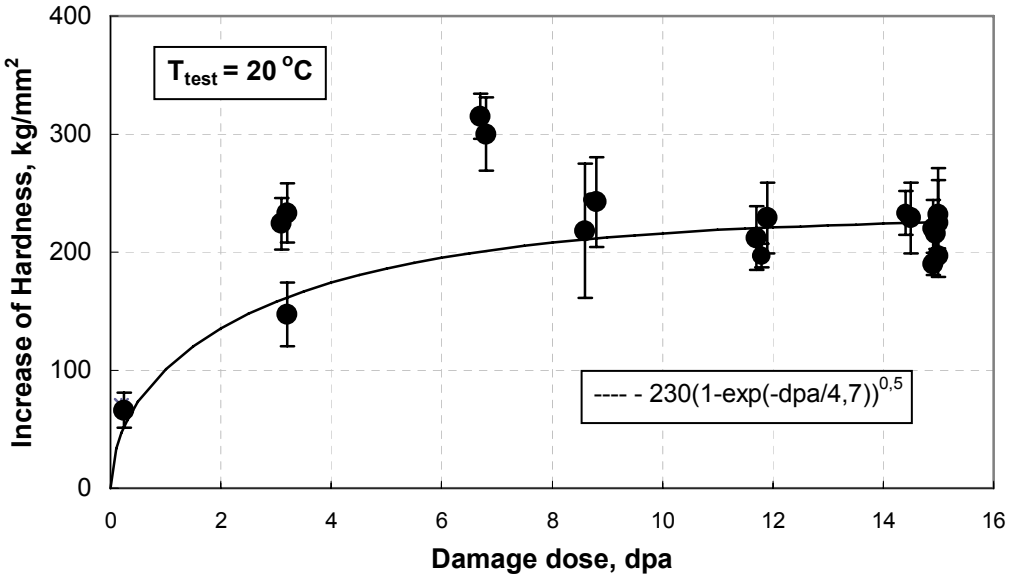

Fig. 3. Dose dependence of microhardness increase.

The ring specimen has another positive feature from the viewpoint of microhardness examination. Since the specimen has two working ligaments, and rupture usually occurs only in one of them, there is another deformed but still intact ligament on the other side of the ring where the specimen progressively narrows toward the likely failure position. This “narrowing” area allows microhardness change measurements in the longitudinal direction, i.e., at progressively changing deformation levels within the ligament.

In non-irradiated specimens, changes of microhardness with distance from the rupture are easily observed (Fig. 4). In this case a noticeable strain hardening is observed that is consistent with an increase of deformation-induced dislocation density. The local deformation was calculated by measuring the local thickness decrease of the non-irradiated specimen at a given distance from the thinnest section. In the irradiated specimen the strain hardening was much lower, as seen in the lack of variability in the hardness vs. distance curve, a behavior consistent with the hardening induced by high densities of small Frank loops during irradiation [14].

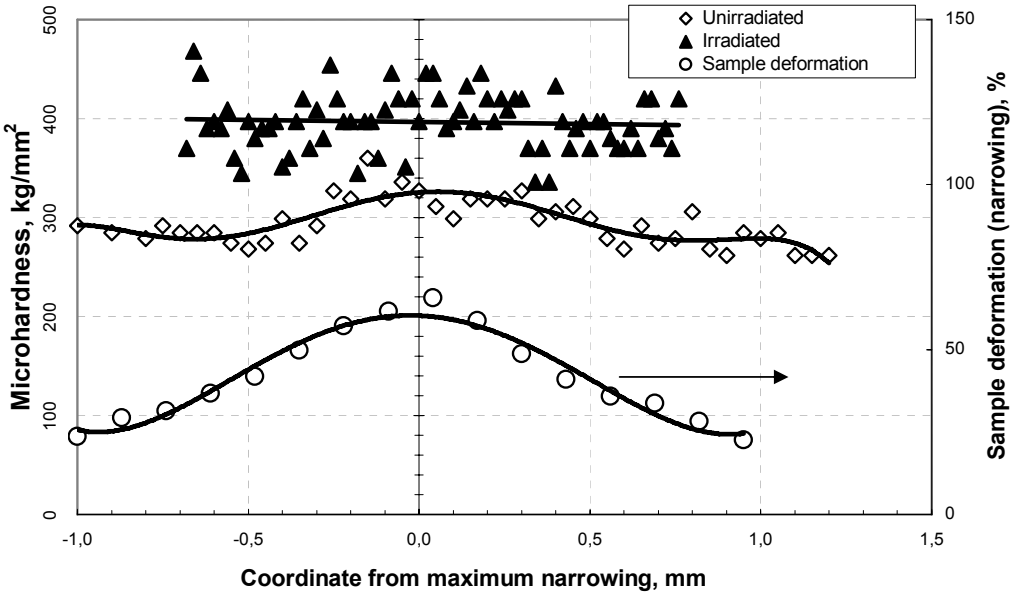

Fig. 4. Changes of microhardness in unirradiated and irradiated (290°C, 8.4 dpa) specimen of Fe-0.06C-18Cr-10Ni-0.4Ti austenitic stainless steel. Narrowing of the unirradiated specimen is also shown.

Discussion

Busby and his colleagues [15] analyzed and published an extensive correlation of published yield stress and microhardness data on austenitic steels (AISI 316, 347 and 304) irradiated in both fast reactors and thermal reactors. A ratio of $\Delta\sigma_{0.2}/\Delta H_{\mu} = 3.03$ was obtained when the changes in tensile and hardness properties, rather than their absolute values, were used. Busby noted that published data frequently involved complicating factors that might account for the scatter associated with these results. One of the most important sources of scatter was the tendency to conduct tensile tests at the irradiation temperature while the hardness tests were made at room temperature. Gusev and coworkers [16] recently conducted a similar study on Fe-0.06C-16Cr-11.4Ni-1.6Mn-1.8Mo steel irradiated in the BN-350 fast reactor, but noted that additional scatter might arise from specimens that were irradiated in flowing sodium. Such exposure changes both the composition of the near-surface region but also frequently produces an undetected ferrite layer on the surface.

Hardness measurements are more sensitive to such surface modifications than are tensile measurements which involve the full thickness of the specimen. In Gusev's study the surface layers were removed before testing and the correlation coefficient was found to be 2.96, essentially identical to the 3.03 of Busby.

In this paper, however, we observe for Fe-0.06C-18Cr-10Ni-0.4Ti a correlation coefficient of only 2.61 derived using all the data, but we can not ascribe this lower value solely to surface modification. The compositional and phase changes observed during sodium exposure do not occur to any significant degree in the water coolant of PWRs and VVERs. Note that when we compare our data with that of Busby's compilation and also that of Gusev in Fig. 5, we see that our lower exposure data initially tend to follow a correlation coefficient of ~3 but then plateau out at yield stresses of ~600 MPa for hardness increases >200kg/mm^2. This behavior was not observed by Gusev, however.

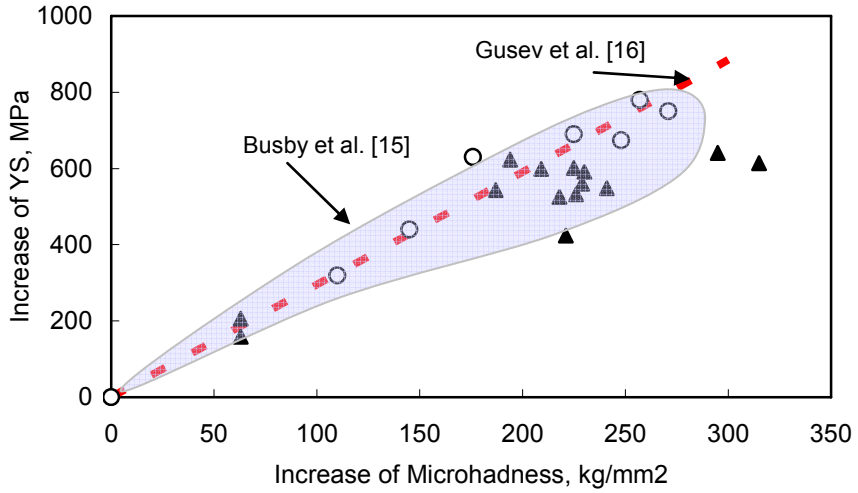

Fig. 5. Correlation between yield stress increase and microhardness increase of Fe-0.06C-18Cr-10Ni-0.4Ti austenitic stainless steel after low-temperature irradiation in VVER-1000 reactors. Also shown are the data band of Busby and coworkers [15] and the data (o) and trend line (---) of Gusev and coworkers on Fe-16Cr-11.4Ni-1.6Mn-1.8Mo irradiated in BN-350 [16].

The difference between our results and those of Gusev lie primarily in the composition of the steels and not the radiation/coolant environment. The Fe-16Cr-11.4Ni-1.6Mn-1.8Mo steel of Gusev has higher nickel content than our steel, and is therefore more resistant to formation of deformation martensite. Microhardness measurements involve much greater amounts of local deformation when compared to that associated with yielding.

In an earlier study Kadyrzhanov and Maksimkin clearly showed that in Fe-0.06C-18Cr-10Ni-0.4Ti steel that the microhardness behavior of this steel is strongly determined by martensite formation as compared with the behavior of yield stress and other characteristics of mechanical properties [17]. Martensite instability is enhanced by lower test temperatures and the strength and microchemical changes induced by irradiation, shifting the regime of martensite formation to higher temperatures. Experiments currently underway appear to confirm that martensite formation in our rings increases strongly with increasing deformation moving from the relatively undeformed to strongly deformed regions in the unbroken ligament.

Conclusions

Ring-pull tensile tests on tube sections can be used to measure radiation-induced hardening, and when coupled with microhardness measurements can be used to study and make predictions of anticipated mechanical behavior for both light water reactors and ITER.

The development of radiation-induced hardening in Fe-0.06C-18Cr-10Ni-0.4Ti austenitic steel irradiated in VVER-1000 reactors at ~300°C reaches a saturation level of 600 MPa at ~5 dpa at T_{test}=20 °C. The tensile hardening relationship can be described by

$$\Delta\sigma_{0,2} = A\sqrt{1 - e^{(-Kt/D_0)}}$$

where D_o is 4.7 dpa, and the factor A [MPa] depends on test temperature.

A similar relationship can be used to describe the increase in microhardness with D_o = 4.7 dpa and A = 230 kg/mm^2 for tests conducted at 20°C.

At higher hardness levels reached during low temperature irradiation the well-established correlation between changes in yield stress and microhardness breaks down for low nickel steels when deformed at room temperature. The breakdown is suggested to arise from the onset of deformation martensite, a process that impacts microhardness measurements much more than it affects determination of yield stress.

References

[1] F. A. Garner, L. R. Greenwood, and D. L. Harrod, Sixth International Symposium on Environmental Degradation of Materials in Nuclear Power Systems—Water Reactors, TMS, 1993, p. 783.
[2] V. S. Neustroev, V. K. Shamardin, Z. E. Ostrovsky, A. M. Pecherin, and F. A. Garner, Proceedings of the Fontevraund IV International Symposium, Contribution of Materials Investigation to the Resolution of Problems Encountered in Pressurized Water Reactors, 1998, Vol. 1, 261–270.
[3] S. I. Porollo, A. N. Vorobjev, Yu. V. Konobeev, A. M. Dvoriashin, V. M. Krigan, N. I. Budylkin, E. G. Mironova, and F. A. Garner, J. Nucl. Mater. 258–263 (1998) 1613–1621.
[4] V. M. Troyanov, Yu. I. Lihachev, M. Ya. Khmelevsky, V. I. Tsofin, N. V. Shary, V. P. Yuremenko, V. K. Shamardin, V. I. Prokhorov, V. S. Neustroev, Proceedings of the 5th Russian Conference of Reactor Materials Science, Dimitrovgrad, Russia, 1998, Vol. 2, Part 1, 3–24.
[5] V. S. Neustroev, V. G. Dvoretzky, Z. E. Ostrovsky, V. K. Shamardin, and G. A. Shimansky, Effects of Radiation on Materials, 21st International Symposium, ASTM STP 1447, M. L. Grossbeck, T. R. Allen, R. G. Lott, and A. S. Kumar (eds.), ASTM International, West Conshohocken, Pa., 2004, 32–45.
[6] J. L. Seran, V. Levy, P. Dubuisson, D. Gilbon, A. Maillard, A. Fissolo, H. Touron, R. Cauvin, A. Chalony, and E. Le Boulbin, Effects of Radiation on Materials: 15th International Symposium, ASTM STP 1125, R. E. Stoller, A. S. Kumar, and D. S. Gelles (eds.), ASTM International, West Conshohocken, Pa., 2004, 1209–1233.
[7] R. S. Daum, S. Majundar, H. Tsai, T. S. Bray, D. A. Koss, A. T. Motta, and M. C. Billone, Small Specimen Test Techniques: Fourth Volume, ASTM STP 1418, M. A. Sokolov, J. D. Landis, and G. E. Lucas (eds.), ASTM International, West Conshohocken, Pa., 2004, 195–210.
[8] T. Yoshitake, Y. Abe, N. Akasaka, N. Ohtsuka, S. Ukai, and A. Kimura, J. Nucl. Mater. 329–333 (2004) 342–346.
[9] Ring-Pull Test Standard 086-288-99, Dimitrovgrad, Russia, State Scientific Centre, Research Institute of Atomic Reactor, 1999, in Russian.
[10] O. Yu. Makarov, V. I. Prokhorov, A. V. Goryachev, V. P. Smirnov, L. A. Egorova, E. P. Kaplar, and K. V. Lyutov, Proceedings of the 6th Russian Conference on Reactor Material Science (September 11–15, 2000, Dimitrovgrad), 2001, Vol. 2, Part 2, 209–220.
[11] S. I. Porollo, A. M. Dvoriashin, Yu. V. Konobeev, and F. A. Garner, J. Nucl. Mater. 329–333 (2004) 314–318.
[12] A. M. Dvoriashin, S. I. Porollo, Yu. V. Konobeev, N. I. Budylkin, E. G. Mironova, and F. A. Garner, Journal of Nuclear Materials (accepted), Proceedings of ICFRM-12.
[13] G. M. Kalinin, B. S. Rodchenkov, and V. A. Pechenkin, J. Nucl. Mater. 329–333 (2004) 567–574.
[14] V. S. Neustroev, Z. E. Ostrovsky, Ye. V. Boev, and S. V. Belozyorov, Evolution of Microstructure of Fe-18Cr-10Ni-Ti Stainless Steel Irradiated in VVER-1000 Reactors and Its Correlation with Hardness, Report on main research works performed in 2004, Dimitrovgrad, FSUE SSC RIAR, 2005, 85–87.
[15] J. T. Busby, M. C. Hash, and G. S. Was, J. Nucl. Mater. 336 (2005) 267–278.

[16] M. N. Gusev, O. P. Maksimkin, O. V. Tivanova, N. S. Silnaygina, and F. A. Garner, Correlation of Yield Stress and Microhardness in 08Cr16Ni11Mo3 Irradiated to High Dose in the BN-350 Fast Reactor, Journal of Nuclear Materials (in press).
[17] K. K. Kadyrzhanov and O. P. Maksimkin, Martensitic Transformation in Neutron Irradiated and Helium Implanted Stainless Steels, Effects of Radiation on Materials, 21st International Symposium, ASTM STP 1447, M. L. Grossbeck, T. R. Allen, R. G. Lott, and A. S. Kumar (eds.), ASTM International, West Conshohocken, Pa., 2004, 105–119.

7.0 MHD INSULATORS, COATINGS, INSULATING CERAMICS, AND OPTICAL MATERIALS

COMPATIBILITY ISSUES FOR A HIGH TEMPERATURE DUAL COOLANT BLANKET – B. A. Pint
(Oak Ridge National Laboratory, USA)

OBJECTIVE

One proposed U.S. test blanket module (TBM) for ITER uses ferritic-martensitic alloys with both eutectic Pb-Li and He coolants at ~475°C. In order for this blanket concept to operate at higher temperatures (~750°C) for a DEMO-type reactor, several Pb-Li compatibility issues need to be addressed. A SiC/SiC composite flow channel insert is proposed to reduce the steel dissolution rate (and the magnetohydrodynamic pressure drop). Prior capsule testing examined dense, high-purity SiC in Pb-Li at 800°-1200°C and found detectable levels of Si in the Pb-Li after 2,000h at 1100°C and 1,000h at 1200°C. Current capsule experiments are examining several different SiC/SiC composite materials at 1000°C. Another issue involves Pb-Li transport between the first wall and heat exchanger. Aluminide coatings on type 316 stainless steel and Al-containing alloys capable of forming an external alumina scale have been studied in capsule experiments at 700° and 800°C.

SUMMARY

Compatibility experiments are being conducted to support higher temperature Pb-Li dual coolant concepts. Based on prior work on monolithic SiC at 1100°-1200°C, SiC/SiC specimens were evaluated at 1000°C. The high O content in the commercial PbLi led to oxide layer formation on monolithic SiC specimens and small mass changes for composite materials. Further characterization is needed to determine the degree of interaction observed for the composite specimens. Aluminum-containing alloys and aluminide coatings performed well in PbLi at 800°C compared to uncoated 316SS. Model aluminide coatings made by chemical vapor deposition reduced the dissolution rate for 316SS at 800°C by a factor of 50. The superior compatibility performance of the alloys containing Y and Zr dopants suggests that similar additions may be beneficial for the performance of protective aluminide coatings in this temperature range. Higher resolution characterization of the thin alumina layer is needed to determine the effect of exposure to Pb-Li.

PROGRESS AND STATUS

Introduction

A recent focus of the U.S. fusion energy program has been on developing a proposal for a test blanket module (TBM) for ITER. The dual coolant Pb-Li (DCLL) TBM concept has both He and eutectic Pb-Li coolants and uses ferritic steel as the structural material and a SiC/SiC composite flow channel insert (FCI).[1] The interest in this concept has focused compatibility-related research on Pb-Li. Many materials have poor compatibility with liquid Li,[2] but the activity of Li is much lower in Pb-17Li,[3] and this allows a wider range of materials to be considered. However, Pb-Li still readily dissolves many conventional alloys. While the TBM maximum operating temperature will be <500°C, this blanket concept would be more attractive for a reactor with a higher maximum operating temperature, perhaps >700°C if oxide dispersion strengthened ferritic steels[4] were used. However, at these higher temperatures, compatibility is even more of a concern. Therefore, static capsule testing is being conducted on SiC/SiC composites and corrosion resistant coatings are being investigated to protect metallic components.

Experimental Procedure

Static capsule tests were performed using dense chemical vapor deposited (CVD) β-SiC (99.9995% purity) or Mo inner capsules and type 304 stainless steel or alloy 600 outer capsules to contain the inner capsule and prevent oxidation. When an unsealed CVD SiC inner capsule was used, a welded

intermediate Mo capsule also was included.[5] The specimens were held in the bottom of the CVD SiC crucible with a CVD SiC spacer. For Mo inner capsules, the specimens were hung with Mo wire. The capsules were loaded with either commercial Pb-17Li or high purity (99.9999%) Pb shot and Li in an argon-filled glove box. Specimens were (1) monolithic CVD SiC (3 x 8 x 12mm), (2) sintered NITE[6] SiC matrix material (provided by T. Hinoki at Kyoto Univ.), (3) SiC/SiC composites (3 x 8 x 12mm coupon, Figures 1a and 1b) supplied by B. Riccardi at ENEA, Italy, and ~11mm OD tube supplied by H. Feinroth at Gamma Engineering, Figures 1c and 1d), (4) type 316 stainless steel (316SS) and (5) Al-containing alloys (Table 1). The alloy specimens were ~1.5mm thick and 4-5cm^2 in surface area with a 0.3µm surface polish. The Al-containing alloys were pre-oxidized for 2h at 1000°C in dry, flowing O_2 to form an external Al_2O_3 scale. Two specimens of 316SS were CVD aluminized for 4h at 1050°C in a laboratory scale reactor and then immediately annealed for 2h at the same temperature.[7,8] These conditions produce a ~200µm thick coating with and a ~20µm thick Al-rich outer layer, $(Fe,Ni)_3Al$. One of the coated specimens was pre-oxidized for 2h at 800°C in laboratory air. Specimen mass was measured before and after exposure on a Mettler-Toledo balance with an accuracy of ±0.04mg. Exposures were performed in resistively heated box furnaces for 1000h.

To remove residual Pb-Li after exposure, the specimens were soaked in a mixture of acetic acid, hydrogen peroxide and ethanol for 24-72h. The composition of the Pb-Li after testing was determined by inductively coupled plasma analysis and combustion analysis. Post-test surfaces were examined using Auger electron spectroscopy (AES) and secondary electron microscopy (SEM). Cross-sections of the metal specimens were examined using electron probe microanalysis (EPMA).

Results and Discussion

SiC/SiC compatibility with Pb-Li. Prior work on CVD SiC specimens in Pb-Li showed dissolution (detectable Si levels in the PbLi after exposure) after 2,000h at 1100°C and 1,000h at 1200°C.[9,10] No dissolution was detected after 5,000h at 800°C. Therefore, the present testing was performed at 1000°C

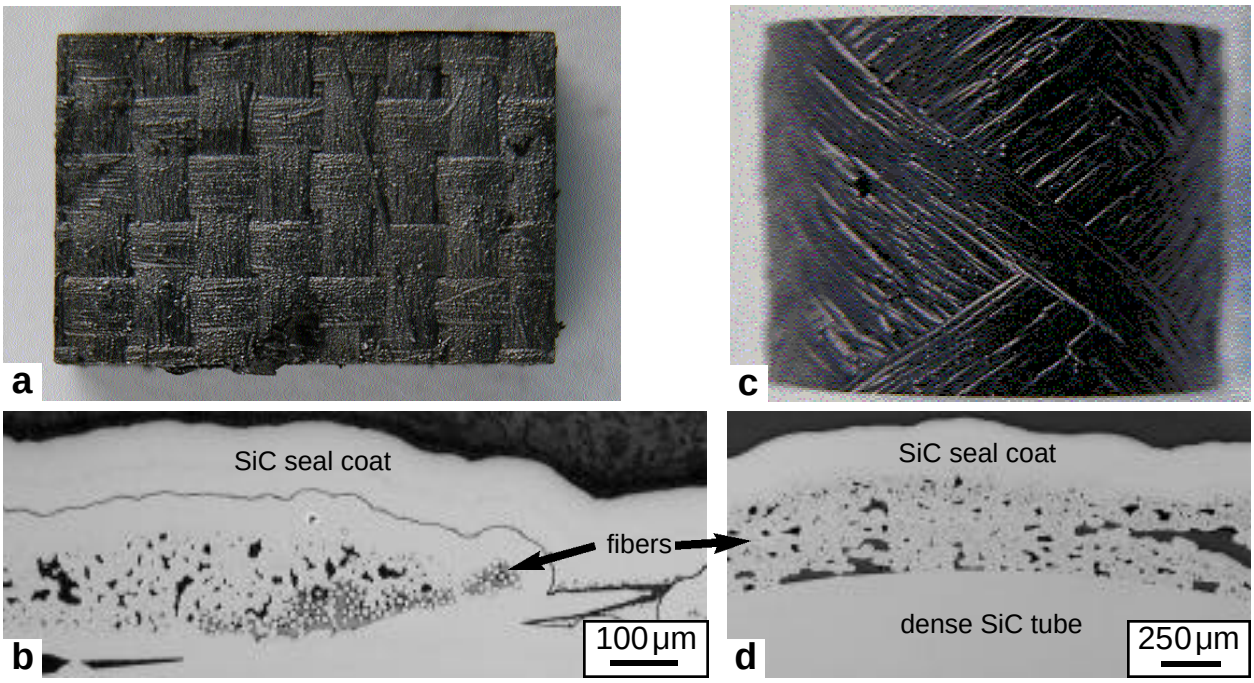

Figure 1. Photographs (a,c) of the SiC/SiC specimens and (b,d) polished sections showing the dense SiC seal coat on the surface of both composites. (a,b) coupon supplied by E.U. and (c,d) U.S. supplied tube.

Table 1. Alloy chemical compositions (atomic% or ppma) determined by inductively coupled plasma analysis and combustion analysis.

Material	Fe	Ni	Cr	Al	O	C	N	S	Other
316SS	65.1	8.9	19.9	0.02	490	3360	2380	68	1.94Si,1.67Mn, 1.38Mo,0.21Cu
ODS FeCrAl	67.8	0.02	20.0	10.6	7430	340	210	50	0.44Ti,0.23Y 0.04Si, 0.04Mn
Fe-28Al-2Cr+Zr	70.0	<	2.0	27.9	70	400	<	46	0.026Zr, 0.005Hf
Ni-42.5Al	<	57.3	<	42.6	40	380	<	<	<

< indicates below the detectability limit of <0.01% or <0.001% for interstitials

on SiC/SiC composites. This temperature is much higher than would be used for a DCLL FCI but SiC/SiC composites also are being evaluated for structural materials in higher temperature concepts.[11] The specimens were exposed in individual CVD SiC crucibles to avoid cross contamination. These exposures were recently completed so only initial characterization results are currently available.

Unlike the previous tests on CVD SiC where high purity Pb and Li were heated together in the capsule test, commercially prepared Pb-17Li was used for these tests. The major difference was higher N, C and especially O contents in the starting commercial material, Table 2. (Based on the high Li-O affinity and prior results, the high O content likely suppressed the measured Li in the commercial PbLi.) Initially, one specimen of CVD SiC was exposed. Prior work with high purity Pb and Li at 800°-1200°C typically showed mass changes of ±0.01 mg/cm^2.[9,10] With commercial Pb-Li, the mass gain was much higher at 1,000°C (Figure 2). Wetting of the specimens by Pb-Li did not occur after exposure at 800°C[12] but did occur in this case. Some residual PbLi was removed during cleaning, ~150 mg. Because the CVD SiC is fully dense, there is little opportunity for liquid metal penetration and there was no evidence of such in the prior work. Thus, the likely explanation for the mass gain is the formation of a surface oxide layer. For comparison, the mass gain for a CVD SiC specimen isothermally exposed for 1,000h at 1000°C in laboratory air also is shown in Figure 2. The mass gain for the sintered SiC NITE matrix sample was

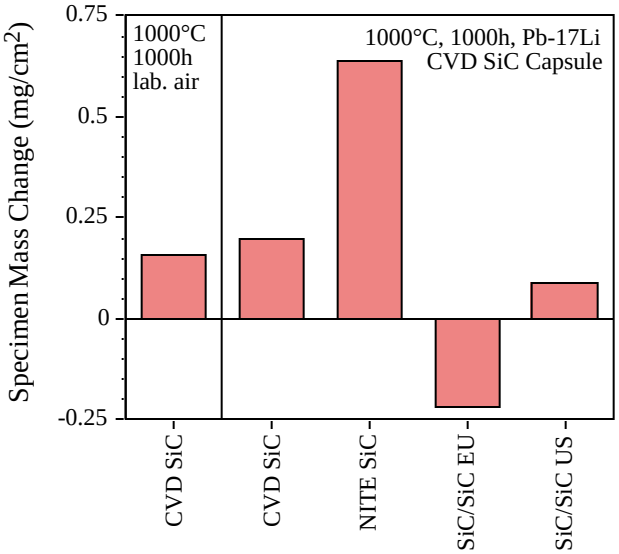

Figure 2. Specimen mass change for SiC and SiC/SiC composite specimens after 1,000h at 1000°C in commercial Pb-17Li.

Table 2. Chemical composition using inductively coupled plasma and combustion analysis of the starting Pb, commercial Pb-Li ingot and the Pb-Li after capsule exposures at 800°C for 1000h (in ppma except for Li in atomic%).

Test	Li	Fe	Cr	Ni	Mn	Si	Al	Mo	C	O	N	S
Starting Pb	n.d.	<4	<4	<4	<4	<40	<8	<2	<170	1270	<40	<50
Comm. PbLi	14.3%	<30	<70	<30	<30	<120	<60	<40	750	4820	180	<50
316SS	16.5%	<30	<30	**270**	<30	<120	<60	<20	480	2040	<40	<50
316SS+Al	17.6%	<30	<30	<30	<30	<120	<60	<20	590	1370	<40	<50
316SS+Al/O	17.5%	<30	<30	<30	<30	<120	<60	<20	730	2100	<40	<50
FeCrAl	17.3%	<30	<30	<30	<30	<120	<60	**90**	460	5280	<40	<50
Fe_3Al	16.3%	<30	<30	<30	<30	<120	<60	<20	540	1230	<40	<50
NiAl	16.7%	<30	<30	**150**	<30	<120	<60	<20	520	2640	<40	<50

significantly higher than the CVD SiC specimen. This may be due to reaction with the Al-Y-Si oxide sintering aid.[6]

The mass gains for the two SiC/SiC composite specimens after cleaning are shown in Figure 2. Because of the possibility of liquid metal becoming entrapped in the composite during exposure, the net mass change may be a combination of oxidation (mass gain), dissolution (mass loss) and mass gain due to entrapped metal. The mass changes should not be used to compare the relative behavior of these materials. Significant differences in behavior can be attributed to a dense SiC seal coat on the composites (Figures 1c and 1d) which may prevent interaction of the fibers and fiber interfaces with PbLi. Both the EU and US SiC/SiC specimens were seal coated on the outer surfaces but the fibers were exposed on the cut sides. Complete characterization of the PbLi chemistry and composite microstructure is needed to fully evaluate the differences between these materials.

Using AES, the initial post-exposure characterization of the reaction products on the CVD SiC specimens has been performed. The oxide formed during oxidation in air at 1000°C was uniform across the specimen and ~6.5 μm thick. In contrast, the oxide formed in PbLi at 1000°C was not uniform in thickness. In some areas the oxide was only 0.1 μm thick. In other areas, oxide nodules containing Fe and Si were observed. The source of Fe is not apparent. No Pb or Li was detected in the surface oxide.

In order to test the experimental procedure, a CVD SiC specimen also was exposed in a Mo capsule instead of a CVD SiC capsule. The mass gain was almost identical. The oxidation of the specimens in the commercial PbLi may have obscured any difference between the tests. Future work with commercial PbLi may require purification of the PbLi or gettering during the capsule test.

Corrosion Resistant Coatings in Pb-Li. Because of the low activity of Li in Pb-17Li, alloys or coatings that form an adherent external Al_2O_3 scale should be resistant to dissolution in Pb-Li.[13] This has been confirmed at fairly modest temperatures.[14,15] Similar aluminide coatings also are being evaluated as tritium permeation barriers.[16] To assess the potential performance of aluminide coatings or alumina-forming alloys at higher temperatures, some baseline compatibility data are being examined using static capsule testing. The first experiments were conducted on model materials (Table 1). A Fe_3Al composition was selected as being similar to aluminide coatings formed on Fe-base alloys[7,8] and a Ni-42Al composition is similar to the composition of a CVD aluminide coating on a Ni-base alloy.[17] In addition, an ODS FeCrAl (Plansee alloy PM2000) was tested as this alloy could be used without a coating. Based on positive results for these model materials at 700°C,[9,10] the model materials as well as CVD aluminide coatings on 316SS substrates were tested at 800°C for 1,000 h using high purity Pb and Li.

Table 3. Mass change of specimens after 1000h at 800°C in Pb-17Li with a Mo capsule

Specimen	Pre-oxidation	Mass Change (mg)	Mass Change (mg/cm^2)
316SS	none	-79.51	-17.30
316SS + CVD Al	none	- 1.55	- 0.34
316SS + CVD Al	2h at 800°C	- 1.93	- 0.43
ODS FeCrAl	2h at 1000°C	+ 1.58	+ 0.24
Fe-28Al-2Cr+Zr	2h at 1000°C	- 1.55	- 0.37
Ni-42.5Al	2h at 1000°C	-12.12	- 2.72

The mass change results after exposure and cleaning are shown in Table 3. The selective removal of Ni (e.g. see Ref. 18) produced a very high mass loss from the uncoated type 316SS specimen. Aluminized type 316SS substrates showed much lower mass gains, Table 3. Figure 3 summarizes the observations for 316SS at 700° and 800°C in Pb-17Li and shows the improvement due to aluminizing. However, pre-oxidation of the coating for 2h at 800°C did not result in a decrease in the amount of dissolution. Similar low mass changes were observed for the ODS FeCrAl and Fe_3Al specimens, Figures 4a and 4b. The Fe_3Al specimen had one ~3 mm diameter region of bare metal (arrow in Figure 4b) which may explain the mass loss. The NiAl specimen (Figure 4c) showed a more substantial loss (>50%) of the oxide layer after exposure and a larger mass loss, Table 3. One obvious reason for the oxide spallation is the lack of reactive element (e.g. Y or Zr) in this material compared to the other alumina-formers, Table 1. These dopants promote alumina scale adhesion.[19]

All of these specimens have been examined in plan-view by SEM and in cross-section using EPMA. No Pb was detected in any of the cross-sections. The post-test Pb-Li chemistry is shown in Table 2. The depleted surface layer on uncoated 316SS was similar to that observed at 700° with lower levels of Ni, Mn and Si and increased Mo content, Figure 5. However, the layer thickness increased from ~6µm at 700°C to ~20µm at 800°C and the Cr depletion was not as severe as observed at 700°C.[9] Dissolved Ni was detected in the PbLi chemistry, Table 2.

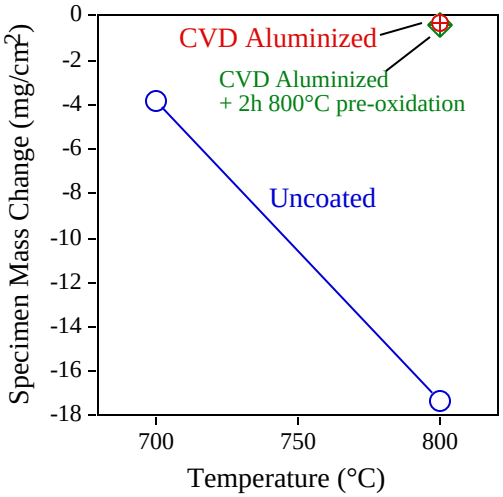

Figure 3. Specimen mass loss after 1,000h in Pb-17Li as a function of temperature for uncoated and coated type 316 stainless steel.

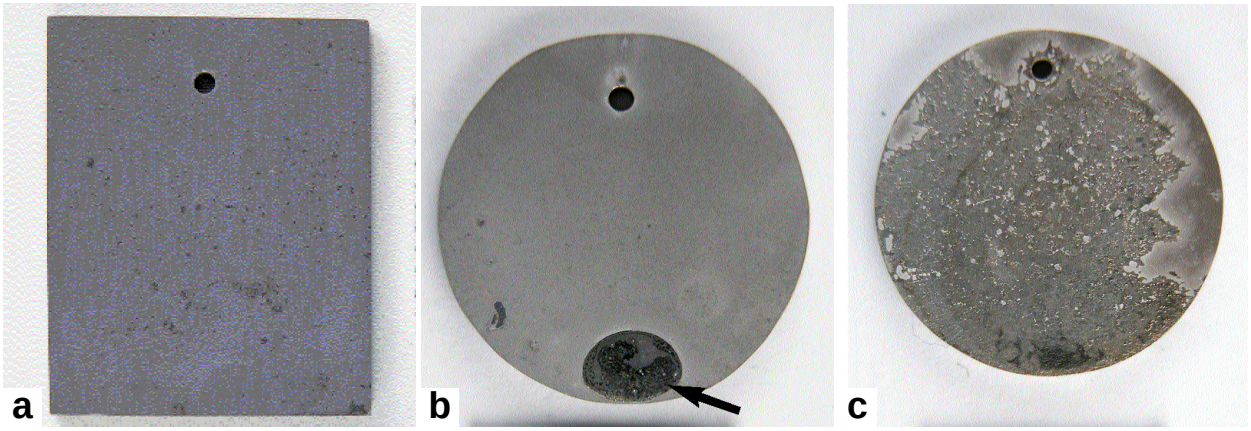

Figure 4. Photographs after exposure for 1000h at 800°C in PbLi (a) ODS FeCrAl, (b) Fe-28Al-2Cr+Zr and (c) NiAl.

Figures 6a and 6b show the aluminized coating after exposure. As predicted, the total coating thickness was ~200µm with a ~20µm outer layer, shown in Figure 6b. This layer was enriched in Ni and Al, Figure 4. However, in some regions the Ni content was much lower (dashed line in Figure 7) which may be due to local dissolution.

Figure 6c shows a cross-section of the NiAl specimen. No Ni depletion was detected in the metal, but in areas without an oxide layer, there appeared to be recession of the metal (arrow). Figure 6d shows the alumina scale formed on ODS FeCrAl, which was similar to that formed on Fe_3Al. The thin alumina scale was difficult to characterize but, in plan-view (Figure 8b), appeared to have a much larger grain size than was observed after a 2h pre-oxidation (Figure 8a). The grains are the size expected after exposures at ~1300°C,[20] suggesting accelerated grain growth during the Pb-Li exposure at 800°C. Larger grains are

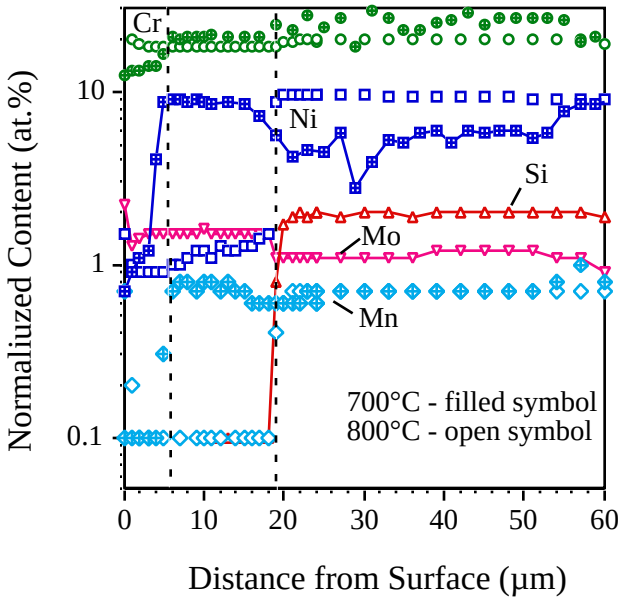

Figure 5. Composition line profiles of a polished cross-section of 316SS after exposure in Pb-17Li for 1,000h at 700°C (filled symbols) and 800°C (open symbols). The depletion zone increases with exposure temperature.

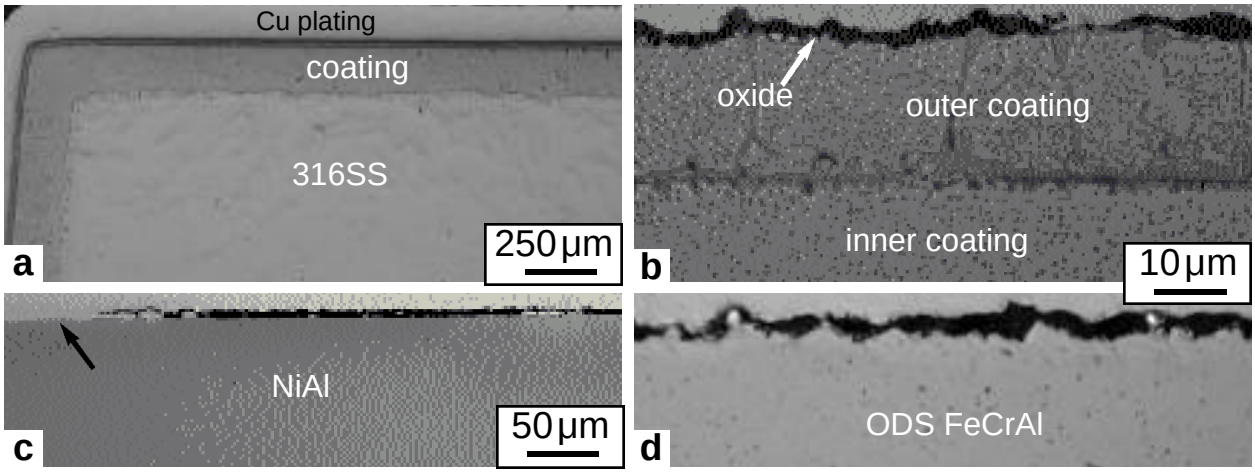

Figure 6. Light microscopy images of specimens after 1000h at 800°C in Pb-Li. (a) Aluminized 316SS, and pre-oxidized (b) aluminized 316SS, (c) NiAl and (d) ODS FeCrAl. Arrow in (c) shows missing oxide layer.

sometimes associated with the formation of a Fe-rich surface oxide. Further characterization is needed. Prior work on alumina layers exposed to Pb-Li concluded that the oxide was degraded during exposure.[21]

An important future step in this work will be to conduct experiments in flowing Pb-Li with a temperature gradient. Static capsule experiments can only produce limited compatibility information because saturation of one or more dissolving components can inhibit further reaction.

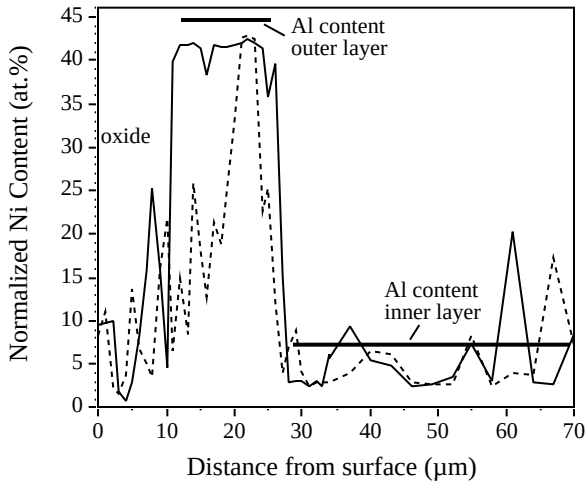

Figure 7. Nickel profiles from aluminized 316SS. The outer layer is rich in Ni and Al but in some regions (dashed line) this outer layer has been depleted.

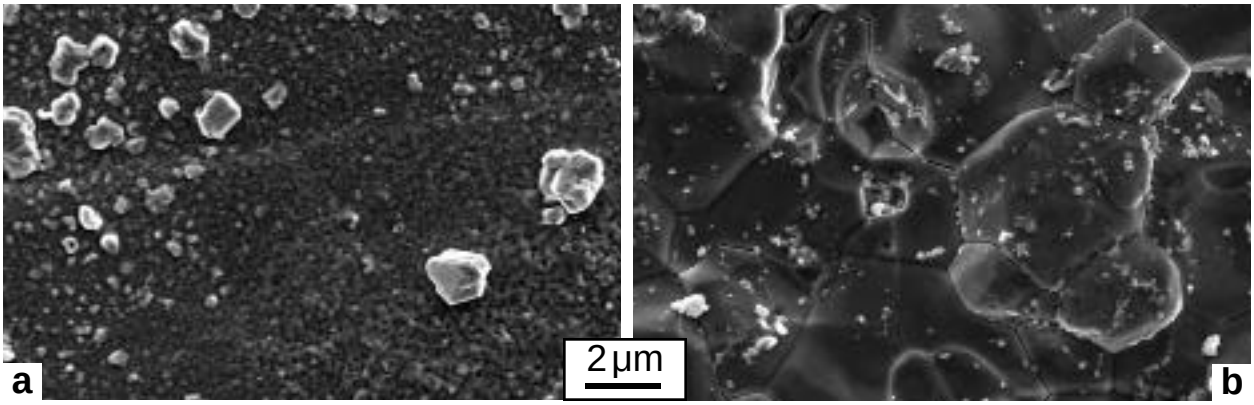

Figure 8. SEM secondary electron plan-view image of the oxide on ODS FeCrAl (a) after oxidation for 2h at 1000°C and (b) after oxidation and exposure to PbLi at 800°C.

References

[1] M. Abdou, D. Sze, C. Wong, M. Sawan, A. Ying, N. B. Morley, and S. Malang, Fusion Sci. Technol. 47 (2005) 475.
[2] J. E. Battles, Int. Mater. Rev. 34 (1989) 1.
[3] P. Hubberstey, J. Nucl. Mater. 247 (1997) 208.
[4] S. Ukai and M. Fujiwara, J. Nucl. Mater. 307 (2002) 749.
[5] B. A. Pint, L. D. Chitwood, and J. R. DiStefano, DOE/ER-0313/35 (2003) 13.
[6] Y. Katoh, A. Kohyama, T. Nozawa, and M. Sato, J. Nucl. Mater. 329-333 (2004) 587.
[7] Y. Zhang, B. A. Pint, J. A. Haynes, I. G. Wright, and P. F. Tortorelli, Oxid. Met. 62 (2004) 103.
[8] Y. Zhang, B. A. Pint, G. W. Garner, K. M. Cooley, and J. A. Haynes, Surf. Coat. Technol. 188-189 (2004) 35.
[9] B. A. Pint, J. L. Moser, and P. F. Tortorelli, Journal of Nuclear Materials (submitted).
[10] B. A. Pint J. L. Moser and P. F. Tortorelli, Fusion Eng. Des. 81 (2006) 901.
[11] R. H. Jones, L. Giancarli, A. Hasegawa, Y. Katoh, A. Kohyama, B. Riccardi, L. L. Snead, and W. J. Weber, J. Nucl. Mater. 307-311 (2002) 1057.
[12] B. A. Pint, K. L. More, H. M. Meyer, and J. R. DiStefano, Fusion Sci. Technol. 47 (2005) 851.
[13] P. Hubberstey, T. Sample, and A. Terlain, Fusion Technol. 28 (1995) 1194.
[14] H. Glasbrenner, Z. Peric, and H. U. Borgstedt, J. Nucl. Mater. 233-237 (1996) 1378.
[15] H. Glasbrenner, J. Konys, Z. Voss, and O. Wedemeyer, J. Nucl. Mater. 307-311 (2002) 1360.
[16] J. Konys, A. Aiello, G. Benamati, and L. Giancarli, Fuson Sci. Technol. 47 (2005) 844.
[17] Y. Zhang, W. Y. Lee, J. A. Haynes, I. G. Wright, B. A. Pint, K. M. Cooley, and P. K. Liaw, Met. Trans. 30A (1999) 2679.
[18] P. F. Tortorelli, J. Nucl. Mater. 191-194 (1992) 965.
[19] B. A. Pint, Oxid. Met. 45 (1996) 1.
[20] B. A. Pint, P. F. Tortorelli, and I .G. Wright, Mater. High Temp. 16 (1999) 1.
[21] T. Sample, A. Perujo, H. Kolbe and B. Mancinelli, J. Nucl. Mater. 283-287 (2000) 1272.

8.0 BREEDING MATERIALS

No contributions

9.0 RADIATION EFFECTS, MECHANISTIC STUDIES, AND EXPERIMENTAL METHODS

No contributions

10.0 DOSIMETRY, DAMAGE PARAMETERS, AND ACTIVATION CALCULATIONS

No contributions

11.0 MATERIALS ENGINEERING AND DESIGN REQUIREMENTS

No contributions

12.0 IRRADIATION FACILITIES AND TEST MATRICES

No contributions